The Galactic plane in gamma-rays above 10 TeV as seen with H.E.S.S.

Dissertation

zur Erlangung des akademischen Grades
'doctor rerum naturalium'
(Dr. rer. nat.)
in der Wissenschaftsdisziplin 'Astroteilchenphysik'

vorgelegt von

Iryna Lypova

Mathematisch Naturwissenschaftlichen Fakultät
der Universität Potsdam

September 2020

Disputation erfolgt am 30. März 2021

1. Gutachter: Prof. Dr. Christian Stegmann
2. Gutachter: Prof. Dr. Jamie Holder
3. Gutachter: Prof. Dr. Lutz Wisotzki

Published online on the
Publication Server of the University of Potsdam:
https://doi.org/10.25932/publishup-50931
https://nbn-resolving.org/urn:nbn:de:kobv:517-opus4-509317

Abstract

The High Energy Stereoscopic System (H.E.S.S.) is an array of five imaging atmospheric Cherenkov telescopes located in the Khomas Highland of Namibia. H.E.S.S. operates in a wide energy range from several tens of GeV to several tens of TeV, reaching the best sensitivity around 1 TeV or at lower energies. However, there are many important topics – such as the search for Galactic PeVatrons, the study of gamma-ray production scenarios for sources (hadronic vs. leptonic), EBL absorption studies – which require good sensitivity at energies above 10 TeV. This work aims at improving the sensitivity of H.E.S.S. and increasing the gamma-ray statistics at high energies. The study investigates an enlargement of the H.E.S.S. effective field of view using events with larger offset angles in the analysis. The greatest challenges in the analysis of large-offset events are a degradation of the reconstruction accuracy and a rise of the background rate as the offset angle increases. The more sophisticated direction reconstruction method (DISP) and improvements to the standard background rejection technique, which by themselves are effective ways to increase the gamma-ray statistics and improve the sensitivity of the analysis, are implemented to overcome the above-mentioned issues. As a result, the angular resolution at the preselection level is improved by 5 - 10% for events at 0.5° offset angle and by 20 - 30% for events at 2° offset angle. The background rate at large offset angles is decreased nearly to a level typical for offset angles below 2.5°. Thereby, sensitivity improvements of 10 - 20% are achieved for the proposed analysis compared to the standard analysis at small offset angles. Developed analysis also allows for the usage of events at large offset angles up to approximately 4°, which was not possible before. This analysis method is applied to the analysis of the Galactic plane data above 10 TeV. As a result, 40 sources out of the 78 presented in the H.E.S.S. Galactic plane survey (HGPS) are detected above 10 TeV. Among them are representatives of all source classes that are present in the HGPS catalogue; namely, binary systems, supernova remnants, pulsar wind nebulae and composite objects. The potential of the improved analysis method is demonstrated by investigating the more than 10 TeV emission for two objects: the region associated with the shell-type SNR HESS J1731−347 and the PWN candidate associated with PSR J0855−4644 that is coincident with Vela Junior (HESS J0852−463).

Kurzfassung

H.E.S.S. ist eine System von fünf abbildenden atmosphärischen Cherenkov Teleskopen im Khomas-Hochland von Namibia. H.E.S.S. arbeitet in einem weiten Energiebereich von einigen zehn GeV bis zu einigen zehn TeV und erreicht die beste Sensitivität um 1 TeV oder bei niedrigeren Energien. Es gibt jedoch viele wichtige Themen – wie die Suche nach galaktischen PeVatrons, die Untersuchung von Gammastrahlen-Produktionsszenarien für Quellen (hadronische vs. leptonische), EBL-Absorptionsstudien – die eine gute Sensitivität bei Energien oberhalb von 10 TeV erfordern. Diese Arbeit zielt darauf ab die Sensitivität von H.E.S.S. zu verbessern und die Gammastrahlenstatistik bei Energien über 10 TeV zu erhöhen. Untersucht diese Studie das effektive Gesichtsfeld von H.E.S.S. durch die Verwendung von Ereignissen mit größeren Versatzwinkeln in der Analyse (insbesondere bis zu 4° anstelle von 2.5°) zu vergrößern. Die größten Herausforderungen bei der Analyse von Ereignissen mit großem Versatzwinkeln sind eine Verschlechterung der Rekonstruktionsgenauigkeit und ein Anstieg der Hintergrundrate mit zunehmendem Versatzwinkeln. Die ausgefeiltere Richtungsrekonstruktionsmethode (DISP) und Verbesserungen der Standard-Hintergrundunterdrückungstechnik (die selbst auch wirksame Methode zur Erhöhung der Gammastrahlenstatistik und zur Verbesserung der Sensitivität der Analyse sind) sind zur Überwindung der oben genannten Probleme eingesetzt. Infolgedessen wird die Winkelauflösung auf der Vorselektionsebene um 5 - 10% für 0.5° und um 20 - 30% für 2° Versatzwinkeln verbessert. Die Hintergrundrate bei großen Versatzwinkeln wird fast auf ein Niveau gesenkt, das bei Versatzwinkeln unter 2.5° typisch ist. Letztendlich erreicht die hierentwickelte Analysis eine ein um 10 - 20% verbesserte Sensitivität bei kleinen Versatzwinkeln und erlaubt die Verwendung von Ereignissen bei großen Versatzwinkeln bis zu etwa 4°, was vorher nicht möglich war. Diese Analysemethode wird bei der Analyse der Daten der Galaktischen Ebene oberhalb von 10 TeV angewandt. Als Ergebnis werden 40 der 78 Quellen, die in der H.E.S.S. Durchmusterung der Galaktischen Ebene (HGPS) vorgestellt wurden, oberhalb von 10 TeV detektiert und charakterisiert. Darunter befinden sich Vertreter aller Quellklassen, die im HGPS-Katalog etabliert sind. Das Potenzial der verbesserten Analysemethode wird auch durch die Untersuchung der Emission oberhalb von 10 TeV für zwei Objekte demonstriert: die Region, die mit dem Schalenüberrest SNR HESS J1731−347 assoziiert ist, und der PWN-Kandidat, der mit PSR J0855−4644 assoziiert ist und mit HESS J0852−463 zusammenfällt.

Contents

Chapter 1

Introduction

In the last century, thanks to fast progress in technology and science, the field of gamma-ray astronomy opened a new window for the exploration of the Universe. It started more than 100 years ago (in 1912) when Victor Hess discovered that the level of ionising radiation in the atmosphere increases above the altitudes of approximately 1 km [128]. The conclusion was that the radiation originates from outer space and later it was called *cosmic rays*.

The spectrum of cosmic rays has been measured by many experiments [177]. Current theory predicts that the cosmic protons with energies at least up to about 10^{15} eV or even higher have a Galactic origin [57, 113]. For example, supernova remnants are predicted to be effective cosmic ray accelerators [65, 107]. However, being charged particles, cosmic rays are deflected by magnetic fields on the way to Earth and their arrival directions cannot point back to their origin. Gamma rays, on the other hand, can. They are produced via the cosmic-ray interactions with the media in the vicinity of the source and can be detected using orbital or ground-based gamma-ray instruments.

Nowadays, *Imaging Atmospheric Cherenkov Telescopes* (IACT) are the most common type of ground-based gamma-ray instruments. This technique requires the detection of the short bursts of Cherenkov radiation emitted by secondary particles in the cascades caused by gamma or cosmic rays interacting with the atmosphere [184]. It was pioneered by the Whipple telescope in Arizona, which detected the first TeV source, the Crab Nebula, in 1989 [185]. Today, after several decades of gamma-ray astronomy development and a few generations of Cherenkov telescopes [132], there are more than 200 detected TeV sources in our own Galaxy as well as sources of extragalactic origin (Figure 1.1) [179].

The *High Energy Stereoscopic System* (H.E.S.S.) in Namibia is one of the current generation IACTs [130]. Its Galactic plane survey, published in 2018 [5], includes 78 gamma-ray sources detected in the energy range from hundreds of GeV to more than 50 TeV. Among them there are sources identified as supernova remnants, pulsar wind nebulae, composite sources and binary systems. Nevertheless, more than half of the sources presented in the survey are unidentified. Moreover, the particle acceleration and gamma-ray production mechanisms remain a mystery for many of these sources until this day. Further studies of the spectrum, morphology at different energy and the full multi-wavelength picture might shed some light into the open questions and unknown properties of some of the most extreme environments in the Universe.

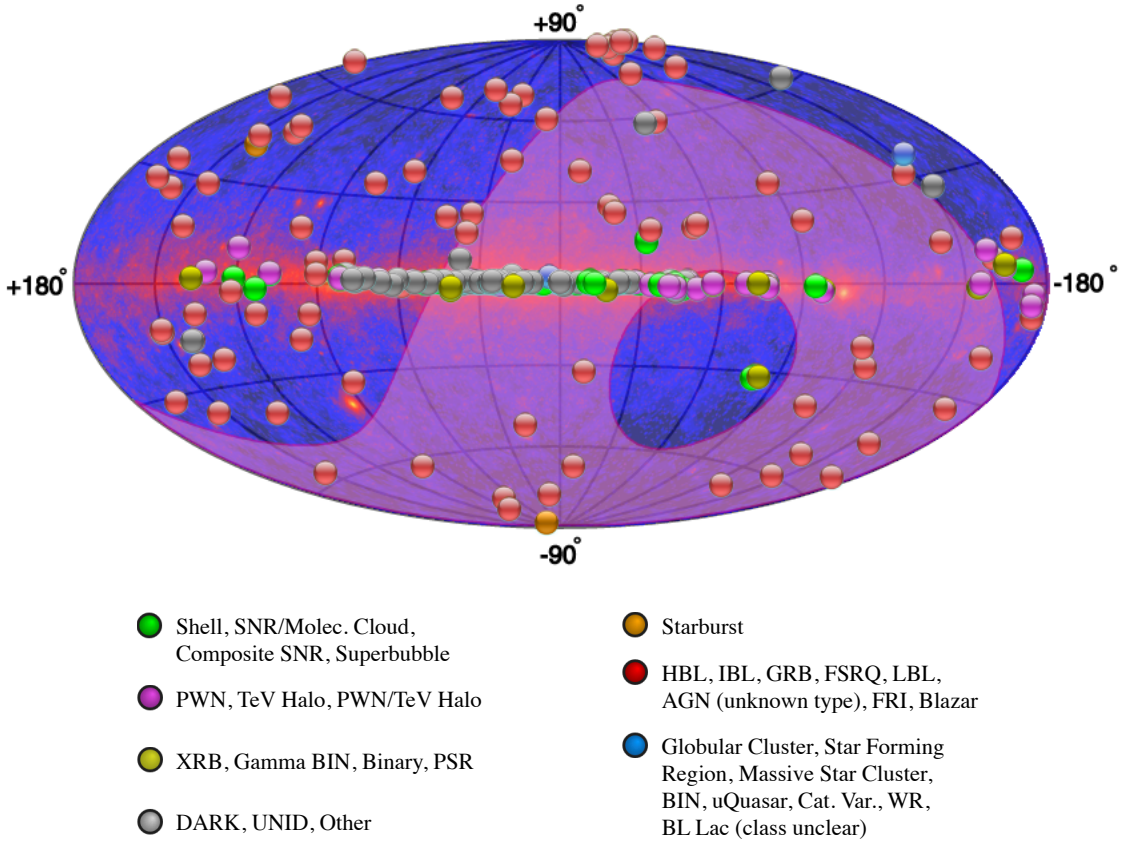

Figure 1.1: Gamma-ray sources detected in TeV domain. The background image shows the *Fermi*-LAT skymap overlayed with the region visible by the H.E.S.S. telescopes. Image credit: TeVCat online source catalog [179].

The spectra of many Galactic gamma-ray sources extend beyond 10 TeV, the energy domain where the knee of the cosmic ray spectrum, i.e. steepening of the spectral index at about $3 \cdot 10^{15}$ eV, starts to be probed. But the event statistics at high energies is typically poor, which limits the sensitivity of the experiment in this regime. The study presented in this thesis investigates a few ways to improve the high-energy sensitivity. The resulting analysis approach improved at high energies is applied for exploration the Galactic plane at energies above 10 TeV.

The thesis consists of seven chapters:

- Chapter 2 introduces the reader to the technical aspects of very-high-energy gamma-ray astronomy. It discusses the basics of extensive air shower physics and their detection by ground-based Imaging Cherenkov instruments. In particular, the chapter describes the design and main features of the H.E.S.S. experiment.

- Chapter 3 presents an overview of the event analysis methods currently available within one of the H.E.S.S. analysis frameworks. It also discusses the analysis complications associated with gamma rays at energies above 10 TeV, which motivates the next chapters of the thesis.

- Chapter 4 discusses one of the ways to improve the gamma-ray statistics above 10 TeV by extending the maximum allowed event offset beyond the size of the H.E.S.S. telescope cameras. Since the analysis of events at offsets beyond the physical size of the telescope camera has a few challenges, such as degraded quality of the event reconstruction and increased background rate, an additional reconstruction method and modifications for the background rejection method were implemented into one of the H.E.S.S. analysis chains.

- Chapter 5 shows the performance of the proposed analysis approach. It covers topics of reconstruction quality, background rejection efficiency and analysis sensitivity as well as compares the analysis performance obtained with simulated gamma rays and real observational data.

- Chapter 6 presents the application of the method, developed in this work, to the survey of the Galactic plane performed by the H.E.S.S. telescopes during the first decade of their operation. More than half of the known Galactic sources emit at energies above 10 TeV and all object classes identified in the Galactic plane survey are among them. In addition, the region associated with the shell-type SNR HESS J1731−347 and the PWN candidate associated with PSR J0855−4644 are discussed in greater details.

- Chapter 7 concludes the study presented in this work and gives an outlook on future perspectives.

Chapter 2

Cherenkov technique

Gamma rays are typically divided into two classes depending on their energy: *High-Energy* (*HE*) and *Very-High-Energy* (*VHE*) gamma rays. A typical energy range of HE gamma rays extends from approximately 100 MeV to about 100 GeV. The Earth's atmosphere is opaque to such photons; thus, direct HE observations are conducted from orbit. A current generation HE instrument such as *Fermi*-LAT [62], observes from around 20 MeV to more than 300 GeV[1]. However, space-based detectors are limited in size, and since source flux drops as the photon energy increases, orbital instruments are too small for efficient gamma-ray detection at energies above a few hundreds of GeV. Thus, in the VHE domain (above 100 GeV), ground-based experiments come into play. One of the techniques capable of VHE gamma-ray observation from the ground is the *Imaging Atmospheric Cherenkov Technique* (*IACT*[2]) [184], which detects gamma rays by observing their interactions in the atmosphere. This way, the Earth's atmosphere acts as part of the detector, i.e. as a tracker and calorimeter. This chapter discusses the main principles of gamma ray propagation in the atmosphere and its subsequent detection by the Cherenkov telescopes.

2.1 Extensive air showers

When a high energy cosmic or gamma ray interacts with the nuclei in the atmosphere, they create showers of secondary particles – *Extensive Air Showers* (*EAS*). EASs are divided into two subclasses, depending on the type of the primary particle. Gamma rays and electrons[3] produce *electromagnetic* (*EM*) showers, while protons and heavier nuclei create *hadronic* showers. Irrespective of the primary particle type, all relativistic charged particles that are produced in the EAS emit *Cherenkov light* as they travel through the atmosphere. Detection of such light is the basis of the IACT. The camera of a Cherenkov telescope records the flashes of Cherenkov light from the EASs, which allows for a reconstruction of the energy and direction of the primary particles, as well as identification of their type [184].

[1] 3FHL *Fermi*-LAT catalog contains sources significantly detected up to 2 TeV [53].
[2] IACT is also often spelt out as Imaging Atmospheric Cherenkov Telescope.
[3] Hereafter, 'electrons' is a reference for both electrons and positrons, since they behave very similarly.

2.1.1 Cherenkov radiation

Cherenkov light is produced when a charged particle moves in a dielectric medium faster than the phase velocity of light in this medium [117], i.e. faster than c/n, where c is speed of light and n is the refractive index of the medium. As the particle travels, it polarises molecules along its trajectory. When these molecules return to the ground states, they emit electromagnetic waves. If the velocity of the initial particle is smaller than c/n, polarisation along the track is more symmetrical and emitted waves from the neighbouring parts of the track interfere and cancel each other. But if the particle moves faster than c/n, the polarisation is asymmetrical and emitted electromagnetic waves interfere constructively in the phase under the Cherenkov angle θ (Figure 2.1, left):

$$\cos\theta = \frac{1}{n\beta} = \frac{c}{nv}, \tag{2.1}$$

where v is a velocity of the initial particle. This way, light is emitted in a cone with an opening angle θ as shown on the right side of Figure 2.1.

Particles in the EAS experience different layers of the atmosphere at different altitudes. At high altitudes, the air is thinner and refractive index is close to 1. The density increases at lower altitudes resulting in a higher refractive index. This leads to an increase of the Cherenkov cone opening angle as the particle penetrates deeper into the atmosphere. As a result, a single particle leaves a footprint on the ground shaped like a thin ring.

For a given medium, the energy threshold for Cherenkov light production is:

$$\beta_{\text{thresh}} = 1/n, \tag{2.2}$$

with particles emitting light at $\cos\theta = 1$ at the threshold. The Cherenkov angle increases ($\cos\theta$ decreases) with increasing particle energy. Most of the particles in the EAS are ultrarelativistic with β close to 1, resulting in emission of Cherenkov light at an angle:

$$\theta_{\text{max}} = \arccos(1/n), \qquad \beta = 1. \tag{2.3}$$

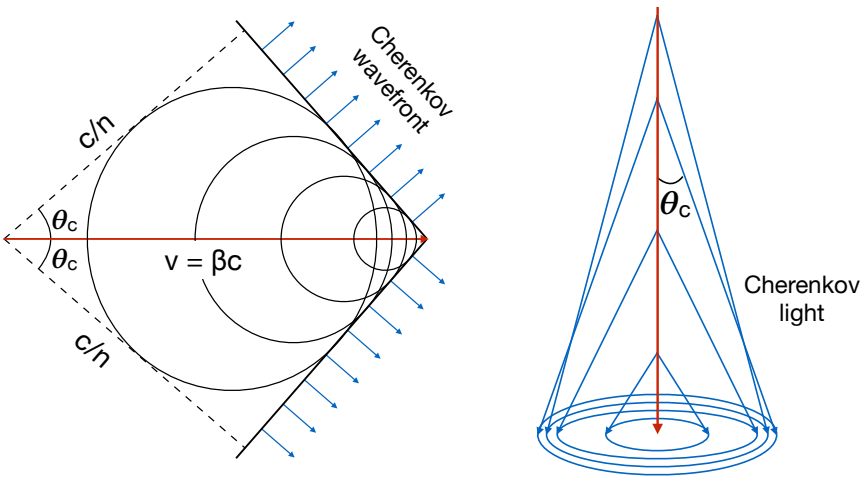

Figure 2.1: Cherenkov light production.

The number of Cherenkov photons emitted per unit track length x of the particle and wavelength λ is described by the Frank-Tamm formula [177]:

$$\frac{\mathrm{d}^2N}{\mathrm{d}x\mathrm{d}\lambda} = \frac{2\pi z^2\alpha}{\lambda^2}\left(1 - \frac{1}{n^2\beta^2}\right) = \frac{2\pi z^2\alpha}{\lambda^2}\sin^2\theta, \tag{2.4}$$

where α is the fine-structure constant and ze is the charge of the particle. As can be seen from Equation 2.4, the number of emitted photons is inversely proportional to λ^2, resulting in more photons produced with shorter wavelengths. Thus, most of the Cherenkov photons are emitted in the ultraviolet and blue range.

2.1.2 Electromagnetic air showers

Electrons and gamma rays interact predominantly via EM interactions and therefore, produce EM showers. In the field of the atmosphere nucleus, the primary gamma ray creates an electron-positron pair via pair production. This electron and positron undergo the bremsstrahlung process and emit secondary high-energy photons, which in turn produce more electron-positron pairs [158]. The process repeats, resulting in the production of an EM cascade of secondary particles. Such a simplified model of EM shower development is often called the *Heitler model* [126] and is schematically illustrated in Figure 2.2.

EM processes can be characterised by the radiation length X_{brems}. This is the mean distance over which a high-energy electron loses $1/e$ of its energy due to radiation losses, normally measured in $\mathrm{g\,cm^{-2}}$ [116]. The electron radiation length X_{brems} is equal to $7/9$ of X_{pair}, the mean free path for the pair production of a high-energy photon. They are often considered to be equal, i.e. $X_{\mathrm{brems}} = X_{\mathrm{pair}} = X_0$, for simplicity. This way, when a primary gamma ray with energy E_0 travels the distance X_0, it produces an electron-positron pair with each particle receiving an energy of $E_1 = E_0/2$. The two particles continue propagating, and after another X_0 ($2X_0$ from the top of the atmosphere), each of them also emits bremsstrahlung photons with energy $E_2 = E_0/4$. After a distance nX_0, there are 2^n secondary particles in the cascade, where $2/3$ of the particles are electrons and positrons and $1/3$ are photons. Each of them carries energy $E_n = E_0/2^n$.

Such a development continues until the energy of the electrons drops below the critical level E_{c}, at which point the ionisation losses dominate over the radiation losses. In the air, the electron critical energy is around 88 MeV [177]. At this point, the shower typically penetrates to a depth of $n_{\mathrm{c}}X_0$ and reaches the maximum of development. At this point, the number of particles in the cascade decreases and the shower starts to die out. At the maximum, the cascade contains around $N = 2^{n_{\mathrm{c}}} = E_0/E_{\mathrm{c}}$ particles [116]. From this, it can be seen that:

$$n_{\mathrm{c}} = \frac{\ln(E_0/E_{\mathrm{c}})}{\ln 2}, \tag{2.5}$$

and the maximum of the shower is located at atmospheric depth:

$$X_{\mathrm{max}} = \frac{\ln(E_0/E_{\mathrm{c}})}{\ln 2} \cdot X_0. \tag{2.6}$$

Showers induced by cosmic electrons develop similarly to the gamma-ray-induced ones. However, they have a few distinctions [100]. First of all, as mentioned above, the radiation

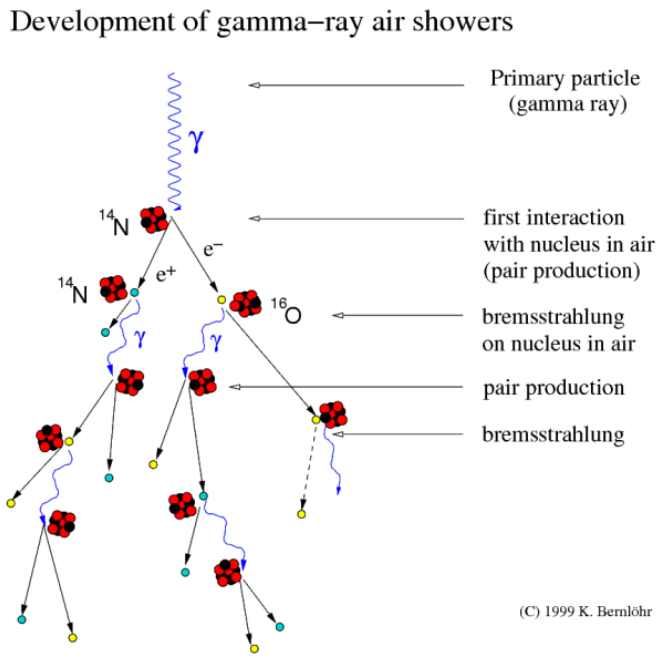

Figure 2.2: A simplified model of a gamma-ray-induced electromagnetic air shower. Credit: K. Bernlöhr [68].

length X_{brems} and the mean free path X_{pair} in reality are different ($X_{\text{brems}} = 7/9 X_{\text{pair}}$), which means that electron-induced showers start to develop earlier in the atmosphere. Second, being a charged particle, the primary electron also emits Cherenkov light (*direct Cherenkov light*) before the first interaction in the atmosphere. Nevertheless, gamma and electron-induced showers are almost indistinguishable for the current generation of Cherenkov telescopes.

2.1.3 Hadronic air showers

Highly relativistic cosmic protons and heavier nuclei produce hadronic air showers as shown in Figure 2.3. A primary proton or heavier cosmic ray interacts strongly with nuclei in the air [151]. All kinds of pions (π^0, π^+, π^-), as well as heavier hadrons, are the products of such a collision. After the collision, the atmospheric nucleus stays in the highly excited state and as a result can be unstable. One of the possible outcomes is an emission of spallation fragments, which are parts of the nucleus.

Charged pions have a relatively short mean lifetime of 2.6×10^{-8} s [177]. They are likely to decay into muons and neutrinos; of these, muons are also unstable and decay within 2.2×10^{-6} s into electrons and neutrinos:

$$\pi^+ \longrightarrow \mu^+ + \nu_\mu \qquad \mu^+ \longrightarrow e^+ + \nu_e + \bar{\nu}_\mu \tag{2.7}$$

$$\pi^- \longrightarrow \mu^- + \bar{\nu}_\mu \qquad \mu^- \longrightarrow e^- + \bar{\nu}_e + \nu_\mu \tag{2.8}$$

Neutral pions decay even faster than charged ones. The mean lifetime of neutral pions is 8.4×10^{-17} s [177]. They then decay into two high energy photons, which travel further in

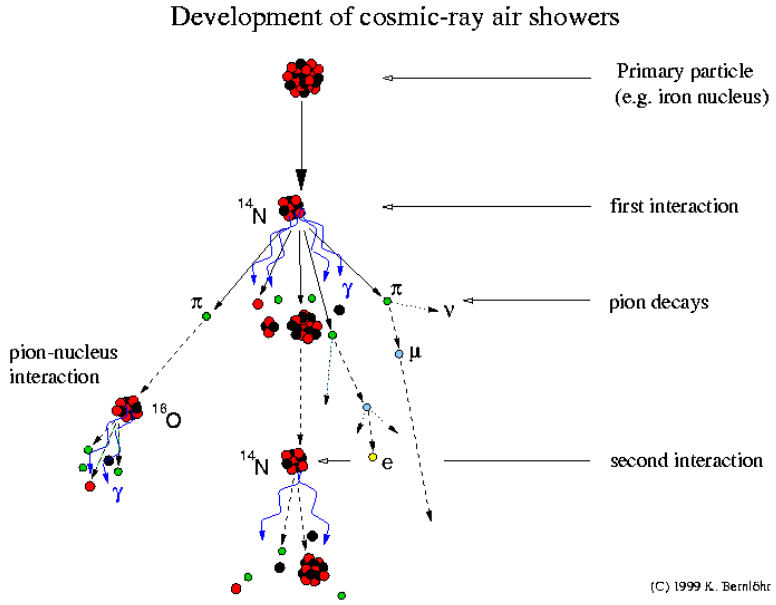

Figure 2.3: A simplified model of hadronic air shower. Credit: K. Bernlöhr [68].

the atmosphere and create an EM component of the hadronic shower as discussed in the previous section.

2.1.4 Difference between electromagnetic and hadronic showers

The neutral pions in the hadronic shower carry a part of the primary hadron energy and feed it into the subsequent EM cascade. Almost all Cherenkov light that is seen from the hadronic shower is produced in the EM sub-showers. Due to this fact, the hadronic showers can mimic the gamma-ray-initiated ones, leaving a similar footprint in the camera of Cherenkov telescope and, thus, it can be difficult to distinguish between these two types of showers.

Nevertheless, gamma-ray and hadron-induced showers are different. Figure 2.4 shows an example of the Cherenkov light lateral distribution for these shower types. The distinctive features of the hadronic showers are [116]:

- Brightness of the shower. As mentioned above, most of the Cherenkov light in hadronic cascade comes from EM sub-showers, where only a fraction of the initial energy is deposited. This means that hadronic showers are fainter than EM ones for the same energy of the primary particle.

- Presence of muons. Some muons can be very energetic and live long enough to penetrate deep into the atmosphere and even reach the ground. Since muons do not produce a cascade of secondary particles, the Cherenkov light leaves a circular footprint in the camera. This is one of the most characteristic signs of a hadronic

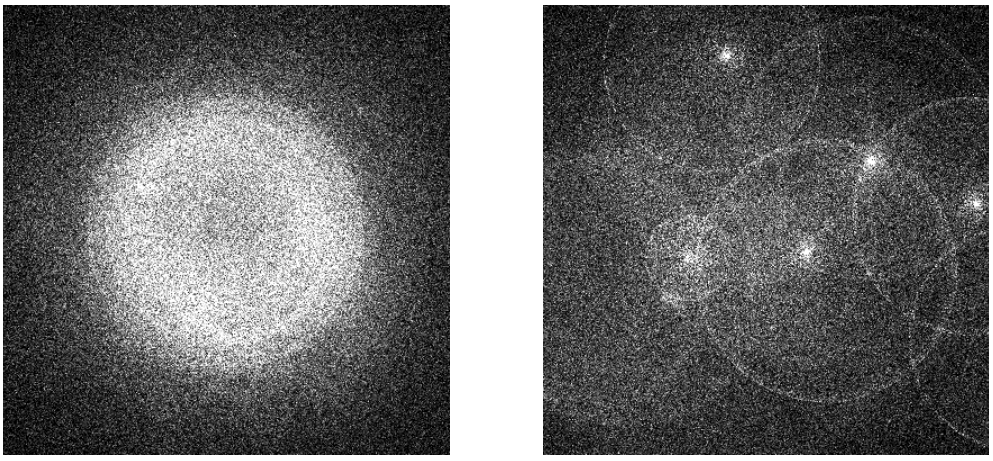

Figure 2.4: The lateral distribution of the Cherenkov light produced in showers that are caused by a 300 GeV gamma ray (left) and 1 TeV proton (right). Both plots show the area of 400 m by 400 m with the shower core position in the centre. Credit: K. Bernlöhr [68].

shower.

- Spatial structure. Hadronic showers have large transverse momentum transfer, which leads to an irregular structure in the images taken by the Cherenkov telescope camera. They can also consist of more than one bright EM sub-shower and, thus, have images with multicore structure. On the other hand, images of the EM showers have a more compact elliptical shape, nicely pointed in the direction of the shower origin.

2.2 The High Energy Stereoscopic System

The *High Energy Stereoscopic System* (*H.E.S.S.*) is one of the currently operating IACTs [130] together with MAGIC [55] and VERITAS [186]. H.E.S.S. is an array of five Cherenkov telescopes located in Namibia at an altitude of 1835 m above sea level. Figure 2.5 shows a photo of the array with:

- four small-sized telescopes (*CT 1 - 4*) that each have a 12 m diameter dish and are situated in the corners of a square with a 120 m side length [46]. They were built in 2002 - 2003 and constitute the first phase of the experiment (*H.E.S.S. I*). CT 1 - 4 have a 5° *field of view* (*FoV*) and operate in the energy range from approximately 100 GeV to more than 50 TeV. The best sensitivity is achieved at energies around 1 TeV. At low and medium energies, the sensitivity is limited by the cosmic-ray background, while at high energies, it is limited by the low statistics due to typical steeply falling energy spectra.
- a big telescope (*CT 5*) was constructed in the middle of the array in 2012, starting the second phase of H.E.S.S. operations (*H.E.S.S. II*) [139]. CT 5 has a large dish (28 m), which lowers the energy threshold of the system to a few tens of GeV. On the other hand, it has a smaller FoV (around 3.2°) and, as explained in Chapter 4, is not considered in this work.

Figure 2.5: The High Energy Stereoscopic System (H.E.S.S.) in the Khomas Highland of Namibia [130]. CT 1 - 4 are located in the corners of the array and CT 5 is in the middle. In front of each telescope, there is a camera shelter, in which cameras are secured during the day or bad weather. A control building, from where the telescopes are operated, is seen in the bottom of the photo. Credit: H.E.S.S. Collaboration, Christian Föhr.

The distance between telescopes in the array is a compromise between larger area coverage and the necessity of having multiple telescopes observe a shower, known as stereoscopic shower detection, which is particularly important for the small telescopes as discussed in Section 3.1.2. The gamma-ray showers are rather compact. At energies of a few TeV and below, the distribution of Cherenkov light on the ground (also known as the *light pool*) at H.E.S.S. altitude is approximately uniform up to about 120 m from the shower axis. Outside the light pool, the density of Cherenkov photons drops exponentially [153]. At higher primary energies, the photon density gradient within the light pool is stronger but the overall behaviour is similar. Figure 2.6 shows examples of Cherenkov photon density lateral distribution at different observation altitudes for showers induced by gamma rays with primary energies of 1 TeV and 30 TeV.

The design of a Cherenkov telescope is quite simple and, in some sense, similar to optical telescopes. One of the small H.E.S.S. telescopes is schematically illustrated on the left side of Figure 2.7. It uses an *alt-azimuth mount*: a steel base-frame rotates around the vertical (azimuth) axis, supporting a dish that can rotate around the horizontal (elevation) axis [74]. The dish contains a telescope reflective surface. For simplicity and cost effectiveness, the reflective surface consists of 382 round 60 cm mirror facets and is not a big single mirror. Nevertheless, such a design has a sufficiently precise optical *Point Spread Function* (*PSF*) to resolve structures in the air showers [84]. The mirror facets focus Cherenkov light from showers into the camera, located in the focal plane as shown in the right part of Figure 2.7.

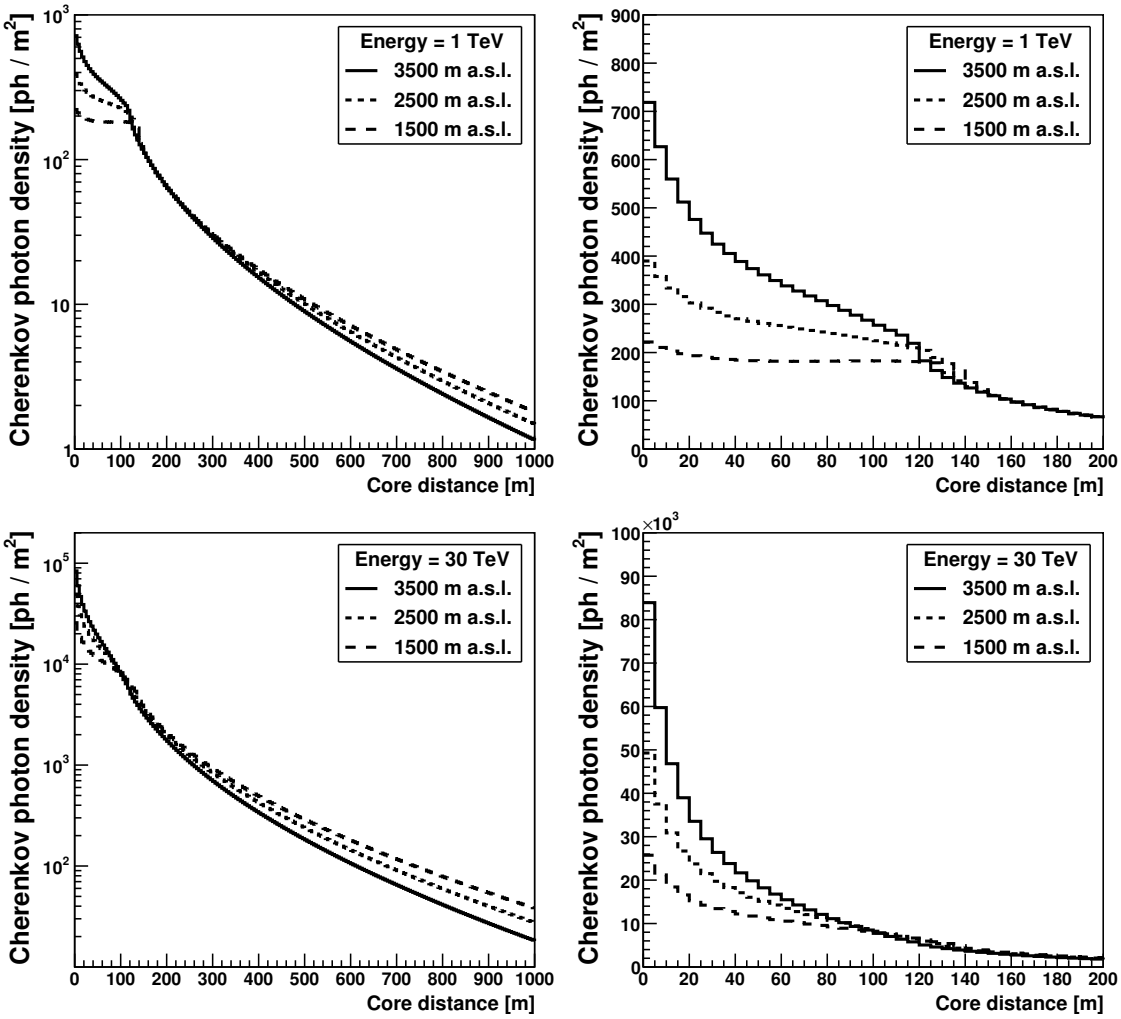

Figure 2.6: The average density of Cherenkov photons from vertical gamma-ray-induced air showers for two different primary energies at different observation altitudes [122]. The left and right columns show the density distributions for a broader distance range from the shower core position and zoomed in view, respectively. The H.E.S.S. telescopes are located at an altitude of about 1835 m above sea level.

2.2.1 Telescope camera

The air shower development is a very fast process, producing faint Cherenkov light flashes that last only a few tens of nanoseconds. Therefore, the camera must be able to record the photons on similar timescales. Many IACTs, including H.E.S.S., use *Photomultiplier Tubes* (*PMTs*) to detect such flashes. Each camera of the CT 1 - 4 telescopes contains 960 PMTs (pixels). To avoid photon losses in the gaps between PMTs, they are covered with *Winston cones*, special light reflectors that focus light into the PMTs [74]. The left side of Figure 2.8 shows a photo of the Winston cones in one of the H.E.S.S. cameras.

Inside the PMT, a Cherenkov photon hits the *photocathode* and an electron is emitted due to the *photoelectric effect* [121]. Several electrodes (*dynodes*) with positive potential

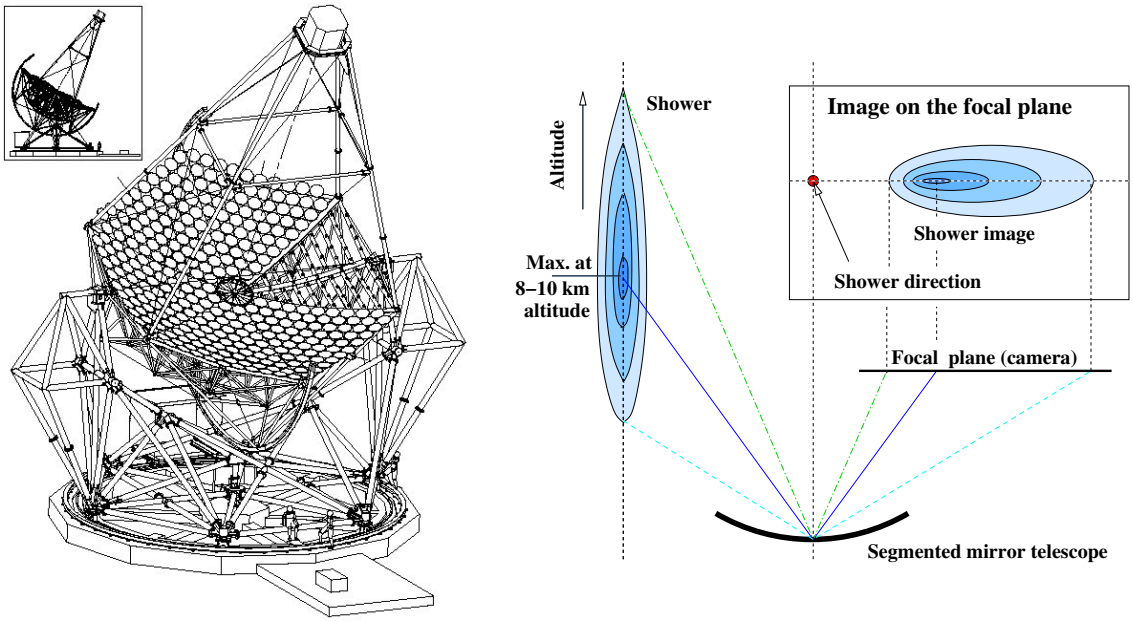

Figure 2.7: A schematic illustration of the H.E.S.S. small telescope (left panel, image credit: H.E.S.S. Collaboration [130]) and the main principle of the EAS detection by IACTs (right panel, image credit: K. Bernlöhr [183]).

are located inside PMT. They are organised in such a way that each dynode has a higher potential than the previous one. A primary electron is accelerated by an electric field and strikes the first dynode, resulting in the emission of several secondary electrons. These electrons move towards the second dynode, where the process of electron emission repeats. Thus, the number of secondary electrons inside the PMT grows from dynode to dynode until they reach an *anode* and create an output signal.

The PMTs are grouped into 60 modules, which are called *drawers*, and each drawer contains 16 PMTs. Each PMT is connected to *analog* and *slow control* electronic boards. There are two analog boards in each drawer. Eight PMTs in a drawer are connected to the left analog board, composing a left half-drawer, while another eight are connected to the right analog board, a right half-drawer. A signal from the PMT then goes through a pre-amplification step and is split into three branches: one *trigger* channel and two *readout* channels[4].

2.2.2 Trigger and readout system

PMTs are very sensitive devices and operated with high voltage, which is why it is preferable to conduct the Cherenkov telescope observations during moonless nights[5]. But even

[4]The next section discusses the trigger and readout channels of the CT 1 - 4 telescopes before their upgrade in 2016 (see Section 2.2.3 and [61]). It is done because the studies presented in the following chapters focus on data taken by the H.E.S.S. CT 1 - 4 telescopes between 2004 and the end of 2012, i.e. before the camera upgrade.

[5]Very intensive light can damage PMTs or considerable shorten their lifespan. Moreover, additional noise would make the data analysis more challenging later on. Nevertheless, MAGIC, VERITAS and, since recently, H.E.S.S. telescopes perform moonlight observations in order to increase the duty cycle [52, 59, 182].

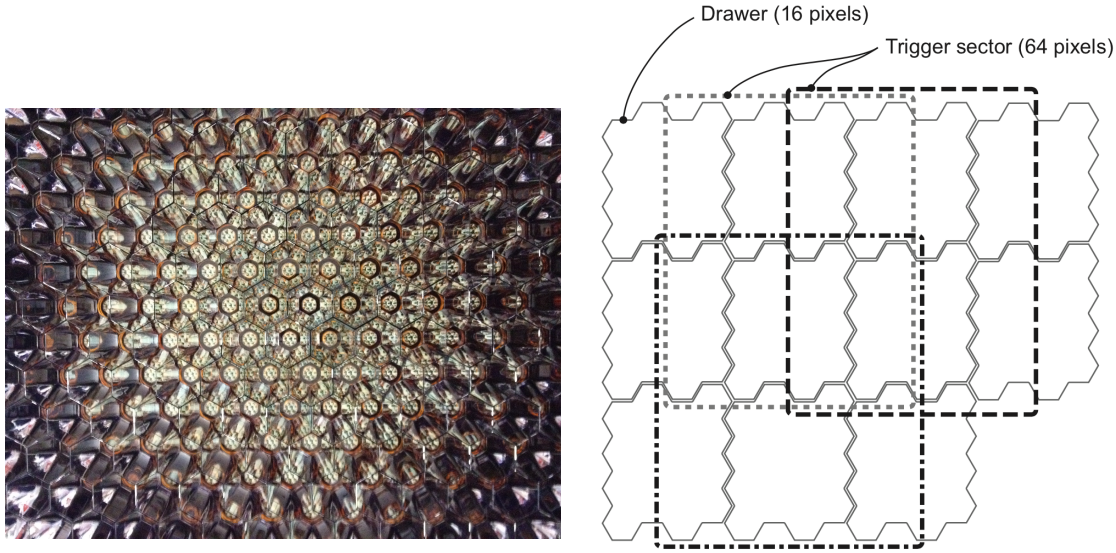

Figure 2.8: The left panel shows a photo of the H.E.S.S. camera covered with the Winston cones, whose front side has a hexagonal form. In the depths of each cone, one can see a PMT input window. Photo credit: H.E.S.S. Collaboration, A. Balzer [130]. The right panel schematically illustrates the organisation of camera pixels into sectors, which are required for the trigger algorithm [75].

then, the sky is full of bright stars and *Night Sky Background* (*NSB*) light, which consists of direct and scattered stellar light, zodiacal light, etc. The NSB is bright enough to continuously produce noise signals in each pixel across the cameras. Therefore, the trigger system is built in a way to efficiently identify air showers and minimise accidental triggering on NSB light. H.E.S.S. uses a two-level trigger system: a *local camera trigger* and a *central trigger*.

The triggering process starts at the *pixel level* and is referred to as the *L0 trigger* [104]. An amplified AC-coupled analog signal from the PMT is sent to a comparator located in the corresponding analog board. Here, it is compared with a programmable threshold value, which is typically set to a few photoelectrons. A pixel is triggered when the signal exceeds the threshold. The next trigger level is a *sector* or *L1* trigger. The whole camera is divided into 38 overlapping sectors comprising up to 64 pixels each, as shown on the right side of Figure 2.8. The overlap width is a half and a whole drawer in the horizontal and vertical direction, respectively. This way, a half-drawer can belong to a maximum of four sectors. In the H.E.S.S. experiment, the *N-majority* trigger is implemented, which requires N pixels in the same camera sector to fire.

The L0 trigger signals from the analog board are routed to the respective slow control board, where they are summed. In the end, there are two output signals, which correspond to two halves of the drawer. Since all comparators responsible for the L0 trigger have the same fixed output amplitude, the size of the slow control board output signal corresponds to the number of triggered pixels in the half-drawer. Hereafter, the signal proceeds to the sector sum, where it is added up with other half-drawer signals constituting the actual trigger sector. Finally, the total signal is sent to the sector comparator and if it exceeds the threshold value (N fired pixels), the sector, and thus, the telescope trigger occurs. The

pixel and sector comparator thresholds are programmable and can be changed depending on the NSB rate and a desired telescope trigger rate. For the H.E.S.S. CT 1 - 4 cameras, typical threshold values of 4 photoelectrons (p.e.) in 3 pixels are applied.

The *Central Trigger System* (*CTS*) [104] is located in the control building. It receives the trigger information from each telescope. At this level, the trigger differs depending on the telescope type [75]. Normally, the CT 1 - 4 telescopes should always trigger in coincidence with another or with CT 5 because the quality of the shower reconstruction improves with an increase in telescope multiplicity (stereo reconstruction). This means that at least two telescope triggers must be received within an 80 ns time window. In contrast, CT 5 telescope can work in the *mono regime* and issues central trigger having L1 signal only from CT 5 itself, since it alone has a lower energy threshold and detects very faint air showers, which typically do not trigger smaller telescopes.

In any scenario, if the array is triggered, the system gives a command to acquire and save the data from the buffers, which contain the information from the readout channels, the other two branches of the PMT signal [37]. A two-channel readout system is chosen to cover the required large dynamic range. One channel is used in the range 1 - 200 p.e. and has a higher amplification (*high gain* channel). The second readout channel covers higher intensities 15 - 1600 p.e. and has lower amplification (*low gain* channel). Signals in both channels are sampled with a frequency of 1 GHz using *Analog Ring Samplers* (*ARS*) [93]. Every ring buffer contains 128 cells which are continuously overwritten. As soon as a camera gets triggered, writing to the buffers stop. The content of the cells within a specified readout window (16 ns for normal readout mode) is sent to *Analog-to-Digital Converter* (*ADC*), where the signal is digitised. Then the digital signals are summed and sent to another buffer, where it is stored until a decision by the CTS to acquire the data.

2.2.3 H.E.S.S. CT 1 - 4 Camera upgrade

The first H.E.S.S. telescopes have been operating for more than a decade in the harsh environment of the Namibian desert. The continuous operation resulted in ageing electronics, which led to an increased failure rate. At the same time, a new modern fifth telescope had been built in the middle of the array, lowering the threshold and increasing the trigger rate of the system from 200 - 300 Hz to more than 1.5 kHz. The original CT 1 - 4 cameras had a large dead time[6], around 450 μs, compared to approximately 15 μs for CT 5 [75]. For such high rates, the 450 μs dead time of the telescope camera would have lead to a fractional dead-time of 10 - 20%, reducing the telescope multiplicity and, as a result, worsening the event reconstruction quality and the sensitivity of the whole array.

This required an upgrade of the CT 1 - 4 cameras, which was successfully performed in 2015 - 2016 [61]. During the upgrade, a number of security sensors and systems were installed and the camera ventilation was improved. The new ventilation system allows for controlling the camera temperature and creates an air overpressure to prevent dust accumulation inside the camera. And, most importantly, all electronics inside the cameras were refurbished except the PMTs and their bases.

The trigger and readout logic of the CT 1 - 4 cameras has undergone very minor changes.

[6]The triggered event cannot be recorded if the system is still 'busy' recording the previous one.

In the trigger channel, the only difference is a sampled output of the comparator at the L0 trigger level. Such a scheme allows for the easy introduction of more sophisticated trigger schemes and gives an opportunity to perform tests for the future generation of Cherenkov experiments. The other parts of the trigger channel have stayed the same. The notable modification of the readout channel is a *NECTAR* chip [165]. It combines a ring memory buffer with an increased number of cells (1024) and digitising function. A readout of the NECTAR chip is able to work much faster than the old readout electronics, which were responsible for the large dead time of the cameras [104]. Since the upgrade, the dead time of the CT 1 - 4 telescopes significantly decreased and became comparable to the CT 5 dead time. This increased the number of recorded stereoscopic events, which will result in an improvement in sensitivity and array performance. The dynamic range was also expanded. The low gain is linear now up to 4200 p.e., which prevents pixel saturation for very high energy events.

2.3 Simulation technique

Nowadays, the Monte Carlo method of simulation [160] is widely used in different spheres of life [147], especially in science. Many physics experiments, including H.E.S.S., use Monte Carlo simulations to understand the measurements obtained by the instrument and analyse these data. In VHE gamma-ray astronomy, simulations typically proceed in two steps:

- First, the EAS development in the atmosphere is simulated using the CORSIKA package [85], which was originally developed for the KASCADE experiment [94] and has now become arguably the most popular program for air shower simulation. It allows for the production of air showers initiated by photons, protons, nuclei and other particles [124]. It models particle interactions, decays and various energy losses, including Cherenkov light production [125]. CORSIKA also takes into account the impact of the atmosphere on Cherenkov light (e.g. extinction) [70] and records photons that would hit the telescope reflector.
- Then, the second step is the detector simulation, which is done by the `sim_telarray` package [69]. `sim_telarray` provides optical ray-tracing in the telescope, the photon detection by the PMTs and the following response of the electronics [72, 73]. In order to make the simulation close to the real observation, it also emulates the NSB in the camera pixels. Electronics simulation starts at the PMT level and includes the local and central triggers as well as readout channels described in Section 2.2.2. In the output, the simulated data have similar properties as the data from the real telescope.

In this work, CORSIKA and `sim_telarray` are applied for the production of gamma-ray simulations, which were heavily used for the analysis method development, discussed in Chapter 4, and performance study in Charter 5.

Chapter 3

Standard event analysis

Before it can be analyzed, the raw camera data must first be calibrated [37], i.e. the signal recorded from each pixel is converted into light intensity measured in photoelectrons. In the H.E.S.S. experiment, there are several analysis chains, which have different calibration schemes and event reconstruction techniques [46, 92]. They are used to cross-check each other for consistency. This chapter is devoted to the description of the event analysis schemes, which are implemented within the *H.E.S.S. analysis package* (*HAP*), one of the software packages for data analysis in H.E.S.S.

3.1 Image preparation

As mentioned in the previous chapter, the camera records not only Cherenkov photons from the EAS, but also NSB light. In the standard HAP analysis, all shower images should be cleaned of NSB noise before the reconstruction starts. Cleaned images undergo a procedure of parametrisation and quality selection, which is usually referred to as *preselection*. Thus, only good grade images are selected for event reconstruction.

3.1.1 Image cleaning and parametrisation

The identification and rejection of pixels mainly containing NSB photons is done by the *image cleaning* procedure. In the HAP standard analysis, pixels dominated by the shower signal are selected for further analysis, and pixels dominated by the NSB noise are discarded [46]. For this purpose, a two-level filter is applied. Each image is required to contain pixels with amplitudes exceeding 10 p.e., that have neighbour pixels with the amplitude above 5 p.e. However, the filter cuts can be also set to different values. For example, thresholds of 7 and 4 p.e. are typically used in another analysis approach within the HAP framework, which is briefly discussed in Section 3.4.

The footprint of the EM shower in the camera has an elliptical shape. Therefore, after the cleaning, each image is parametrised by the ellipse moments of multiple orders. Parameters derived from such an approach are known as *Hillas parameters* [131]. They and other commonly used parameters are listed below and schematically depicted in Figure 3.1:

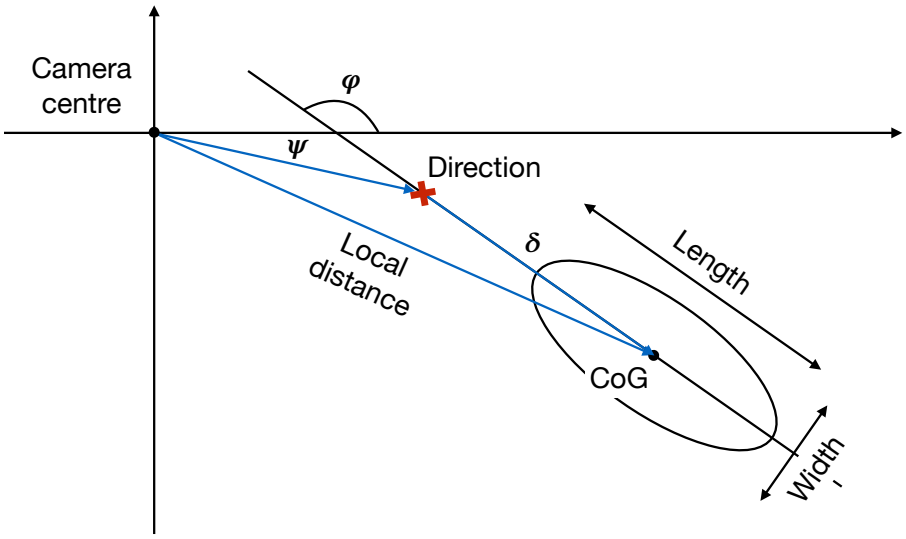

Figure 3.1: The sketch illustrates the shower image in the camera plane and some of the image parameters, which are typically used for the event analysis. The red cross marks the shower direction.

- *Amplitude* or *Size* is the zero-order ellipse moment. It corresponds to the sum of all pixel amplitudes contained in a shower image.
- *Centre of Gravity* (*CoG*) is the first-order ellipse moment and defines the shower image position in the camera.
- *Local distance* is the distance from the camera centre to the CoG of the image.
- *Length* and *Width* are defined as the size of the major and minor ellipse axis, respectively.
- *Image orientation* is the orientation angle of the ellipse's major axis with respect to the x-axis in the camera coordinate system. This angle is denoted as φ. Together with the *Length* and *Width* parameters, the φ angle is derived from the second-order moments of the ellipse.
- *Skewness* and *Kurtosis* are third- and fourth-order ellipse moments. They describe the asymmetry and shape of the image intensity distribution.
- *Displacement* is the distance from the image CoG to the shower direction. It is typically referred to as δ.
- *Event offset* is the distance from the camera centre to the shower direction. It is denoted by ψ.

3.1.2 Selection cuts

In order to achieve a good analysis performance, only high quality images should proceed to the event reconstruction level [46]. For this reason, all images undergo the preselection cuts:

- The *amplitude* (or *size*) cut rejects faint images, which are hard to reconstruct. Depending on the gamma-ray source brightness and its spectral slope [46], as well as background (i.e. cosmic rays) rejection method applied, the amplitude cut can be as low as 40 p.e. or increased up to 200 p.e. In the standard case, an image size of at least 60 p.e. or 80 p.e. is required. Table 3.1 summarises typical analysis configurations used within HAP and the corresponding amplitude cut values.

	Simple background rejection (see Section 3.3.1)	High-performance method (see Section 3.3.2)
loose	40 p.e.	40 p.e.
std	80 p.e.	60 p.e.
hard	200 p.e.	160 p.e.

Table 3.1: The amplitude selection cut for the different analysis configurations in the HAP framework.

- The *local distance* cut selects images that are maximally contained in the camera, because images truncated by the camera edge lose a lot of information about the shower. The typical local distance cut value is 0.525 m, which corresponds to 2°. Therefore, the CoG of the image should lay within 2° from the camera centre. The cut size is the same for the major analysis configurations in the HAP framework, which are listed in Table 3.1.

The preselection cuts strongly affect the number of shower images that are available for the event reconstruction. Typically, the stereoscopic reconstruction with multiple images is more accurate than the mono reconstruction, which uses only one image. In the H.E.S.S. experiment, mono analysis is applied only to the CT 5 telescope data[1]. If an observation is conducted with two or more telescopes and stereoscopic reconstruction is required, a *multiplicity cut* selects events with multiple images. Thus, the event passes to the next stage in the analysis if two or more shower images pass the aforementioned preselection cuts.

The efficiency of the cuts, which are discussed above, varies with the primary energy and offset angle of events. Figure 3.2 shows the number of events at different stages of the event selection (successive cuts are applied) as a function of energy for 0.5° and 2.5° event offset. As seen in the figure, the size cut strongly impacts the low-energy events independently of their offset. In turn, the local distance cut affects mainly high energies since images at these energies have larger extents and are more likely to be clipped at the camera edge. However, its influence at the low-energy part of the spectrum also increases at larger event offsets. The reason is the same as for the high energies: the image is truncated by the camera edge because, with the offset increase, the image CoG moves towards the camera edge. Although the topic of background rejection is discussed later, in Section 3.3, the effect of the cuts is also shown here. They reject a relatively constant amount of gamma-ray showers throughout the whole energy range. The efficiency of these cuts is rather

[1] CT 5 has a bigger dish than the CT 1 - 4 telescopes and can collect sufficient amount of Cherenkov photons from the shower for accurate event reconstruction. In addition, its energy threshold is lower, allowing it to record low-energy showers, which do not trigger the CT 1 - 4 telescopes.

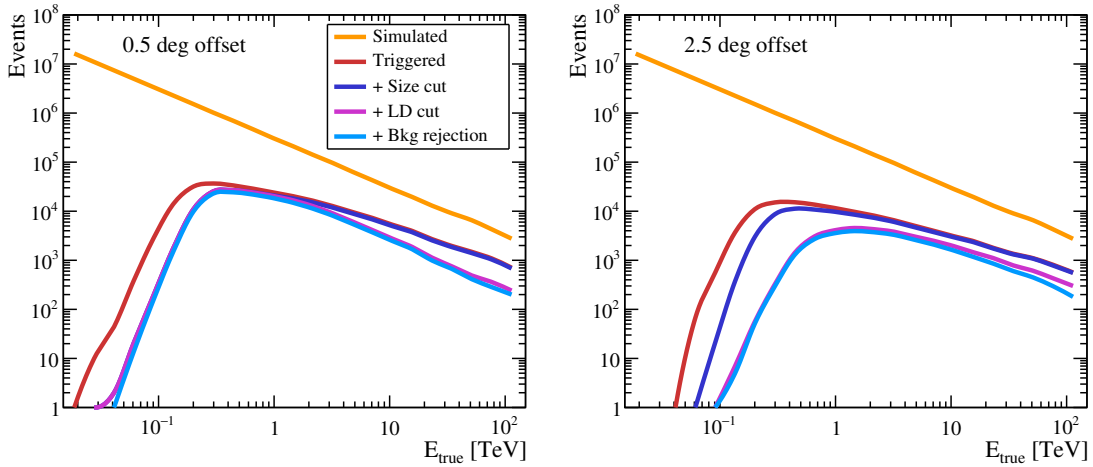

Figure 3.2: Impact of the selection cuts on the number of events as a function of energy. Results are shown for a point-like gamma-ray source, simulated at 20° zenith angle with 0.5° (left) and 2.5° (right) offset angle. The orange line in each panel indicates the initial simulated spectrum, while the red line shows the distribution of events that trigger the telescopes. Then selection cuts are applied one after another: dark blue line – events that pass size cut; magenta – size + local distance cut (i.e. preselection cuts); light blue – preselection and background rejection cuts (see Section 3.3). In addition, all mentioned selection cuts automatically include the multiplicity cut.

high and almost all gamma rays that pass size and local distance cuts also survive the background rejection [66].

3.2 Event reconstruction

The events that successfully pass the preselection step proceed to the reconstruction procedure. This section describes the standard approach to reconstruct the showers direction, the position of the shower axis on the ground, the primary energy, and other parameters that are important for further event analysis.

3.2.1 Direction reconstruction

There are several event direction reconstruction algorithms. In the H.E.S.S. standard analysis, the direction of the primary particle is reconstructed using the *geometry technique* (*Algorithm 1*) [136]. In this approach, the shower direction in the camera system is estimated by determining the intersection of the major axes of the images. The method is schematically illustrated in Figure 3.3. The major axes are intersected in pairs, and the shower direction is the weighted average position of all possible intersections. The weight of each image pair is given by:

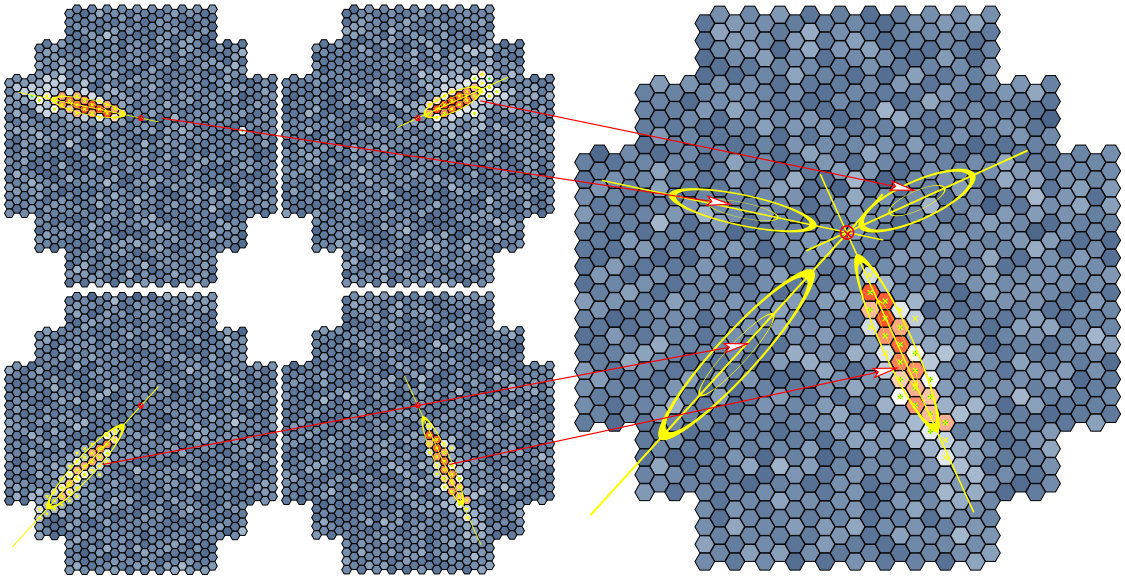

Figure 3.3: A schematic illustration of the shower direction reconstruction using geometry method. The left panel shows images of the gamma-ray shower seen by individual telescopes. On the right side, the images are superimposed in the common camera plane, where direction reconstruction takes place. Image credit: K. Bernlöhr [183].

$$\omega = \frac{|\sin(\xi)|}{\left(\frac{1}{A_1} + \frac{1}{A_2}\right)\left(\frac{W_1}{L_1} + \frac{W_2}{L_2}\right)}, \tag{3.1}$$

where ξ is the angle between the major axes; A, L and W are the size, length and width of two images, respectively. Indices denote the first and second image per pair. Thus, a pair that consists of bright long images with an angle between them close to 90° would have a higher weight in the shower direction calculation.

The position of the shower core is reconstructed in a similar way as the shower direction [136]. The main difference is that in the case of the direction reconstruction the image major axes are intersected in the camera plane, while the shower core is reconstructed in a different coordinate system (related to the ground) [112].

3.2.2 Energy reconstruction

The parameters of the shower images in the camera depend on the energy of the primary gamma ray and its distance to the telescope array. For the same primary energy, images are brighter for showers that are located closer to the telescope than for more distant ones. This fact is used for the primary energy reconstruction. Simulations of point-like gamma rays are used to build a relation between the inherent gamma-ray property – the primary energy – and the observed properties – the shower distance to the telescope (*impact parameter*) and recorded image amplitude. Based on these simulations, two *lookup tables* are created: energy- and energy-sigma-lookup tables, which are represented by 2D histograms [110]. Each distance-amplitude bin contains a distribution of corresponding

primary energies. The mean value and the spread of this distribution are written into an energy- and energy-sigma-lookup table, respectively, as a function of impact parameter and image size. During the event analysis, both lookup tables are used for energy estimation. Examples of such tables are shown in the left column of Figure 3.4.

However, the brightness of the shower footprint depends not only on the distance to the telescope but also on the optical efficiency of the telescope. In the rough desert environment, mirrors and other optical parts degrade quickly resulting in a deterioration of the telescope's reflectivity. Therefore, the mirrors and Winston cones have to be recoated or exchanged regularly. Between the exchanges, the degradation of reflectivity is carefully monitored and taken into account during the event reconstruction [81]. In particular, the issue is addressed during the lookup table production. Thus, energy- and energy-sigma-lookup tables are binned in optical *phases* and filled for each telescope individually, taking into account its optical efficiency during a particular phase. Optical phases and corresponding telescope optical efficiencies are listed in Table 3.2 for the H.E.S.S. I era, the period of the H.E.S.S. observations relevant to this work.

Phase	CT1	CT2	CT3	CT4
100	100	100	93	100
101	70	70	70	70
102	60	54	60	60
103	60	54	85	60
104	60	72	78	60
105	75	70	75	53
106	70	70	70	70

Table 3.2: A list of optical phases and respective telescope optical efficiencies during the H.E.S.S. I era, which covers a period of time roughly from approximately 2002, when the first small telescopes were built, until the end of 2012, when CT 5 started operations. The quantities presented for each telescope show the percentage of the optical efficiency with respect to the nominal value. The increase of the optical efficiency indicates the time when the mirror facets of the corresponding telescope were recoated.

In addition, the amplitude-distance relation also depends on the location of the gamma-ray origin in the sky (zenith and azimuth) and on its distance to the telescope pointing position (event offset). Showers that originate from large zenith angles produce the most light, i.e. have shower maximum, further away from the observer. They also travel through a larger column of the atmosphere than the ones from low zenith angles. A longer track in the atmosphere leads to greater absorption of Cherenkov photons and, as a result, fainter images in the camera for the same primary energy. In addition, the azimuth angle of the observation also has an effect on the shower images, due to the different configuration of the geomagnetic field [71]. Charged particles are deflected in the geomagnetic field, leading to the shower broadening [80]. Therefore, in addition to the binning in optical phases, the lookup tables are produced for different zenith, azimuth and offset angles, which are listed in Table 3.3.

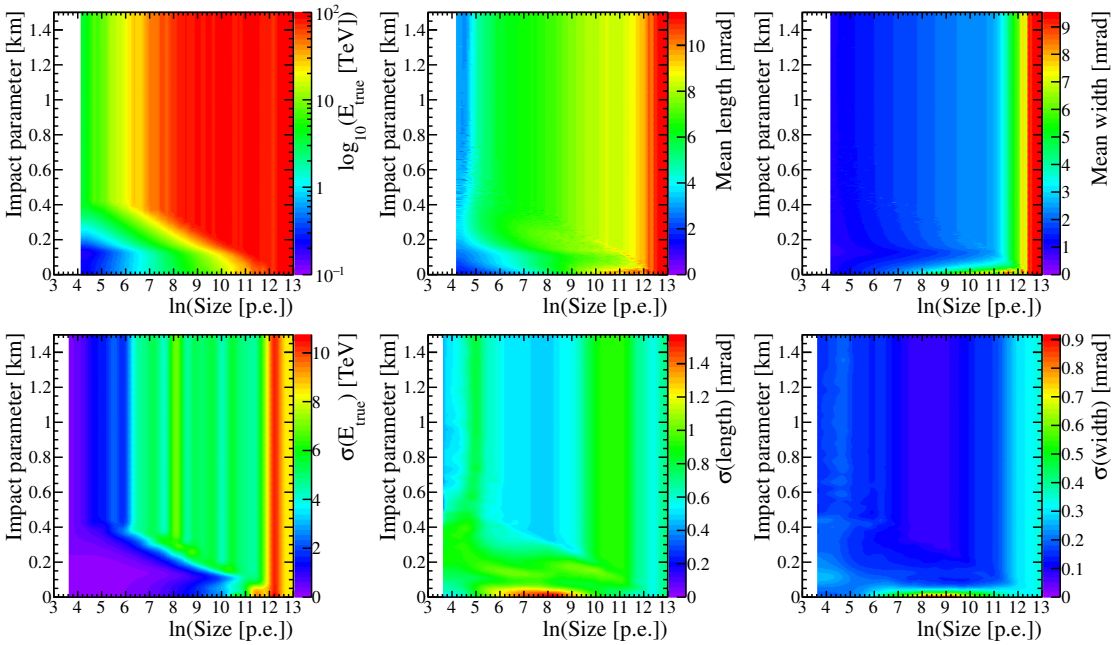

Figure 3.4: An example of lookup tables, designed for energy reconstruction (left column) and gamma-hadron separation (central and right columns). The top row shows mean values of the primary energy, shower image length and width, while bottom row presents the corresponding uncertainty values of these parameters. These histograms have been produced using gamma rays simulated with 70% optical efficiency, 20° zenith and 180° azimuth angle, 0.5° offset angle.

Zenith	0, 20, 30, 40, 45, 50, 55, 60, 63, 65°
Azimuth	0 and 180°
Offset	0, 0.5, 1, 1.5, 2.0, 2.5°

Table 3.3: A list of zenith, azimuth and offset angles for which the lookup tables are produced in the standard HAP analysis. The distance travelled by a shower in the atmosphere increases inversely with the cosine of zenith angle. Therefore, the spacing of the lookup tables become smaller at larger zenith angles.

Eventually, the energy of the primary gamma-ray is reconstructed in two steps [66]. First, the energy is estimated for each telescope individually from the energy-lookup tables using the previously reconstructed impact distance and image intensity. Since the lookup tables are produced for the discreet values of the above-mentioned parameters, the energy is evaluated by interpolating in the phase-space of these parameters. Then the primary energy is calculated by averaging the weighted energy estimations from individual images:

$$E_{\text{prim}} = \frac{\sum_i E_i \cdot \frac{1}{\sigma_i^2}}{\sum_i \frac{1}{\sigma_i^2}}, \tag{3.2}$$

where E_{prim} is the reconstructed energy of the primary particle; E_i is the energy evaluated for each telescope using the energy-lookup tables and σ_i is the uncertainty of the energy estimation from the energy-sigma-lookup tables.

The lookup tables are made in different optical efficiency bands, but these are coarsely spaced and cannot account for small deviations in the telescope reflectivity. Thus, there is a mismatch between the actual optical efficiency during the observations and the one used for the lookup tables production. In order to compensate for such an inconsistency, the reconstructed energy is multiplied by a correction factor:

$$f_{\text{corr}} = \frac{F_{\text{data}}}{F_{\text{sim}}}, \tag{3.3}$$

where f_{corr} is the correction factor and F_{data} is the efficiency parameter derived from the real data [133, 161]. F_{sim} is the similar efficiency parameter to F_{data}, but obtained from the gamma-ray simulation, produced with the optical efficiency that matches the one used for the production of the lookup tables.

3.3 Gamma-hadron separation

Unlike gamma rays, whose arrival directions tend to point back to individual sources, cosmic rays (mainly protons) are distributed more isotropically over the sky and continuously bombard the atmosphere, creating a background for VHE gamma-ray observations. As discussed in Section 2.1.4, electromagnetic and hadronic showers have a number of differences, which are used to distinguish between the gamma-ray signal and hadronic background. Since *gamma-hadron separation*, in fact, is another selection procedure, it is usually referred to as *postselection*. In the standard HAP analysis, there are two methods of gamma-hadron separation: image-shape box cuts and a method based on a machine learning technique.

3.3.1 Box-cut classification

The easiest way to discriminate hadronic showers produced by cosmic rays from the gamma-ray-induced showers is via the differences in their image shapes [131, 89]. Gamma rays produce regular, elliptical images, while images of hadronic showers are more irregular. Therefore, parameters derived from the image shape can be used for the gamma-hadron separation. For this purpose, shape- and shape-sigma-lookup tables are created in a similar way to the lookup tables used for the energy reconstruction as discussed in Section 3.2.2 [110]. They contain the mean and spread values of the *Length* and $Width$ image parameter

distributions filled into 2D histograms as a function of the image size and impact parameter. An example of these tables are shown in the right and centre columns in Figure 3.4.

Following the aforementioned analogy with energy-lookup tables, shape- and shape-sigma-lookup tables are produced using point-like gamma-ray simulations and are binned in the same optical efficiency, zenith, azimuth and offset angle bands as the energy-lookup tables. However, instead of creating these lookup tables for each individual telescope, the values are averaged over all telescopes that observed the event.

During the event reconstruction, the described shape- and shape-sigma-lookup tables are used to calculate *Scaled Length* and *Width* (*SCL* and *SCW*) image parameters [66]:

$$SCL_i = \frac{L_i - \langle L_i \rangle}{\sigma_{L_i}}, \tag{3.4}$$

where L_i is the length of the particular image; $\langle L_i \rangle$ and σ_{L_i} are the length and its uncertainty, evaluated from the shape- and shape-sigma-lookup tables, respectively, for the measured impact parameter and image size. The calculation of the SCW parameter is done in the same way.

For the event characterisation, *Mean Scaled Length* and *Width* (*MSCL* and *MSCW*) are applied by combining the information from individual images:

$$MSCL = \frac{\sum_i SCL_i \cdot \omega_{L_i}}{\sum_i \omega_{L_i}}, \qquad \omega_{L_i} = \left(\frac{\langle L_i \rangle}{\sigma_{L_i}}\right)^2, \tag{3.5}$$

where ω_{L_i} is the weight of a contributing image. The same approach is used for the $MSCW$ parameter calculation.

The distributions of $MSCL$ and $MSCW$ for the simulated gamma rays and data-derived background sample are shown in the upper panel of Figure 3.5. Since the shape of the shower images is compared to the lookup tables, which are produced with simulated gamma rays, the distributions of the $MSCL$ and $MSCW$ parameters for gamma rays are narrow and centred around zero, i.e. deviations from the expectation are small. In contrast, the same distributions for the cosmic rays are much broader and shifted from the zero position. These differences in the distributions are the basis of the background rejection procedure, which consists of a box-cut application that accepts events around the gamma-ray peak (*gamma-like events*) and rejects all others (*background-like events*). The cut values depend on the analysis configuration and typical values are given in Table 3.4.

3.3.2 Classification with machine learning algorithm

A more sophisticated, as well as a more efficient method of background rejection uses *machine learning techniques*. The *Toolkit for Multivariate Analysis* (*TMVA*) [135] provides multivariate *classification* and *regression* techniques and is integrated into the *ROOT* software framework [76], which is used for the storage and analysis of H.E.S.S. data. The regression algorithms are used to determine a relationship between input and output (target)

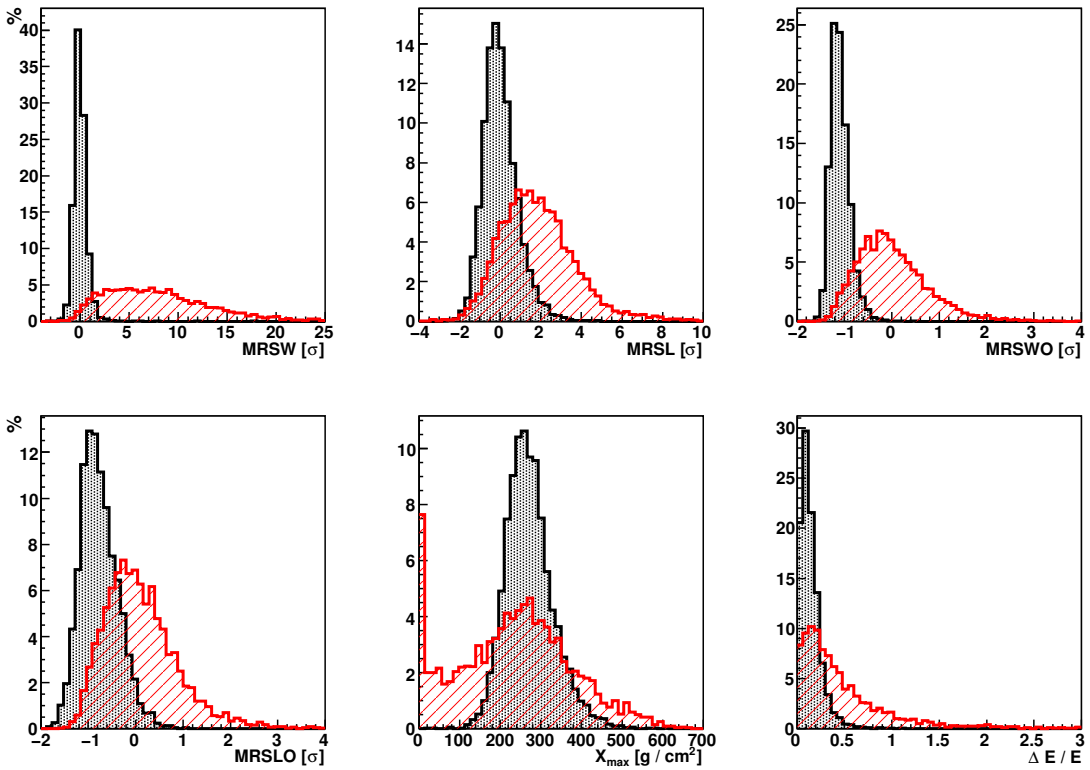

Figure 3.5: Distribution of parameters that exhibit gamma-hadron discrimination potential [167]. The first two parameters in the upper panel, $MSCL$ and $MSCW$ (denoted on the plot as $MRSL$ and $MRSW$, respectively), are the basis for the simple box-cut classification method, while all six illustrated parameters are used as an input for the TMVA based classification. Similarly to $MSCL$ and $MSCW$, the $MSCLO$ and $MSCWO$ parameters are denoted on the plot as $MRSLO$ and $MRSWO$, respectively. The black distributions show the signal sample, represented by point-like gamma rays simulated with 0.5° offset, while the real background data is depicted in red. The energy of the samples lie in the range 0.5 - 1.0 TeV and the zenith angles are from 15° to 25°.

loose	$-2 < MSCW < 1.2$	$-2 < MSCL < 2$
std	$-2 < MSCW < 0.9$	$-2 < MSCL < 2$
hard	$-2 < MSCW < 0.7$	$-2 < MSCL < 2$

Table 3.4: The gamma-hadron separation cuts for the box-cut approach in the HAP framework. As seen in Figure 3.5, the $MSCW$ parameter has a larger separation power than $MSCL$. Thus, it is sufficient to change only the $MSCW$ cut for different analysis configurations, while keeping the $MSCL$ cut the same.

variables, and can be used to estimate a certain property of the particle. For example, its

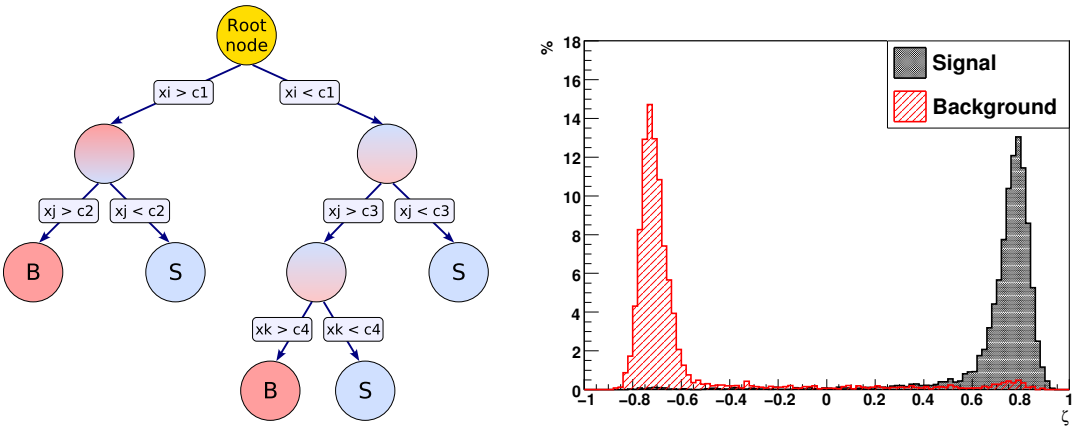

Figure 3.6: Event classification with Boosted Decision Trees. The sketch of a simple decision tree is illustrated in the left panel [135]. 'B' and red colour labels the background, while 'S' and blue colour marks the signal. x_i indicates discrimination variables and c_i is a cut, made on this variable. An example of a BDT response is shown in the right panel [167].

application on the shower direction reconstruction is discussed in Chapter 4. In particle and astroparticle physics, the classification methods are typically used to identify a type of particles. Thereby, one of the classification algorithms available within the TMVA package, *Boosted Decision Trees* (*BDT*), is used in the HAP analysis to separate gamma-ray showers (signal) from cosmic rays (background) [167].

Boosted Decision Trees

A *decision tree* is a classifier, structured as a binary tree [172]. An example of such a tree is shown on the left in Figure 3.6. The root node of the tree contains an entire training dataset. The classifier makes a decision on one of the input variables and splits the dataset into two sub-sets trying to maximise the separation. The tree grows with successive splits until the point when a predefined stop criterion is fulfilled. Usually, this happens when the node contains events of one class only or a number of events in the node reach a minimum value. For each split, the classifier chooses a variable and corresponding decision value that give the best separation between signal and background.

When there are limited statistics, decision trees easily learn on fluctuations in the training sample, which results in *overtraining*. One of the ways to avoid that is *tree pruning*. When the tree has grown to a maximum size, statistically insignificant nodes are cut away starting from the bottom to top of the tree. In the end, all events in the sample are characterised by one output variable, where a $+1$ value indicates signal (gamma-like events) and -1 value signifies background (hadron-like events).

A single decision tree is a weak classifier and becomes more powerful when *boosting* is applied. This approach consists of training that is performed using several decision trees instead of the single tree. Hence, the method is referred to as *Boosted Decision Trees* (*BDT*). In this method, all trees grow from the same dataset, but events are reweighted depending on the performance of the previous tree training.

One of the boosting algorithms implemented in TMVA is *Adaptive Boost* (*AdaBoost*) [103]. In this algorithm, all events in the first trained tree have weights of 1. In the following trees, misclassified events get a higher weight, by multiplying them with a boost factor α:

$$\alpha = \frac{1 - err}{err}, \tag{3.6}$$

where err is a misclassification rate of the previous tree. The misclassification rate err_j of one particular node j is computed as:

$$err_j = 1 - \max(p, 1-p), \qquad p = \frac{S_j}{S_j + B_j}, \tag{3.7}$$

where S_j and B_j are the numbers of signal and background events in the node, respectively. Then, the weights of the whole dataset are renormalised in order to have the same sum of weights in each training. Eventually, the response of the boosted classification is:

$$y_{\text{boost}} = \frac{1}{N_{\text{trees}}} \cdot \sum_i \ln \alpha_i \cdot h_i, \tag{3.8}$$

where N_{trees} is the number of trees in the classifier; h_i is the result of each individual tree. An example of such a classifier response is illustrated on the right of Figure 3.6.

During the classification, the event is classified on a majority vote done by each tree in the forest. Such a training and classification approach not only improves the performance of the classifier but is also more robust against statistical fluctuations in the training sample.

Gamma-hadron separation with BDTs

As discussed above, BDTs are applied for background rejection in the H.E.S.S. analysis [167]. The BDT training is performed using six input parameters, which are shown in Figure 3.5 and listed below:

- $MSCL$ and $MSCW$ are the mean scaled length and width. They are the same parameters as in the case of the background discrimination with box cuts, discussed in Section 3.3.1.
- $MSCLO$ and $MSCWO$ are the *mean scaled length* and *width off*. The meaning and calculation of these parameters are very similar to $MSCL$ and $MSCW$. The only difference between these parameters and the usual $MSCL$ and $MSCW$ is that they are calculated by comparing the shower image parameters to lookup tables filled with background events obtained from data instead of lookup tables filled with point-like gamma-ray simulations. This causes the distributions of $MSCLO$ and $MSCWO$ parameters to be centred around zero for background events and shifted for signal events.
- $X_{\max}/\cos(\theta_{\text{zen}})$ is the depth of the shower maximum in $\mathrm{g\,cm^{-2}}$ [144]. The position of shower maximum is first reconstructed for the pairs of the telescopes that pass the preselection cuts. Then, it is averaged over all available telescope pairs.

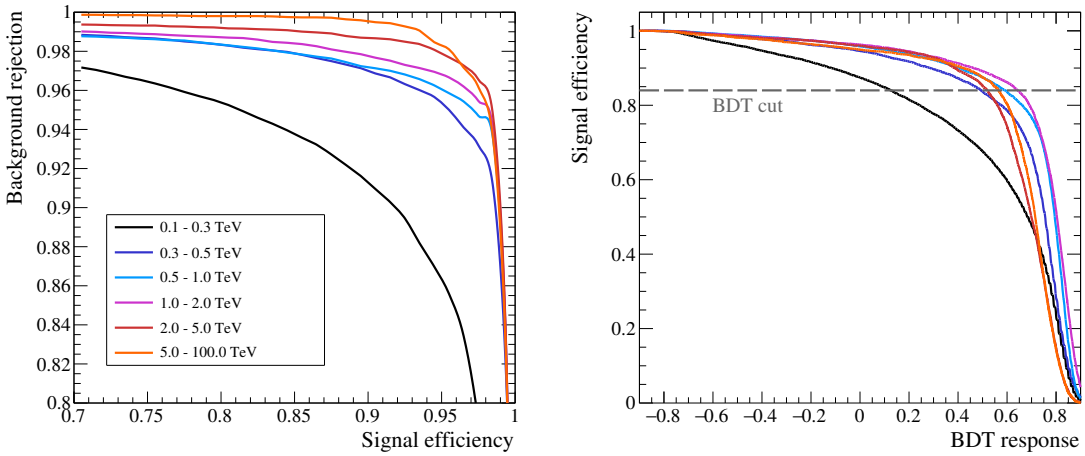

Figure 3.7: Performance of the BDT classifier in standard HAP analysis. The ROC and signal efficiency curves for events at zenith angles of around 20° are shown in the left and right panel, respectively. Different line colours indicate energy bands used for the BDT training. The grey dashed line illustrates an example of the discrimination cut, set to 84% gamma-ray efficiency.

- $\Delta E/E$ is the relative spread of reconstructed energy. Initially, the event energy is reconstructed for each telescope individually as described in Section 3.2.2. These individual energy estimations are used to calculate the average spread ΔE. More irregular structures, common for hadronic showers, result in a larger spread of energies reconstructed by individual telescopes. As a result, $\Delta E/E$ is typically larger for hadronic showers than for gamma-ray-induced ones.

The signal sample for the BDT training consists of the simulated point-like gamma rays. In turn, the background sample is represented by real observation data taken by H.E.S.S. in sky regions without significant gamma-ray sources. This results in a background sample dominated by protons, heavier nuclei as well as electrons. Such an approach helps to avoid high computational costs of background simulations, mainly due to the computational complexity of hadronic shower production.

Similarly to the lookup tables, BDTs are produced for different zenith angles in the range between 0° and 60° [166]. However, in this case, only one offset angle of 0.5° is used. All parameters used for the BDT input contain relative values and are independent of the optical properties of the telescopes. Therefore, there is no binning in optical efficiency. On the other hand, there is an energy dependence in the input variable distributions, which leads to BDT training in six energy bands (shown in Figure 3.6): 0.1 - 0.3, 0.3 - 0.5, 0.5 - 1.0, 1.0 - 2.0, 2.0 - 5.0 and 5.0 - 100.0 TeV.

The discrimination performance of the classifier can be characterised by the *receiver operating characteristic curve* (*ROC curve*), which shows a background rejection power with respect to a signal selection efficiency. An example of the ROC curves for the BDT classifier used in the HAP analysis chain is presented in the left panel of Figure 3.7. The curve is obtained by sliding the cut value along the BDT response distribution (Figure 3.6, right) and estimating the amount of rejected background and remaining signal. A position of the curve closer to the upper right part means better performance of the classification.

During the process of gamma-hadron discrimination, BDT response (also referred to as ζ_{BDT}) is evaluated for each event. The separation cut is always set on signal efficiency. The efficiency value that corresponds to the evaluated ζ_{BDT} can be retrieved from the *signal efficiency curves*, which are shown in the right panel of Figure 3.7. If the obtained efficiency value is smaller than the cut, this event is considered to be gamma-like, otherwise it is considered to be a background-like event. Current settings in the standard HAP analysis are: cut at 84% of gamma-ray efficiency for the *std_zeta*[2] analysis configuration and at 83% for the *hard_zeta* [167].

3.4 ImPACT reconstruction

A few years ago, a new high-performance event reconstruction algorithm was implemented in the HAP analysis framework: an *Image Pixel-wise fit for Atmospheric Cherenkov Telescopes* (*ImPACT*) [169]. It uses an image template fitting technique to determine the shower parameters. The approach was developed for the CAT telescope [64] [148] and later was re-implemented in another H.E.S.S. analysis chain, referred to as *model* analysis [92]. The method uses a semi-analytical model of shower development for the image template production. This affects the reconstruction quality at energies above 10 TeV since a large number of particles reach ground level, resulting in large fluctuations, which are hard to parametrise analytically within a simplified analytical model.

The ImPACT reconstruction technique uses gamma-ray simulations to create the shower image templates that allow for a better handling of high-energy events. Similar to the lookup tables, the template library is binned in zenith and azimuth angles, as well as: 17 energy bands (0.08 - 100 TeV) /$\cos(\theta_{\mathrm{zen}})$, 25 impact distance bands (0 - 1000 m) and bins in X_{max} with 25 g cm^{-2} width, distributed around the expected X_{max} for a shower with a given energy. However, there is no binning in offset bands and all events are simulated at 0° offset.

Each template is represented by a 2D histogram that contains the expected image amplitude at all pixel positions within the camera for a given set of parameters. An example of image templates is shown in Figure 3.8. Event reconstruction is done by comparing recorded and expected shower images. The method uses a likelihood function[3] that is minimised in a 6-dimensional fit over direction (x, y), shower core position $(x_{\mathrm{c}}, y_{\mathrm{c}})$, X_{max} and primary energy. Figure 3.9 displays an example of the 2D projection of the likelihood surface in the camera plane.

Before applying the ImPACT method, events undergo geometry pre-reconstruction, and the pre-reconstructed shower parameters then serve as seeds for the minimisation. The gamma-hadron separation remains the same as discussed in Section 3.3.2. Since the ImPACT minimisation procedure has a high degree of computational intensity, background rejection is performed beforehand in order to decrease the number of events in the pipeline and make the data analysis faster.

[2] Analysis configurations that use TMVA based gamma-hadron separation get suffix *_zeta* in their names, e.g. *std_zeta* or *hard_zeta*.

[3] Originally, this likelihood function was developed for the *model* analysis, which is another H.E.S.S. analysis chain [92].

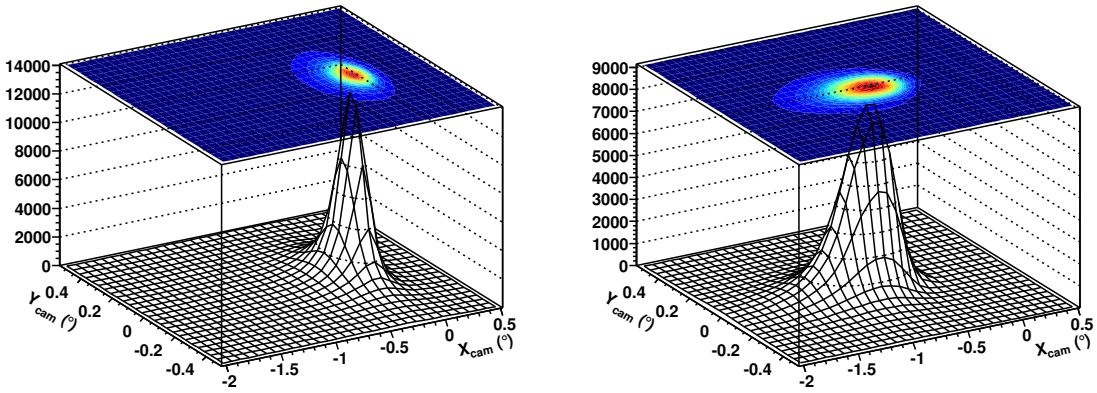

Figure 3.8: Image templates used in the ImPACT reconstruction technique [169]. Both examples are performed for gamma rays simulated with 1 TeV primary energy and expected $X_{\max}$ at 300 g cm^{-2}. Left and right panels show the templates with shower core distance of 20 and 100 m, respectively. The z-axis is in units of photoelectrons per square degree.

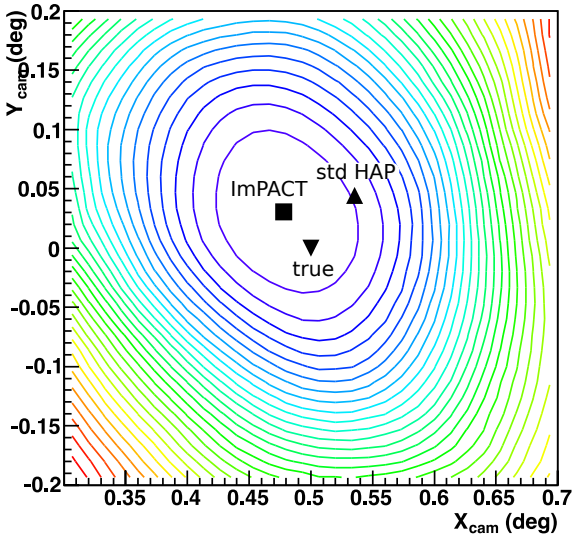

Figure 3.9: Example of a 2D projection of the likelihood surface in the camera plane [169]. The square and triangle show the reconstructed shower direction derived using ImPACT and standard geometry reconstruction methods, respectively. The inverted triangle indicates the true direction of the simulated shower.

3.5 Outlook of the standard analysis technique

Over the last 15 years of H.E.S.S. operation, new analysis techniques have been developed or adapted from the previous generation of Cherenkov telescopes. The methods implemented within the HAP framework, especially ImPACT in combination with TMVA based background rejection, proved to be efficient high-performance analysis techniques. However, the H.E.S.S. experiment covers an energy range of several decades. Most of the

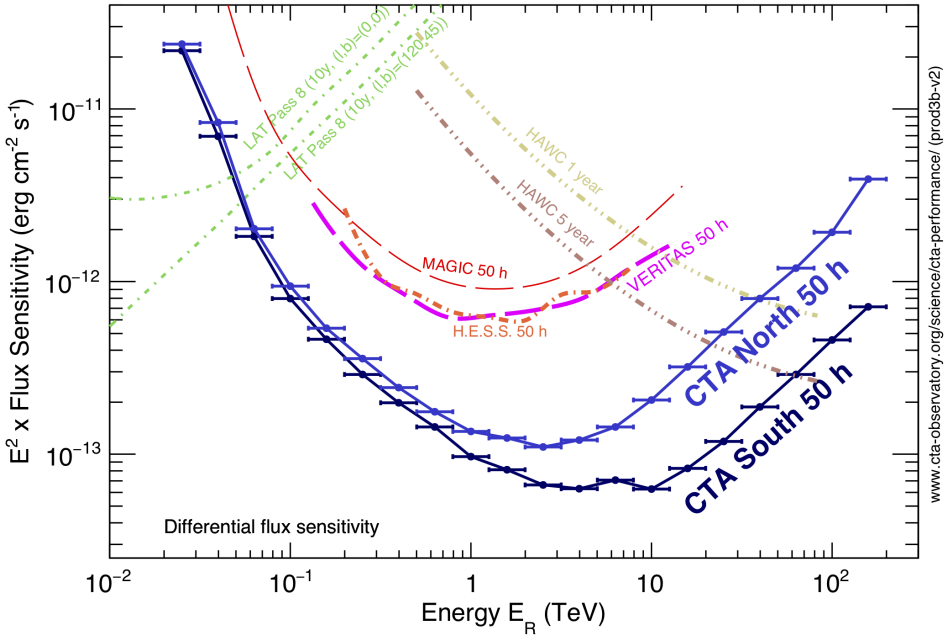

Figure 3.10: A comparison of differential sensitivity for different gamma-ray instruments. Image credit: CTA Consortium [86].

VHE sources visible to H.E.S.S. emit gamma rays at energies from approximately 100 GeV to a few TeV. Therefore, the discussed analysis methods are optimised to have a good performance in this energy range, achieving the best sensitivity at about 1 TeV (see Figure 3.10).

However, there are many important topics – such as the search for Galactic PeVatrons, the study of gamma-ray production scenarios for sources (hadronic vs. leptonic), EBL absorption studies – which require good sensitivity at energies above 10 TeV. In addition, until the southern part of the CTA [122] is constructed and operational, H.E.S.S. is the only VHE gamma-ray instrument in the Southern Hemisphere. Thus, the experiment would benefit from an analysis optimised for the high energy domain, i.e above 10 TeV.

At the highest energies, the main limiting factor is the available statistics of gamma rays from a source due to both the typically steeply falling source spectra and the limited effective detection area. Better sensitivity can be attained by increasing the statistics after all of the selection cuts. For example, at preselection level, the largest impact on high-energy statistics is due to the local distance cut, discussed in Section 3.1.2. Weakening this cut would increase the number of events at high energies, although at the cost of reconstruction accuracy.

Another part of the analysis that can be optimised for high energies is gamma-hadron separation (Section 3.3). The TMVA based technique is already a powerful method but could be further enhanced by finding additional variables that show background separation capabilities. Furthermore, currently in the HAP analysis, BDTs are trained for one wide band at high energies, between 5 and 100 TeV, and only one offset angle of 0.5°. Finer binning at high energies as well as training in several offset bands could bring an additional improvement in background rejection.

Interestingly, analysis of the events at large offsets, beyond the camera FoV, is one of the least explored territories in present-day Cherenkov techniques. In the HAP analysis, the maximum offset of the events is typically restricted to 2.5° radius from the camera centre. Usage of the offset band beyond this limit could potentially increase the gamma-ray source exposure and, hence, high-energy statistics, by extending the allowed distance range between the source and telescope pointing position. The next two chapters of this work, Chapters 4 and 5, discuss a possible way to reconstruct events and improve the background rejection for events with offset angles beyond, as well as below, the 2.5° offset limitation, in order to achieve higher gamma-ray statistics and better sensitivity at energies above 10 TeV.

Chapter 4

Event reconstruction at large offset angles

The precision of the event reconstruction degrades as the event offset increases [66]. As a result, typically only events with an offset angle up to 2.5°, the *maximum event offset*, are used in the H.E.S.S. analyses. This chapter investigates the feasibility to use events beyond the 2.5° limitation. In addition, it discusses the ways to resolve the challenges associated with the event analysis at large offset angles, in particular, the degraded reconstruction accuracy and increased background rate.

The FoV of the CT1 - 4 telescopes is 5°, while the CT 5 telescope has only 3.2° FoV. Therefore, the study presented in this chapter focuses only on CT1 - 4 telescopes and does not take into account the CT 5 telescope.

4.1 Maximum run and event offset

The above-mentioned cut on the event offset is a part of the event selection procedure and is performed after the reconstruction and gamma-hadron separation in the analysis. Its value is dictated by the physical size of the telescope camera and it works well for events in the core region of the energy range accessible with H.E.S.S. Figure 4.1 shows the acceptance curves that characterise the system capability to detect and reconstruct air showers at different offset angles from the camera centre. The maximum event offset cut discards less than 20% of the events in the full energy range. But if one considers only events with energies above 10 TeV, nearly 50% of the reconstructed events are beyond the offset threshold.

A *run*[1] or *observation offset* is the angular distance between the pointing position and source of interest. A *maximum run offset* cut is normally applied during the run selection for the analysis of a particular source. Similarly to maximum event offset, its typical value is around 2.5°. In the case, when several sources are located close to each other, runs taken on neighbouring sources can contribute to the analysis of the given source if

[1] In particle and astroparticle experiments, *run* denotes a time period of one observation. In H.E.S.S., an observation run is normally 28 minutes long.

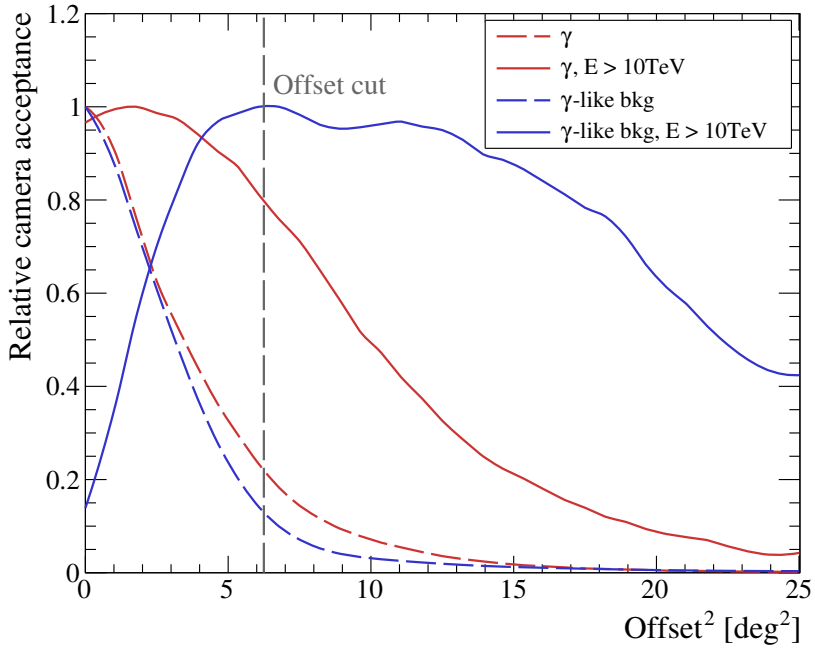

Figure 4.1: Acceptance of the CT1 - 4 cameras to gamma-like events. The dashed line represents the camera acceptance in the energy range from approximately 100 GeV to 150 TeV, while the solid line denotes acceptance only for events with primary energy above 10 TeV. The colour shows different types of events after gamma-hadron separation. All curves are normalised to the number of events within corresponding energy ranges. Red lines show simulated diffuse gamma rays with spectral index of $\Gamma = -2$ in a view cone with 5° opening angle at 20° zenith angle. Blue lines show real background data, obtained by analysing PKS 2155−304 observation runs in zenith angle range from 15° to 25°. The events at the position of PKS 2155−304 are excluded from acceptance calculation. The typical size of the maximum event offset in the H.E.S.S. analysis is marked by the grey dashed vertical line.

their offsets are within the maximum allowed run offset. This is a typical situation for the observations in the Galactic plane and is shown in Figure 4.2, giving Vela X and Vela Junior as an example. Both objects are VHE sources and have been observed with H.E.S.S. The telescope pointing positions are indicated by white crosses. The smaller dashed ring with 2.5° radius around the Vela X position outlines the runs that would be normally considered for the analysis in the standard case. By enlarging the maximum observational offset, e.g. up to 4.5° (larger ring), more Vela Junior runs can be used for the analysis of Vela X. This way, Vela X can gain a deeper exposure and, as a result, an increase in statistics at high-energies. However, expansion of the maximum run offset is only possible if the maximum event offset is increased up to the same value because the runs with offsets, which are larger than the sum of the maximum event offset and size of the source of interest, are not able to contribute events for the source analysis.

In summary, simultaneous enlargement of the maximum event and run offsets from 2.5° up to 4.5° can result in an increase in exposure of a given source, which can lead to an increase in high-energy statistics and potentially to an improvement in the sensitivity at energies

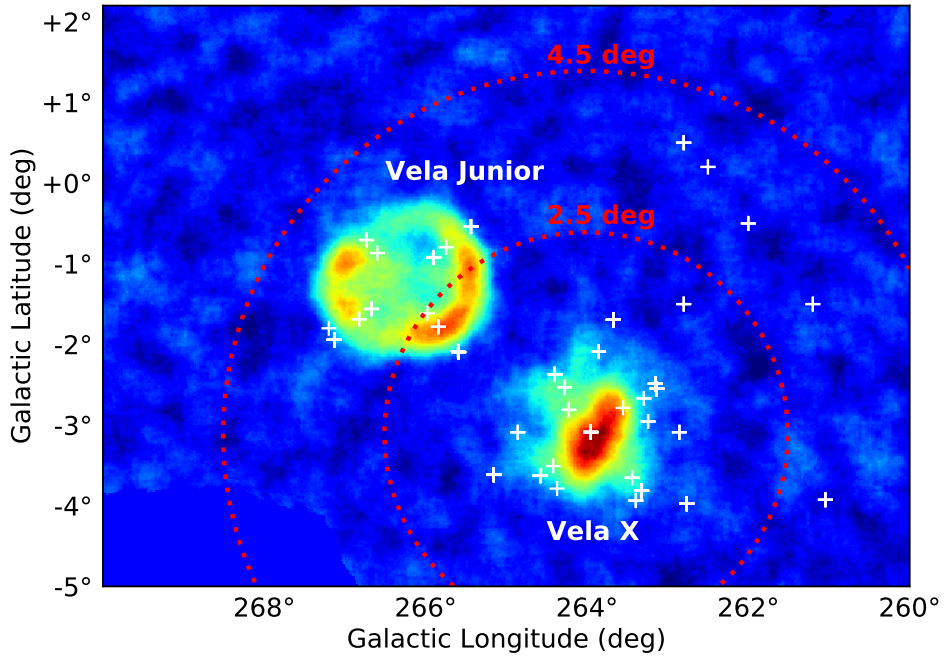

Figure 4.2: A schematic illustration of selection cut on maximum run offset. The example displays two VHE sources, Vela X and Vela Junior, which are located within about 3° of each other. White crosses indicate telescope pointing positions during the H.E.S.S. observations. Red dashed rings show the maximum run offset from the Vela X position, i.e. runs within the ring are considered for the analysis. The smaller ring shows 2.5° radius around the source and is a typical size of maximum offset used in H.E.S.S. About 94 h of observations fall into this ring. But for high-energy studies, the observational offset cut could be increased up to about 4.5°, which allows for 124 h of data to be analysed and is shown with a larger ring. The data are taken from [129].

above 10 TeV. Also, high-energy observations can benefit from an increase in effective FoV from 5° to approximately 9°.

4.2 Analysis challenges at large offset angles

Using large-offset events in the analysis has advantages but also comes with a number of challenges. The behaviour of shower and image parameters changes as the event offset increases. The distributions of shower core distances for different event offsets are shown on the left side of Figure 4.3. The distribution is quite narrow and peaks just a few hundred meters from the telescopes for the events originating at 0.5° offset angle, and becomes broader as the event offset increases. This happens first because the large-offset showers are inclined with respect to the telescope axis and can be seen from a greater distance. Secondly, more distant showers start to pass the image-based selection cuts, which are discussed in Section 3.1.2. At small offset angles, the local distance of the shower images grows almost linearly as a function of the impact parameter as shown in Figure 4.4. Thus, images of distant showers have large local distances, i.e. they are located

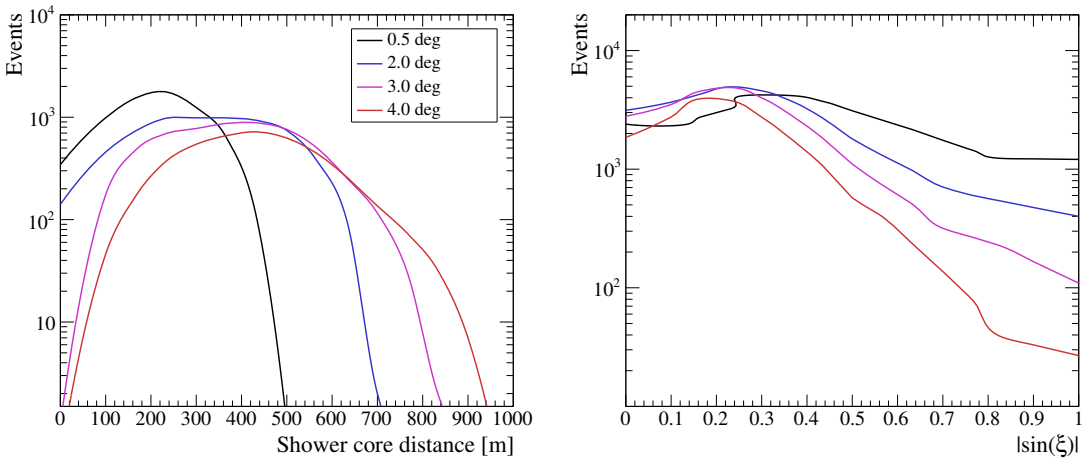

Figure 4.3: Evolution of shower parameters for different event offsets at energies above 10 TeV. The distribution of shower core distance with respect to the centre of the H.E.S.S. array is displayed in the left panel. The right panel shows the orientation of the shower images with respect to each other in the camera plane. The x-axis represents the absolute value of sine of the angular distance between major axes in each image pair recorded for the particular event. All distributions are shown for gamma-ray source with a spectral index of $\Gamma = -2$ simulated at 20° zenith angle.

at the camera edge, and are rejected by the local distance cut. At larger offset angles, the relation between the image local distance and impact parameter changes. Images of nearby showers are located near the camera edge, while images of distant showers appear closer to the camera centre. This results in distant showers passing the preselection cuts and broadening the core distance distributions in Figure 4.3 at larger event offsets.

From geometry, the angles between the shower images get smaller as the shower distance to the array centre increases. Since the proportion of distant showers grows as the offset angle increases, the number of nearly parallel image pairs also rises. The right panel of Figure 4.3 shows the sine of the angle between shower image major axes. The events originating at lower offset angles tend to produce images with more than 20° angles ($\sin(\xi) \approx 0.4$) between them. While the events at larger offset angles are dominated by image pairs with less than 20° separation angle.

The accuracy of the event reconstruction is one of the main challenges at large offset angles. Since the standard geometry reconstruction (Section 3.2.1) depends on the respective image orientation, smaller angles between the shower images will result in even greater degradation of the reconstruction performance at large event offsets. Another difficulty is the background rejection. The intensity of Cherenkov light from the shower drops with distance to the core position (see Figure 2.6 in Section 2.2). Because of this, images of distant cosmic-ray showers are less bright and information about their irregular structure can be smeared out. This can result in cosmic rays looking similar to gamma-ray-induced showers, worsening the efficiency of gamma-hadron separation.

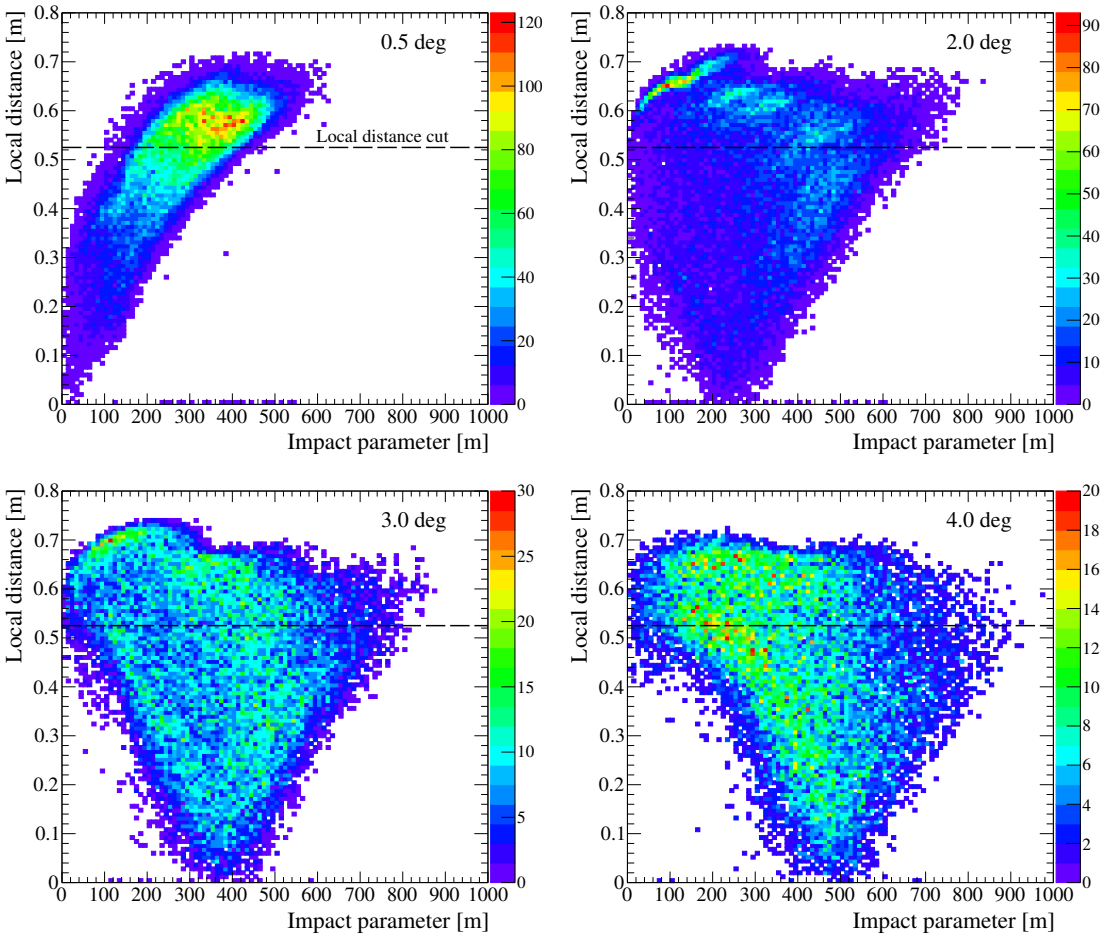

Figure 4.4: Evolution of the image local distance as a function of the shower distance to the telescope for different event offsets at energies above 10 TeV. All distributions are produced using point-like gamma rays after the trigger level. The dashed black line shows the typical local distance cut value of 0.525 m. Colour bar shows the number of event per bin. The gamma rays used for the plots are simulated at 20° zenith angle with a spectral index of $\Gamma = -2$.

4.2.1 Lookup tables for large-offset events

Both aforementioned challenges of the analysis at large event offsets are discussed in greater details later in Section 4.2.2 and 4.2.3, while this section considers the lookup tables necessary for the large-offset event analysis. The standard energy- and shape-lookup tables cover the event offset bands only up to 2.5°. In order to reconstruct the energy and to perform the gamma-hadron separation for the events beyond 2.5° offset angle, lookup tables are expanded up to 5° in this work. They are extended for 180° azimuth angle[2] and for all standard zenith angles up to 60°. Current work is focused on the CT1 - 4 telescopes and the H.E.S.S. I phase of data taking, therefore, lookup tables are re-produced only for

[2]Up to now, the lookup tables are reproduced only for the azimuth angle of 180°. However, in order to better account for the effects of the geomagnetic field, lookup tables should be also reproduced for at least 0° azimuth angle.

the optical phases 100 - 105, which correspond to data taken before the end of 2012. The parameter space covered by the standard lookup tables can be found in Section 3.2.2. New lookup tables are filled using point-like gamma rays simulated with $\Gamma = -1$ spectral index. Usually, $\Gamma = -2$ slope is used in simulations, but a harder spectrum allows for more statistics at high energies.

At large zenith angles, showers have emission production site further away and travel through more atmosphere, which leads to a rise of the energy threshold with zenith angle. In order to save computing resources, events with energies far below the threshold usually are not simulated. For this reason, the low energy cutoff is adjusted for each zenith band. The events are simulated over a certain area, which should be large enough and be able to accommodate sufficiently distant showers that can possibly trigger the telescopes. As zenith angle increases, showers become more inclined and can be seen from greater distances. Hence, the simulated area also grows with zenith angle. Additionally, events originating at large offset angles have a wider core distance distribution (Figure 4.3, left) and can be triggered farther from the array centre than events at small offset angles. Accounting for that, the radius of the simulated area is set to a value which is $\sim$100 - 200 m larger than the standard one for the corresponding zenith angle. Low-energy cutoff values and radii of the simulated area for each zenith angle are summarised in Table 4.1.

Zenith angle [deg]	Min. energy [GeV]	Max. radius [m]
0	15	1000
20	15	1000
30	15	1000
40	60	1300
45	70	1500
50	100	1800
55	150	2100
60	200	2400

Table 4.1: Parameters of the gamma-ray simulations used for lookup-table production.

4.2.2 Angular resolution of the standard analysis at large offset angles

As discussed earlier, the fraction of distant showers, and hence, events that have relatively small angles between major axes of their images, rises as the event offset increases. Since the standard geometry reconstruction works better when angles between images are close to 90°, a large number of distant showers may adversely affect the event reconstruction quality, resulting in degradation of the angular resolution of the analysis.

The angular resolution is defined here as the radius of the area containing 68% of all simulated events that reconstructed closest to the true direction position. The resolution of the standard analysis after the postselection, as a function of simulated energy[3], is compared in the left panel of Figure 4.5 for different event offsets. In this example, the standard analysis is represented by the *std* configuration, i.e. geometry reconstruction and box-cut background separation as well as the ImPACT analysis. Since nominal lookup

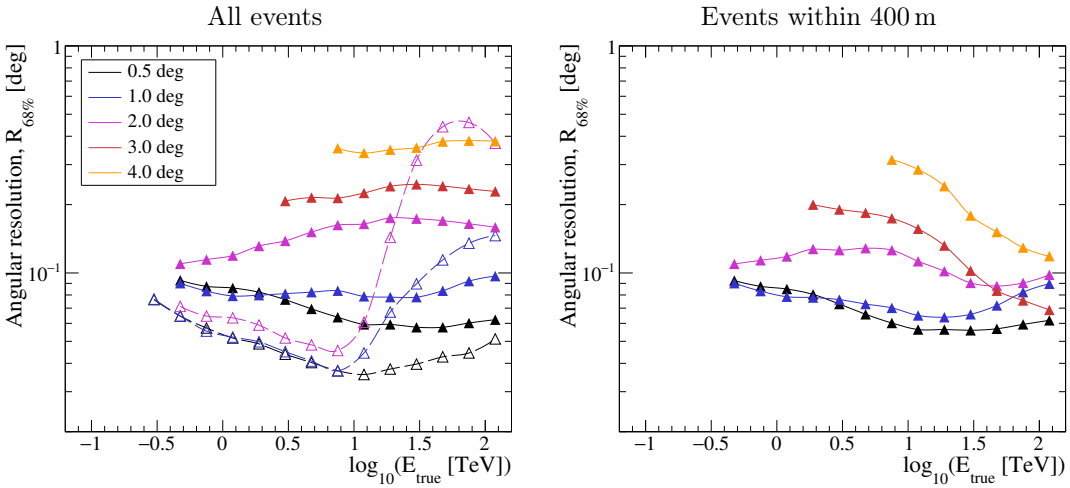

Figure 4.5: Angular resolution of the standard analysis as a function of true energy at different event offsets. Solid lines denote the *std* analysis (geometry reconstruction + background separation with box cuts) and dashed lines show the ImPACT analysis with BDT-based background rejection. Additionally, the right part shows only events with the shower core distance within 400 m from the array centre. All plots show the resolution above the energy threshold[4]. The curves for the *std* analysis are produced using re-produced lookup tables. The ImPACT analysis resolution is shown only up to 2° offset, where it can use standard BDT training for the background rejection. The plots are produced using point-like gamma rays simulated with $\Gamma = -1$ spectrum at 20° zenith angle.

tables cover only offset angles up to 2.5°, the *std* analysis here uses re-produced lookup tables that are extended for large event offsets as discussed above. As seen from the figure, the angular resolution of the *std* analysis worsens dramatically for each next event offset band and at 3° offset angle, it is already larger than 0.2°, which is hardly acceptable for the source analysis.

The ImPACT analysis technique uses BDTs for the gamma-hadron separation that are nominally produced only for the 0.5° offset angle. Parameter distributions, which are used for the BDT training, change as the event offset increases (this topic is investigated in Section 4.4). Thus, the performance of the standard BDTs can significantly worsen for the events at large offset angles. Due to this, the ImPACT angular resolution curves are shown only for the offset bands which are normally used in the H.E.S.S. analysis, i.e. offset angles smaller than 2°. However, as shown in Figure 4.5, the resolution of the ImPACT analysis at high energies starts to degrade significantly even for the events with offset angles as low as 1°. This may be caused by events with nearly parallel images whose CoG falls outside the camera [168]. Typically, such events should be rejected by the local distance cut (see Section 3.1.2). But sometimes the cut fails to identify these events. In this case, there is a degeneracy in the ImPACT fit parameters, specifically the event position, $X_{\max}$ and

[3]Here and hereafter, the axis indicating primary energy is divided so as to have five bins per decade for all performance plots.

[4]The energy threshold is defined as 10% of the effective area peak. More details on effective area can be found in Section 4.2.3.

shower core distance, which results in the fit trying to reconstruct the event position to the centre of the camera.

Taking into account the behaviour of the shower core distance parameter at different offset angles (Figure 4.3) and its relation to the degradation of the angular resolution, one of the possible ways to improve the analysis performance is to reject distant showers. The right plot in Figure 4.6 shows the angular resolution of the *std* analysis configuration after the standard postselection for the events with the shower core distance smaller than 400 m. The cut has a negligible effect at 0.5° offset angle but significantly improves the resolution at larger offset angles. However, as is discussed in the next section, this cut rejects a significant fraction of gamma rays that leads to a necessity of finding a more sophisticated way to improve the reconstruction accuracy.

4.2.3 Background rate and effective area of the standard analysis at large offset angles

Other important characteristics of the analysis performance are the *effective area* and *background rate*, which are key components of the instrument sensitivity. The effective area is the area A_{eff} where the instrument is sensitive to the particles of interest (in this case, gamma rays) assuming 100% efficiency and is defined as:

$$A_{\text{eff}} = \frac{N_{\text{cuts}}}{N_{\text{sim}}} \cdot A_{\text{sim}}, \tag{4.1}$$

where N_{cuts} is the number of events that pass background rejection cuts; N_{sim} is the number of events simulated over the area A_{sim}. The effective area depends on zenith, azimuth and offset angles, optical efficiency, primary energy of the gamma rays as well as applied selection cuts (stricter cuts decrease the effective area).

The background rate characterises the number of cosmic-ray particles that are detected with the instrument and pass all gamma-hadron separation cuts (gamma-like background). It depends on the same set of parameters as the effective area. In the end, a larger effective area and lower background rate result in a better sensitivity of the instrument.

The effective area and background rate for the *std* analysis configuration are displayed in Figure 4.6 for different event offsets. The left column shows the corresponding curves after the standard gamma-hadron separation using box cuts. As seen from the plots, the effective area degrades as the event offset increases. However, a bigger problem is the background rate that significantly rises at high energies at large offset angles in comparison to 0.5° event offset.

The right column in Figure 4.6 shows the result of the additional selection cut application on the shower core distance that selects events less than 400 m away from the array centre. Although the use of this one additional cut lowers the number of background events at large offset angles nearly to the level obtained at 0.5° offset and improves the angular resolution above 10 TeV (see Figure 4.5), it cuts away a large fraction of gamma-ray events at large offset angles as seen from the respective effective area curves.

For a better understanding of how many gamma rays are lost, Figure 4.7 illustrates the signal efficiency of the 400 m cut for different event offsets. Displayed curves are the ratios

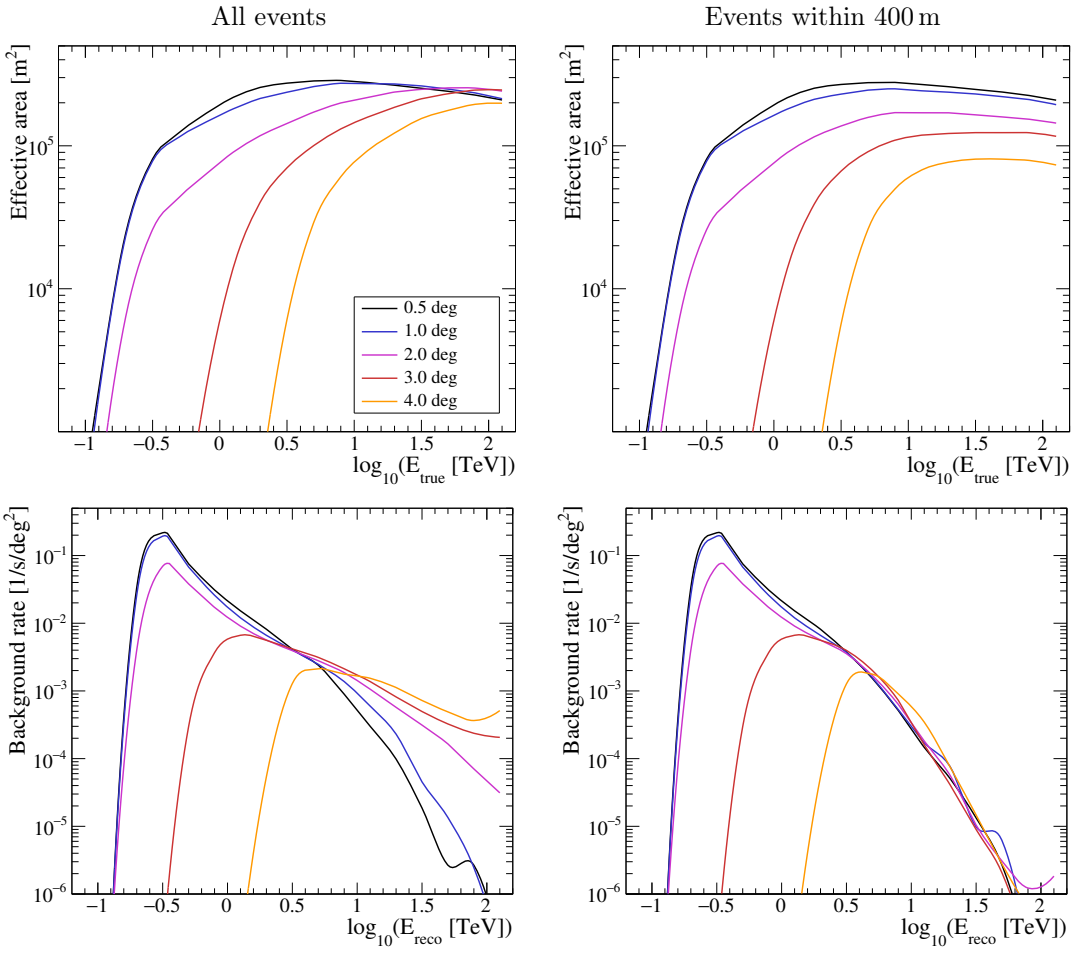

Figure 4.6: The performance characteristics of the standard analysis at different event offsets that are indicated with different line colour. The standard analysis (*std*) implies geometry reconstruction and box-cut background rejection. Additionally, the plots in the right column use the cut on the shower core distance parameter of 400 m. All curves here are produced using updated lookup tables that include larger offset angles. The top panels show the effective area plots produced using point-like gamma rays simulated with $\Gamma = -1$ spectrum at 20° zenith angle. The bottom panels depict the rate of cosmic rays estimated using observations of PKS 2155−304 between 15° and 20° zenith angle.

between the number of events after and before the application of the 400 m distance cut. Already for 2° offset, gamma-ray efficiency drops rapidly for energies above a few TeV. Thus, in order to obtain a satisfactory resolution and background rate level, and at the same time have an acceptable effective area, more sophisticated methods for the event reconstruction and improved gamma-hadron separation should be applied.

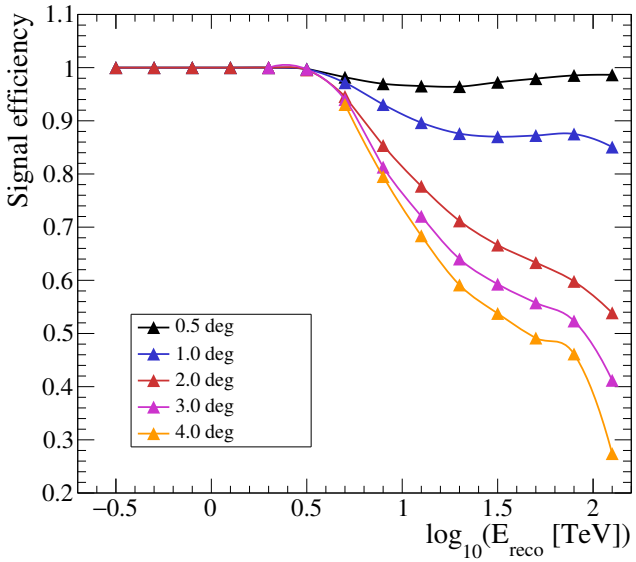

Figure 4.7: Gamma-ray selection efficiency for the cut on the shower core distance for different event offsets. Curves are generated for the core distance cut of 400 m using point-like gamma rays simulated with $\Gamma = -1$ spectrum at 20° zenith angle.

4.3 Direction reconstruction with the DISP method

One of the ways to improve the angular resolution is the application of the *DISP* method (short for displacement) for the shower direction reconstruction. Displacement is one of the image parameters and is defined as an angular distance between the image centre of gravity (CoG) and the shower direction. In the HAP analysis, it is denoted as δ parameter and is introduced in Section 3.1.1 (see Figure 3.1). Originally, the DISP method was invented for the shower direction reconstruction in the case of a single telescope operation such as Whipple [149], MAGIC I [95, 54] or H.E.S.S. CT 5 mono [164]. Nowadays it is widely used for stereoscopic systems such as MAGIC II [55] and VERITAS [142]. In this work, the DISP method is implemented for the H.E.S.S. CT1 - 4 telescopes and is used for the stereoscopic reconstruction of the shower direction and core position.

4.3.1 Reconstruction procedure using the DISP method

From the principle of the Cherenkov telescope technique, the shower direction should be located along the major axis of the image ellipse. Displacement δ, the distance between the image CoG and event direction, can be estimated based on the shape of the shower image in the camera. If the shower landed near the telescope, it has a fairly round footprint, while images of distant showers are more elongated.

The idea of the method is schematically displayed in Figure 4.8. The value of δ is evaluated separately for each shower image that passes the preselection (see Section 4.3.3 for more details). However, the location of the shower direction along the ellipse axis with respect to the image CoG is unknown. It can be in front as well as behind the image like it is

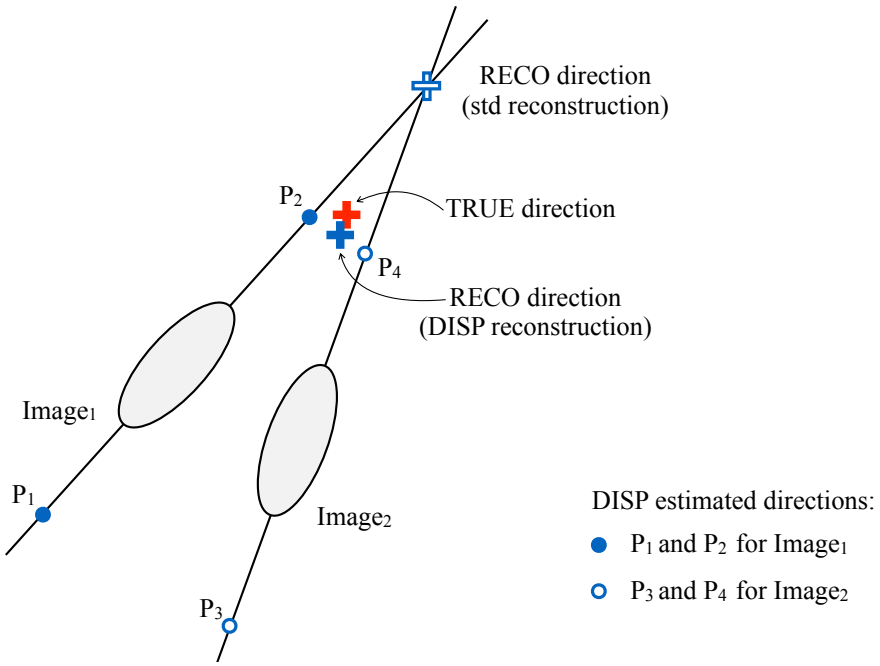

Figure 4.8: The main principle of the DISP direction reconstruction algorithm. The sketch shows the event direction reconstruction in the case of two telescopes. The red cross marks the true shower direction. The blue open cross shows the direction reconstructed with standard geometry technique by intersecting the major axes of both image ellipses. Filled and open circles indicate pairs of the direction estimates evaluated with DISP method for Image_1 and Image_2 respectively. Blue filled cross is the shower direction reconstructed using the DISP method by averaging the most likely image directions.

illustrated in the sketch. Pairs of blue filled and open circles mark the estimated locations of the direction, reconstructed for Image_1 and Image_2, respectively. This way, each image has two reconstructed direction positions. When observations are conducted with a single telescope, the event direction can be chosen by using the image asymmetry [163]. In systems with several telescopes, this ambiguity problem can be solved stereoscopically, i.e. by averaging the directions estimated for each image to obtain the overall shower direction[5].

The H.E.S.S. CT1 - 4 telescopes typically observe in stereoscopic mode. In this work, the shower direction is obtained by considering all possible combinations of the individual image directions and picking the one with the smallest uncertainty. Since every image has two estimated directions and only one of them can be used in time, there are $2^{N_{\text{tels}}}$ possible combinations, where N_{tels} is the number of telescopes used in the reconstruction. For example, in the case of two telescopes (see Figure 4.8), there are four possible combinations: P_1P_3, P_1P_4, P_2P_3 and P_2P_4. Each combination is an average position of individual image directions that enter the computation with a weight ω_i. The weight is calculated based on the parameters of the corresponding image i:

[5]The same approach is applied for the shower core position reconstruction. In this case, a role of δ is played by the *Impact* parameter, a distance between the shower core position and corresponding telescope.

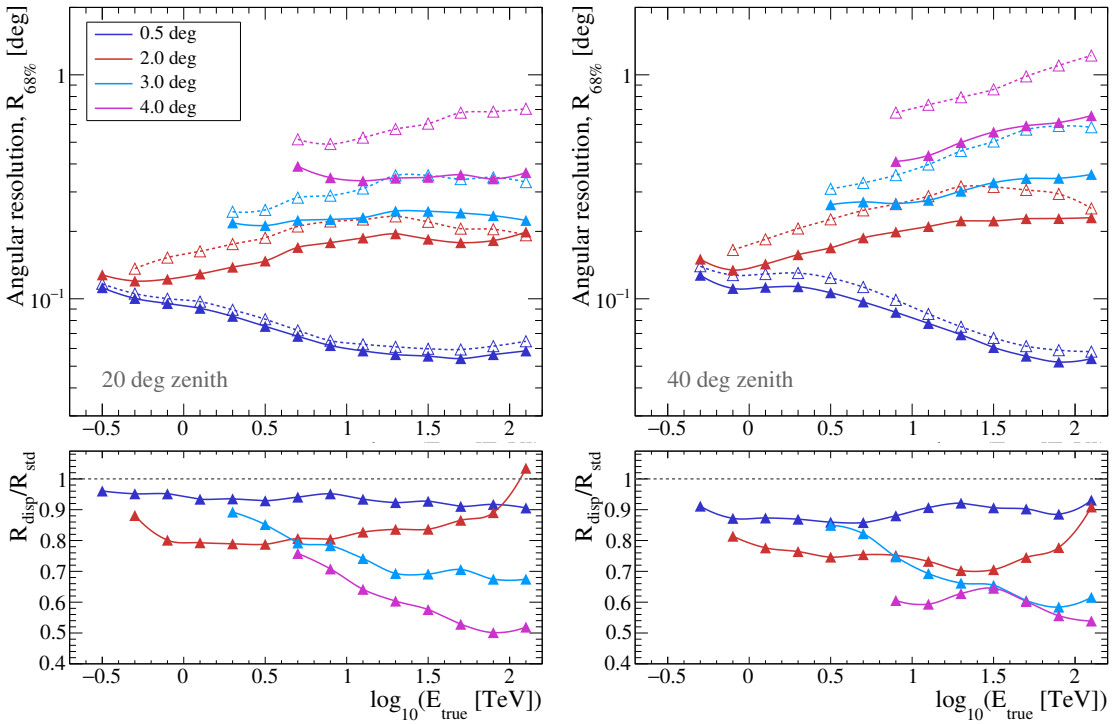

Figure 4.9: Performance of the DISP reconstruction method at the preselection level of the analysis. Displayed plots show a comparison of the angular resolution for the DISP method (solid lines) and standard geometry reconstruction (dashed lines) for 20° and 40° zenith angle. Colour of the lines indicate different event offsets.

$$\omega_i = \frac{Size_i \cdot Length_i}{Width_i}. \tag{4.2}$$

The uncertainty Err of each shower direction estimate is computed as:

$$Err = \frac{\sum err_i \cdot \omega_i}{\sum \omega_i}, \tag{4.3}$$

where err_i is the angular distance between the individual image direction and shower direction estimate; ω_i is the weight of the individual image contribution.

Improvement of the DISP direction reconstruction over the standard geometry method after preselection is depicted in Figure 4.9. For the lowest offset angle, the effect is 5 - 10% but rises as offset angles increase. At 2° event offset, the improvement reaches 20% and 30% for 20° and 40° zenith angle, respectively. As seen, the improvement also increases for large zenith angles. Naturally, it happens due to a larger fraction of distant showers with nearly parallel images at large zenith angles than at lower ones [152].

4.3.2 Artificial Neural Networks

In this work, a machine learning technique is used to estimate the value of the δ and $Impact$ parameter for the shower direction and core position reconstruction, respectively. For this purpose, a regression algorithm, specifically an *Artificial Neural Network* (*ANN*) in the TMVA package [135], is applied. ANN can be described as a collection of interconnected neurons, which can receive input signals and produce a certain response to it. This work, as well as the CT 5 mono analysis[6] [163], uses *Multi-layer perceptron* (*MLP*), one of the neural networks implementations in TMVA.

The MLP architecture is schematically depicted in Figure 4.10. It consists of neurons organised in layers. Only direct connections between neurons from a given layer to the following one are allowed. MLP belongs to the class of feed-forward neural networks, which means that information is transferred only in a forward direction and cannot go backwards and create information loops or feedbacks [34].

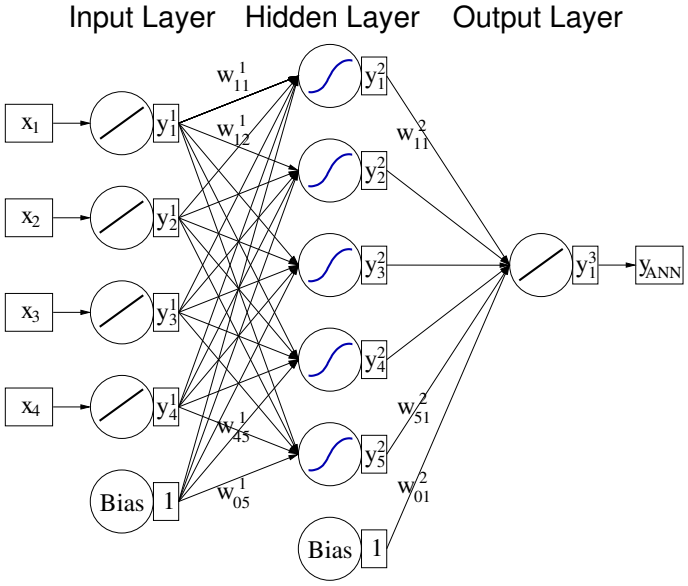

Figure 4.10: Multilayer perceptron with one hidden layer [135].

MLP contains at least three layers:

- *Input layer* – the first layer that is composed of the neurons containing information from N input variables $x_1 \dots x_N$.
- *Hidden layers* – one or more intermediate layers. Hidden layers can have an arbitrary number of neurons that can be specified by one of the configuration options during the network initialisation set up. Typically, it is recommended to set the number of neurons to a value greater than the number of input parameters. If the training dataset is large enough, the network can reach the desired performance by having only one hidden layer with as many neurons as needed for that. On the other hand, the same performance can likely be achieved using more hidden layers and a smaller

[6] MLPs are also used for the CT 5 mono reconstruction of the shower parameters (direction, core position and energy) and gamma-hadron separation [163].

total number of neurons, which results in a shorter training time and a more robust network [135].

- *Output layer* – the last layer, which holds typically one output variable y_{ANN}[7].

ANNs are inspired by biological neural networks and connections between artificial neurons can be considered as an analogy to synapses between biological neurons. Following this similarity, in ANNs the strength of the real synapses is represented by weights that are assigned to each artificial connection. This way, a certain neuron j will receive signal $y_i\omega_{ij}$ from the neuron i in the previous layer, where y_i is an output of the neuron i and ω_{ij} is a connection weight between these two neurons. Since the neuron j is connected to all n neurons in the previous layer, total input from precursor neurons is $\sum_{i=1}^{n} y_i\omega_{ij}$.

Additionally, input and hidden layers contain one more neuron, which is called a *bias node* (see Figure 4.10) and constitute an important ingredient for the network training. It keeps a constant value that is typically equal to one. It does not have input connections from the previous layer but is connected to all neurons in the following layer. Analogously to other artificial connections in the network, bias synapses have their own weights ω_{0j}. Eventually, the final input (*synapse function* κ) to the neuron j takes a shape:

$$\kappa = \omega_{0j} + \sum_{i=1}^{n} y_i\omega_{ij} \tag{4.4}$$

The output of each neuron is generated by *neuron response function* ρ, which is a composition of synapse function κ and *neuron activation function* α. The activation function defines the form of neuron output and helps to keep its values within an acceptable range (typically [0; 1] or [-1; 1]). In this study, MLP uses two hidden layers composed of $N + 5$ and $N + 4$ neurons, whose activation function is chosen to be a tanh function:

$$\alpha_{\text{tanh}} = \frac{e^x - e^{-x}}{e^x + e^{-x}}. \tag{4.5}$$

MLP training is done using *supervised learning techniques*, which means that the true output (*target*) is known and the technique utilises it for a better approximation of the mapping function from input to output. The neural network produces an output $y_{\text{ANN},i}$ for each training event i and compares it with true output y_i. Agreement between network response and the target can be expressed by the *error function* E as:

$$E = \sum_{i=1}^{N_{\text{event}}} E_i(x_i|w) = \sum_{i=1}^{N_{\text{event}}} \frac{1}{2}(y_{\text{ANN},i} - y_i)^2, \tag{4.6}$$

where $x_i = (x_1, \ldots, x_{N_{\text{var}}})$ represents input parameters and w – an ensemble of adjustable weights used by the network. Thus, the process of the learning is constituted by finding the optimal connection weights and biases to minimise the error function. For this purpose, there are several algorithms implemented in TMVA. The one used in this work is

[7]Except for the case of multi-target regression where each target is represented by its own output neuron.

called *Broyden-Fletcher-Goldfarb-Shanno* (*BFGS*) algorithm [135, 34]. It uses the second derivative of the error function to update the weights. An advantage of this method is a smaller number of iterations required for convergence and better robustness with respect to minimum overshooting or convergence in the local minimum compared to other methods.

A training dataset goes through the training procedure $N_{\text{cycles}} = 2000$ times. For speeding-up the training process, MLP allows for sampling of the dataset. In this case, only a fraction of events is used in a training cycle. Additionally, dataset sampling may lead to an increase in training robustness. It is possible to set a number of epochs for which dataset sampling is performed. In this work, one-third of the full dataset is used for the first 80% of the training cycles. Afterwards, all available events are taken for the training. During the sampling mode, events are selected randomly.

4.3.3 ANN input parameters

Training of δ and *Impact* parameter is organised in two separate neural networks and uses seven input parameters. Six of them[8] are the same for both networks and based on the image shape: $Width$, $Length$, $Width/Length$, $\log(Size)$, $Skewness$ and $Kurtosis$ (introduced in Section 3.1.1). Mean values of these parameter distributions are displayed as a function of energy in Figure 4.11 for average 20° and 60° zenith angle. RMS values for the corresponding distributions are presented in Appendix A.1 in Figure A.1.

Naturally, image intensity, width and length increase with energy. Above a certain energy, $Length$ growth slows down noticeably. There are two effects that can lead to such behaviour. First of all, the image can be clipped by the edge of the camera. Second, images of high-energy showers are very likely clipped in time. As described in Section 2.2.2, the standard readout window in the H.E.S.S. camera is 16 ns. The duration of high-energy showers can be longer than this standard readout setting [111, 188], which results in only partial image record. Such behaviour of $Length$ has an influence on the evolution of image roundness ($Width/Length$ parameter). At first, it decreases fast with energy rise and images become more elongated. But then roundness starts to increase again roughly at the point where there is a break in the $Length$ graph. The same reason can also lead to a $Kurtosis$ decrease at high energies since spread in time, clipped images would have a less prominent central peak of light intensity distribution across the image.

The seventh input variable is a seeding parameter. Indeed, an additional study showed that training has better performance if expected displacement (or impact in the case of core reconstruction) is included as an input parameter. Thus, before applying the DISP method, each event undergoes the standard geometry pre-reconstruction[9] (major image axes intersection) to find the preliminary shower direction and core position. This way, an angular distance from the pre-reconstructed direction to the image CoG, displacement δ_{reco}, serves as a seventh input variable for the network training set intended for the shower direction reconstruction. Similarly, the preliminary impact parameter $Impact_{\text{reco}}$, the distance from the pre-reconstructed core position to the telescope, is included in the shower core reconstruction network. Accordingly, the targets for these two training sets are

[8] The first six parameters are similar to the ones used for the MLP training in the CT 5 mono analysis [163].

[9] Similar approach is applied in the ImPACT analysis method [169], which uses the shower parameters pre-reconstructed with the geometry method as a seed for the minimisation algorithm (see Section 3.4).

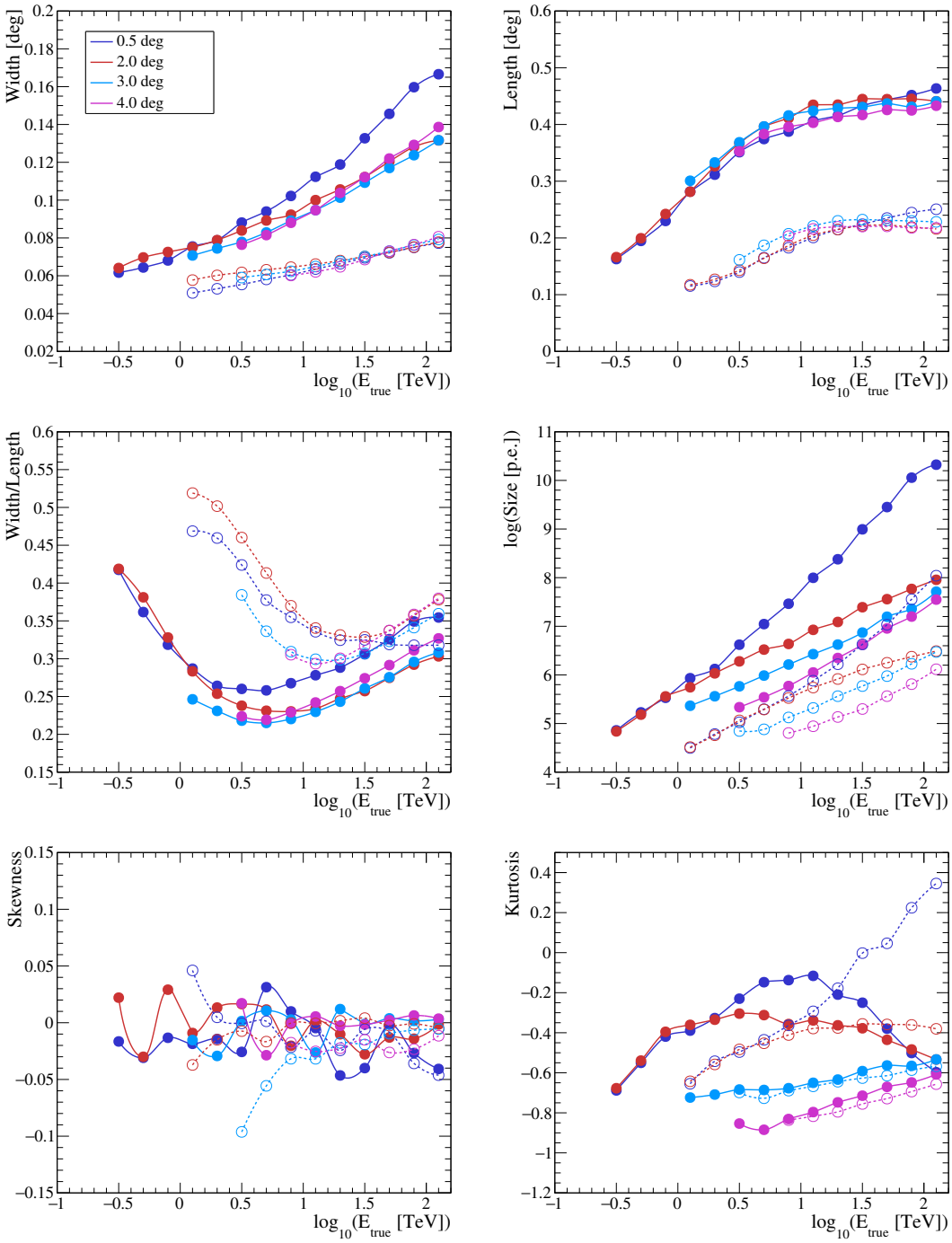

Figure 4.11: Mean values of the input variable distributions for the MLP training at different event offsets. All figures are produced using simulations of diffuse gamma rays that eventually serve as an MLP training dataset, which is described further in the text. Six plots represent the energy dependence of input variables, which are based on the image shape parameters. Solid lines represent gamma rays simulated with average zenith angle of 20°, while dashed lines depict zenith angles around 60°.

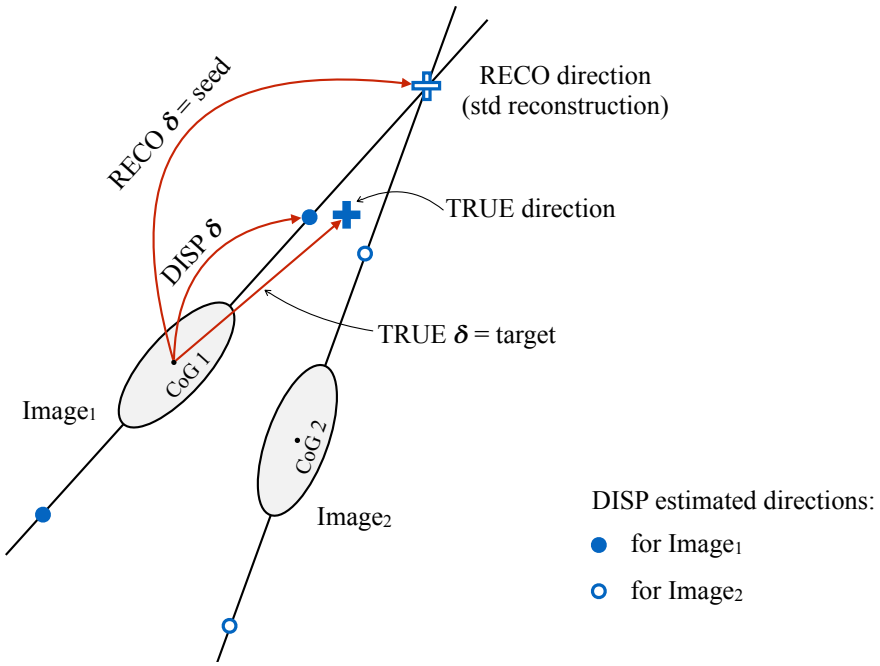

Figure 4.12: Schematic illustration of an example of seed, target and output parameter arrangement in the case of direction reconstruction in the DISP method. Further explanation can be found in the text.

the δ_{true} and $Impact_{\text{true}}$ variables, which are actual values and known from the simulation. Figure 4.12 schematically illustrates the meaning of the seed, target and output variables for the example of the direction reconstruction.

Mean values of the δ_{true} and δ_{reco}, as well as $Impact_{\text{true}}$ and $Impact_{\text{reco}}$ parameter distributions, are compared in Figure 4.13 for 20° zenith angle. As expected, high-energy showers can be seen from greater distances and their mean $Impact$, as well as δ, grows as the energy increases. Similarly, the mean parameters plotted for an average zenith of 40° and 60° and the corresponding RMS graphs can be found in Appendix A.1 in Figures A.2 and A.3, respectively.

Correlation coefficients

The characteristics of the input data strongly influence the training performance. By definition, the target variable is dependent on input parameters. Thus, the input variables should be correlated with the target. The *Pearson correlation coefficient* ρ measures a linear relationship between the variables and is computed as [135]:

$$\rho(x, y) = \frac{\text{cov}(x, y)}{\delta_x \delta_y}, \tag{4.7}$$

where *cov* stands for covariance; x is the input variable and y is the training target; δ_x and δ_y are the standard deviations of x and y distributions, respectively. The values of the correlation coefficients lies within the range $[-1,1]$.

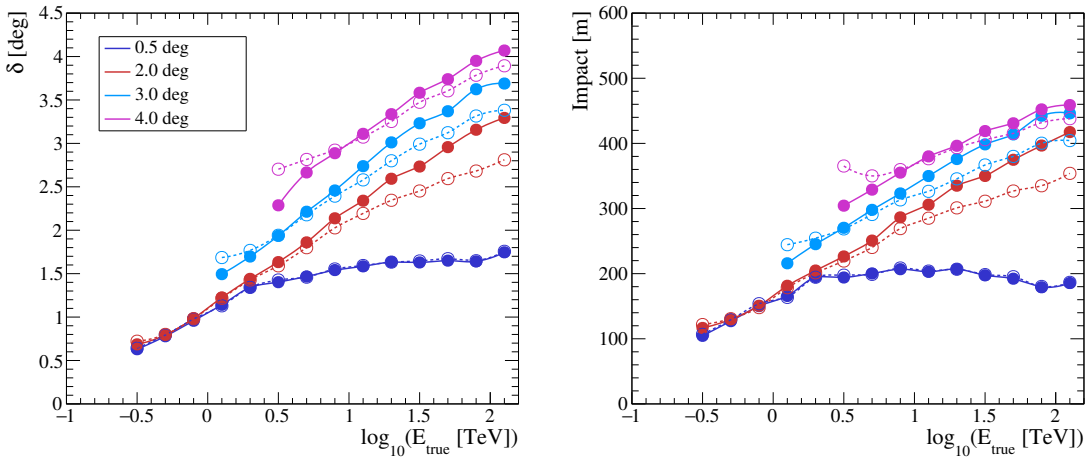

Figure 4.13: Mean values of the seed and target variable distributions for the MLP training. Line colours indicate different event offset bands. Left panel shows the comparison of δ_{true} (target, solid lines) and δ_{reco} (seeding parameter, dashed lines) for the network training used for the shower direction reconstruction. Right panel shows the comparison of $Impact_{\text{true}}$ (target, solid lines) and $Impact_{\text{reco}}$ (seeding parameter, dashed lines) for the network training used for the shower core position reconstruction. All plots are produced for an average 20° zenith angle using diffuse gamma-ray simulations.

Figure 4.14 shows the absolute values of the correlation coefficients between the input and target parameter (δ_{true} in this case) for 20° and 60° zenith angle. As expected, the true and reconstructed δ parameters are strongly correlated and the same conduct would be seen for the $Impact$ parameter. But there are a few depressions in the correlations between these parameters. This can be explained by the outliers in the input distributions of δ_{reco} and $Impact_{\text{reco}}$, which were not cut off before the training. Such behaviour of the input dataset slightly decreases the training performance and results in the angular resolution worsening by a few per cent. A similar drop occurs in the correlation with the target for the $Length$ and $Width/Length$ parameters. In this case, the drop is always located around 1.5 - 2.5° offset angle and is likely not caused by the outliers in the corresponding input distributions. One of the possible explanations could be the relative proximity of the above-mentioned offset bands to the camera edge.

The figure also shows that the $Skewness$ parameter has minimal importance for the MLP training. In future, the list of input variables should be optimised by at least removing the $Skewness$ parameter. This would decrease the probability of an overtraining occurrence and could also result in a better training performance.

In contrast to the above-mentioned correlation with the target variable, there should not be a strong correlation between the input variables. Otherwise, this can result in nonoptimal weight values and a decrease in the training performance. Figure 4.15 shows the level of correlation between the input parameters themselves used for the δ training in 20° zenith and 0.5° offset angle band. On average, the behaviour of the correlation is similar for other zenith and offset angles. There is a strong correlation between the $Width$, $Length$ and $\log(Size)$ variables, which is quite natural. Larger images are usually brighter and thereby

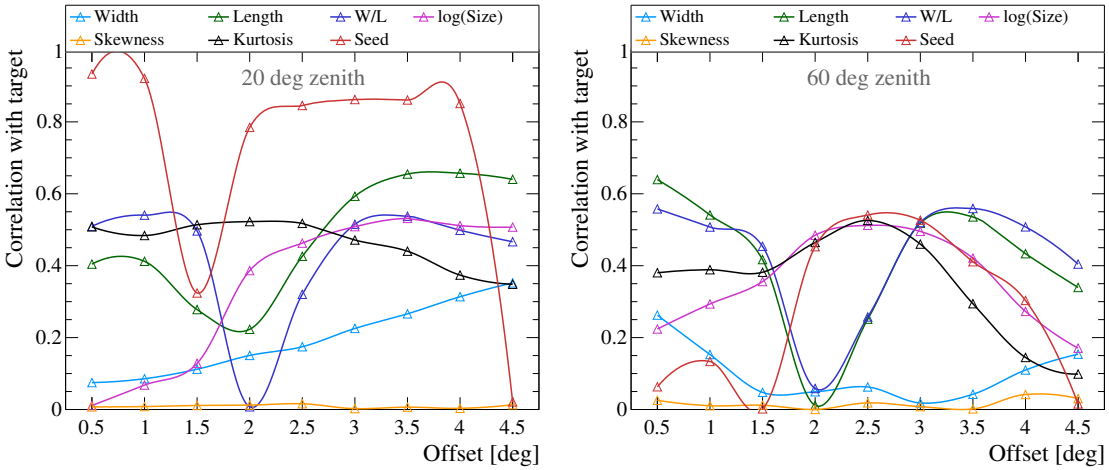

Figure 4.14: The correlation coefficients between the δ_{true} target parameter and input variables. Shown coefficients are computed for the same training dataset as in Figure 4.11.

have higher log(*Size*). And the *Width*/*Length* variable is correlated with *Width* and anticorrelated with *Length* since it is computed using these parameters. The figure also shows a noticeable anticorrelation between the δ and *Width*/*Length* as well as *Kurtosis* parameter. And the picture is similar in the case of the *Impact* parameter instead of δ. This can be explained as a result of the images from more distant showers (δ and *Impact* increases) become more elongated, which leads to a decrease of the image roundness. However, images are also clipped in time, which might affect pixel intensity distribution resulting in a decrease of *Kurtosis*.

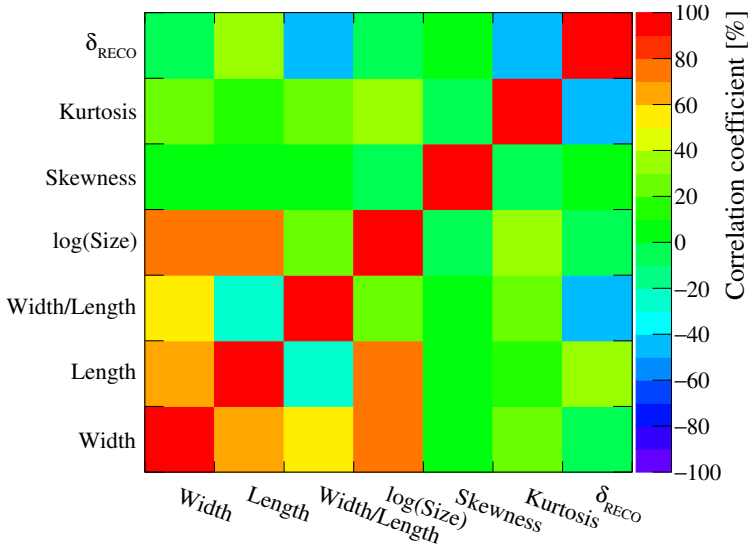

Figure 4.15: The correlation coefficients between the input variables in the case of the δ parameter training. Shown coefficients are computed for the training dataset simulated at average 20° zenith angle and with 0.5° offset angle.

4.3.4 ANN training

In this work, diffuse gamma-ray simulations are used as input data for the neural network training. From the technical point of view, it is much easier to use point-like simulations instead of diffuse ones, because the point-like sources simulated at different offset angles use the same CORSIKA output. Therefore, considering similar statistics per offset band, point-like simulations require less computing time. On the other hand, all events in the case of the point-like simulation originate from the same direction representing one point in the camera. In turn, diffuse simulations provide a dataset that is homogeneously distributed across the offset band, and its usage as a training input yields more stable performance throughout the whole camera. Both simulation types were tested in terms of the obtained angular resolution and distribution of reconstructed event directions in the camera plane. The later can be seen in Appendix A.2, Figure A.4. As a result, the diffuse simulation type is found to be preferable for the training compared to the point-like simulations.

Gamma rays are simulated within a 5° view-cone. The energy range and simulation area are the same as for point-like simulations used in the lookup-table production (see Table 4.1). In order to accumulate larger statistics at high energies for the training, the index of the simulated spectrum is chosen to be $\Gamma = -1$. It is particularly important for the large offset angles since the energy threshold increases as the event offset increase.

Training bands and statistics

Since the MLP input variables are based on image shape parameters and intensity, which are affected by detector condition and observation position as well as event direction with respect to the camera centre, training is performed in bands. Similarly to the lookup-table production (Section 3.2.2), the DISP training is performed in optical efficiency, zenith and offset angle bands[10]. But in this case, instead of the standard optical phases (see Table 3.2), optical efficiency binning for the DISP method is done in the form of a regular grid. Such an approach allows for training of the network grid only once and then using it for the telescope combinations with any optical efficiency. Details on the training bands are stated in Table 4.2.

Zenith	0, 20, 30, 40, 45, 50, 55, 60°
Azimuth	180°
Offset	0.5 - 4.5° with 0.5° step
Optical efficiency	50 - 100 % with 5 % step

Table 4.2: The binning used in the MLP training for the event direction and core position reconstruction.

Among all network input parameters, *Size* is most sensitive to changes in the optical efficiency. Graphs on the left side of Figure 4.16 show mean values of the image intensity

[10]Here, MLPs are trained only for one azimuth angle of 180°. Normally, training for 0° azimuth angle should be also performed. However, since it would double the amount of simulations required for the training purpose, only one azimuth angle is covered in this work.

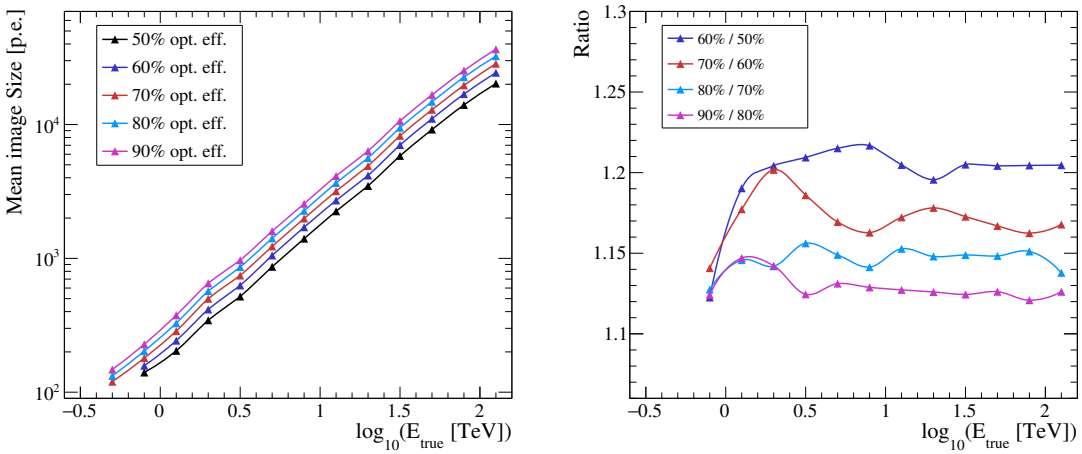

Figure 4.16: Comparison of the image intensity for different optical efficiencies. The left panel shows the energy dependence of the mean value of the intensity parameter distribution; right panel shows the ratios between those mean values. Gamma-ray showers used for the plot are simulated at 20° zenith angle with 0.5° event offset. Line colours indicate different optical efficiencies specified during the telescope simulations. In order to reject outliers in the intensity distributions and decrease the number of fluctuations, only images from the telescopes within the impact distance range from 150 to 250 m are used here.

distributions for showers simulated at the same zenith and offset angles, but with different optical efficiency of the telescopes. Ratios of those graphs are depicted on the right side of the same figure. Considering some fluctuations, they appear to be almost constant and equal to a ratio of the corresponding optical efficiencies.

Therefore, during the event reconstruction *Size* is corrected to compensate for the difference between optical efficiency at the moment of data taking and the one that is used for the MLP training. The correction factor f_{corr} is already implemented in the analysis and introduced earlier in Section 3.2.2 in Equation 3.3. Its role is accounting for the difference between the optical efficiency during the data taking and H.E.S.S. optical phases (see Table 3.2), for example during the energy reconstruction. Since the chosen optical efficiency binning in DISP does not match the standard optical phases, an additional correction is applied, in order to compensate for the mismatch between them. Finally, the corrected value for the *Size* variable takes the form[11]:

$$Size_{\mathrm{corr}} = Size \cdot f_{\mathrm{corr}} \cdot \frac{\rho_{\mathrm{DISP}}}{\rho_{\mu}}, \tag{4.8}$$

where ρ_{μ} is the optical efficiency of the telescope during the particular optical phase; ρ_{DISP} corresponds to the optical efficiency bin in the DISP training. Since the binning in optical efficiency is made with a step of 5 %, the largest mismatch between H.E.S.S. and DISP optical phases is 2.5 %.

In turn, the *Width* and *Length* parameters are also affected by the optical efficiency

[11] A similar approach is used in ImPACT technique, which is discussed in Section 3.4. The image templates are produced only for one optical efficiency of 70% and then the correction is applied to compensate for the difference between the optical efficiency during the data taking and the one used for the template production.

change. When the optical efficiency is higher, the image size for the same shower appears to be larger. This can be understood as the result of pixels of the image tails collecting more light and passing the image cleaning cuts. Figure A.5 in Appendix A.3 displays the mean of the *Width* and *Length* parameter distributions for different optical efficiencies and the corresponding ratios (similar to Figure 4.16). Graphs show that the variation of the *Width* values is just a few per cent for efficiencies that differ by 10 %. In the case of *Length*, the parameter behaviour is alike at low energies. But at high energies, images are clipped by the readout window and camera edge and their lengths nearly do not depend on the optical efficiency. Taking into account a rather small effect on *Width* and complicated behaviour of *Length*, these two parameters are not corrected for the discrepancy in the optical efficiency between the real data and the MLP training in this work.

In order to increase training statistics and better account for the different image orientations in the camera, each event image that passed preselection joins the training dataset as a separate independent entry. This way, training statistics in the most zenith-offset bins are around a few tens of thousands of events. An example of the training statistics for 20°, 40° and 60° zenith angle bands is shown in Table 4.3. In the case of diffuse simulations, events are distributed across a specified view-cone. Therefore, the area where lower offset events originate, is smaller than the one from where larger offset events come. As a result, the statistics in the lowest offset band are noticeably smaller and increase with offset. On the other hand, the energy threshold also rises with offset angle causing the statistics to decrease at large event offsets. The second trend, which is seen from the table, is that statistics increase with zenith angle, despite the growth of the energy threshold with zenith. This happens because the effective area for high energies is bigger at large zenith angles than at low ones. Thanks to the hard spectral index of the simulations, the dataset contains a significant amount of high-energy events.

Zenith, deg \ Offset, deg	0.5	1.0	1.5	2.0	2.5	3.0	3.5	4.0	4.5
20	8 k	14 k	18 k	25 k	26 k	25 k	23 k	18 k	25 k
40	19 k	33 k	43 k	58 k	55 k	48 k	39 k	29 k	40 k
60	39 k	63 k	78 k	90 k	69 k	45 k	25 k	12 k	21 k

Table 4.3: An example of the gamma-ray dataset statistics for the MLP training in the DISP method. The table presents gamma-ray samples at the different zenith and offset angles for 70 % optical efficiency.

Training in offset angle bands

As discussed above, diffuse gamma rays are used for the training. Therefore, offset bands are generated by taking rings of events with appropriate offset angle. In general, the width of each ring is half a degree. The exceptions are the first and the last offset band. The first band is in the middle of the camera and embraces all events within 0.75° offset angle from the camera centre. The last band is located on the edge of the simulated view-cone and includes gamma rays with offset angles in the range from 4.25° to 5°.

There are two ways of allocating events to the offset band dataset:

- 'true direction' – the event is included in the data sample if its true direction is located within the borders of the corresponding offset band;

- 'reco direction' – respectively, if the event's direction reconstructed with geometry method lays within the corresponding offset band.

Performed tests do not provide a clear answer regarding the mode that should be used to form the training dataset: for the low offset bands the 'true direction' approach is preferred, while larger offset angles show better angular resolution for the samples selected by 'reco direction'.

In addition, further investigation revealed that the energy bias is sensitive to the slope of the dataset spectrum. Especially for the large offset angles, that leads to a necessity of having $\Gamma = -2$ spectral index for the training sample instead of $\Gamma = -1$, in order to keep the energy bias within the acceptable range $[-10\,\%,\ 10\,\%]$ above the energy threshold[12]. In turn, low offset angles exhibit angular resolution worsening at high energies for $\Gamma = -2$ index training sample.

Taking into account the energy bias and the angular resolution behaviour, possibly the better way would be training in energy bands. However, this approach requires larger simulated statistics and, as a result, a larger amount of computational resources. Therefore, this work uses a varied type of input data selection for different offset bands. For the low-offset training (offset bands of less than 2°), $\Gamma = -1$ spectral index is used and event samples are generated in the 'true direction' way. While the large offset angles (larger or equal to 2°) make use of the dataset formed with the 'reco direction' approach and $\Gamma = -2$ spectral index, accomplished by re-weighting of the available $\Gamma = -1$ spectrum during the training by

$$\omega = E_{\mathrm{true}}^{\Gamma - \Gamma_{\mathrm{sim}}}, \tag{4.9}$$

where E_{true} is the primary energy of the event. Γ_{sim} and Γ are the indices of the simulated and desired spectrum, respectively. In the current case, $\Gamma_{\mathrm{sim}} = -1$ and $\Gamma = -2$.

An example of the neural network output for different offset bands is displayed in Figure 4.17. Plots compare MLP estimated δ values for two datasets. One of them is used to train the network and another one is produced for testing purposes. In general, the distributions for both datasets are consistent. There is a small discrepancy for the 4° offset band. But it is not an indication of the training performance decrease with the offset angle since the corresponding distributions for 3.5° and 4.5° offset band (not shown in the figure) are found in the agreement.

Each band is a separately trained MLP, whose outcome is written to an individual XML weight file. During the event reconstruction for the δ and *Impact* evaluation, the algorithm chooses the weight files which best match the data conditions: zenith angle of the observational position and the telescope optical efficiency. The evaluation procedure is performed for all offset bands at the same time and results are interpolated between offset bands using a spline function. Since preliminary event offset is known from the geome-

[12]The energy bias and threshold definitions are described later in Section 5.1.2 and 5.1.3, respectively.

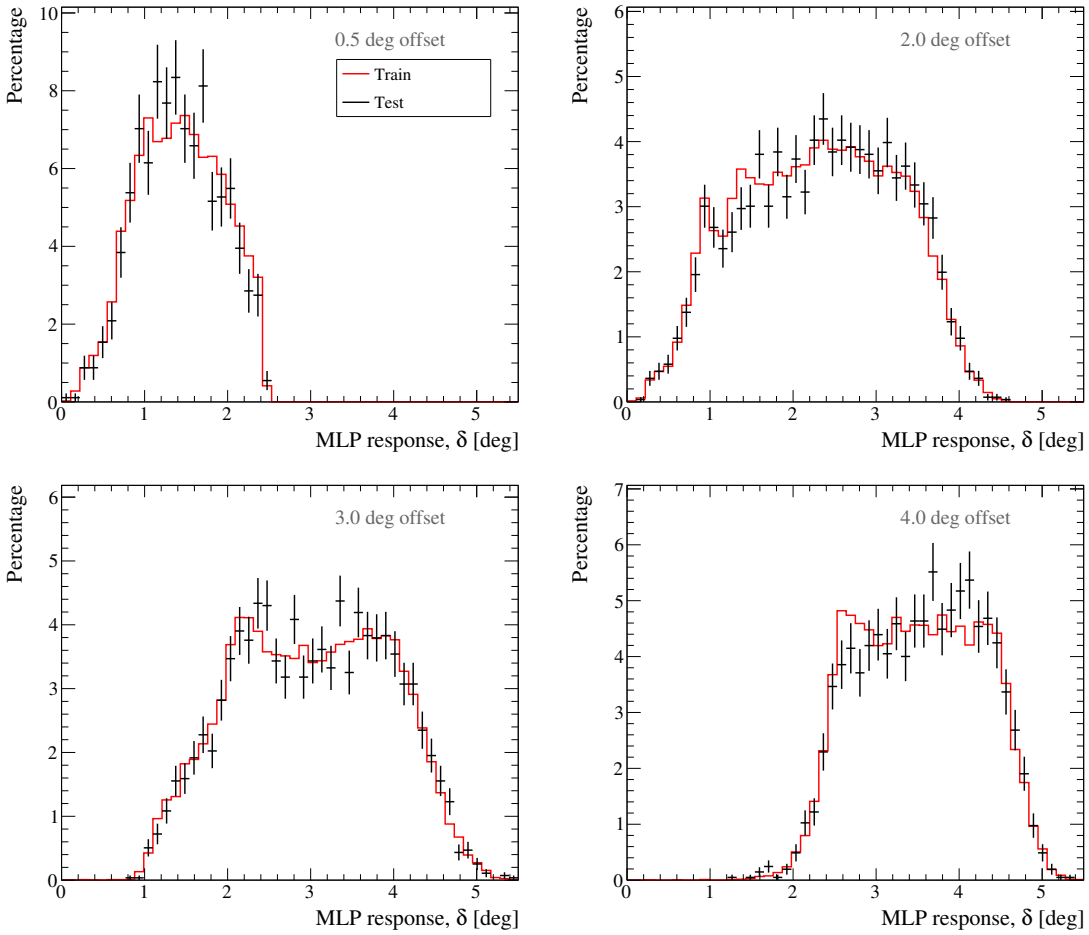

Figure 4.17: Example of the MLP response for different offset bands. Solid lines represent the sample used for the MLP training, while marker points show a corresponding test dataset. Both datasets are composed of diffuse gamma rays simulated at 20° zenith angle.

try pre-reconstruction, it is used to evaluate δ and *Impact* from the interpolation for this specific value.

4.4 Improved gamma-hadron separation

The background rate rises dramatically as the mean offset of events increases at high energies. The background rejection poses one of the major challenges for the large-offset analysis. As is discussed in Section 4.2.3 and shown in Figure 4.6, the performance of the standard box-cut based gamma-hadron separation method is not sufficient for this work. Thus, a more sophisticated machine learning method should be applied. This way, the gamma-hadron separation is this study is based on the second method implemented within the HAP framework [167] that uses a BDT training for the background rejection and is discussed in Section 3.3.2.

4.4.1 BDT training and input parameters

In the standard version of the TMVA based gamma-hadron separation approach, BDTs are trained for one offset angle of 0.5°. At large offset angles, event parameters differ from the ones at low offset angles, resulting in a worsening of the separation efficiency. In addition, there is only one 5 - 100 TeV training band at high energies. The BDT input parameters change as a function of energy and the introduction of a larger number of more narrow high-energy bands could yield better performance. This work uses a modified version of the standard BDT classification, aimed at refining background rejection in the high-energy part of the spectrum and at large offset angles.

Input parameters

The modified version of the BDT training uses configuration options that are similar to the ones used in the standard BDT training[13]. The usual list of input variables is $MSCW$, $MSCL$, $MSCWO$, $MSCLO$, $\Delta E/E$ and $X_{\max}$[14]. Mean values of these variables as a function of reconstructed energy are shown in Figure 4.18. They show a distinction between gamma and cosmic rays as expected from the difference between hadronic and electromagnetic cascades discussed in Section 2.1.4. Corresponding RMS plots can be found in Appendix A.4 in Figure A.6.

On average, cosmic rays leave much wider images in the camera than gamma rays, which can be seen from the $MSCW$ and $MSCWO$ plots. They also have a larger difference in energy reconstructed per telescope ($\Delta E/E$ parameter). Both features are caused by the irregular structure of cosmic-ray showers. Typically, hadronic cascades have a large transverse momentum and can have several electromagnetic sub-showers due to the decay of mesons such as π_0. Therefore, different telescopes can register separate sub-cascades whose reconstructed primary energy would vary a lot from image to image. Furthermore, electromagnetic sub-showers can be surrounded by other irregular parts of the hadronic cascade that emit Cherenkov light and contribute to the recorded shower image, making it larger.

As discussed in Section 2.1.2 (Equation 2.6), $X_{\max}$ should increase as the logarithm of the primary energy, which deviates from the behaviour shown in Figure 4.18. Only $X_{\max}$ values of the gamma rays simulated with 0.5° offset angle show the expected logarithmic behaviour[15]. Deviations from the anticipated picture that are seen for cosmic and gamma rays at large event offsets can be explained by the way how $X_{\max}$ is reconstructed [144]. The $X_{\max}$ parameter is estimated assuming that the image CoG corresponds to the location, where the Cherenkov photons emitted at the shower maximum land in the camera. Often, this relation does not hold for the distant showers, which constitute a large fraction of events at large offset angles (Figure 4.3). In this case, the telescopes might record the photons from larger heights (smaller depths) than the maximum of the shower development. This is also seen in Figure 4.21 later in this section, which shows an anticorrelation behaviour between

[13] Except for the parameter that has been deprecated in newer TMVA version and was replaced by the one with similar functionality.

[14] Here and after $X_{\max}$ implies the depth of the shower maximum divided by the cosine of the zenith angle, i.e. $X'_{\max}/\cos(\theta_{\text{zen}})$.

[15] In turn, the mean of the true shower maximum as a function of the true primary energy follows the behaviour expected from Equation 2.6 as is discussed in Appendix A.4 Figure A.7.

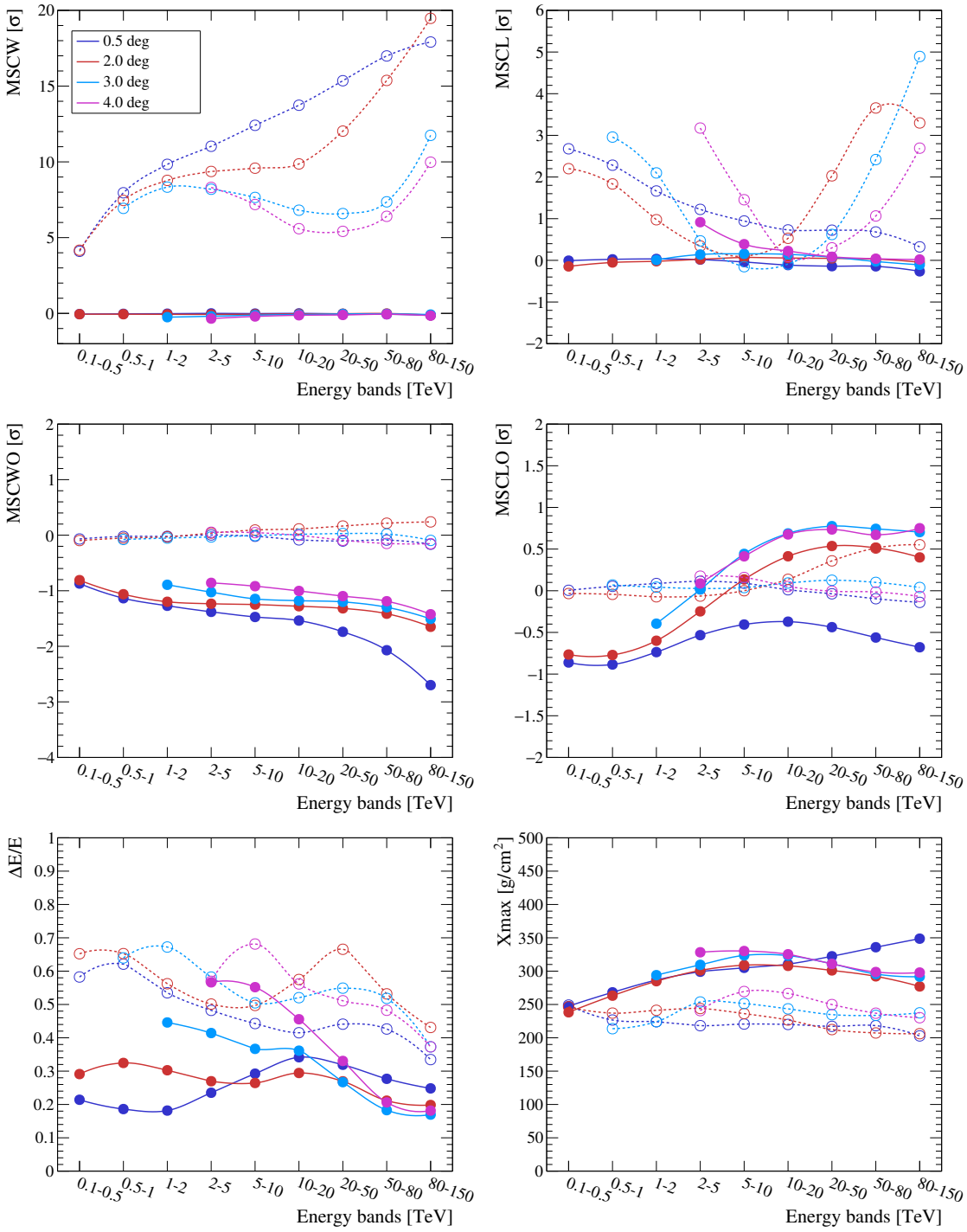

Figure 4.18: Mean values of the input variable distributions in the BDT training. Line colours denote different event offset bands. Solid lines show point-like gamma rays simulated at 20° zenith, while dashed ones indicate real observations of the empty fields, i.e. cosmic rays, in zenith angle range between 15° and 25°.

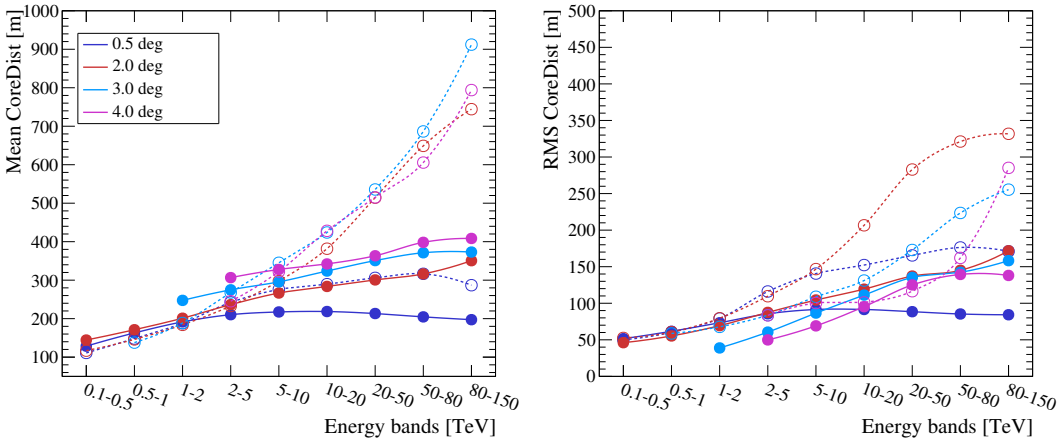

Figure 4.19: A comparison of the *CoreDist* distribution behaviour for gamma- and cosmic-ray training samples. The curves display the mean (left) and RMS (right) values of the *CoreDist* distributions as a function of energy. Solid lines denote point-like gamma rays simulated at 20° zenith, while dashed ones indicate real observations of the empty fields, i.e. cosmic rays, in the zenith angle range between 15° and 25°.

the $X_{\max}$ and *CoreDist* parameters, i.e. reconstructed depth of the shower maximum decreases as the shower distance to the telescope array increases.

Despite the fact that $\Delta E/E$ is a standard parameter, its definition is slightly modified in this work. Nominally, ΔE is calculated using the energy reconstructed per telescope, which is not corrected for the mismatch in the optical efficiency between the data and lookup tables that are applied for the energy reconstruction. But, the reconstructed energy of the shower in the denominator of the $\Delta E/E$ formula is the corrected one. Such a treatment can introduce a small inconsistency during the ζ_{BDT} evaluation since the simulations used for the BDT training have the same optical efficiency as the energy lookup tables and do not require an energy correction. Therefore, ΔE is calculated using the corrected energy per telescope in this work. Further tests showed that the $\Delta E/E$ distributions for real data and for simulated gamma rays are in better agreement if such a correction is used. More on data-simulation comparison in regard to the BDT training is discussed in Section 5.2.1.

An additional investigation shows a separation potential of the *CoreDist* parameter, which is defined as the distance from the array centre to the shower core position. The behaviour of the measured mean and RMS values of the *CoreDist* parameter for gamma- and cosmic-ray showers are shown in Figure 4.19 for different offset bands. The difference between *CoreDist* distributions for gamma- and cosmic-ray showers is minimal for low energies but rises as the energy increases, which is favourable for better background rejection at high energies.

Training bands and statistics

Unlike the standard classification [167], in this work, the training is performed in event offset bands. They cover the range from 0.5° to 4.5° in 0.5° steps[16]. The energy binning

[16]The BDT training in event offset bands is also proposed in [134].

was also modified. Instead of one band at high energies from 5 to 100 TeV, five energy bands have been introduced: 5 - 10, 10 - 20, 20 - 50, 50 - 80, 80 - 150 TeV[17]. This requires larger statistics at high energies to be able to train the classifier with such a fine energy binning. Therefore, the same gamma-ray simulations for the signal sample are used here as for the lookup-table production as discussed in Section 4.2.1. They are produced with $\Gamma = -1$ spectrum instead of the standard $\Gamma = -2$. However, this approach cannot ensure sufficient statistics at all energies. Thus, in the low energy part, the first two bins are merged into one 0.1 - 0.5 TeV bin. This will affect classification performance in the low energy band, but it is considered acceptable since the current work is focused on the high energies.

The minimum number of events in the training dataset is set to 2000. On average, the size of the dataset can reach $\sim$30 k events or more in each training bin. But at the same time, it can drop to less than 10 k for energy bands that are close to the threshold or end of the spectrum. An example of signal statistics at 20° zenith angle is listed in Table 4.4.

	Energy, TeV								
Offset, deg	0.1 - 0.5	0.5 - 1	1 - 2	2 - 5	5 - 10	10 - 20	20 - 50	50 - 80	80 - 150
0.5	17 k	22 k	31 k	48 k	38 k	36 k	19 k	3 k	2 k
1.0	16 k	20 k	25 k	41 k	34 k	35 k	39 k	6 k	4 k
2.0	5 k	9 k	12 k	23 k	24 k	27 k	40 k	22 k	26 k
3.0	-	-	2 k	11 k	15 k	19 k	33 k	20 k	26 k
4.0	-	-	-	-	5 k	12 k	22 k	14 k	21 k

Table 4.4: An example of gamma-ray statistics in the training dataset for the gamma-hadron separation. The table presents the statistics for the 20° zenith angle band and lists all energy bands used for the training.

Similar to the standard approach, extragalactic observations of empty fields are used as the background training sample. Background samples have a similar size. In some training bands, the background statistics is much larger then the signal statistics. In such a case, it is limited to have a maximum size that is twice larger than the signal statistics.

Importance and correlation coefficients

The role of any input variable in the classification process can be characterised by the *Importance* parameter [135]. In the BDT method, this depends on the frequency of the variable usage during the tree growth, the number of events in the nodes that were split by this variable and the achieved separation. Figure 4.20 shows the energy and zenith angle dependence of the importance parameter for the BDT input variables. On average, the behaviour of the importance across different zenith angle bands for a given offset angle and energy band stays similar. For low offset bands, the importance of the $MSCW$ parameter is very pronounced, especially at high energies. As offset angle increases, it becomes almost equally important ($\sim$15%) as the majority of separation parameters. On the other hand,

[17] Energy bands are defined in terms of reconstructed energy.

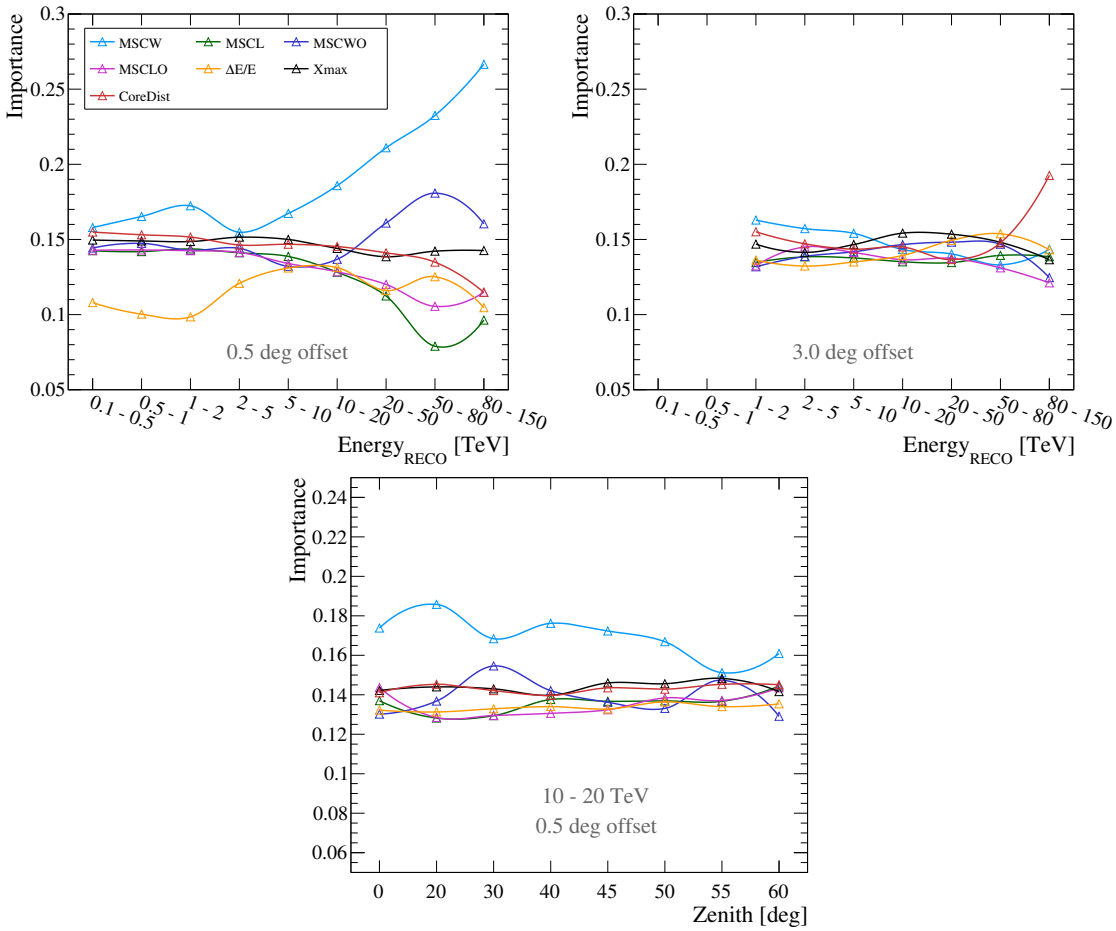

Figure 4.20: The importance of the input parameters for the gamma-hadron separation training. The top row shows the importance as a function of reconstructed energy for 0.5° and 3° event offsets. In this case, zenith angles lay in the range between 15° and 25° for both plots. The bottom row displays the evolution of the parameter importance with zenith angle. For this plot energy range and offset angle are fixed to 10 - 20 TeV and 0.5°, respectively.

for energies below approximately 5 TeV, the least important parameter is $\Delta E/E$ but then its role slightly rises with offset angle and energy.

In the classification training, input parameters should have different correlations in different classes of events in order to yield better learning and separation performance. A matrix of correlation parameters for the signal and background training sample is shown in Figure 4.21. Hadrons show a significant correlation between all image shape parameters. In addition, within each offset band, the level of the correlation rises as the energy increases. At the same time, the correlation strength between parameters related to the width and length of the image decreases for the background events at large offset angles. This can be the result of irregularities in the hadronic shower development, which might be more pronounced in images of showers that originated at small offset angles.

Some shape-related parameters are strongly correlated in the case of the signal sample. For example, if the shower appears to be gamma-like, its $MSCLO$ and $MSCL$ parameters are

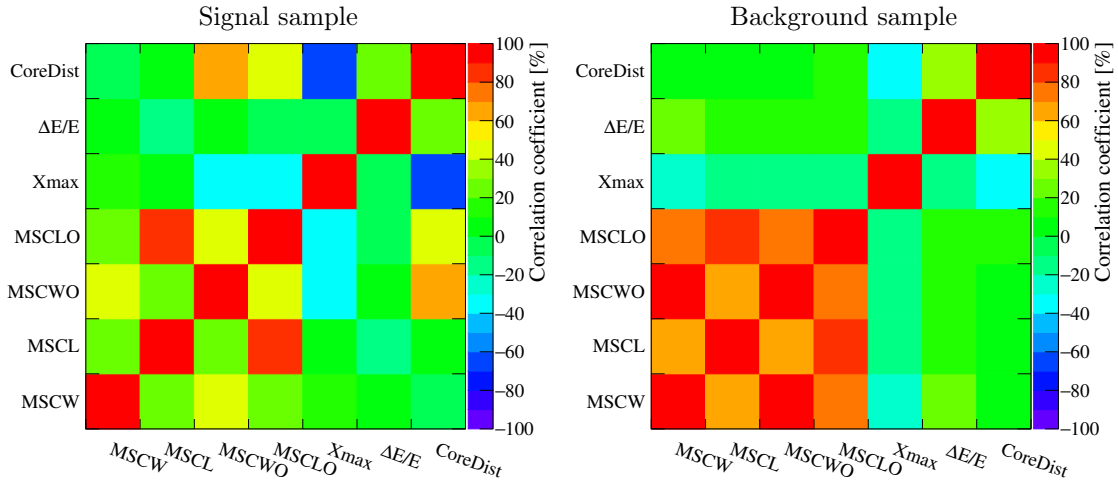

Figure 4.21: The correlation between input parameters of the BDT training in the case of the modified gamma-hadron separation. The left panel displays a correlation matrix for the signal sample used in the training, while the right panel shows the same for the background sample. Plots are performed for the same dataset bin: 15 - 25° zenith angle band, 0.5° offset band, 10 - 20 TeV energy band.

small and they both rise for gamma rays that look more like background. The same can be concluded for pairs of the $MSCWO$ and $MSCW$, $MSCLO$ and $MSCWO$ parameters. Unlike background, the gamma-ray sample shows a correlation between the $CoreDisp$ and $MSCWO$ as well as $MSCLO$ parameter. $MSCWO$ and $MSCLO$ grow from negative values towards zero as the core distance increases, i.e. gamma rays become more hadron-like. This may happen due to the decrease of light intensity with increasing distance between shower and telescope array, resulting in similarity between hadron and gamma-ray showers. The $CoreDisp$ parameter is also anti-correlated with X_{max}, which actually can be an effect related to the X_{max} reconstruction implying that the quality of the shower depth estimation worsens as the distance to the shower increases.

4.4.2 BDT response

Similarly to the MLP training for the direction reconstruction, individual BDTs are trained for each energy-zenith-offset band and the output is saved in XML format. During the gamma-hadron separation process, the BDT response ζ_{BDT} is evaluated for all offset bands for a given energy and zenith angle and then converted into efficiency values using signal efficiency curves (see Section 3.3.2). The obtained results are interpolated between different offset bands and the final gamma-ray efficiency, which is used for the gamma-hadron separation, is estimated for the event offset angle computed based on the reconstructed shower direction position. Usage of the interpolation procedure helps to smooth irregularities in the camera acceptance, caused by the binning in offset angle.

Examples of the BDT response for the signal and background datasets for 0.5° and 4° offset angles are displayed in Figure 4.22. As expected, signal-like events occupy the right side of the distribution with the positive ζ_{BDT} values, while background-like events are in the left

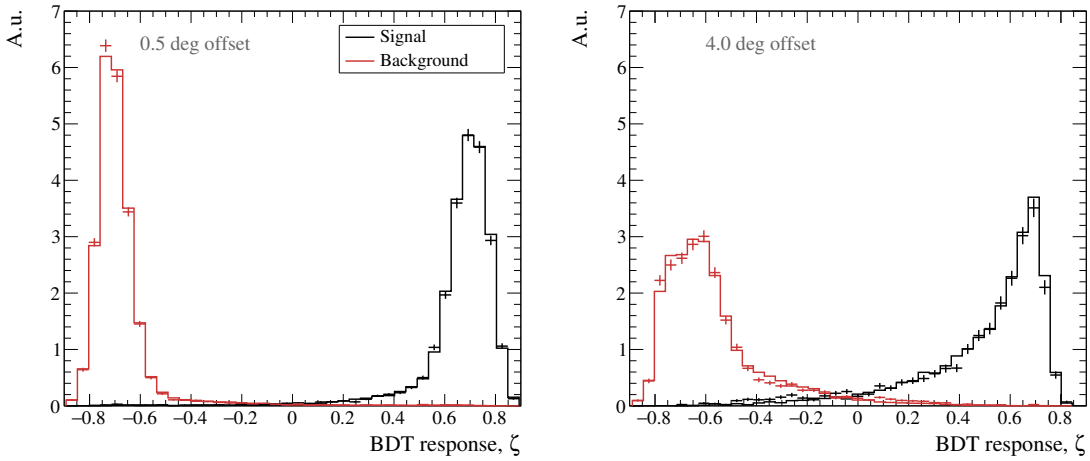

Figure 4.22: Example of the BDT response for 0.5° (left) and 4° offset angle bands (right panel). The training is performed for the energy range 10 - 20 TeV. The signal sample is denoted by black colour and consists of point-like gamma rays simulated at 20° zenith angle. Red colour represents a background sample that is obtained by analysing the blank field observations conducted between 15° and 25° zenith angle. Solid lines show signal and background samples used for the BDT training, while marker points reflect corresponding test datasets.

corner and are represented by the negative ζ_{BDT} values. As expected, training performance worsens as the event offset increases. Thus, for the 4° offset angle, response distributions for signal and background appear to be broader and have larger overlap. Figures also compare the BDT response for the training and test data samples. Both samples are in good agreement, which indicates that no significant overtraining takes place.

Training performance

In order to understand the classification performance, ROC curves are built. They show the efficiency of background rejection depending on signal survival (see also Section 3.3.2). On the left side of Figure 4.23, the ROC curves for newly introduced high energy bands are compared to the standard ROC curve for 5 - 100 TeV energy range. This shows how training performance improves at very-high energies when a finer binning in this domain is used. The ROC curves for all trained energy bands can be found in Appendix A.5 (Figure A.8).

In addition, the right panel of Figure 4.23 illustrates the signal efficiency curves for the high-energy training bins that are used to perform the gamma-hadron separation during the event analysis. The background rejection is done by a cut on fixed gamma-ray efficiency. In this work, the standard efficiency cut value (84 %, grey line on the plot) is used. Currently, no further cut optimisation based on the best sensitivity is performed[18]. In the end, the evaluated ζ_{BDT} translates to efficiency, which is applied to select gamma-like events.

[18]Cut optimisation is beyond the scope of this work. However, it would be beneficial in future studies, since it is important for the improvement of the analysis performance.

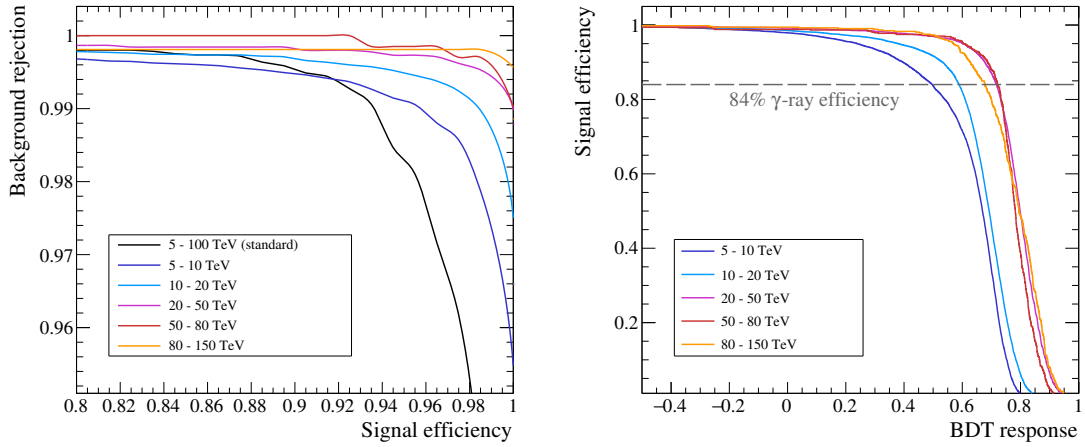

Figure 4.23: The performance of the BDT training at high energies. The left panel shows the ROC curves for the introduced five high energy bands (coloured lines) and its comparison to the standard 5-100 TeV band (black line). The right panel displays the signal efficiency curves for the new bands. The grey dashed line indicates the gamma-ray efficiency cut value used for the gamma-hadron separation. All presented curves are taken from training performed at 20° zenith angle and 0.5° offset angle band.

4.5 Summary

The knowledge of the source spectrum and morphology at high energies is an important key for understanding the source environment and processes that are ongoing or took place in the past. Due to the steep spectra of gamma-ray sources, the statistics at high energies are typically rather low and becomes a limiting factor of the instrument sensitivity in this energy range. Thus, it is very important to be able to reconstruct and identify high-energy gamma rays as good and as many as possible. In this chapter, a possibility of the maximum event offset increase from approximately 2.5° to around 4° is investigated as one of the ways to increase the high-energy statistics, since the study shows that the standard maximum event offset cut rejects a significant fraction of detected high-energy events. An application of this approach could be useful in the densely populated Galactic plane regions, where VHE sources are located rather close to each other and observations taken for the nearby sources can be considered for the analysis of the source of interest at high energies.

The two main challenges of this approach are the deteriorated reconstruction accuracy and increased background rate. In order to overcome these issues, a more sophisticated direction reconstruction method (the DISP method) and several modifications to the standard TMVA-based background rejection technique are implemented within the HAP framework. Moreover, improvements of the angular resolution and gamma-hadron separation by themselves are also the ways to improve the gamma-ray statistics and sensitivity in the high-energy range. The next part of this work, Chapter 5, discusses the overall performance obtained using the analysis approach proposed in this chapter as well as compares the results to the standard analysis method.

Chapter 5

Performance of the high-energy analysis

The previous chapter describes the DISP reconstruction method and modifications applied to the gamma-hadron separation. This chapter discusses the performance of the developed method based on gamma-ray simulations and real data. Also a comparison with the standard analysis is performed, based on all relevant system properties, such as angular and energy resolution, energy bias and threshold, effective area, background rate and sensitivity.

5.1 Performance characteristics

In this and further chapters, the analysis proposed in this work is referred to as *high-energy* (*HE*) analysis since it is developed for energies above 10 TeV. As discussed in Chapter 3, there are several different configurations of the standard analysis. They have different cut values, which are optimised for each analysis configuration depending on the source strength and slope of the spectrum [46]. This work focuses on a general method development, while the cut-optimisation investigation is beyond the scope of this work. This way, the analysis proposed in this study is based on the standard cut configuration, specifically on *std_zeta*, since both of them use a similar approach for the gamma-hadron separation (TMVA based technique). It uses the amplitude cut set to 60 p.e. and the image local distance cut of 0.525 m from the camera centre for the image selection, i.e. preselection discussed in Section 3.1.2. For the background rejection, i.e. postselection, the cut value is 84% of the gamma-ray efficiency as described in Section 3.3.2.

In this section, the *std_zeta* analysis is used as a standard benchmark and is referred to as the standard analysis. Since it is optimised for events only up to 2.5° offset angle, the comparison between the standard and high-energy analysis is only possible at low event offsets. The studies of the performance and corresponding figures presented in this section are performed after applying all image and shower selection cuts, i.e. after postselection. All plots that involve gamma-ray simulations use a $\Gamma = -1$ spectrum. When necessary, the simulated spectrum is re-weighed to $\Gamma = -2$, which is highlighted in the text. For most performance studies, re-weighting is not strictly necessary if the quantity is displayed as a

function of energy or only for a narrow energy band.

5.1.1 Angular resolution

One of the most important analysis characteristics is the angular resolution. Typically, it is defined as the 68% containment radius of the reconstructed directions of gamma rays simulated at a fixed sky position. The angular resolution of the system determines a minimum size of the *On-region* for the source analysis. The On-region is a test-region, which typically contains the source of interest. Smaller resolution allows for smaller On-region, which leads to lower diffuse background accumulation and better signal-to-noise ratio and, as a result, to a better source detectability. In addition, more precise angular resolution will better reveal morphological details of extended sources, which is very important for the source modelling and interpretation.

Figure 5.1 shows the angular resolution at different offset angles as a function of true energy for 20° and 40° zenith angles. For comparison, it also presents the resolution curves for the standard analysis at 0.5° and 2° event offset. For the smallest offset angle, the difference in resolution between the two analyses is minimal at low zenith angles but rises as zenith angle increases. At 60° zenith angle (not shown in the figure), the improvement compared to the standard analysis is more significant and the angular resolution at 2° offset angle using the high-energy analysis is nearly the same as the resolution at 0.5° using the standard analysis.

The standard analysis angular resolution curve at 2° offset angle shows a peculiar behaviour, which can be misleading. It implies that in this offset band, the standard analysis reconstruction works better than the high-energy one. But this improved resolution is obtained at the expense of a lower effective area discussed later in Section 5.1.3 (see Fig-

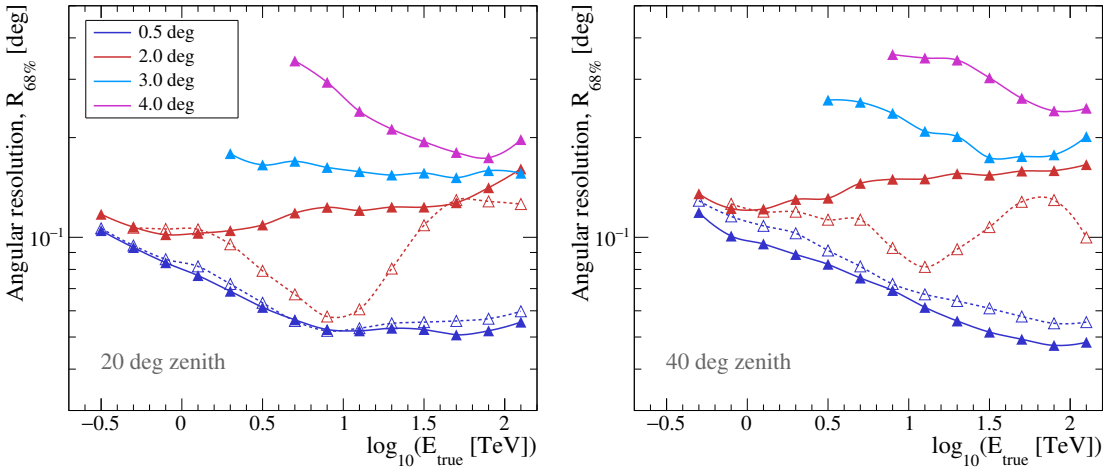

Figure 5.1: The angular resolution as a function of simulated energy for different event offsets for two different zenith angles. The resolution curves are shown only for events above the energy threshold. At low offset angles, the figure compares the resolution for the high-energy and standard analysis denoted by solid and dashed lines, respectively.

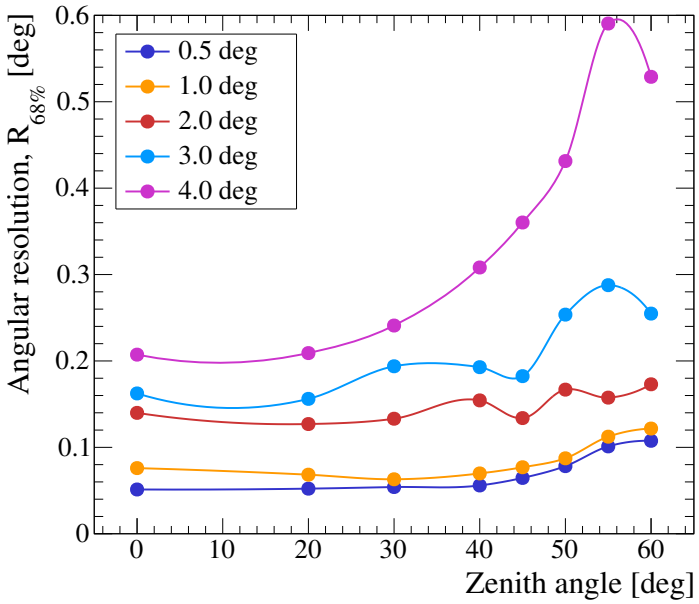

Figure 5.2: The angular resolution of the high-energy analysis above 10 TeV as a function of zenith angle for different event offsets. The resolution computation is performed using gamma rays simulated with the spectral index of $\Gamma = -1$ and re-weighted to have the index of $\Gamma = -2$.

ure 5.5). A possible reason for this effect can be the standard BDT training, which is performed only for 0.5° offset band. Shower parameters of events at 0.5° and 2° offset angle have significant differences, resulting in a worse performance of the standard classification at 2° event offset in comparison to the nominal offset band of 0.5°.

Figure 5.2 shows the angular resolution at different event offsets as a function of zenith angle. Points represent the angular resolution estimated for energies above 10 TeV. For zenith angles above 50°, the energy threshold is higher than 10 TeV for the offset angle of 4°. In this case, the angular resolution is computed above the energy threshold, which is discussed in more detail in Section 5.1.3 and its offset-zenith dependency is displayed in Figure 5.6. The angular resolution depends on the primary energy. Normally, high-energy events are reconstructed more accurately and, as a result, have better angular resolution than the low-energy ones. Assuming the same number of events, a hard spectrum would contain more high-energy events and better resolution above fixed energy than a soft spectrum. Because of this, the assumed spectral index of the gamma-ray simulation is important for the angular resolution shown in Figure 5.2. Thus, the initial $\Gamma = -1$ simulated spectrum is re-weighted to obtain $\Gamma = -2$ spectrum for this figure.

As seen from the plot, the angular resolution within each event offset band degrades as the zenith angle increases. At low zenith angles, the resolution for most offset bands is below 0.2°, which is considered an acceptable value for the source analysis. The 4° offset curve only slightly exceeds this value up to 30° zenith angle. At larger zenith angles, the resolution for 4° offset angle deteriorates very fast. In turn, the resolution at 3° event offset falls within the desired accuracy range up to 50° zenith angle.

5.1.2 Energy resolution and bias

The distribution of the relative error of the energy reconstruction, $(E_{\text{reco}} - E_{\text{true}})/E_{\text{true}}$, for a narrow slice in a true energy, is shown on the left side of Figure 5.3. On the plot, the distribution is fitted with a Gaussian function, which is used to determine the quality of the energy reconstruction. The energy bias is measured as the mean value of the relative energy uncertainty distribution, i.e. mean parameter μ of the Gaussian function, while the energy resolution is defined as one standard deviation σ from the mean. The presented example is produced for a true energy of about 12 TeV. It shows that at this energy the bias is approximately 2.3% and the resolution is 15%. The right side of Figure 5.3 shows the energy resolution as a function of simulated energy for the high-energy analysis. As seen in the figure, the energy resolution above 10 TeV is less than 30% for all offset bands at zenith angle of 20°. Similarly to many other performance parameters, the energy resolution degrades as the zenith angle increases. It is approximately 5 - 10% worse at 60° zenith angle (not shown in the figure) compared to a zenith angle of 20°. At low event offsets, the plot also shows the energy resolution curves for the standard analysis. Most likely, the nature of the 2° energy resolution curve behaviour for the standard analysis is the same as for the angular resolution that is discussed in Section 5.1.1.

The energy bias as a function of simulated energy for 20°, 40° and 60° zenith angles is displayed in Figure 5.4 for the high-energy analysis. Positive bias values imply an overestimation of the event energy, while negative values denote an underestimation. Showers fluctuate while travelling through the atmosphere. The ones that are below the detection threshold can fluctuate up and be detected by the telescopes. Such events are likely to

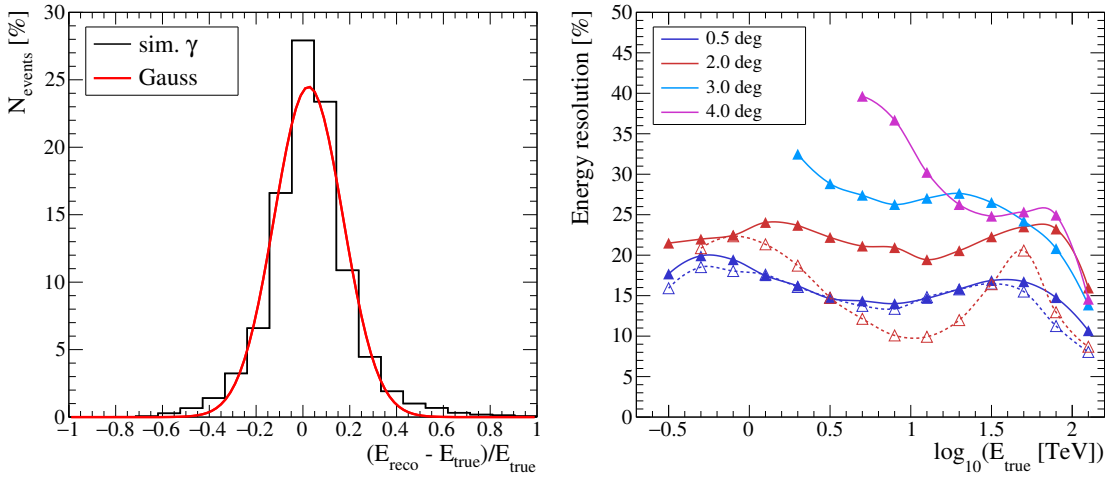

Figure 5.3: The energy resolution. The relative error of the reconstructed energy is shown in the left panel. The example is produced for events with a primary energy around 12 TeV. The distribution is fitted by a Gaussian function with $\mu = 0.023$ and $\sigma = 0.15$. The right panel displays the energy resolution as a function of simulated energy. The curves are shown only for energies above the energy threshold. Solid and dashed lines denote resolution obtained with the high-energy and standard analysis, respectively. Both plots are produced for a zenith angle of 20°.

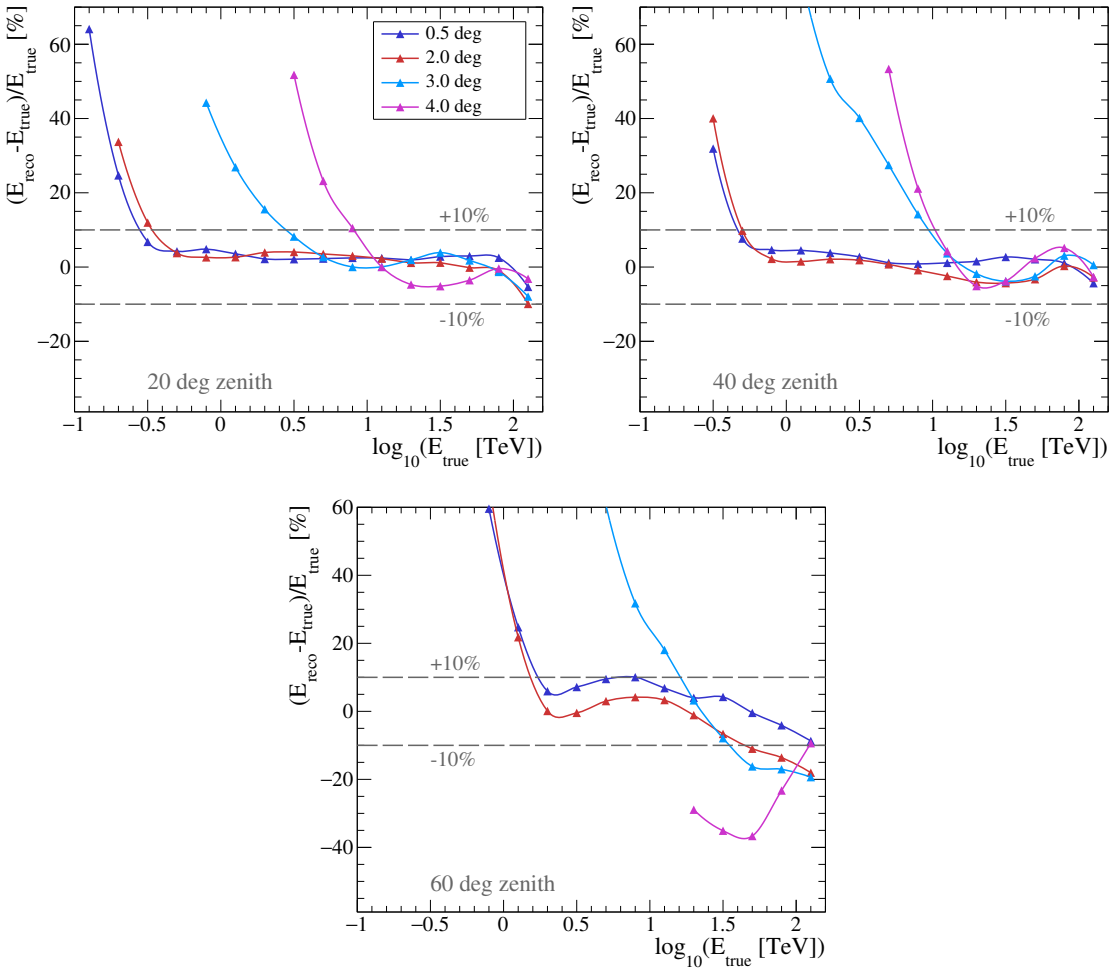

Figure 5.4: The energy bias as a function of simulated energy for different offsets shown for 20°, 40° and 60° zenith angle. Grey dashed lines indicate a safe range of ±10% energy bias.

be reconstructed to higher energies than they actually are. Therefore, the energy bias curve has an upturn towards low energies. In contrast, there is typically a downturn in the bias curve towards high energies due to event misreconstruction since high-energy showers fluctuate a lot, their images are very big, often truncated in time and by the camera edge. This way, high-energy events are reconstructed to lower energies. In most cases, the bias curves in Figure 5.4 behave as anticipated. The exception is the energy bias at 60° zenith angle.

The figure also displays a 'safe' bias range, which is considered to be from −10% to +10% of the true shower energy. It is expected to have a flat bias curve in this range. At 20° and 40° zenith angles, the energy bias above 10 TeV lies within the acceptable range for all event offsets. At 60° zenith angle, the bias curves lie outside of the safe range, especially for large event offsets.

5.1.3 Effective detection area

The effective area is one of the key components of the analysis sensitivity (see Section 5.1.6). Its definition is discussed in Section 4.2.3. The effective area for the high-energy analysis after the gamma-hadron separation is shown in Figure 5.5. At low offset angles, the effective area curves are compared for the high-energy and standard analysis. Events in both analysis chains go through the same event preselection. The background rejection cut is applied in the same manner, keeping 84% of the gamma rays that survive the preselection. Thus, despite the fact that lookup tables, reconstruction procedure and the BDTs training for the gamma-hadron separation are different, the effective area for both analyses is expected to be similar. Indeed, the effective area is comparable for the 0.5° event offset. But for the 2° offset angle, the standard effective area curve is significantly lower than the one resulting from the high-energy analysis developed in this work. Being trained only for 0.5° event offset, the standard gamma-hadron separation performs worse at larger offset angles. The ζ_{BDT} value, which meets the 84% of gamma-ray efficiency at 0.5° event offset, likely corresponds to a lower efficiency at larger offset angles.

As the zenith angle increases, the effective area increases at high energies since events arriving from larger zenith angles are more inclined and have a larger light pool. This results in a better chance to detect the shower and, hence, an increase of the effective area. At low energies, the effective area decreases due to the increase of the energy threshold, which is shown in Figure 5.6 for the high-energy analysis as a function of zenith and offset angles. There are several ways to determine the energy threshold. Here, the threshold is defined as the energy where the effective area reaches 10% of its maximum. As expected, the threshold rises as the zenith angle increases since the shower experiences a longer path through the atmosphere resulting in the absorption of a large fraction of Cherenkov light. In addition, the emission region is located farther away for the showers originated at large zenith angles in comparison to the lower ones. For a given zenith angle band, the energy

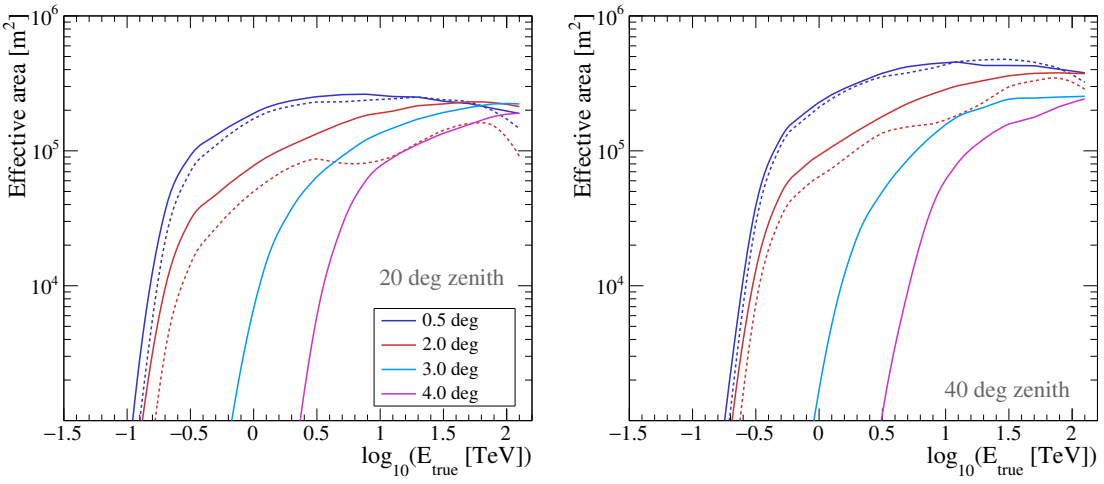

Figure 5.5: The effective area for different offset angles as a function of true shower energy for observations at 20° and 40° zenith angle is shown in the right and left panel, respectively. Solid and dashed lines denote the effective area curves for the high-energy and the standard analysis, respectively.

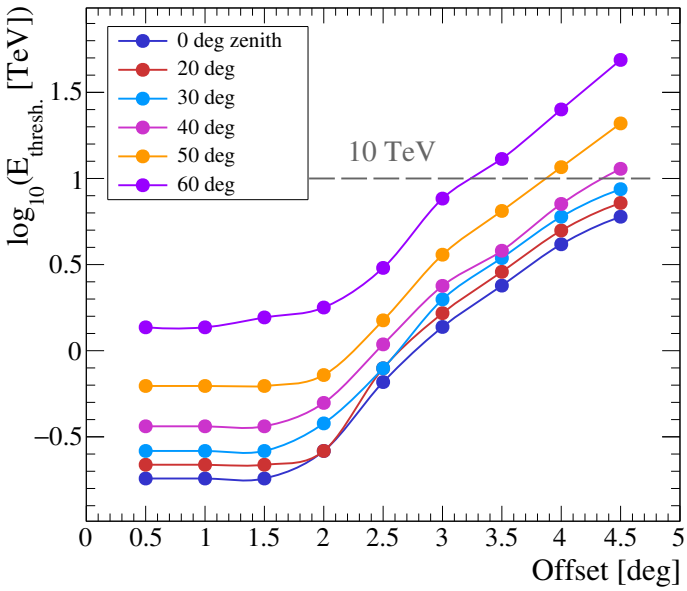

Figure 5.6: The energy threshold of the high-energy analysis at different zenith angles as a function of offset angle.

threshold stays nearly constant up to 2° event offset and grows very fast at larger offset angles. At 50° zenith angle, the threshold appears to be higher than 10 TeV for events with offset above 4°. For 60° zenith angle, the threshold reaches 10 TeV already at 3.5° event offset. This fact implies the limitations of the large-offset usage since the energy range of interest in this study starts at 10 TeV.

5.1.4 Background rate

The background rate is another important component of the analysis sensitivity (see Section 5.1.6). Figure 5.7 shows the rate of the gamma-like background, i.e. background events that pass the gamma-hadron separation cuts, for observations at 20° and 40° zenith angles. The rate is computed by analysing the observations of PKS 2155−304 (a point-like extragalactic VHE source). In order to estimate the background level at different offset angles, the FoV is divided into rings with width of 0.5°. The average ring radius correspond to the offset angle of interest. The contamination by the gamma rays from the source is avoided by excluding the region with radius of 0.25° around the source position. The statistics in the highest energy bins is very low (typically just a few events per bin), which results in the wiggly rate curves.

In addition, the background rate curves for the high-energy analysis are compared to the standard ones at low event offsets. The behaviour is consistent with the results presented in Figure 5.5 that show the corresponding effective area curves. In some energy-zenith-offset bands, the gamma-hadron separation cut in the high-energy analysis appears to be looser than in the standard analysis. It keeps more gamma rays as well as more background events, resulting in higher effective area and background rate. On the other hand, there are bands, where the cut is harder, leading to a decrease in the effective area and background

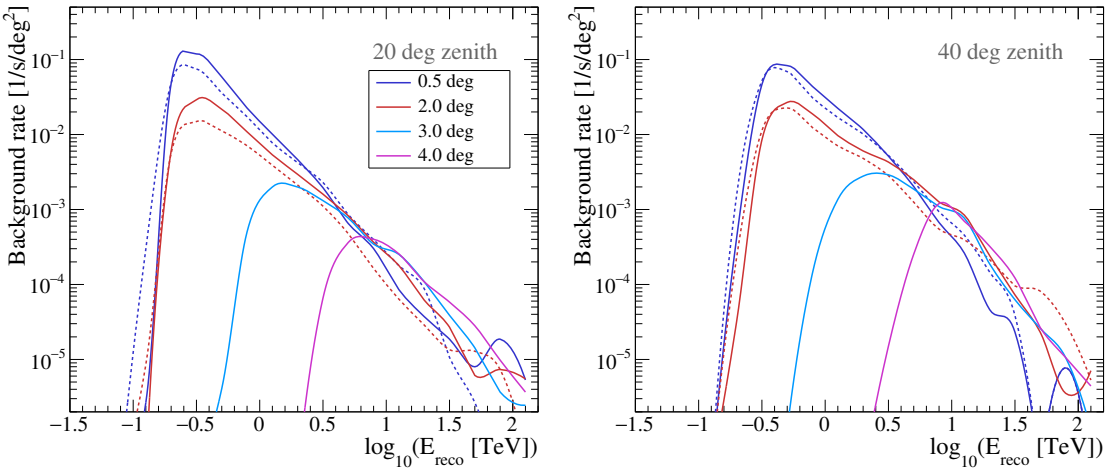

Figure 5.7: The background rate for the different event offsets as a function of reconstructed shower energy for 20° and 40° zenith angle. Solid and dashed lines indicate the background rate curves for the high-energy and standard analysis, respectively. The rate values are computed using observations of PKS 2155−304 conducted in the corresponding zenith angle bands. The source position is excluded from the rate estimation.

rate level in the high-energy analysis in comparison to the standard analysis.

The application of the improved TMVA-based gamma-hadron separation demonstrates significant improvement of the background rejection at large offset angles in comparison with image-shape-based box cuts discussed in Section 4.2 (see also bottom right panel of Figure 4.6). Using the modified method the background rate at large offset angles decreases almost to the level of the rate at 0.5° event offset.

5.1.5 Quality factor

One way to characterise the performance of the gamma-hadron separation cut is the *Quality factor*:

$$Q_{\mathrm{f}} = \frac{\epsilon_\gamma}{\sqrt{\epsilon_{\mathrm{bkg}}}}, \qquad \epsilon = \frac{N_{\mathrm{cut}}}{N}, \tag{5.1}$$

where ϵ_γ and ϵ_{bkg} are the ratios of event numbers before (N) and after (N_{cut}) the background rejection cut for the signal and background sample, respectively. Larger Q_{f} values imply a better background rejection.

The resulting Q_{f} curves for the high-energy analysis as a function of reconstructed energy and zenith angle are displayed in the top row in Figure 5.8. The signal sample consists of point-like gamma-ray simulations, whereas the background sample is extracted from observations of PKS 2155−304 as described in Section 5.1.4. The source position is excluded during the background estimation. On average, the quality factor rises with energy, except for the 0.5° event offset curve, which starts to decrease above approximately 20 TeV. The

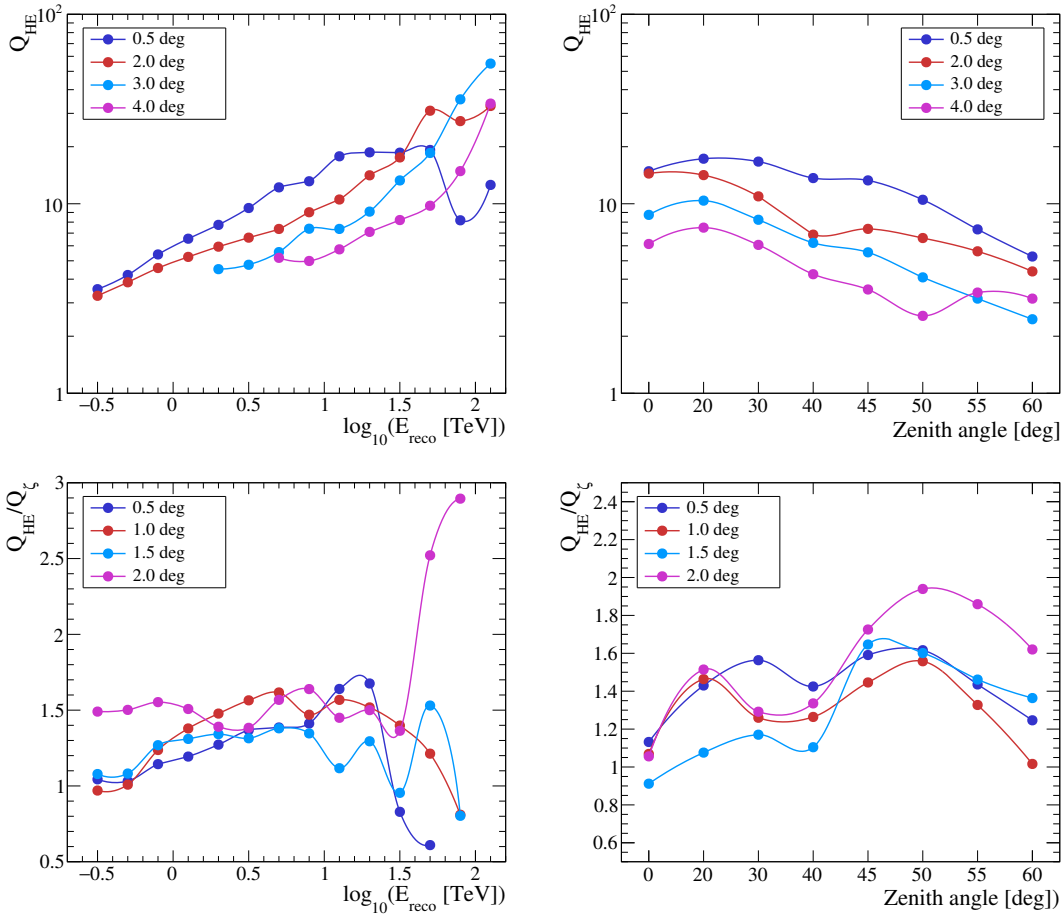

Figure 5.8: The quality factor of the gamma-hadron separation cut for the high-energy analysis for different offset bands. Top panel shows the quality factor as a function of reconstructed energy at 20° zenith angle (left panel) and as a function of zenith angle for energies above 10 TeV (right panel). The bottom panel shows the ratio between the quality factors for low event offset bands calculated for the high-energy and standard analysis for the same zenith and energy range as used in the top panel. The background sample for all three plots is extracted from the PKS 2155−304 observation data.

Q_{f} gradually decreases as the zenith angle increases due to degradation of the direction reconstruction and gamma-hadron separation quality.

At low offset angles, the quality factor can be compared to the standard analysis values. The ratio between the quality factor obtained for the high-energy analysis Q_{HE} and the one for the standard analysis Q_{ζ} are displayed in the bottom panel of Figure 5.8. The ratios as a function of zenith angle are shown only for events above 10 TeV. The resulting curves show an improvement of the high-energy analysis by 20 - 50% at 20° and up to 40 - 80% at 45 - 50° zenith angles.

5.1.6 Sensitivity

The most important analysis characteristic is the detection sensitivity. It indicates a minimal gamma-ray flux from the source that can be detected with $5\,\sigma$ significance during the exposure time T. In this work, sensitivity is defined as $N_{\mathrm{g,\ req}}/N_{\mathrm{g}}$, where N_{g} is the expected number of gamma-ray events detected from the source and $N_{\mathrm{g,\ req}}$ is the gamma-ray excess which is required in order to reach the $5\,\sigma$ significance above the background N_{bkg}. The excess is computed as [67]:

$$N_{\mathrm{g,\ req}} = N_{\mathrm{On}} - N_{\mathrm{bkg}} = N_{\mathrm{On}} - \alpha \cdot N_{\mathrm{Off}}, \tag{5.2}$$

and the significance is estimated according to Li and Ma [150] as:

$$S = \sqrt{2}\left(N_{\mathrm{On}} \ln\left[\frac{1+\alpha}{\alpha} \cdot \frac{N_{\mathrm{On}}}{N_{\mathrm{On}} + N_{\mathrm{Off}}} \right] + N_{\mathrm{Off}} \ln\left[(1+\alpha) \cdot \frac{N_{\mathrm{Off}}}{N_{\mathrm{On}} + N_{\mathrm{Off}}} \right] \right)^{1/2}, \tag{5.3}$$

where N_{On} is the number of events in the *On-region*, which is a test region typically containing the source of interest. The counts measured in this region are composed of background as well as signal events. N_{Off} is the number of events in the *Off-region*, which is used for the background estimation and contains only background events. The α parameter is the normalisation factor, accounting for the differences between On and Off region, such as size, exposure, zenith and offset angles, etc. In the general case, α is defined as [67]:

$$\alpha = \frac{\int\limits_{\mathrm{On}} A^{\gamma}_{\mathrm{On}}(\theta_x, \theta_y, \phi_z, t)\mathrm{d}\theta_x \mathrm{d}\theta_y \mathrm{d}\phi_z \mathrm{d}t}{\int\limits_{\mathrm{Off}} A^{\gamma}_{\mathrm{Off}}(\theta_x, \theta_y, \phi_z, t)\mathrm{d}\theta_x \mathrm{d}\theta_y \mathrm{d}\phi_z \mathrm{d}t}, \tag{5.4}$$

where A^{γ}_{On} and $A^{\gamma}_{\mathrm{Off}}$ are the gamma-like event acceptance for the On- and Off-region, respectively. In turn, they depend on zenith angle ϕ_z and location (θ_x, θ_y) in the FoV. In the simplest case, when there are one or several Off regions which have the same size and offset angle as the On region, the α parameter can be estimated as one over the number of Off regions.

The background data sample in this investigation is extracted from the PKS 2155−304 observations, excluding the source position from the estimation. Since the observation time T_{obs} of PKS 2155−304 is not equal to exposure time T, the number of detected events $N^{'}_{\mathrm{bkg}}$ is scaled as:

$$N_{\mathrm{bkg}} = N^{'}_{\mathrm{bkg}} \cdot \frac{T}{T_{\mathrm{obs}}}. \tag{5.5}$$

As mentioned above, N_{g} is defined as the number of gamma rays from the source detected by the instrument during the time T. For its estimation, an assumption on the source spectrum is required. In this study, the sensitivity is calculated for a Crab-Nebula-like gamma-ray source. The Crab Nebula differential energy spectrum can be fitted by a power

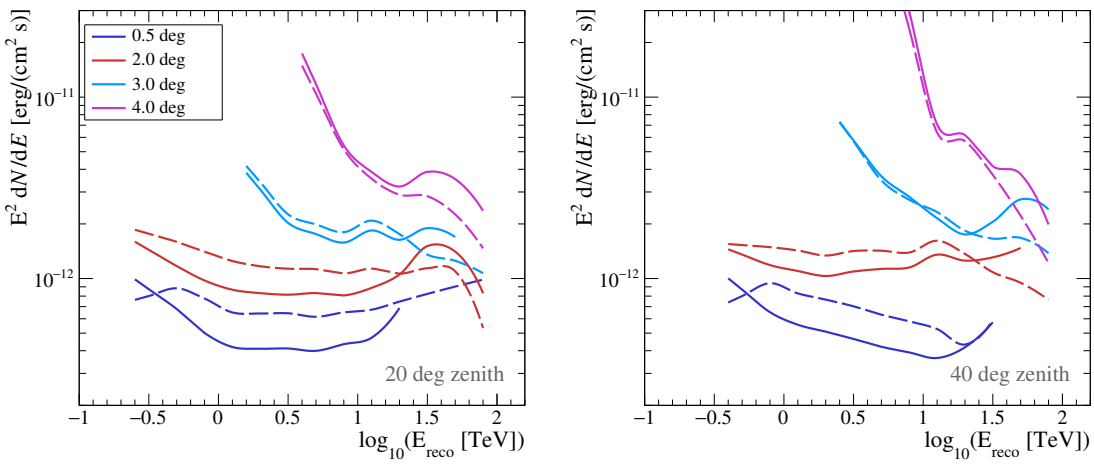

Figure 5.9: The differential sensitivity for the high-energy analysis for 100 h of observation as a function of reconstructed energy for various offset bands at 20° (left) and 40° (right) zenith angles. The sensitivity is shown for two types of gamma-ray sources. Solid lines denote the sensitivity for point-like sources with $\theta^2 = 0.0125$ square degrees and dashed lines indicate the same quantity for slightly extended sources with $\theta^2 = 0.04$ square degrees. Both figures display the sensitivity for energies above the threshold. Similarly to other performance plots, the x-axis is binned in such a way that it contains 5 energy bins per decade.

law with an exponential cutoff [46]:

$$\frac{\mathrm{d}N}{\mathrm{d}A\mathrm{d}E\mathrm{d}t} = \Phi_0 \left(\frac{E}{1\,\mathrm{TeV}}\right)^{-\Gamma} \exp(-E/E_{\mathrm{cut}}), \tag{5.6}$$

where $\Phi_0 = 3.76 \times 10^{-7}\,\mathrm{m}^{-2}\mathrm{s}^{-1}\mathrm{TeV}^{-1}$ is the differential flux normalisation at 1 TeV; $\Gamma = 2.39$ is the spectral index and $E_{\mathrm{cut}} = 14.3\,\mathrm{TeV}$ is the cutoff energy. To estimate the N_{g} value, this theoretical spectrum is folded with the effective area, which is evaluated using point-like gamma-ray simulations [163].

The events from both signal and background samples go through the reconstruction chain and undergo all selection cuts (image selection and gamma-hadron separation), including the θ^2 cut, which defines the size of the source On-region. The obtained differential sensitivity for 100 h of observation at 20° and 40° zenith angles is displayed in Figure 5.9 as a function of reconstructed energy. The figure shows the sensitivity curves for two different θ^2 cuts. In the first case, the θ^2 is equal to 0.0125 square degrees, which is a typical value for a point-like source in the standard analysis. It means that the On-region radius θ is approximately 0.11°. The second θ^2 value is 0.04 square degree in order to estimate the sensitivity for slightly extended sources. In this case, the radius of the On-region is 0.2°, which is comparable with the angular resolution at moderate offsets[1] (see Figure 5.2).

The algorithm for the sensitivity calculation requires at least 5 background events from

[1] As seen in Figure 5.2, the angular resolution at large event offsets is close to 0.2°. Especially this is true for large zenith angles. Therefore, for large zenith-offset bands, the θ^2 value of 0.04 square degree corresponds to a point-like source.

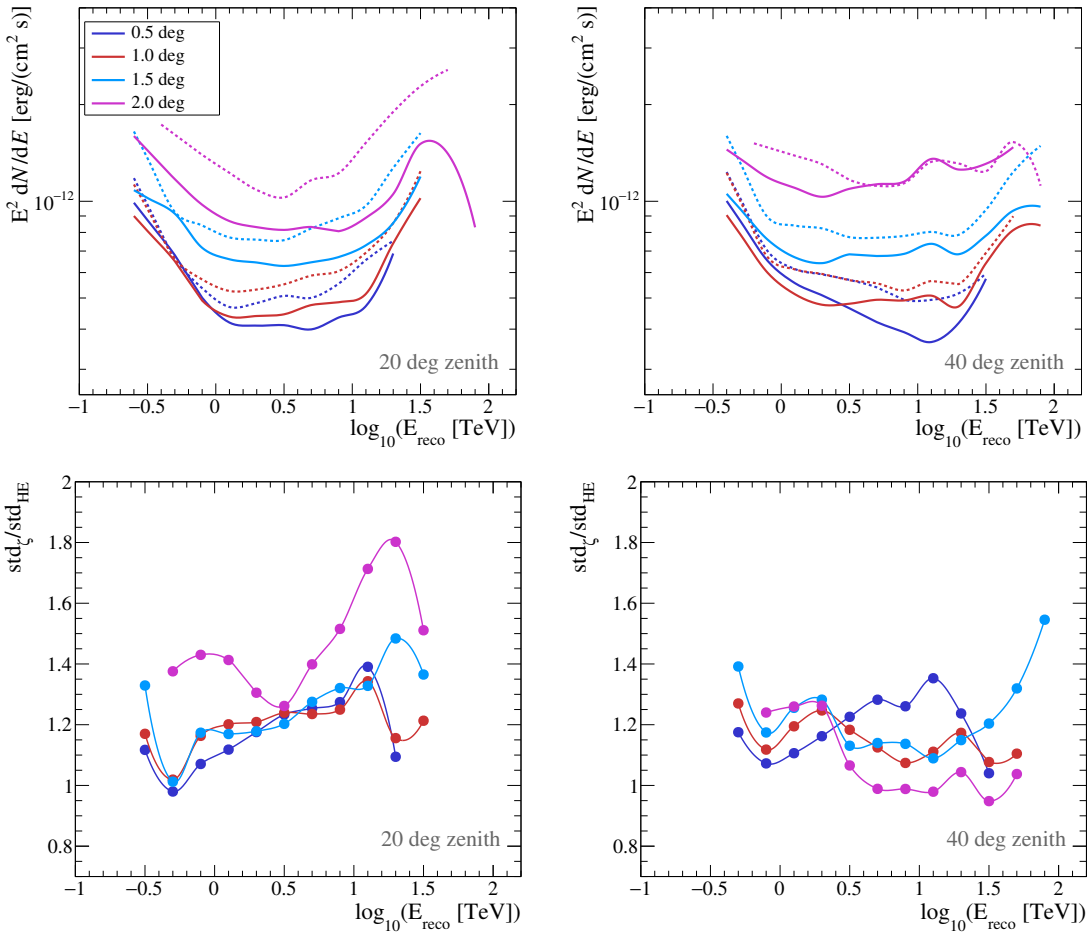

Figure 5.10: The comparison of differential sensitivity for the high-energy and standard analysis for 100 h of observation as a function of reconstructed energy for low event offset bands. The high-energy and standard analysis sensitivity curves for 20° (left) and 40° (right) zenith angles are shown in the top panels and are denoted by solid and dotted lines, respectively. Both plots are produced for $\theta^2 = 0.0125$ square degrees. The bottom panels show the ratios of the sensitivity between the standard and high-energy analysis for the corresponding zenith angle bands. All sensitivity curves are drawn above the energy threshold. The x-axis contains 5 energy bins per decade.

the Off regions in each energy bin during the exposure time. The background rate is low at high energies and sometimes the requirement cannot be fulfilled. For this reason, not all curves are shown at highest energies. But it does not mean that the analysis is not sensitive in that region. Also, there are a couple of additional requirements [106]. First of all, the minimum number of excess counts per bin is 10 events, otherwise the sensitivity is estimated as $10/N_{\mathrm{g}}$. And second, the signal-to-background ratio per bin must exceed 5%. If the requirement is not met, the sensitivity in the particular bin is calculated as $0.05 \cdot N_{\mathrm{bkg}}/N_{\mathrm{g}}$ [163, 138].

Due to limited statistics at high energies, the listed restrictions introduce artefacts in the sensitivity curves as seen in Figure 5.9. Typically, sensitivity for the point-like sources

(smaller θ^2) is better than for the extended ones (larger θ^2) since smaller On-region accumulates less background. However, two corresponding sensitivity curves swap at high energies. This happens because the larger On-region has larger statistics and is less affected by the requirements discussed above. Although at 4° event offset, the sensitivity for larger On-region prevails across the whole energy range. This can be caused by the fact that the angular resolution for this offset angle is approximately equal/larger than 0.2°, which matches the radius of the larger On-region.

At low offset bands, the sensitivity estimated for the high-energy analysis is compared to the one for the standard analysis in Figure 5.10. For ease of comparison, the bottom panel in the figure displays the ratio between those two. On average, the high-energy analysis shows 10 - 20% of improvement in sensitivity over all energies when compared to the standard analysis.

5.2 Monte-Carlo simulation to data comparison

Until this point, almost all performance estimates presented in this chapter were performed using simulated gamma rays. In order to verify that the developed analysis performs in the same way for real data as for simulations, data-simulation comparison is performed. In the following section, two data-simulation comparison investigations are discussed. The first of them evaluates the behaviour of the BDT response, which constitutes the key component of the gamma-hadron separation. In the second investigation, the accuracy of the point-like source reconstruction obtained with the simulated sample is compared to the one obtained with observed dataset, since understanding of the analysis angular resolution is very important for source morphology studies.

5.2.1 Verification of the BDT classifier

For the purpose of the BDT response data-simulation comparison, data taken at the Crab Nebula position are chosen. The Crab Nebula [185] is a strong VHE source and provides reasonable gamma-ray statistics at energies above 10 TeV. During this study, event properties of gamma-like events located in the On-region are compared with the corresponding set of the gamma-ray simulations. For this purpose, Crab Nebula data are analysed and only events that pass preselection cuts take part in further investigation. There are a large number of cosmic-ray events that arrive from the same direction. Several techniques have been developed for the estimation of the cosmic-ray background in the FoV [67]. One of them is the *Reflected-region background method* [102, 35]. In this approach, several Off regions are constructed around the observation position with the same offset as the On-region like it is shown on the left side of Figure 5.11. The right panel of the same figure displays the BDT response evaluated for the events in the On and Off regions. The distribution of On events is represented by a clear peak at about 0.7, since the On region contains the gamma-ray source. The Off regions contain only background events, resulting in the peak of the Off-event distribution to be located in the far negative part of the BDT response and only its tail is seen on the plot.

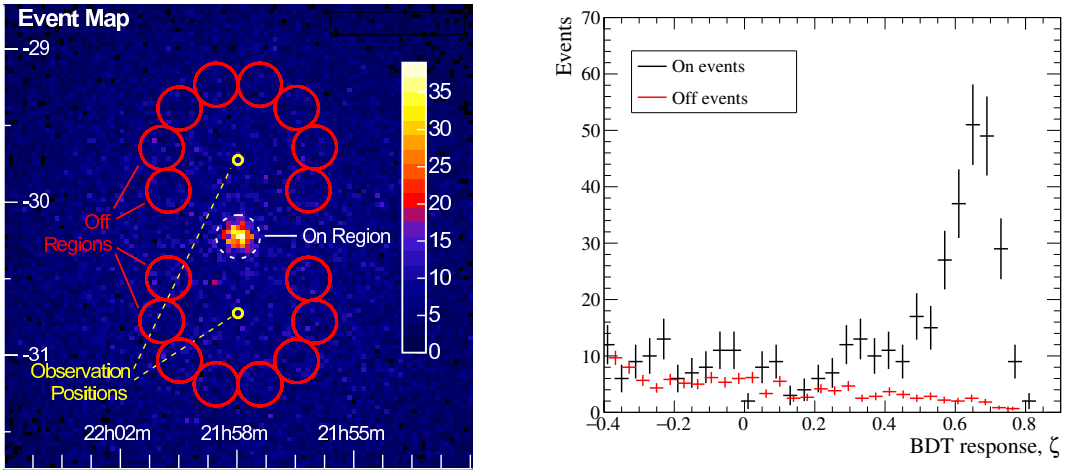

Figure 5.11: Left: Schematic illustration of the Reflected-region background method [67]. The picture shows a relative location of the observation position, On-region that contains the source position and a set of Off regions used for the background estimation. Right: Comparison of the BDT response for the On- and Off-region events. Here, Off events are scaled by α parameter, which is estimated as one over the number of Off regions. Typically ζ_{BDT} values lay in the range from -1 to 1. The x-axis of the plot is selected to show mainly the gamma-like events that correspond to positive ζ_{BDT} values. Most events from the Off regions occupy the far negative end of the ζ_{BDT} range and are not visible here.

The Crab Nebula is nearly point-like[2] and there are no other gamma-ray sources in the relative vicinity, therefore most of the observations are conducted at a comparably low offset angle of 0.5° or 0.7°. The source is always seen by the H.E.S.S. instrument under a large zenith angle and the dataset chosen for the comparison lay approximately within 45 - 50° zenith angle range. Thus, the corresponding simulation set consists of gamma rays originating at 45° and 50° zenith angle with 0.5° offset angle that are scaled accordingly to the number of Crab Nebula excess events in the On-region within these zenith-offset bands. In addition, simulated events are re-weighted from $\Gamma = -1$ to $\Gamma = -2.6$ in order to have a spectral index close to the Crab Nebula spectrum in the energy range of interest[3].

The result of the BDT response comparison for the Crab Nebula excess data and gamma-ray simulation set in the energy range from 10 to 20 TeV is shown in the top panel of Figure 5.12. The number of gamma-ray excess events in the On-region is estimated using Equation 5.2. The bottom panel of the figure displays the residuals between data and simulations that are computed as:

[2] An extension of the Crab Nebula recently has been discovered by the H.E.S.S. Collaboration [8], but the extent is so small that it can be detected only using an analysis method with a very good angular resolution like e.g. ImPACT [169].

[3] The Crab Nebula spectrum has a cutoff around the energy of 14 TeV [46] and it is not easy to make a precise measurement of the spectral shape in the cutoff region. Taking into account that the BDT response comparison here is performed in the narrow energy band 10 - 20 TeV, and thus, the BDT response distribution for simulated gamma rays is not very sensitive to the assumed spectral index, it was decided to re-weight the simulated spectrum to the spectral index, which is slightly steeper than the actually measured value for the entire Crab Nebula spectrum.

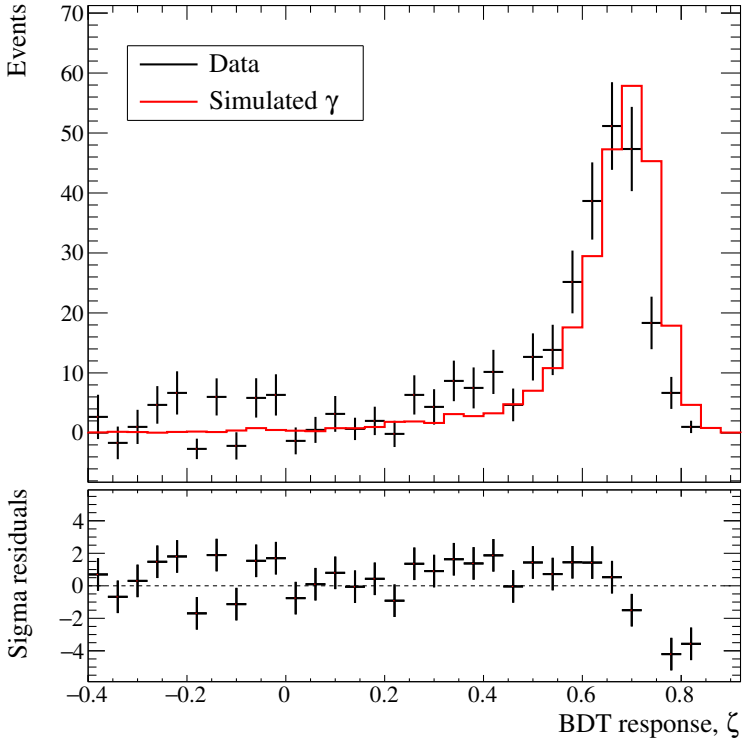

Figure 5.12: Comparison of the BDT response between the Crab Nebula data and simulated gamma rays with zenith and offset angles that correspond to the observational data. The distributions are produced for the energy range between 10 and 20 TeV. Gamma rays used for this comparison are simulated with $\Gamma = -1$ spectral index and reweighed to $\Gamma = -2.6$, which approximately corresponds to the Crab Nebula spectral index at high energies.

$$residual = \frac{N_{\text{data}} - N_{\text{sim}}}{\sigma_{\text{data}}}, \tag{5.7}$$

where N_{sim} and N_{data} are the numbers of simulated gamma rays and data excess events in a particular bin of the BDT response distribution, respectively; σ_{data} is the data statistical uncertainty in the corresponding bin, which is calculated taking into account uncertainties estimated for N_{On} and N_{Off}. The statistical uncertainty for the simulation sample is much smaller in comparison to the σ_{data} values, and therefore, is not taken into account here.

The BDT response distribution shows a slight shift between data and simulations, which can be described as data overshooting the simulations in ζ_{BDT} range from 0.3 to 0.7 and undershooting where ζ_{BDT} values are larger than 0.7. The likely reason for such a behaviour is a discrepancy between data and simulations in the input parameters used for the ζ_{BDT} evaluation. Especially, $MSCW$ as the parameter with the highest importance for the training at high energies in the low offset bands (see Figure 4.20).

The comparison of the BDT input parameters for the corresponding data and simulation set is shown in Figure 5.13. The $MSCW$ and $MSCL$ parameters exhibit a shift in the data distributions to negative values, implying that the real data images are systematically narrower and shorter than expected from the shape lookup tables. Also, there is a perceptible

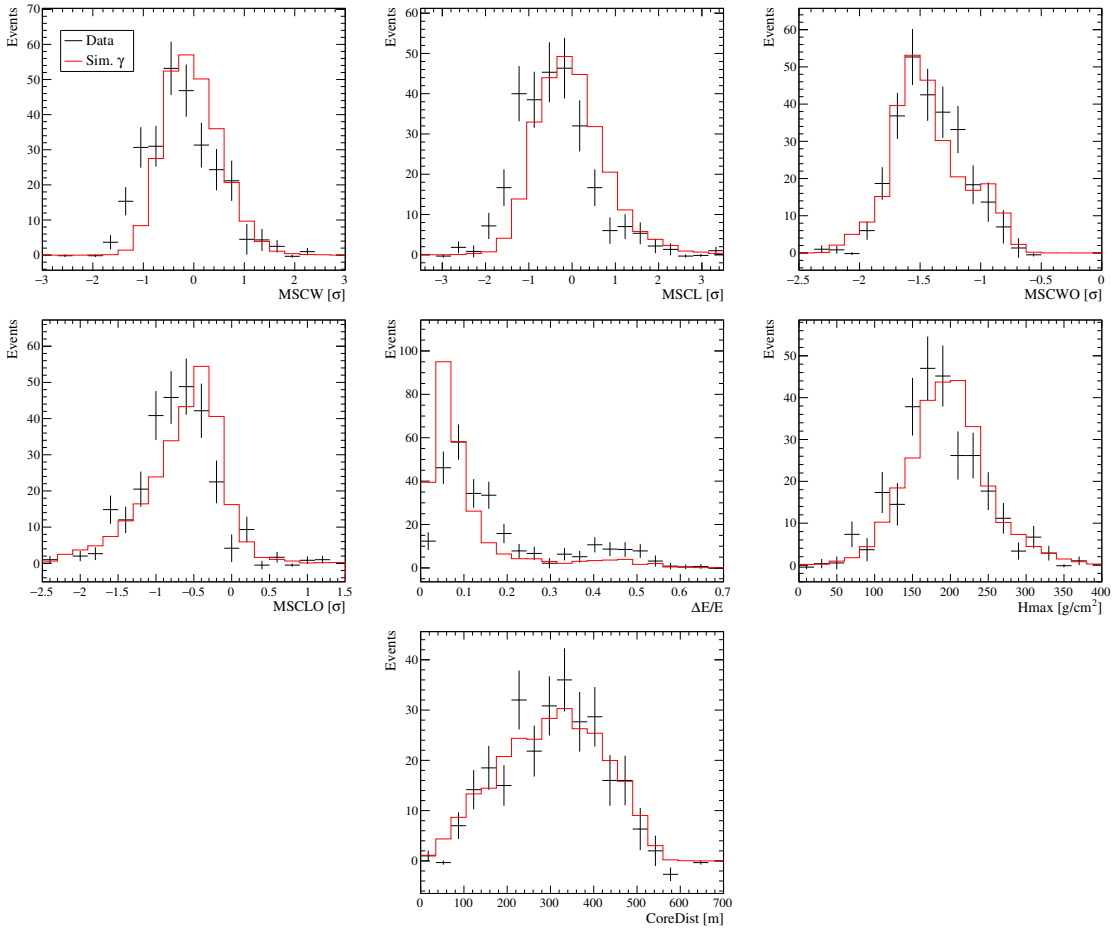

Figure 5.13: The comparison of the BDT input parameters between data and simulation set. The investigation is performed for the same data and simulation set as in Figure 5.12.

discrepancy between data and simulations in the $\Delta E/E$ parameter distribution. Different features in this distribution usually correspond to the telescope multiplicity. A significant fraction of events reconstructed with 2 or 3 telescopes occupies $\Delta E/E$ values around 0.3-0.6 and with large enough statistics it is possible to see a double-peak structure in this region. Four-telescope events typically have a more accurate energy reconstruction resulting in much lower $\Delta E/E$ values (first peak in the distribution). Comparison of $\Delta E/E$ in Figure 5.13 shows that the peak which corresponds to four-telescope events is wider and the second peak is more pronounced in the case of real data than in simulation set.

Currently, the exact reason for such trends is not clear. In this regard, several checks were carried out. For example, the impact of the telescope multiplicity during the data taking and mismatch between optical efficiency in data and in simulation set were checked. In addition, the influence of the simulated spectrum used for the energy and shape-lookup tables production was investigated. Simulated events were re-weighted from $\Gamma = -1$ to the $\Gamma = -2$ spectrum during the lookup table filling. None of these effects could explain the observed disagreement between data and simulation sample in the BDT response or input parameters distributions.

One of the possible explanations can be a presence of broken or switched-off pixels during the observation. The data quality selection procedure allows for a fraction of about 15% of non-working pixels in the camera [119]. This can influence the image intensity estimation resulting in a negative bias when compared to gamma-ray simulations. Lower image intensities at the same impact distances would imply smaller image widths and lengths, which actually would be different from the actual measurement. And as a result, the evaluated values of the $MSCL$ and $MSCW$ parameters would be underestimated, as observed in the corresponding plots in Figure 5.13. In addition, it would also affect the quality of the energy reconstruction leading to a disagreement in the $\Delta E/E$ parameter.

5.2.2 Comparison of the point-source resolution

The ability to reconstruct a point-like source at energies above 10 TeV with the analysis presented in this work is displayed in Figure 5.14 in form of a θ^2 *plot*. The analysis is performed for the two point-like VHE gamma-ray sources that have reasonable statistics above 10 TeV: the Crab Nebula and HESS J1745−290 [25], which is coincident with Sagittarius A* (the Galactic Centre source). The gamma-ray excess is calculated following Equation 5.2. The Crab Nebula observations were conducted mainly with 0.5° offset angle within a zenith angle range between 45° and 50°. Sagittarius A* is seen at much lower zenith angles in Namibia and the chosen observation runs cover zenith angles from 5 to nearly 50°. The mean value of the zenith angle distribution is around 20°. The Galactic Centre region is populated with many sources. Thanks to this fact, there are observations with pointing at different offset angles, namely 0.5°, 1° and 1.5°.

In the analysis of real data, θ is the angular distance between the reconstructed event

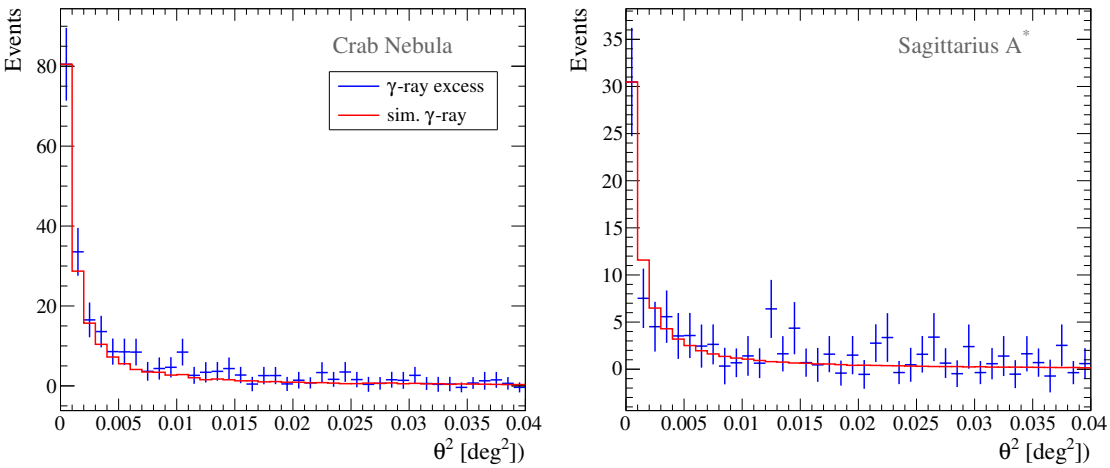

Figure 5.14: The comparison of the squared angular event distribution between observed and simulated point-like gamma-ray source. Blue data points show the distribution of the excess events for Crab Nebula on the left side and for Sagittarius A* on the right side of the figure. Red curves represent the distribution of the simulated gamma rays, which are accordingly re-weighted to the spectral index of the sources. The simulation set is also composed taking into account the offset and zenith angle distribution of the observations.

direction and the supposed source position (test position). In the case of simulations, θ is the angular distance between the reconstructed and simulated event direction. Simulation sets for the comparison with each source are compiled accordingly to the fraction of On-region events of the particular source that fall into the certain zenith-offset band. Since gamma rays are simulated with the $\Gamma = -1$ spectral index, the spectrum is re-weighted to $\Gamma = -2.6$ and $\Gamma = -2.3$, which are close to the Crab Nebula and Sagittarius A* spectrum above 10 TeV, respectively. Similarly to the case discussed in Section 5.2.1, the index of the re-weighted spectrum does not match precisely the index of the source spectra, but the θ^2 plot is also not very sensitive to the small changes in the spectral index. The figure shows a good match between the measured θ^2 parameter distribution for the gamma-ray excess calculated from data and the one predicted from simulations.

5.3 Cosmic-ray system acceptance

In ground-based gamma-ray astronomy, the gamma-like cosmic-ray background is typically much more numerous than the rate of gamma rays detected from a source. This implies that, in almost all cases, the background can only be subtracted on a statistical basis. Although gamma-hadron separation has been improved in this work, there still remains a quasi-irreducible background. Therefore, accurate background modelling is a key task in VHE source analysis and understanding of the *system acceptance* plays a crucial role in it. The system acceptance describes the probability of the background event to survive all analysis cuts depending on its position in the FoV, zenith and azimuth angle, optical efficiency, reconstructed energy, etc [67]. It is represented by a distribution of the squared angular distances between the telescope pointing position and a particular event direction, i.e. squared event offset. There are two ways to construct an acceptance model:

- *Acceptance from data* is built during the source analysis on a run-by-run basis. All event that pass selection cuts and are outside the exclusion regions are filled into 1D histogram as a function of the squared event offset. The exclusion regions include all detected and potential sources of VHE emission in the FoV, On-region and bright stars. The obtained acceptance curve is later corrected for all exclusion regions. If the excluded area is very big, the final event statistics will be not sufficient for the accurate acceptance determination. Such a situation often happens when the observations are conducted in the Galactic plane with a large density of gamma-ray sources. This approach is also not applicable if the system pointing position is within the excluded region.

- *Acceptance from lookup tables* is built using archival observations without significant VHE sources in the FoV. The procedure is similar to the one described above. Obtained event distributions are stored in form of 1D histograms as a function of squared event offset as well as 2D histograms as a function of squared event offset and reconstructed energy. The acceptance lookup tables are produced for different zenith angle bands: 0, 20, 30, 40, 45 and 55°. Unfortunately, there is not enough data to provide a finer binning at large zenith angles, as is done for other lookup tables. The acceptance lookup tables also do not account for changes in NSB level, telescope optical efficiency or atmospheric transparency.

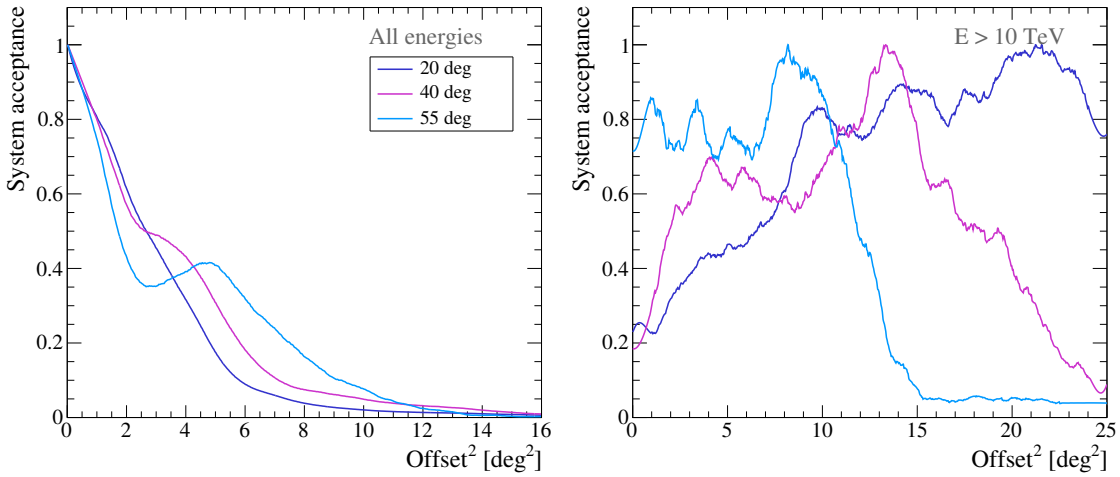

Figure 5.15: The system acceptance obtained for the high-energy analysis. Colour of acceptance curves indicate different zenith angle bands. Left plot shows the acceptance in the full energy range, while the right panel displays the acceptance above 10 TeV.

The system acceptance of gamma-like background events for the high-energy analysis is shown in Figure 5.15. The acceptance curves are presented for 20°, 40° and 55° zenith angle bands in two cases: for the full energy range on the left and for energies above 10 TeV on the right. The acceptance curves appear to have an irregular structure. Most likely, this is caused by the binning in offset bands introduced for the shower direction reconstruction and gamma-hadron separation. In both cases, interpolation of the corresponding quantity is applied between offset bands, which makes the irregularities in the acceptance curve less pronounced, but cannot remove them completely.

Despite the fact that the presented system acceptance has irregularities in its structure, on average, it behaves as expected. In the case of the full energy range, where the majority of events are of low energies, the highest event rate is in the middle of the camera and it drops fast as the offset angle from the camera centre increases. At higher energies the picture is different. The system acceptance does not have a maximum in the centre anymore and peaks at larger offset angles. There are a couple of effects that can contribute to such a trend. For events that originate close to the telescope pointing position, the image CoG lies closer to the edge of the camera. Therefore, the high-energy showers that have larger images, can be rejected by the local-distance cut creating a reduction in the acceptance. Another effect can be related to the shower direction reconstruction since the DISP method uses image parameters for this purpose and is trained using only gamma rays. Hadron images are more irregular and their parameters differ from gamma-ray image parameters. This results in a decrease of the reconstruction accuracy. The largest effect comes from the gamma-hadron separation procedure. At high energies, background rejection is more efficient in the centre than at the edge of the FoV.

5.3.1 Data-model comparison of the system acceptance

In the HAP framework, the system acceptance is assumed to be radially symmetric [66]. However, the spectrum of cosmic rays is steep and the energy threshold rises as the zenith angle increases within the FoV, resulting in a decrease of the event rate. Relaxation of the maximum event offset up to 4.5° results in an increased effective camera FoV up to 9°, which could be large enough to cause zenith-angle related asymmetry in the system acceptance. Considering the energies above 10 TeV, this effect would influence the acceptance at zenith angles as high as 50 - 60°, where the energy threshold at large offsets is close or larger than 10 TeV as discussed in Section 5.1.3 (see Figure 5.6).

In this investigation, the radial symmetry of the system acceptance for the high-energy analysis above 10 TeV is checked and the results are shown in Figures 5.16 and 5.17 for the 20 and 40° zenith angle bands, respectively. The investigation is performed using observations of the Sagittarius Dwarf Spheroidal Galaxy (Sgr dSph) [50] in the range of zenith angles from 15° to 25° and the globular cluster M 15 [18] at zenith angles from 35° to 42°. The sources were used for the indirect searches of Dark Matter and no significant emission was found in the FoV. Both of them are located far from the densely populated Galactic plane, specifically, Sgr dSph at ($l = 5.7°$, $b = -14.3°$) and M 15 at ($l = 65°$, $b = -27.3°$) in Galactic coordinates. Such a location of the test sources is useful for the acceptance study since the FoV is not contaminated by gamma rays from other VHE sources and does not contain large excluded regions, which would reduce the number of events that can be used to construct the model.

The top panel in both figures shows the distribution of arrival directions of the gamma-like background events in the nominal system and compares it for the high-energy and two standard analyses: with box-cut and TMVA-based gamma-hadron separation, which are described in Section 3.3 and usually are referred to as *std* and *std_zeta*, respectively. Despite the fact that the exposure time for both sources is very similar (15.8 and 14.9 h for Sgr dSph and M 15, respectively), the number of detected events at 40° zenith angle is much larger than at 20° as seen in Figure 5.17 and 5.16, respectively. This is a result of the effective area increase at high energies as the zenith angle increases.

At 20° zenith angle, the event distributions for all three analysis methods are very close to being radially symmetrical. In the case of the high-energy analysis, it also can be seen from the FoV slices along x and y-axis that are shown with blue colour in the left and central panel of the bottom row in Figure 5.16, respectively. The slices have a width of 1.2° and are illustrated with red dashed lines in the upper left panel. The statistics in the data sample is small. Nevertheless, there is no indication of a strong gradient in the FoV at energies above 10 TeV. In addition, event distributions within the FoV slices are compared with the model curves, which are shown with the red solid line in the corresponding figures. The model curves are produced by rotating the acceptance curve (extracted from the lookup tables with an appropriate zenith angle) around the camera centre in the nominal system, scaling the obtained 2D model distribution with the number of data events and performing the same slicing procedure as described above. One more data-model comparison plot is displayed in the right bottom panel and shows the event distributions as a function of squared event offset (i.e. the acceptance curve itself). All three comparison plots in the bottom row show a good match between the data and model.

The picture looks different at 40° zenith angle. Results of all three analysis methods

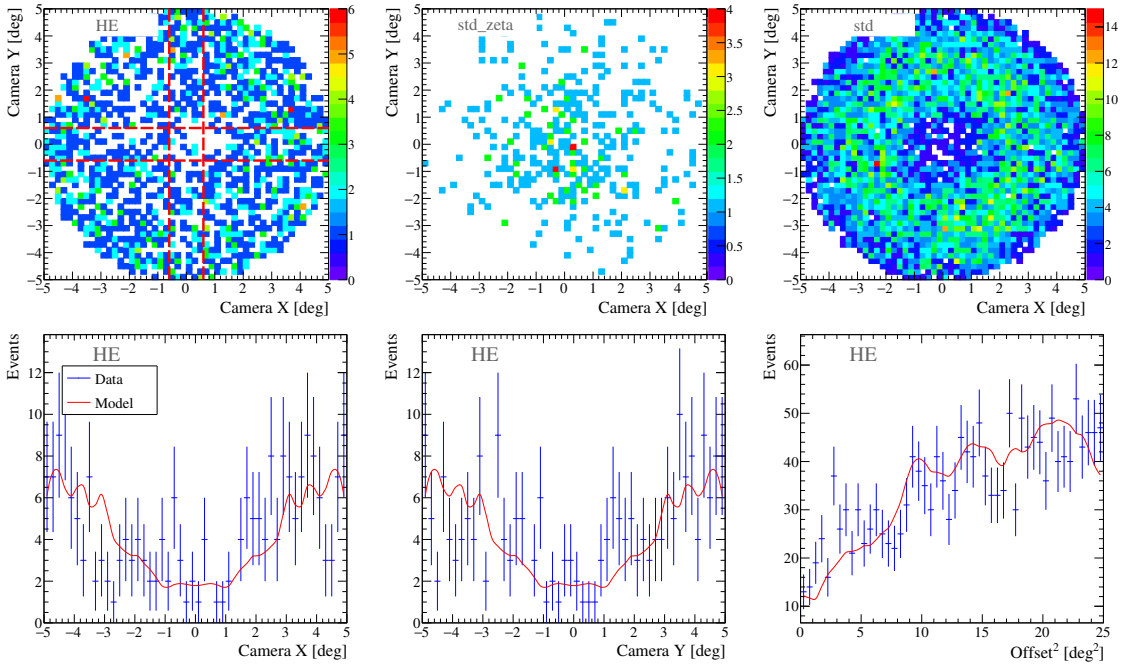

Figure 5.16: The comparison of the system acceptance between data and model for 20° zenith angle band using observation runs of Sgr dSph. The top row shows the distribution of gamma-like events in the camera (nominal system) after data analysis performed with the high-energy analysis (left), standard analysis with TMVA-based (middle) and box-cut-based (right) gamma-hadron separation. The bottom row compares the event distributions extracted from the high-energy data analysis and the background model based on the acceptance lookup tables. The left and the middle plot shows the distribution of events projected along x and y-axis in the nominal system within the regions indicated in the upper left panel with red dashed lines. The positive direction of x-axis indicates the decrease of zenith angle and the positive direction of y-axis denotes the increase of azimuth angle. The right panel in the bottom row shows the distribution of the squared angular distance between the event directions and camera centre.

displayed in the top row in Figure 5.17 show an indication for zenith-dependent asymmetry in the FoV. It is also clearly seen in the bottom left plot that illustrate the FoV slice along the x-axis (i.e. along zenith angle). In turn, the bottom middle plot, which displays the y-axis slice (i.e. along azimuth angle), does not show azimuth-dependent asymmetry. Clearly, at large offset angles, the gamma-hadron separation procedure keeps more gamma-like background events in the part of the FoV that corresponds to lower zenith angles, in comparison to the large-zenith part of the FoV. This effect also generates the difference between data and model acceptance curves seen in the bottom right panel. Such a zenith-dependent asymmetry in the FoV appears as the observation zenith angle increases and requires further investigation, which is beyond of the scope of this work.

Figure 5.18 shows an example of the source analysis high-level results, where the background modelling and, therefore, system acceptance plays a crucial role. The significance

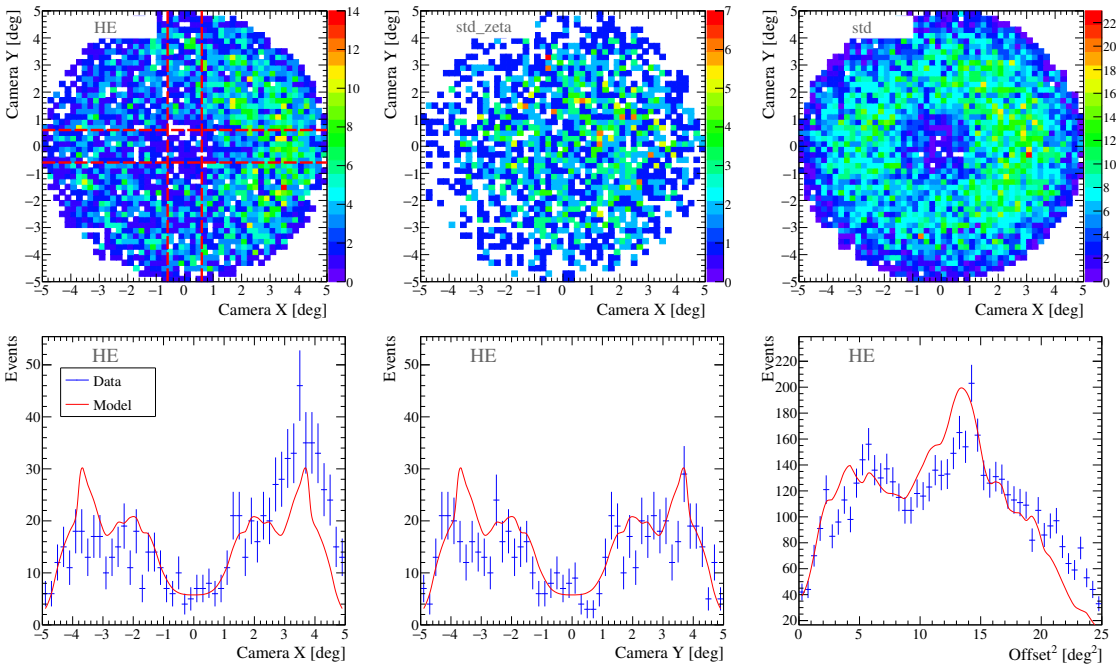

Figure 5.17: The comparison of the system acceptance between data and model for 40° zenith angle band using observation runs of the globular cluster M 15. All panels in this figure show the same information as in Figure 5.16.

maps of the FoV centred at the source positions are displayed in the left column. The significance of each bin is calculated as shown in Equation 5.3, where N_{Off} is evaluated using the background model (a more detailed description of this kind of map production can be found in Section 6.1.1) [67]. Thus, a considerable disagreement between model and real background data would be reflected in the significance map. Typically, quality of background estimation in the map is characterised by the 1D significance distribution as shown with red colour in the right column. The significance distribution of all pixels in the FoV, which does not contain gamma-ray sources, should be centred at 0 and follow gaussian distribution with $\sigma = 1$.

The top and bottom row in Figure 5.18 shows the significance above 10 TeV obtained by analysing the Sgr dSph and M 15 data with the high-energy analysis, respectively. The significance calculation approach (Equation 5.3) requires at least 5 events per bin. The Sgr dSph dataset contains very few events, and therefore, the significance map is nearly empty for this source. The significance distribution shows mainly upward fluctuations and is shifted in a positive direction. The M 15 dataset has more events and the significance distribution looks better. Despite the disagreement between data and background model, the significance map and distribution does not show considerable outliers. However, data-model differences rise as the zenith angle of observation increases and can lead to some analysis artefacts in the significance or excess sky maps. Therefore, the topic should be further investigated in future.

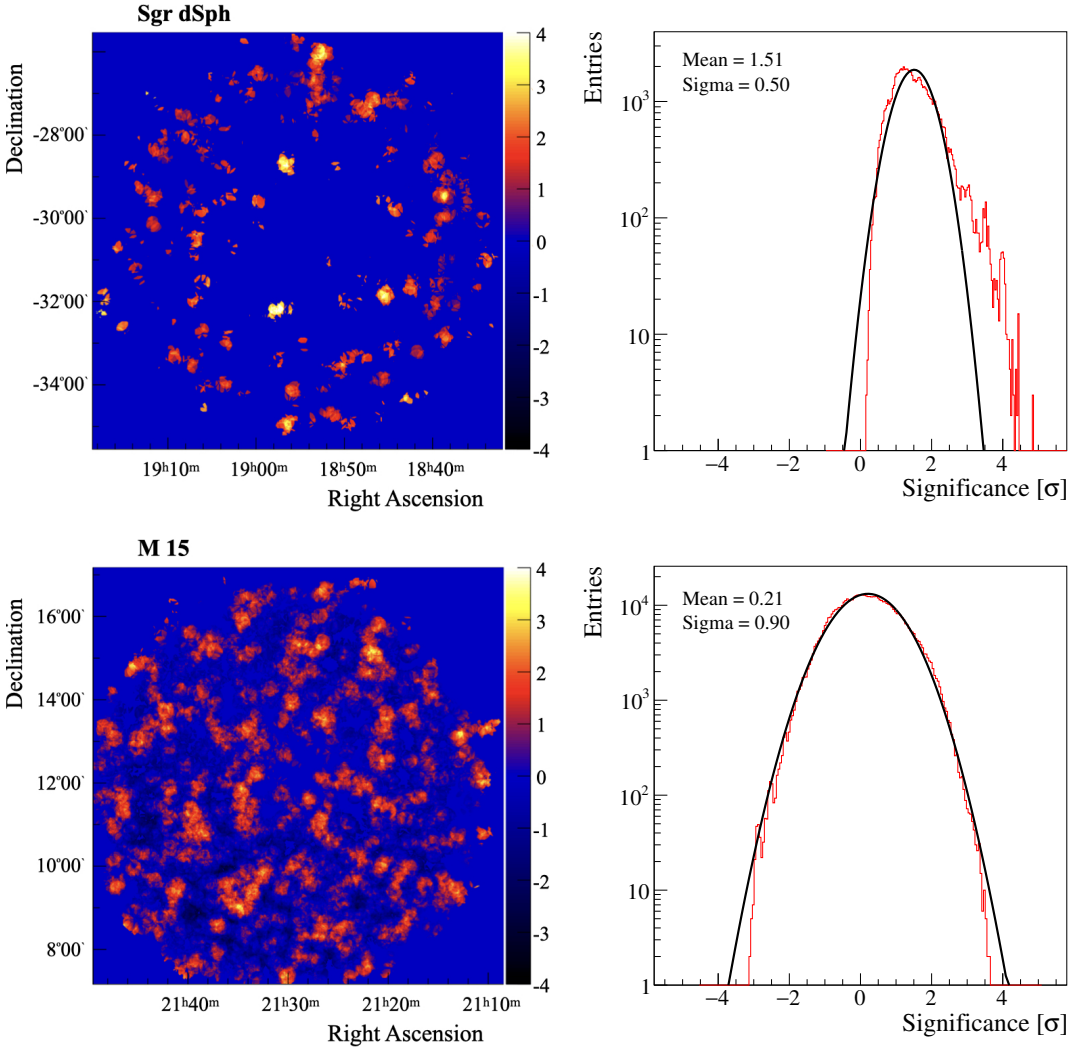

Figure 5.18: The significance distribution in the FoV at energies above 10 TeV with the high-energy analysis. Analysis results for the Sgr dSph and for M 15 are displayed in top and bottom rows, respectively. The left panel in each row shows the significance map centred on the position of the test source. The right panels show the one-dimensional distribution of the pixel significance (red colour) that is fitted with Gaussian function (black).

5.4 Outlook

The analysis method investigated in this work shows promising performance at small and at large offset angles. The next steps can be aimed at an improvement of such performance characteristics as angular resolution and energy bias, especially in the large zenith-offset angle bands. One of the possible actions in this direction could be an increase of the ANN training statistics for the DISP reconstruction and the introduction of energy binning into the training procedure. In addition, the ANN training in this study is produced only for one azimuth angle of 180°. In order to account for the geomagnetic field effects on the shower development, the training should be also performed for 0° azimuth angle.

The modified gamma-hadron separation method significantly improved background rejection at small and large offset angles, while keeping a large fraction of gamma rays. However, the background rate at large offset angles is still higher than for the nominal 0.5° event offset, and the effective area is much lower. Further investigation could reveal new variables with additional gamma-hadron separation power for the BDT training. For example, hadronic showers are more irregular and would have worse accuracy of the direction reconstruction and, thus, larger direction uncertainty than gamma rays. The direction uncertainty as an additional box-cut was proposed in [152] and was used for the angular resolution improvement. In addition, it showed a background rejection power and may yield better performance if used as one of the input parameters for the BDT training.

In this work, several comparison investigations against real data are performed. Comparison of the BDT response shows slight disagreement between data and simulation. And so far no clear reason is revealed that would explain such behaviour. Further investigation could shed light on the nature of this discrepancy and improve performance of the gamma-hadron separation cut. Background modelling is another analysis step that has room for improvement. The corresponding study showed a zenith-dependent asymmetry of the cosmic-ray acceptance at large offset angles. Therefore, a 2D acceptance map would model background more accurately than the 1D acceptance currently used in the HAP analysis, which assumes a radial-symmetric distribution of the background events in the FoV. 2D acceptance for background modelling is already used in the 3D likelihood analysis implemented in *ctools* and *Gammapy* [162].

The cut optimisation plays an essential role in the improvement of the analysis performance. In the current work, standard cut values are used. But since the direction reconstruction and gamma-hadron separation are modified, it is important to find new values of θ^2 and ζ_{BDT} cut, which yield better analysis sensitivity. Another interesting aspect of the cut optimisation is the preselection cuts. As discussed in Section 3.1.2, the local distance cut rejects a significant amount of high-energy events. Relaxation of this cut may increase the effective area and as a result, improve the sensitivity above 10 TeV. However, it also would increase a number of events with images clipped by the camera edge, which are very challenging to reconstruct.

All modifications in reconstruction and gamma-hadron separation that are discussed in this work are proposed as a stand-alone analysis method. However, they can be used in combination with other analysis methods such as ImPACT [169]. First of all, the ImPACT analysis would benefit from the better gamma-hadron separation method. Secondly, ImPACT uses event direction reconstructed with the standard geometry method as a seeding parameter. Studies showed that improvement of the seeding parameter estimation leads to an improvement in the ImPACT performance [140]. The angular resolution obtained with the DISP method is better than the one with the standard intersection of the major image axes. It may be more advantageous to use the direction reconstructed with the DISP method as a seed for the ImPACT analysis at high as well as at lower energies.

Chapter 6

The H.E.S.S. Galactic plane survey in gamma rays above 10 TeV energies

Currently, the *H.E.S.S. Galactic Plane Survey* (*HGPS*) is the largest catalogue of Galactic VHE gamma-ray sources, and its most recent version was published by the H.E.S.S. collaboration in 2018 [5]. The catalogue contains sources analysed over a wide energy range, from 400 GeV up to the highest energies accessible with H.E.S.S. In this work, the HGPS data is analysed at energies above 10 TeV using the high-energy analysis developed in this study. The results are compared to the standard analysis with the respective low-energy cut. Sources detected above 10 TeV in this study are characterised based on key performance parameters such as the detection significance or the gamma-ray excess. In the second part of the chapter, source classes are discussed as well as possible source counterparts. Two sources are exemplarily discussed in more detail at the end of the chapter, namely: the region associated with the shell-type SNR HESS J1731−347 and the PWN candidate associated with PSR J0855−4644 that is coincident with HESS J0852−463.

6.1 Application of the high-energy optimised analysis

The HGPS[1] catalogue contains 78 VHE gamma-ray sources that are located in the Milky Way [5]. Among these are 16 sources that were not known before or for which only a preliminarily detection was published. The HGPS region covers the Galactic longitude range from 250° to 65° and ±3° in Galactic latitude. Its range is shown in Figure 6.1, where it is compared to the surveys conducted by HEGRA [36] and VERITAS [187] from the Northern Hemisphere. The data for the survey were taken between 2004 and 2013 and comprise roughly 2700 observation hours. The lowest panel of the figure shows the distribution of observation time along the Galactic plane. The main observation strategy consisted of dedicated observations taken with 0.7° steps in longitude and distributed between −1.8° and 1° in latitude. For the longitude bands ±5° and from 38° to 48°, the latitude of observation pointing was extended to ±3.5° in order to study the potential high-latitude emission. Additional follow-up observations were conducted for the source candidates ('hotspots') that had been seen in the previous observations, and for other

[1]The HGPS data is available for download from [129].

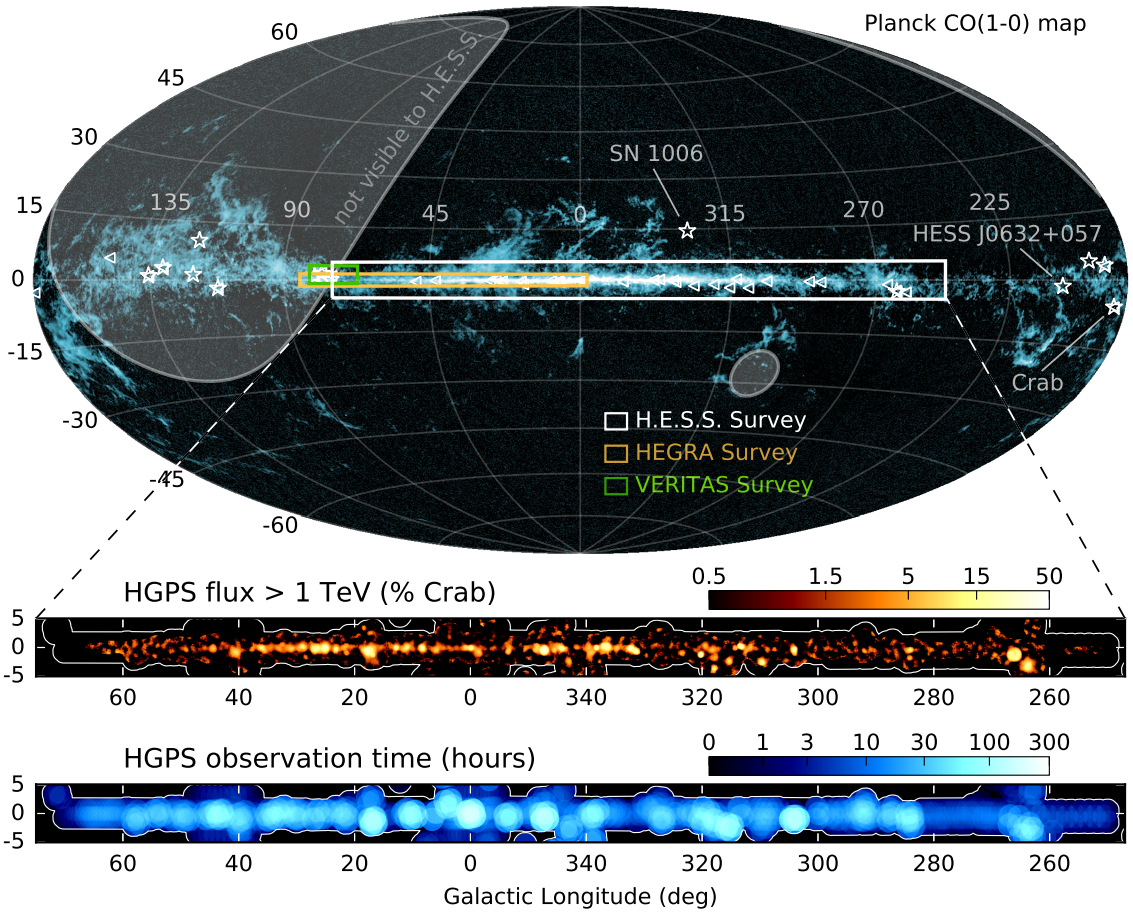

Figure 6.1: An illustration of the region covered by the HGPS catalogue [5]. The main image shows the structure of the Galaxy, represented by an all-sky *Planck* CO(1-0) map [33] with the HGPS region bounds over-plotted with the white box. Orange and green boxes show the HEGRA [36] and VERITAS [187] surveys, respectively. Triangles and stars denote the Galactic sources from the *Fermi*-LAT 2FHL catalogue [32] and other VHE Galactic gamma-ray sources that are outside the HGPS catalogue, respectively. The bottom panels of the figure also show the flux map above 1 TeV and observation time within the HGPS region, respectively.

promising astrophysical sources that could possibly emit VHE gamma rays.

In this study, the HGPS data is analysed above 10 TeV using the high-energy analysis discussed in Chapter 4. A zenith angle restriction is applied to the dataset to take into account the performance of the developed analysis that is presented in Chapter 5. As demonstrated in Figures 5.2 and 5.4, the angular resolution and energy bias are significantly degraded for large event offsets at large zenith angles. According to Figure 5.2, the angular resolution above 10 TeV for events at 4° offset angle already exceeds 0.2° for zenith angles above 30°. For events at 3° offset angle, this effect becomes prominent at zenith angles above 50°. In addition, the energy threshold rises dramatically for the large zenith-offset angle bands. As seen in Figure 5.6, the energy threshold at 50° zenith angle is around 10 TeV for 4° event offset, while for events at 60° zenith angle, the threshold reaches 10 TeV

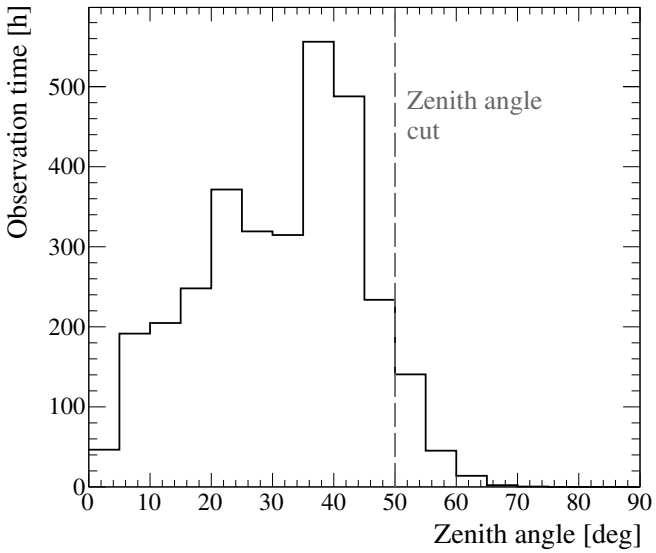

Figure 6.2: The distribution of observation time of the Galaxy plane performed by H.E.S.S. as a function of zenith angle. The grey dashed line shows the zenith angle cut applied during the run selection in this work; observations with zenith angles smaller than this cut are included in the analysis.

above an offset angle of 3°. Moreover, as discussed in Section 5.3, the zenith-dependent asymmetry of the system acceptance appears at large zenith angles, which may deteriorate the discovery potential of the analysis by introducing background systematics.

Therefore, considering all the above-mentioned facts, the observation zenith angle in the HGPS dataset is limited to 50° in this investigation. Figure 6.2 displays the zenith angle distribution of the HGPS data. While the maximum of the distribution, i.e. most of the data, is around 40° zenith angle, there is a rather small number of observations at zenith angles above 50°. This run selection cut rejects approximately 7% of the available survey dataset.

6.1.1 Ring background method and map production

The study presented in this chapter discusses the analysis results based on the significance and excess maps, the most commonly used maps in VHE gamma-ray astronomy. As mentioned in Section 5.3, these sky maps rely on background modelling in the FoV. One of the methods of background estimation, the Reflected-region background method, is already described in Section 5.2. However, this method is difficult to apply for the sky map production since it estimates the background level only at one offset angle (the same offset as the On-region) from the pointing position; this presents a problem since, during the sky map production, each point of the map acts as a test region and requires a background estimation. A more suitable method implemented within the HAP framework, the *Ring background method* [67], can estimate the background at any point of the FoV and, therefore, is very often used to build the sky maps.

The significance and excess maps, as well as other maps in H.E.S.S. analysis, are 2D histograms in celestial coordinates. The main steps of their production are:

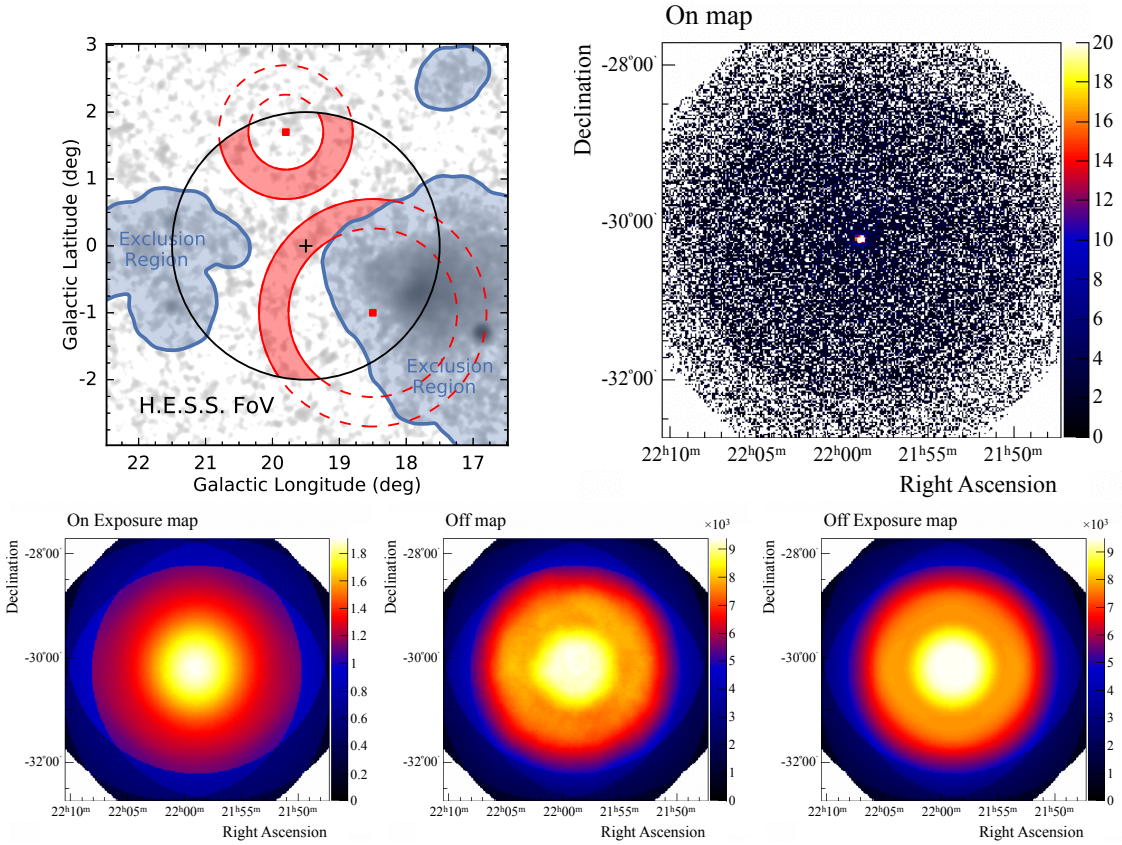

Figure 6.3: The ring background method [67] and its use for map production. The top left panel shows a schematic illustration of the adaptive ring [5]. Rings for two different positions (red points in the middle of the rings) are shown with red colour. The filled part of the ring denotes the region, which is used for the background estimation. Black cross and circle in the middle indicate the observation position and the analysis FoV, respectively. Blue regions are excluded regions. The top right panel and bottom row show the On, Off, On exposure and Off exposure maps, which are centred at the source position. The maps are built for the PKS 2155−304 observations above 1 TeV.

1. The *On* map is created. It contains all events in the FoV that pass the gamma-hadron separation cuts.

2. The *On exposure* map plays a role of the background model in the FoV. It is produced by rotating the acceptance curve around the observation position. As discussed in Section 5.3, the acceptance curve can be obtained from lookup tables or built from data itself. Due to the large exclusion regions in the Galactic plane and the generally limited statistics above 10 TeV, there might not be enough events to build the acceptance curve from data. Hence, the acceptance curves from lookup tables are used for the On exposure map production in this work. The On exposure map is normalised to have maximum of one and scaled with the ratio between the number of entries integrated over the On and On exposure maps. During this procedure, the regions around the gamma-ray sources and bright stars are excluded from the calculation, in order to estimate the level of background only and to avoid contamination with

signal counts in its estimates.

3. The *Off* and *Off exposure* map are produced by scanning the On and On exposure maps, respectively, with a ring. The ring is built around each point in the On (On exposure) map. The events inside the ring but outside the exclusion regions are integrated and filled into the corresponding bin in the Off (Off exposure) map. As mentioned above, the Galactic plane is a densely populated region and, hence, has many exclusion regions. If the ring size is constant, it can happen that the entire ring is located within an exclusion region, creating a hole in the Off (Off exposure) map. In order to avoid such a situation, the *Adaptive ring* method [78] can be used. In this method, the inner ring radius automatically increases if a large part of the ring overlaps with the exclusion region. The approach is schematically illustrated in the top left panel of Figure 6.3. It shows an example of the adaptive ring built for the two different positions in the FoV.

4. The number of excess counts in each bin of the corresponding map is computed in the same way as shown in Section 5.1.6 (Equation 5.2), where N_{On} and N_{Off} are the numbers of events in bin i of the On and Off map, respectively. The normalisation parameter α (more precisely α *map* in this case) is calculated as a ratio of the On exposure and Off exposure maps.

   Similarly, bin values for the significance map are calculated according to Equation 5.3. However, in the case of the significance map, the On and On exposure maps are correlated beforehand. This means that each bin i of the correlated map comprises a sum of the contents of the bins that fall within the *correlation radius* around this particular bin i. The typical correlation radii used for the Galactic survey analysis are 0.1°, 0.2° and 0.4°. In general, the correlation radii are chosen such that the analysis is sensitive to sources with different extensions. A smaller correlation radius better shows different morphological details, while a larger radius can reveal faint extended structures in the map.

An example of the On, Off, On exposure and Off exposure map at energies above 10 TeV are shown in Figure 6.3 for about 72 h of PKS 2155−304 [41] observations. Here, all maps are centred at the source position.

6.1.2 The Galactic plane above 10 TeV

This section discusses the Galactic survey above 10 TeV based on the general significance map of the region covered by the HGPS and analysed with different analysis setups. In this investigation, the HGPS dataset is analysed with the high-energy analysis, which is introduced in Chapter 4, and compared to the results obtained with the standard analysis. The high-energy analysis is performed for three different maximum event offset cuts: 2°, 3° and 4°. Here, the standard analysis is represented by the *std_zeta* configuration, i.e. the event direction is reconstructed using the geometry method and the background rejection is based on the machine learning technique (see Chapter 3). The value of the maximum event offset cut for the standard analysis is chosen to be at 2°, the same as in the original HGPS analysis [5].

Figures 6.4 - 6.8 show the significance maps of the Galactic plane region within the boundaries of the H.E.S.S. survey dataset, i.e. from 260° to 65° in Galactic longitude. Each figure

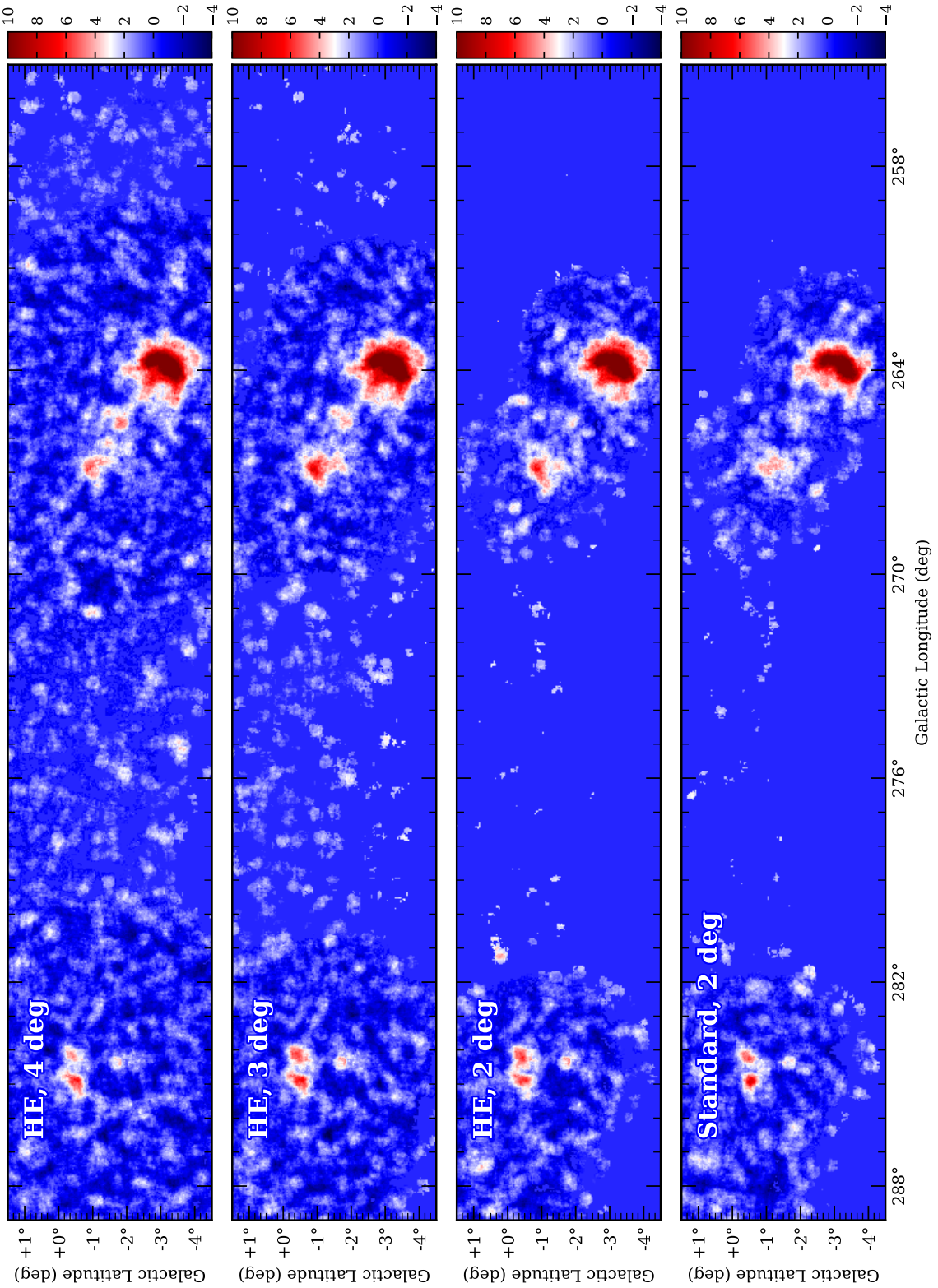

Figure 6.4: A comparison of the significance maps at energies above 10 TeV for the high-energy analysis with 2°, 3° and 4° maximum event offset and the standard analysis with 2° maximum event offset.

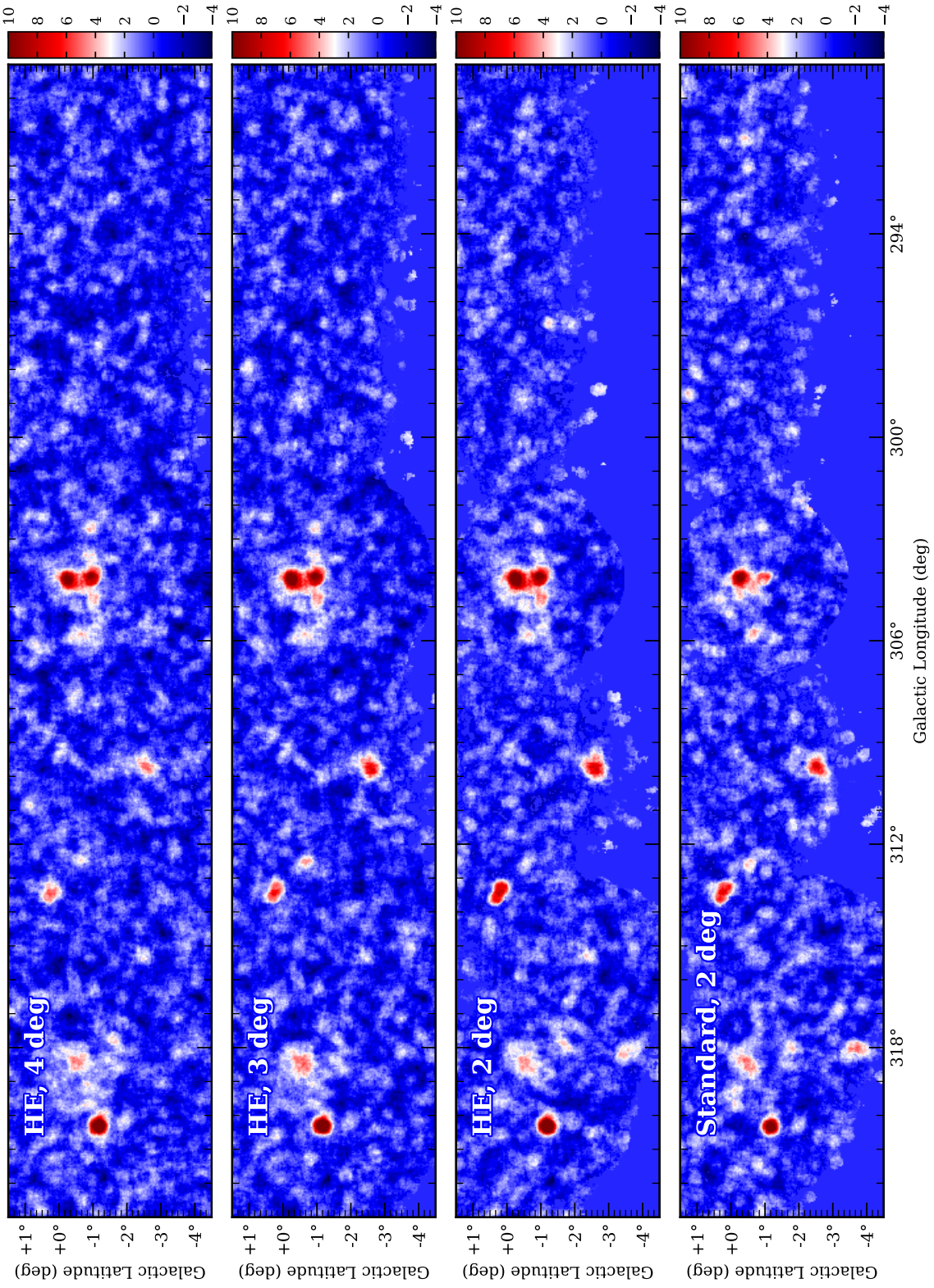

Figure 6.5: A comparison of the significance maps at energies above 10 TeV. Continuation of Figure 6.4.

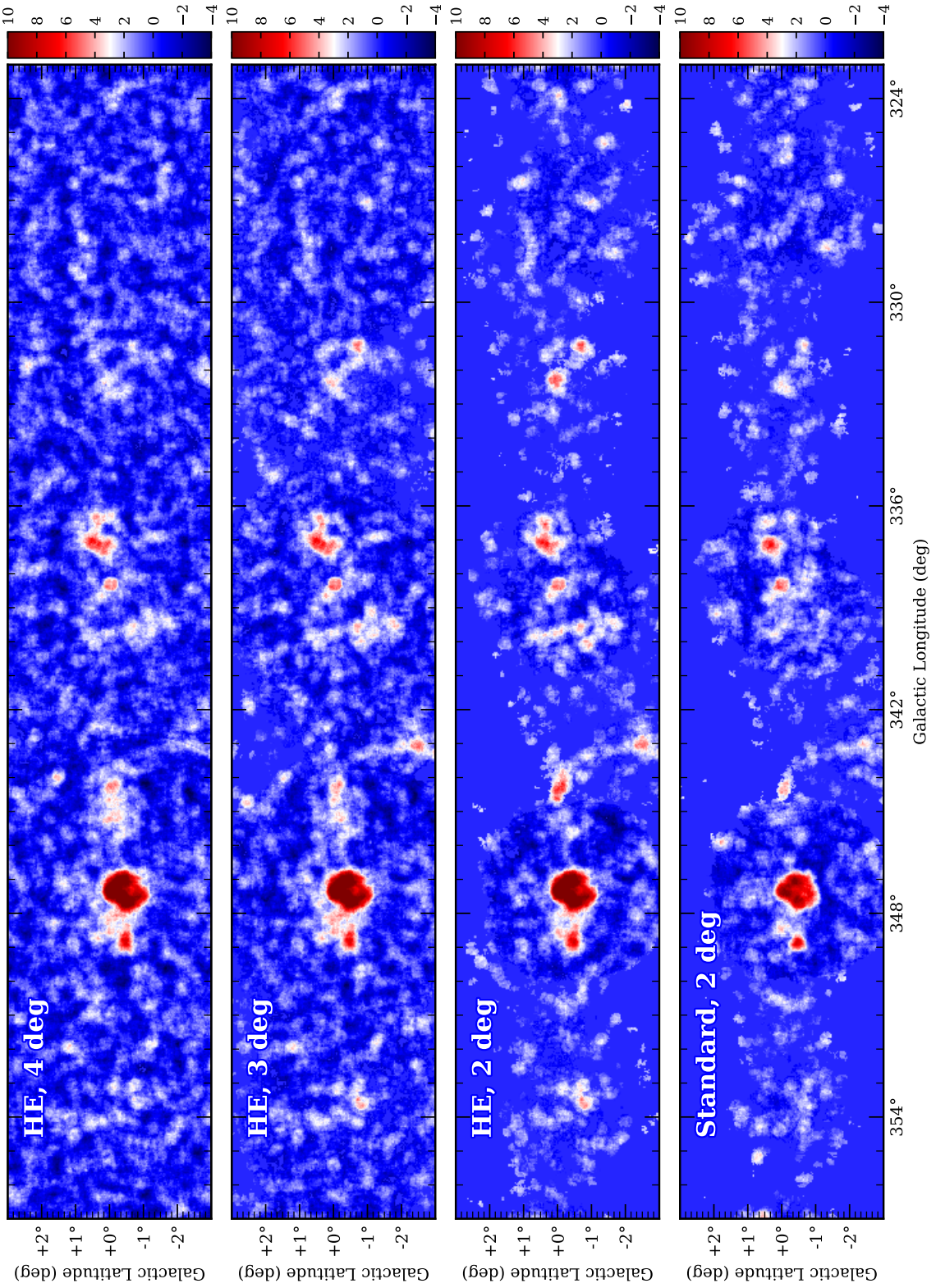

Figure 6.6: A comparison of the significance maps at energies above 10 TeV. Continuation of Figure 6.4.

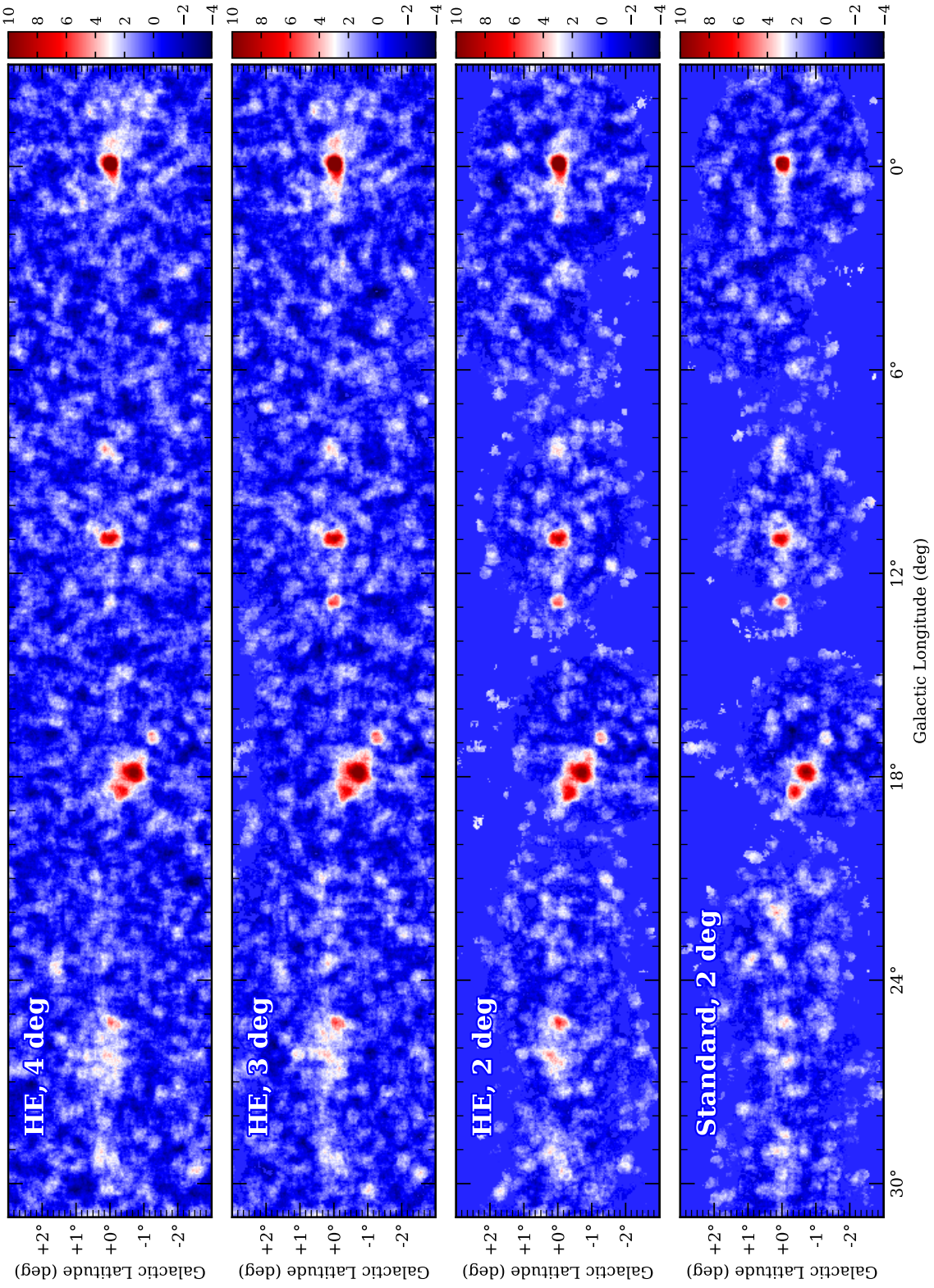

Figure 6.7: A comparison of the significance maps at energies above 10 TeV. Continuation of Figure 6.4.

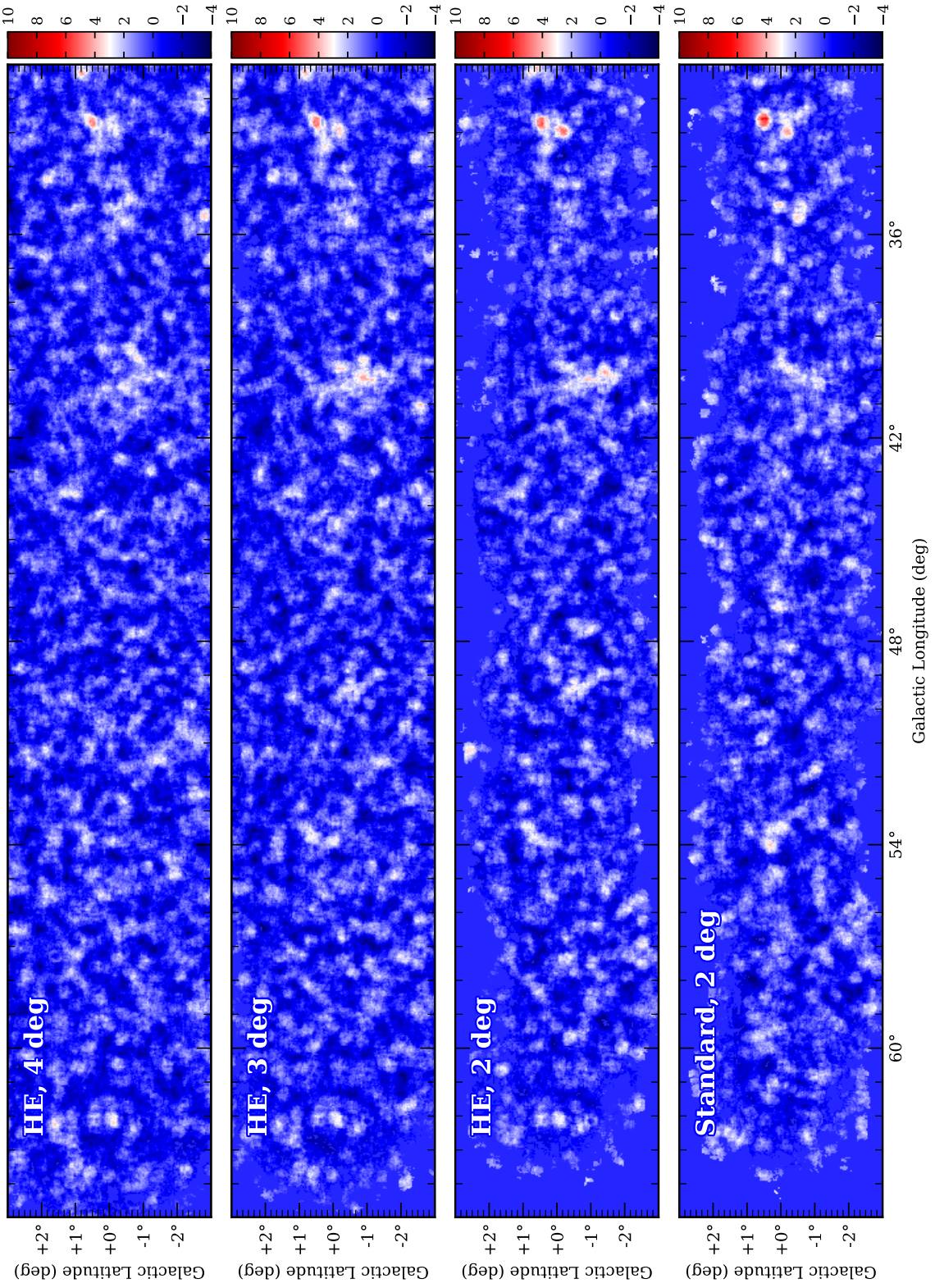

Figure 6.8: A comparison of the significance maps at energies above 10 TeV. Continuation of Figure 6.4.

compares the analysis results for the four above-mentioned analysis setups: the high-energy analysis with 2°, 3° and 4° maximum event offset and the standard analysis. Since most of the Galactic sources are slightly extended [5], all maps presented in these figures are produced with a correlation radius of 0.2°. This value is larger than the typical angular resolution of the high-energy analysis at different offset angles except for the largest offset angle bands, which have comparable angular resolution as discussed in Section 5.1.1 (see Figure 5.2).

As expected, both analyses with 2° maximum event offset result in lower statistics above 10 TeV than the analyses with larger maximum event offset due to the application of the respective offset angle restriction. This can be noticed in the significance maps shown in Figures 6.4 - 6.8. The significance maps that correspond to the analyses with 2° maximum event offset contain a lot of empty bins due to a lack of events for the significance calculation[2]. However, the coverage in the significance maps substantially rises as the maximum event offset increases thanks to the increase in exposure that comes from allowing for the contribution of observation runs with larger offset angles.

The colour bar on the plots is restricted to the range from -4 to $10\,\sigma$ in order to maintain consistency between all the significance maps. The white colour indicates the transition from a significance level of about 2 to $4\,\sigma$. Thus, the red colour with increasing intensity shows the regions in the map that contain promising hotspots up to firmly detected VHE gamma-ray sources above 10 TeV. In the majority of cases, the sources increase in significance when they are analysed with the high-energy analysis with 2° and 3° maximum event offset. However, there are regions where the standard analysis results in higher significances. Unsurprisingly, the high-energy analysis with 4° maximum event offset appears to be the least significant analysis shown here since at these largest offset angles, the background rate is rather high and the reconstruction accuracy is deteriorated. However, as discussed later in Section 6.2.2, which compares different analyses based on the analysis characteristics of particular sources, the analysis with 4° as well as 3° maximum event offset typically gains the highest number of excess counts, which is important for morphology studies and potentially for spectrum reconstruction.

Figure 6.9 displays 1D significance distributions obtained from the excluded significance map, which is the map where all known VHE gamma-ray sources and bright stars are excluded, computed with 0.2° correlation radius. The displayed distributions approximately follow the centred roughly around zero Gaussian with $\sigma = 1$, which shows that the significance outside the excluded regions, i.e. outside the regions with significant VHE gamma-ray emission from known sources, is consistent with the expected distribution from background. As expected, the analyses with low maximum event offset suffer from a lack of statistics, which is also seen in the significance maps in Figures 6.4 - 6.8. Because of this, the maps contain many upward fluctuations of the significance. Thus, the distribution of the excluded significance for these analyses is slightly shifted in the positive direction, as can be seen in the larger values of μ (a similar situation is also discussed in Section 5.3 regarding Figure 5.18). For the analyses that include large-offset events, the excluded significance distribution is centred around zero. Also, despite low statistics and a minor shift of the distribution for some analyses, σ of the distributions stays very close to one. Overall, one can conclude that the background is well normalised and background systematics are

[2]Normally, within the HAP framework, the significance calculation require at least 5 counts in the corresponding bin in both the On and Off maps.

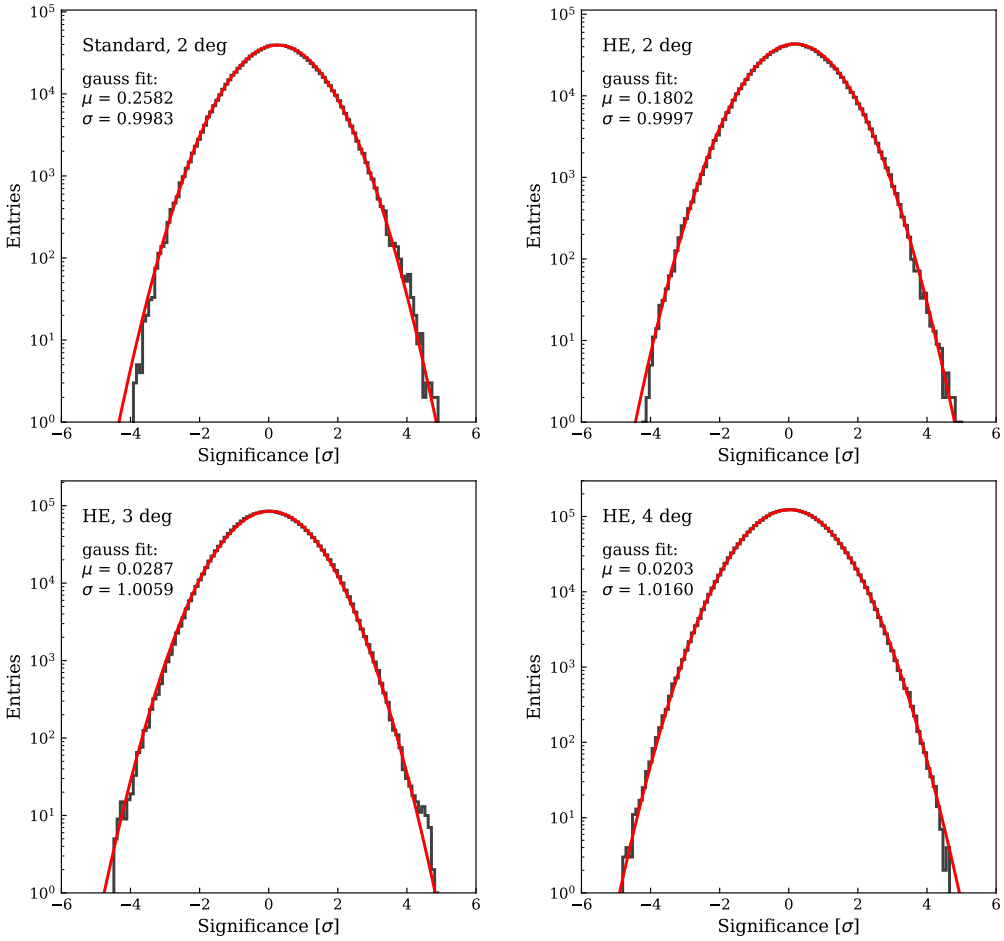

Figure 6.9: The comparison of the excluded significance distributions for the high-energy analysis with 2°, 3° and 4° maximum event offset and the standard analysis with 2° maximum event offset for energies above 10 TeV. The black colour shows the data events observed in the HGPS outside the exclusion regions, while the red colour indicates the Gaussian fit. The correlation radius of the excluded significance map is 0.2°.

under control.

For the 0.1° correlation radius, the situation is somewhat worse. The corresponding 1D distributions of the excluded significance map are displayed in Appendix B.1 in Figure B.1. The width of all distributions is smaller than one and all of them experience a significant shift towards positive values. Nevertheless, such behaviour is expected since the significance maps are affected more by small event statistics when a smaller correlation radius is used.

The hotspot near PSR J1413−6205

A closer examination of the 1D distributions of the excluded significance map reveals a perceptible excess above 4 σ in the distribution obtained for the high-energy analysis with 3° maximum event offset. An investigation of the corresponding excluded significance map shows a cluster of bins with relatively high significance around Galactic longitude $l = 312.5°$

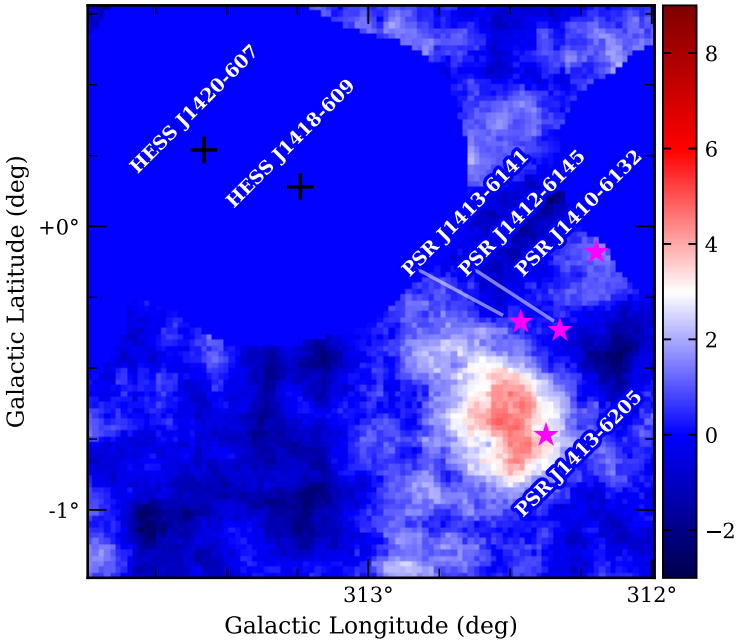

Figure 6.10: The excluded significance map of the hotspot region at energies above 10 TeV. The map is built using the high-energy analysis with 3° maximum event offset. The correlation radius applied for the map production is 0.2°. Magenta stars mark the positions of energetic pulsars in the vicinity of the hotspot: PSR J1413−6205, PSR J1412−6145, PSR J1410−6132 and PSR J1413−6141 [156]. The black crosses show the location of two nearby VHE gamma-ray sources, specifically HESS J1418−609 and HESS J1420−607, which were excluded from the map [5].

and Galactic latitude $b = -0.75°$. For the other analysis configurations, the significance in the same region is lower and barely reaches $4\,\sigma$. Such behaviour is not surprising. The analyses with 2° maximum event offset might have too low statistics in this region. Allowing for a larger maximum event offset, the exposure in the region increases. This fact can also be seen in Figure B.3 in Appendix B.2 that shows the expected gamma-ray map, which in some sense is the measure of exposure of the sky. According to this map, the high-energy analysis with 3° maximum event offset has about double the exposure around the PSR J1413−6205 position than the analyses with 2° maximum event offset. Thus, the exposure increase can result in improved event statistics above 10 TeV leading to the higher significance of the hotspot of interest. However, despite the fact that the largest exposure is obtained in the case of the analysis with 4° maximum event offset, this analysis configuration does not show the highest significance of the hotspot, which can be explained by a higher background level in the largest offset bands as well as degradation of the reconstruction accuracy.

The excluded significance map of the region with the revealed hotspot is shown in Figure 6.10. The hotspot is located in the Kookaburra region close to two VHE gamma-ray sources, HESS J1418−609 and HESS J1420−607 [43]. According to the ATNF catalogue of radio pulsars [156], in the vicinity of the hotspot, there are four energetic pulsars: PSR J1413−6205, PSR J1412−6145, PSR J1410−6132 and PSR J1413−6141. Among them, the position of the pulsar PSR J1413−6205 is the closest to the revealed hotspot.

PSR J1413−6205 is a middle-aged pulsar at a distance of 2.15 kpc with a characteristic age $\tau_c = 62.8\,\mathrm{kyr}$ and spin-down energy loss rate $\dot{E} = 8.3 \cdot 10^{35}\,\mathrm{erg\,s^{-1}}$ [156]. The *Fermi*-LAT measured gamma-ray pulsations from PSR J1413−6205 [174], which are also confirmed to be detectable above 25 GeV [31]. The pulsar is also coincident with the AGILE source 1AGL J1412−6149 [171] and with the source EGR J1414−6244 in the revisited EGRET catalogue [79]. However, besides these associations, PSR J1413−6205 does not have counterparts at other wavelengths so far. The region was briefly observed by *Swift*-XRT, but no significant X-ray emission was identified [174]. Nevertheless, despite a lack of multi-wavelength counterparts, which could be a hint of a pulsar wind nebula (PWN) presence around the pulsar, PSR J1413−6205 has a sufficient spin-down energy loss rate to power a PWN. Thus, the hotspot observed in this study could be an indication of a putative TeV PWN associated with this pulsar.

In addition, the H.E.S.S. data taken in this region was recently re-analysed using a different background estimation method[3] that is more sensitive to weak, very extended sources. As a result, extended emission in the vicinity of PSR J1413−6205 has been revealed above 1 TeV and 5 TeV, whose extent decreases and moves towards the pulsar position as energy increases [109]. These findings are well in agreement with the hotspot seen in this work. Currently, additional observations of the region around PSR J1413−6205 are being carried out with the H.E.S.S. telescopes, which would allow for a more detailed morphological study of the revealed emission, thereby enabling a better understanding of the origin of this emission.

6.2 Properties of the HGPS sources above 10 TeV

The original HGPS catalogue contains 78 VHE gamma-ray sources [5]. The current section of this study discusses the sources within this catalogue that are seen above 10 TeV, and a search for new sources in the Galactic plane is outside of the scope of this work. In particular, apart from a potential new source revealed during the background systematics study discussed in the previous section, the significance map outside the exclusion regions is consistent with there being no new sources above 10 TeV. And, in order to be able to look for new sources inside the exclusion regions, each known source should first be properly modelled and extracted from the significance map. Furthermore, each bin in the significance map acts as a test region. Since the map contains a large number of bins, there is an increased probability to find a highly significant random bin that appears due to random fluctuations of the background. Thus, the measured significance should be corrected for the *trials factor* [118] of the analysis, especially while running a blind search for new sources in the entire HGPS region. If it is required that the source candidate should reach a *post-trial* significance of at least $4\,\sigma$, i.e. the significance after trial factor correction, the *pre-trial* (measured) significance should be at least more than $6\,\sigma$[4] [47]. Due to steeply falling source spectra, there is a very small chance to find a source with such a high significance level that was not previously detected in the HGPS at lower energies.

Since this work primarily searches for emission above 10 TeV from the sources that have already been detected by the H.E.S.S. experiment at lower energies, it is decided to consider

[3] More specifically, the performed analysis uses the *Field-of-View background method* [67].

[4] This value also depends on the number of bins in the map.

the source as detected above 10 TeV if it has a significance of at least $3\,\sigma$ for at least two analysis setups. Hence, the trials factor correction is not taken into account[5].

6.2.1 Identification of sources above 10 TeV in the HGPS

The source candidates for the study are preselected based on the significance maps displayed in Figures 6.4 - 6.8. As discussed above, a source is selected for further analysis if the region around its catalogue position contains bins with significances of at least $3\,\sigma$. This resulted in 42 preselected sources (regions of interest) out of 78 sources listed in the HGPS catalogue. In order to estimate the significance of the source and other analysis characteristics such as excess and signal-to-background ratio, a test region for each source was defined. The peak and extent of the emission above 10 TeV may not be the same as they are for the emission at lower energies. Therefore, the test regions in this work are not entirely based on the source positions and extensions declared in the HGPS catalogue because they are estimated from the source modelling in a wider energy range, which is dominated by the low-energy emission. The test-region determination is illustrated in Figure 6.11 and is done following this procedure:

- Test-region centre. The location of the peak of the more than 10 TeV emission (centre of the test region) is estimated as the average position between the three bins with the highest significances within the region of interest around the catalogue source position. Typically the size of this region of interest is chosen to be about 1.5 - 2 times larger than the source extension. Since the significance distribution in the map depends on the correlation radius used to build it, the estimated test region position will be different for maps with different correlation radii. Therefore, the test region position is evaluated for three correlation radii, 0.1°, 0.2° and 0.4°, and is chosen to be the one that better fits each specific source. Thus, the results obtained with 0.1° correlation radius are chosen for point-like sources or sources with a very small extension. In contrast, for the extended sources and sources with complex morphology, 0.2° or 0.4° correlation radius maps give better results.

- Test-region size. The size of the test regions is estimated using the θ^2 distribution. The description of the θ^2 distribution is discussed in Section 5.2.2 and an example can be seen in the right panel of Figure 6.11. Here, the θ^2 distribution is built using the bin contents of the excess map and their distances to the position calculated in the previous step. The radius of the source test region is then defined as the distance where the θ^2 distribution drops below 10% of its maximum. The minimum size of the test region is set to 0.2°, which is slightly larger than the angular resolution for most offset bands (see Figure 5.2). If the test region radius estimated from the θ^2 distribution is smaller than this minimum size, it is automatically set to 0.2°.

Since this investigation considers four different analysis configurations, the test regions are determined independently for each analysis. The test regions for the majority of sources which are studied here are defined using the procedure described above. However, there are a few sources for which the application of such an approach would be difficult. For example,

[5]However, since this study considers known sources, the trials factor is already implicitly taken into account.

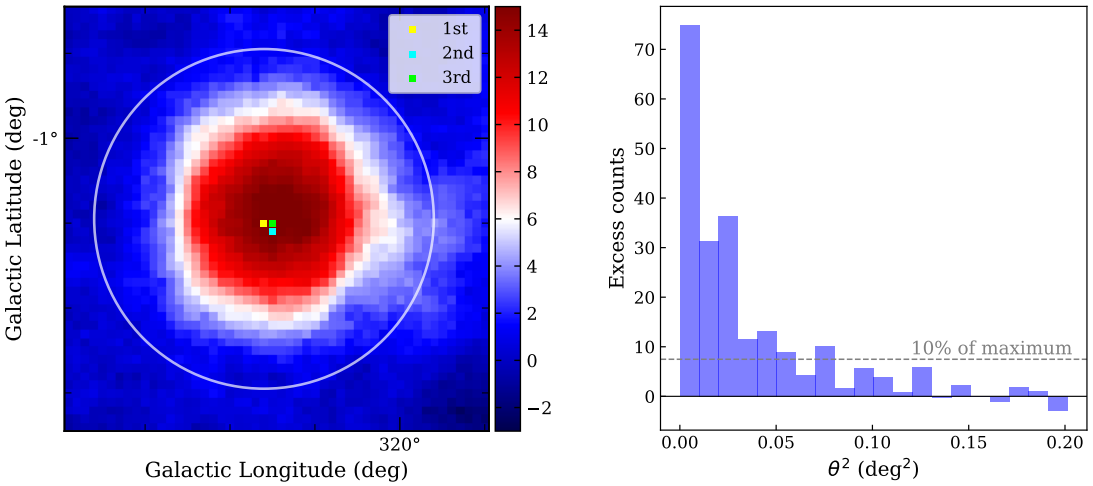

Figure 6.11: An example of the determination of the test-region size and position used in this work. Both panels display the procedure using the HESS J1514−591 data above 10 TeV. The left panel shows the significance map indicating the three brightest pixels found within the region of interest, which is marked by the white circle. These pixels are used to determine the centre position of the test-region for the source. The right panel shows the θ^2 distribution of the excess counts from the region of interest displayed on the left side of this figure.

HESS J1418−609 and HESS J1420−607 [43] are located very close to each other and, in order to avoid the overlap of their test regions, the region positions are set to the values reported in the HGPS catalogue [5] and the sizes of the regions are decreased below the minimum value defined above. The same treatment takes place regarding another two very closely located sources, HESS J1640−465 [22] and HESS J1641−463 [21]. HESS J1745−290 (Galactic Centre source) is a very well known point-like source [25]. Thus, its position is also taken from the HGPS catalogue and the size of the test region is set to the minimum value of 0.2°.

The other exceptions are constituted by the most extended sources within the HGPS, namely, Vela X (HESS J0835−455) [45] and Vela Junior (HESS J0852−463) [39], HESS J1713−397 [38], HESS J1646−458 [19] and HESS J1908+063 [51]. The positions of the test regions for the first three sources are taken from the HGPS catalogue [5]. HESS J1646−458 and HESS J1908+063 are very complex regions and may even consist of multiple sources. This might be a reason for the mismatch between the positions of these sources stated in the HGPS catalogue and dedicated investigations performed earlier [19, 51]. The source positions obtained in [19] and [51] better fit the location of the emission at energies above 10 TeV and are used to define the test regions in this work. The radii of the test regions for these five sources are estimated using their θ^2 distributions. The resulting test region positions for all 42 preselected sources are listed in Tables B.1 - B.2 in Appendix B.3 for all four analysis configurations considered in this work. The corresponding extension radii of the test regions can be found in the second column in Tables B.3 - B.10.

6.2.2 Analysis characteristics of sources above 10 TeV

The test regions defined above are used to calculate the significance, excess, background level and signal-to-background ratio for 42 preselected sources as described below:

- The excess map is one of the maps resulting from the analysis pipeline. The excess values in each bin of the map are calculated using Equation 5.2. The general steps of this map production are discussed in Section 6.1.1. For the excess estimation inside each test region, the excess map is simply integrated within the limits of the corresponding test area.
- Similarly to the excess map, the background map is also provided by the analysis pipeline. It is obtained by multiplying the α and Off maps (see Section 6.1.1). The background level for the test regions is also calculated by integrating the corresponding map within the defined test-region boundaries.
- The signal-to-background ratio for each region is obtained by dividing the excess by the background values that are discussed above.
- Although the significance map is also available from the analysis pipeline, it cannot be simply integrated as is done in the case of the excess or background map. Thus, the significance value for each region is calculated using Equation 5.3, where N_{On} and N_{Off} are the integrals of the On and Off maps within the test region. The parameter α is obtained by dividing the On exposure by Off exposure values integrated inside the test region in the corresponding maps.

Figures 6.12 - 6.15 show the analysis characteristics, which are discussed above, for the 42 sources of interest studied here. Since this work considers four different analysis configurations, the plots compare the results obtained from each of them. To make the comparison easier, the size of the marker reflects the analysis performance for each particular source: the analysis configuration that obtained the highest significance in the source test region is presented with the larger marker in all four figures, and the analysis with the lowest source significance has the smallest marker. The analysis with the highest significance is also indicated by the filled markers. In addition, different analysis quantities – such as the number of On and Off events, α parameter, as well as excess, background, significance and signal-to-background ratio, which are extracted from all test regions – are summarised in Tables B.3 - B.10 in Appendix B.3.

As seen from the significance behaviour shown in Figure 6.12, 20 source regions, nearly half of the preselected sources, gave the highest significance when analysed with the high-energy analysis with 2° maximum event offset. The second-best result is obtained by the high-energy analysis with 3° maximum events offset, for which 13 sources have the highest significance. Only two sources achieved the best performance in the analysis with 4° maximum event offset. Finally, 7 out of 42 preselected sources obtained the highest significance values using the standard analysis. However, not all preselected sources fulfil the requirement of the more than $3\,\sigma$ significance in at least two different analysis configurations. There are two sources, HESS J1641−463 and HESS J1747−281, which exceed the $3\,\sigma$ threshold only once. This results in *40 sources being detected at more than 10 TeV energies with significances above $3\,\sigma$ for at least two analysis configurations.* This constitutes more

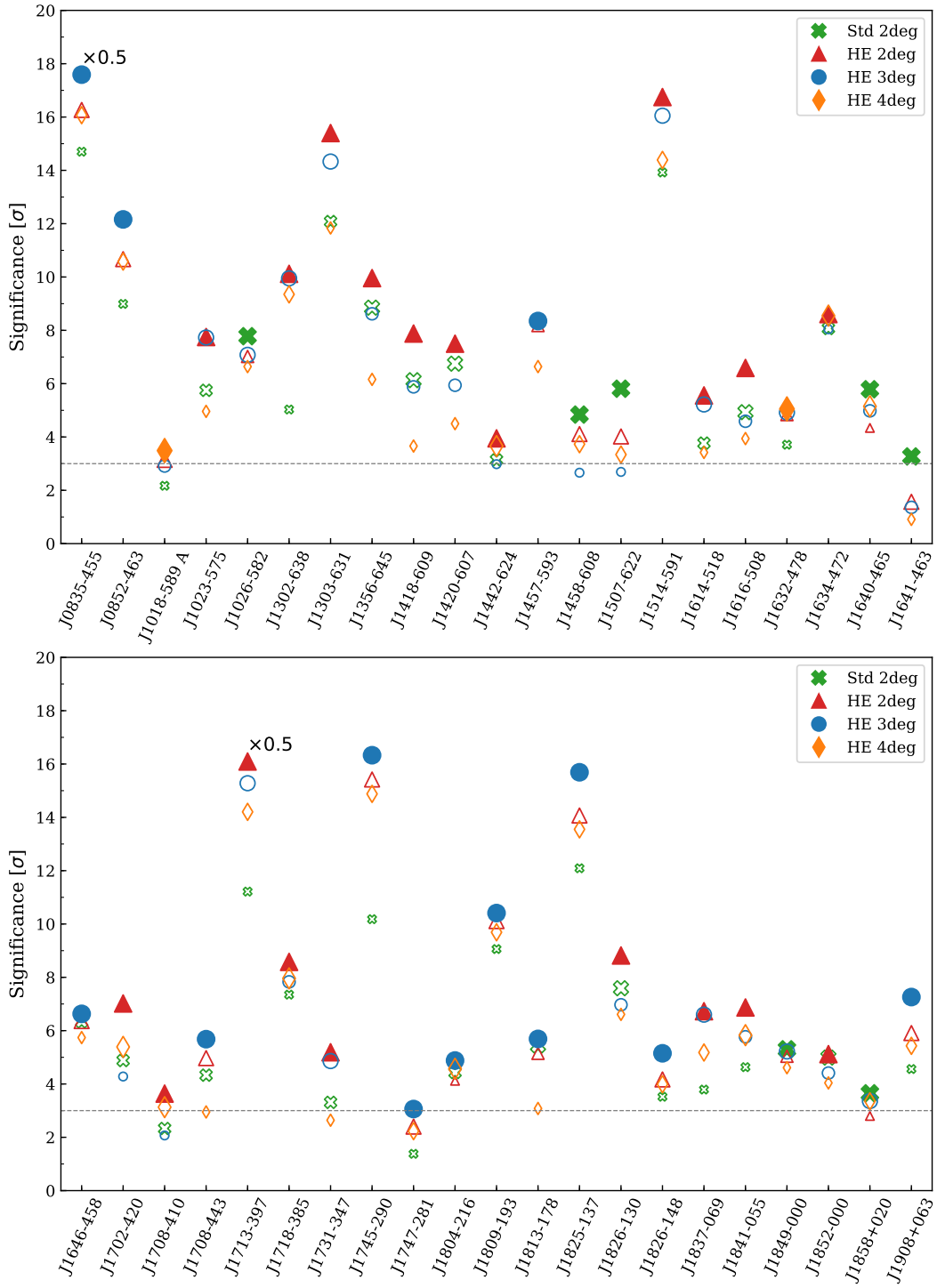

Figure 6.12: The comparison of the source significance at energies above 10 TeV. The results are shown for the four analysis setups considered in this work. The larger marker sizes indicate the analysis with larger significance gain, and filled markers denote the analysis with the largest significance gain. The grey dashed line marks the $3\,\sigma$ threshold value. The significances of HESS J0835−455 and HESS J1713−397 are divided by 2 for visualisation purposes.

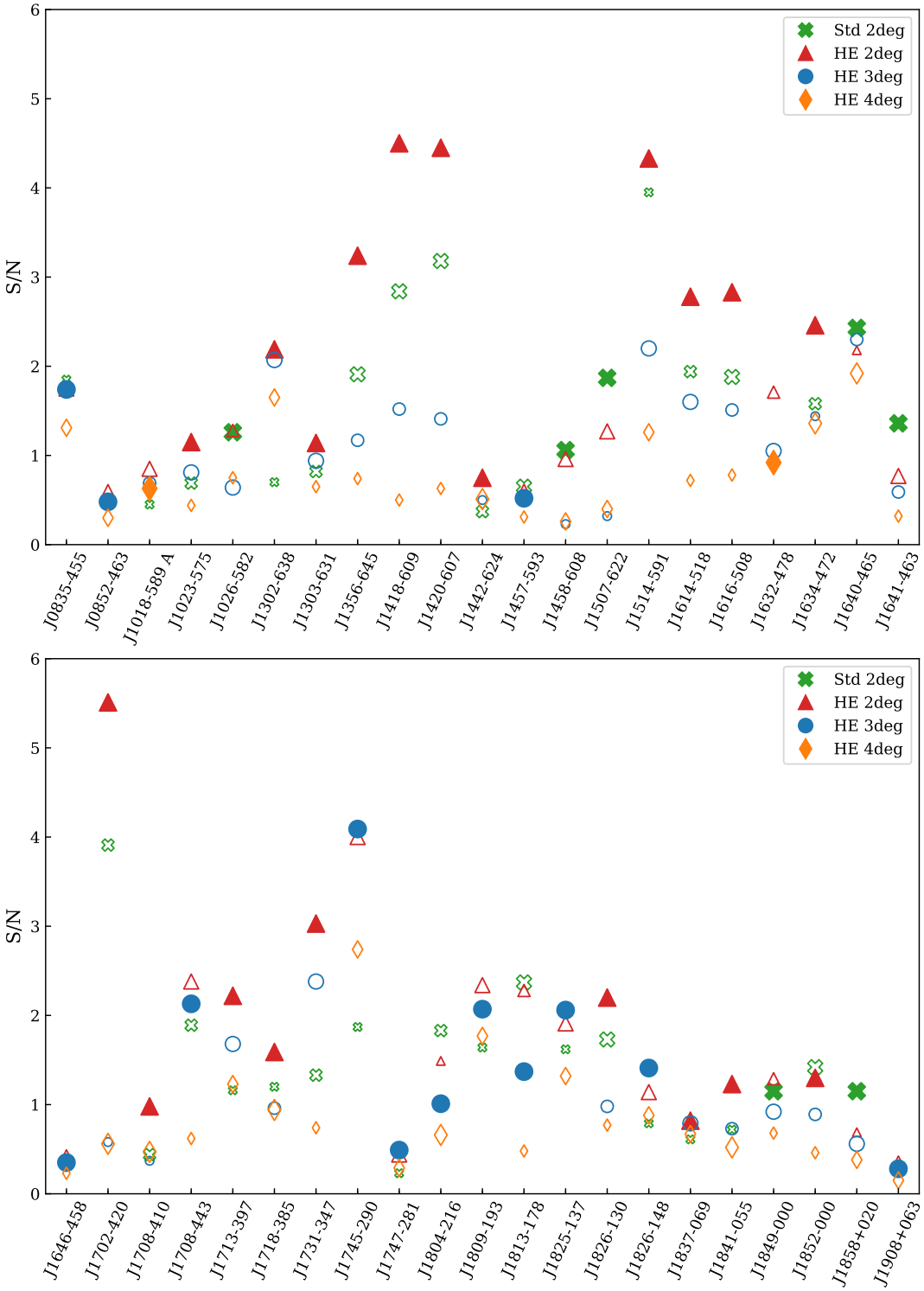

Figure 6.13: The comparison of the signal-to-background ratio at energies above 10 TeV for 42 preselected sources. The results are shown for the four analysis setups considered in this work. The larger marker sizes (filled markers) indicate the analysis with larger (the largest) significance gain as presented in Figure 6.12.

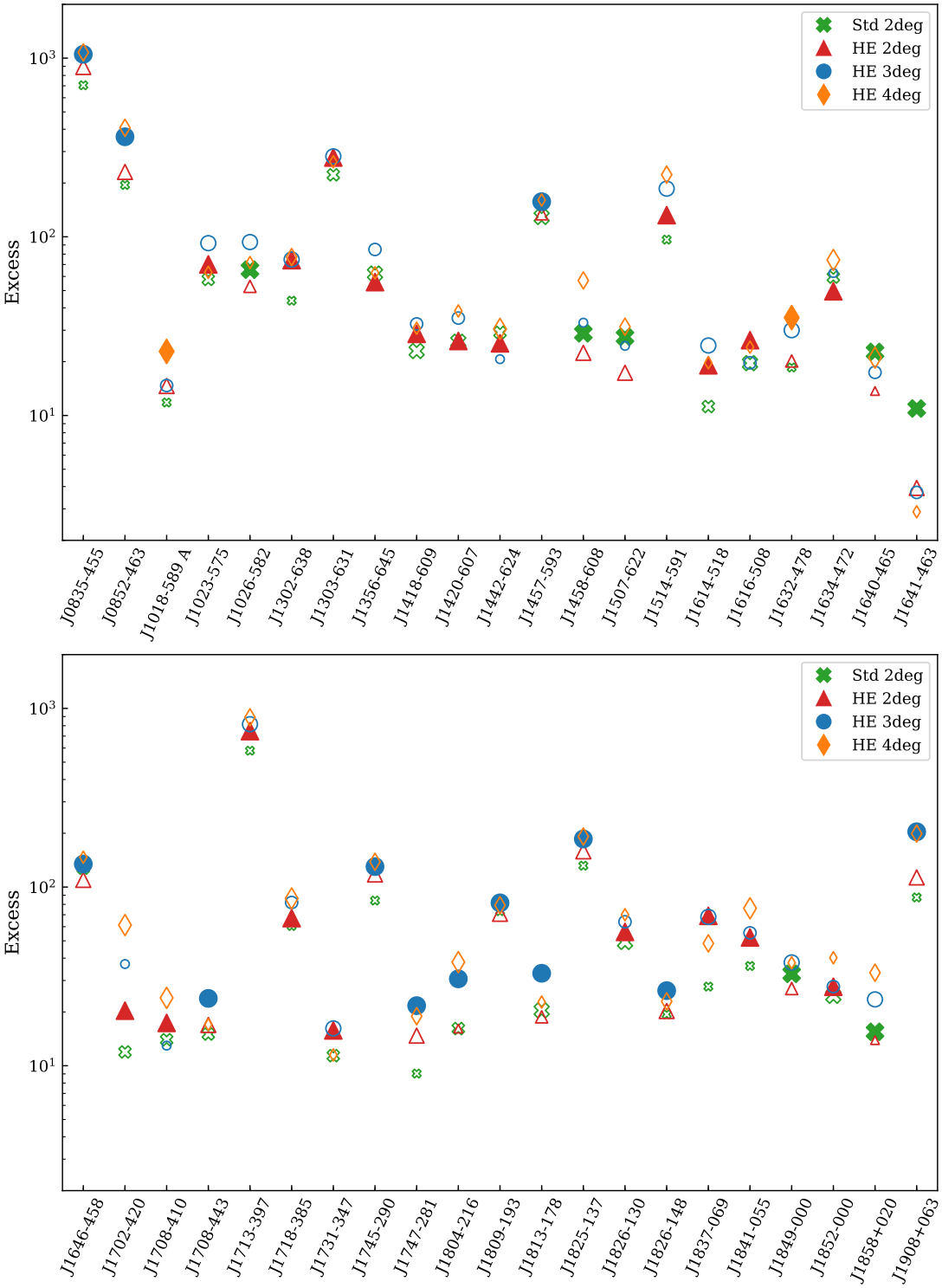

Figure 6.14: The comparison of the number of excess events at energies above 10 TeV for 42 preselected sources. The results are shown for the four analysis setups considered in this work. The larger marker sizes (filled markers) indicate the analysis with larger (the largest) significance gain as presented in Figure 6.12.

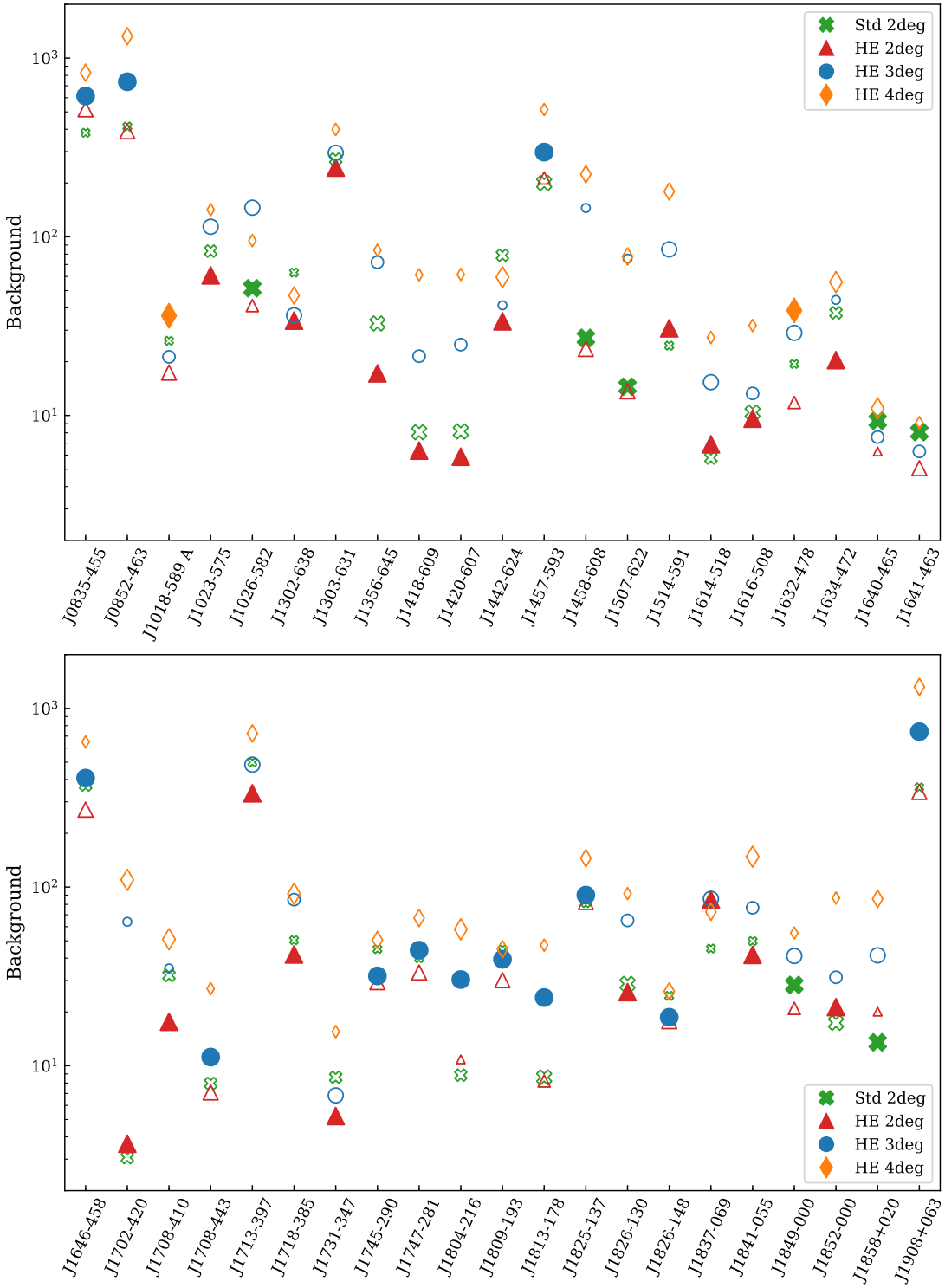

Figure 6.15: The comparison of the number of background events at energies above 10 TeV for 42 preselected sources. The results are shown for the four analysis setups considered in this work. The larger marker sizes (filled markers) indicate the analysis with larger (the largest) significance gain as presented in Figure 6.12.

than half of the sources that are contained in the HGPS catalogue [5]. Figures 6.16 - 6.23 show the significance map of the Galactic plane, where these 40 sources are marked. For a better understanding of the global picture, in parallel to the more than 10 TeV Galactic plane map, the plots display the map of the original HGPS catalogue [5] and denotes 78 Galactic sources detected in a wide energy range as well as their plausible multi-wavelength associations.

Regarding the other quantities presented in Figures 6.12 - 6.15, the general trend shows that, in most cases, the high-energy analyses with 4° and 3° maximum event offset gain the largest number of excess counts. However, at the same time, they also have the highest background levels. In the end, these two factors result in lower signal-to-background ratios in comparison to the two analyses with 2° maximum event offset, which in turn have a lower number of excess and background events. Such behaviour is expected since the analysis performance deteriorates as the event offset increases, as discussed in Chapter 5 (see for example, Section 5.1.6). Nevertheless, for strong sources, which are anyway detected at a high significance level, it is important to gain as many excess events as possible, since they are a substantial component of the morphology and spectra studies.

The highest signal-to-background ratio values are typically reached using the high-energy analysis with 2° maximum event offset. In comparison to the standard analysis, this typically results in higher excess values and lower background levels. However, it should be noted that the test regions of the sources are defined for each analysis configuration individually. This means that the same source may have different test region sizes considered in the different analyses. This can have an impact on all quantities discussed here, especially on the number of background events accumulated within the test region.

Figure 6.24 displays the spectral properties of the 78 sources in the HGPS catalogue and which of these sources are detected above 10 TeV in this work. Since the spectral analysis is not a part of this investigation, the characteristics of the source spectra for the plot are taken from the HGPS catalogue [5]. In general, this plot shows that weak sources with soft spectra are not detected at more than 10 TeV energies, while strong, hard sources typically are detected. However, this plot does not contain information about the source exposure. Thus, a weak, steep source can be measured above 10 TeV if it has a sufficient amount of observations. On the other hand, if the source region was only sparsely observed, this might result in a non-detection even for a strong source. In addition, the presence of a cutoff in the source spectrum, which is also not reflected by this plot, can result in a non-detection of a given source.

For the sources detected above 10 TeV, the figure indicates the analysis setup with which each particular source reaches the highest significance value. As seen from the plot, the high-energy analyses with 2° and 3° maximum event offsets perform best across a wide range of intrinsic source fluxes and spectral indices. The standard analysis shows the best results for the sources with a rather hard index and moderate flux level. However, it is difficult to speculate whether distinct types of sources would prefer a specific analysis configuration.

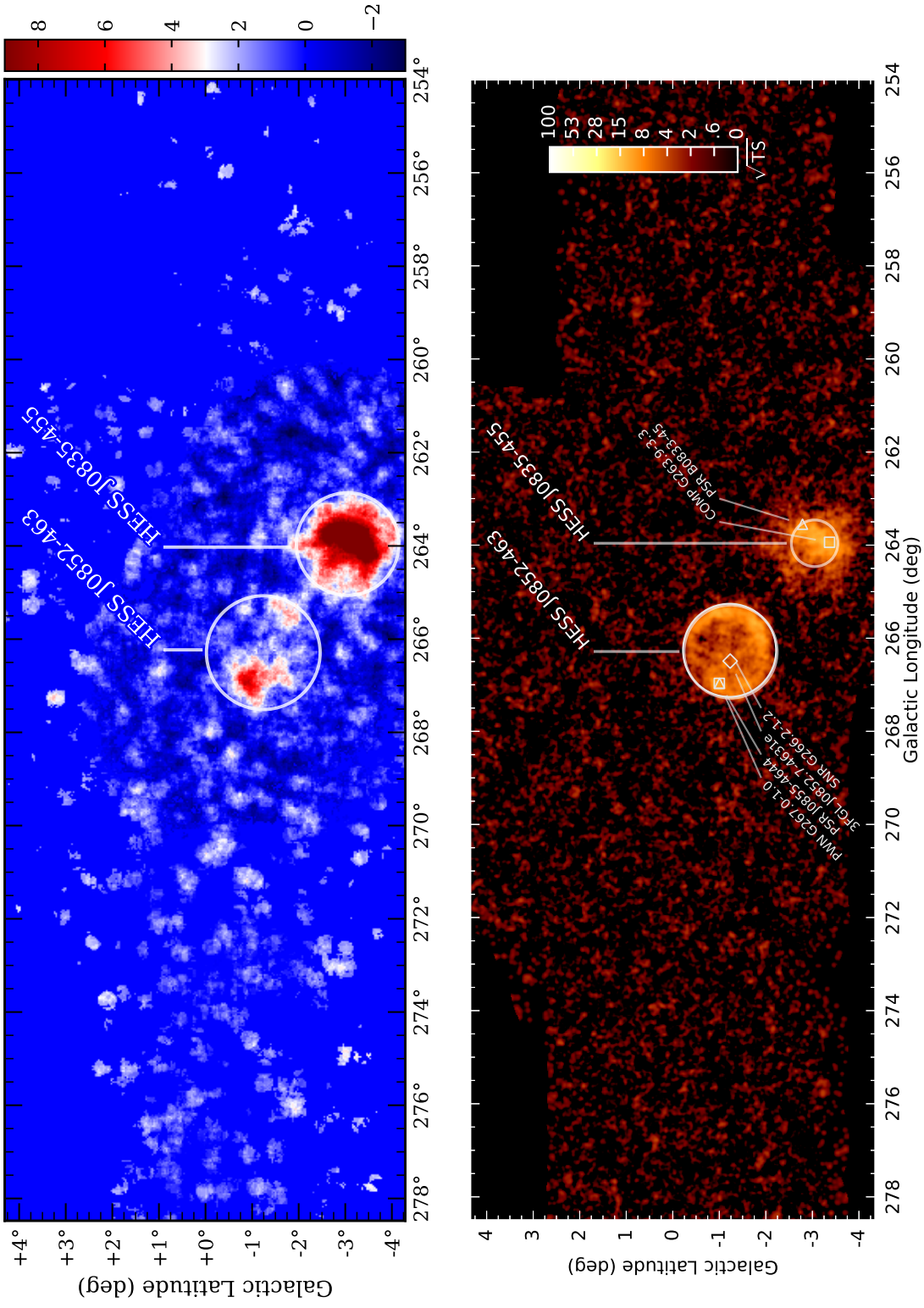

Figure 6.16: The VHE gamma-ray sources above 10 TeV (left panel) and comparison to the HGPS catalogue (right panel) [5]. The background image in the left panel is the significance map produced using high-energy analysis with 3° maximum event offset (0.2° correlation radius).

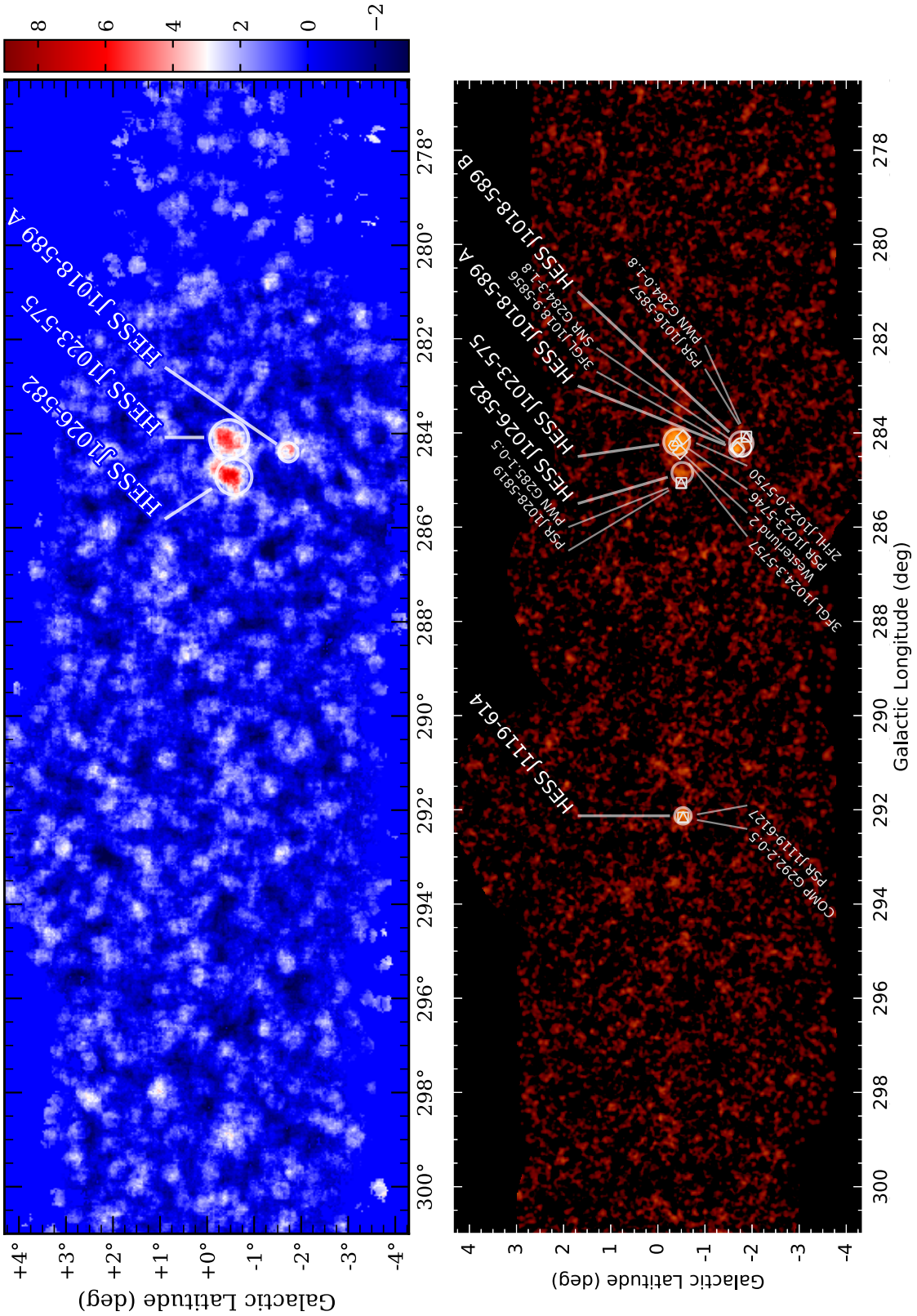

Figure 6.17: The VHE gamma-ray sources above 10 TeV (left panel) and comparison to the HGPS catalogue (right panel) [5]. Continuation of Figure 6.16.

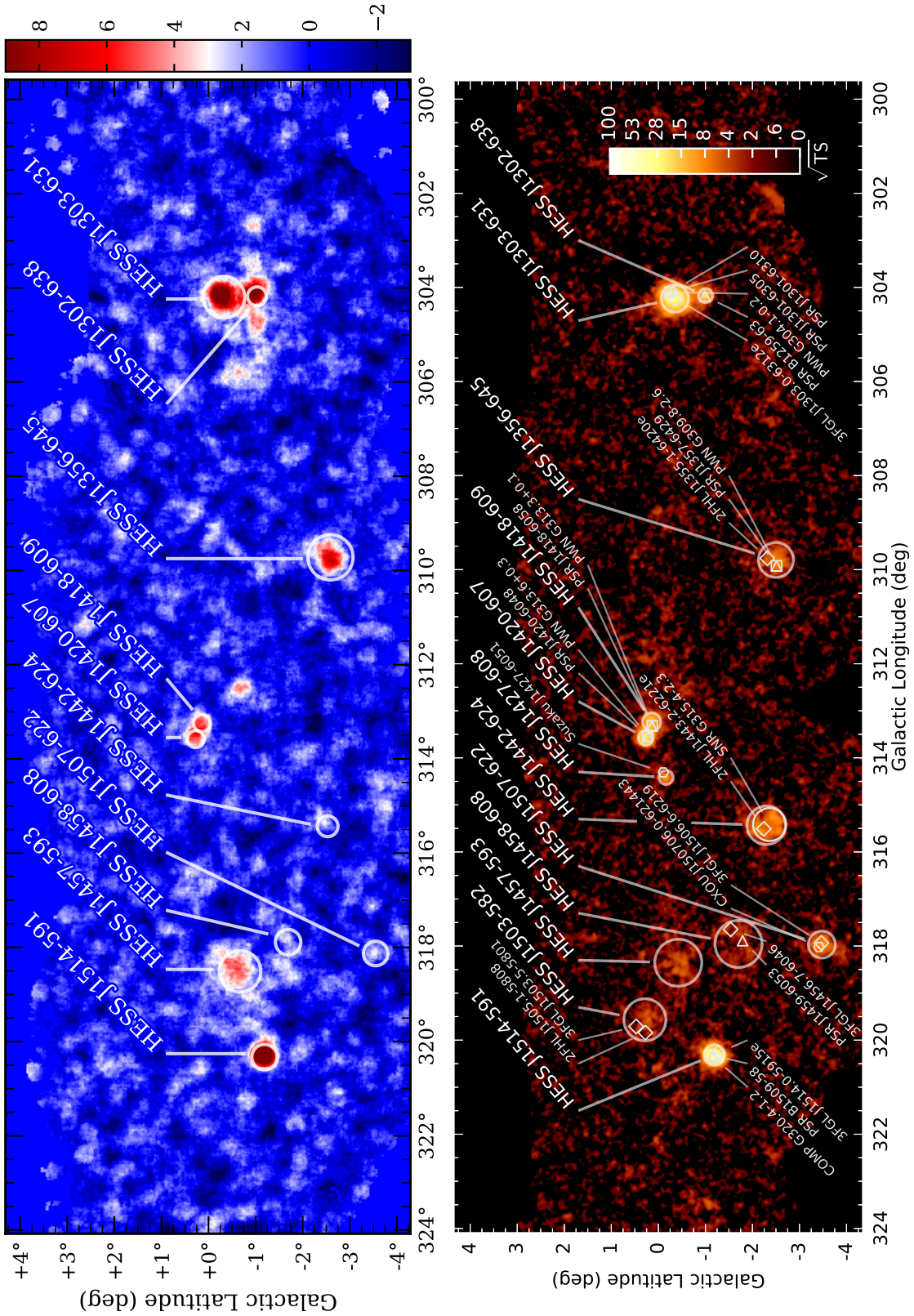

Figure 6.18: The VHE gamma-ray sources above 10 TeV (left panel) and comparison to the HGPS catalogue (right panel) [5]. Continuation of Figure 6.16.

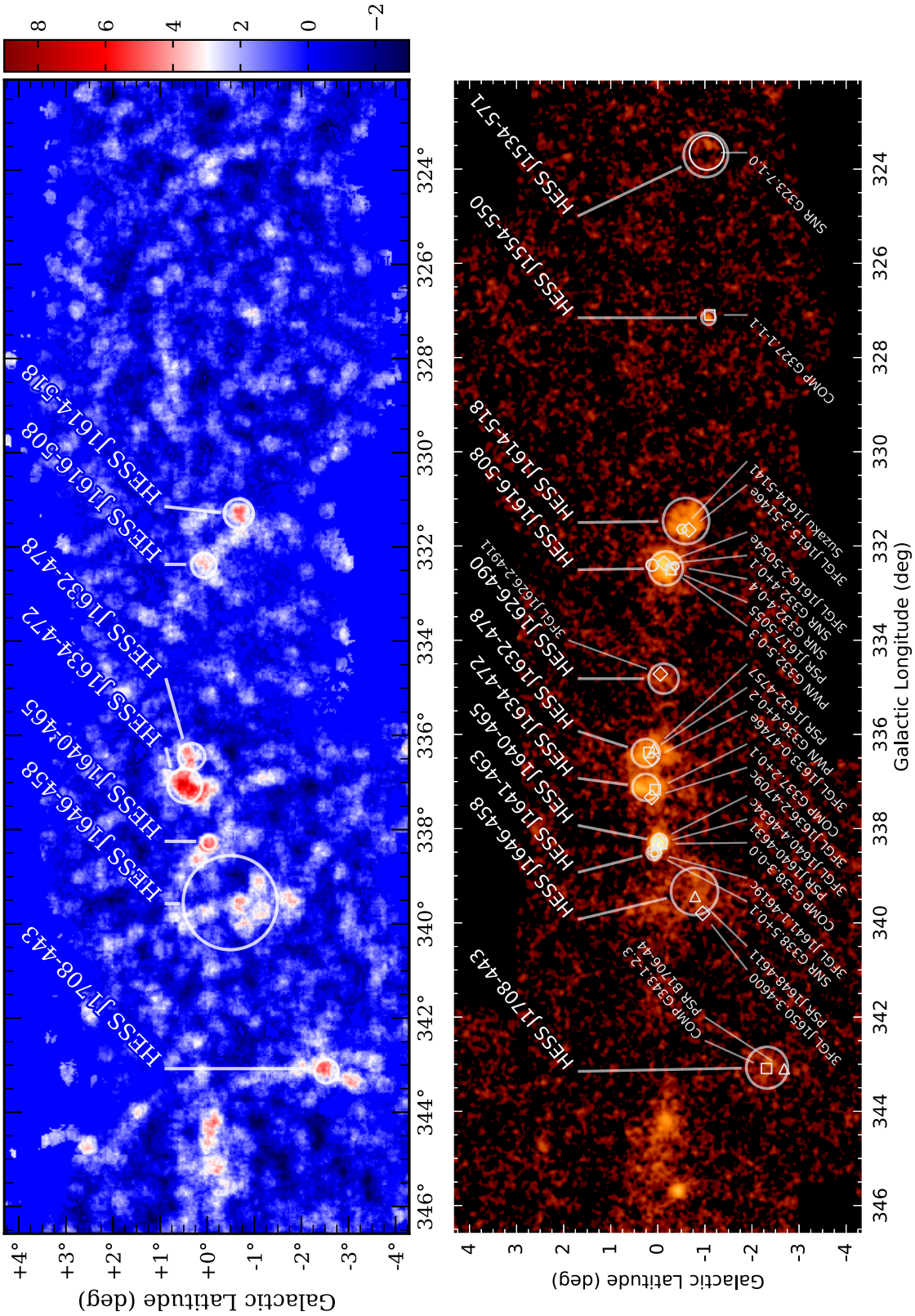

Figure 6.19: The VHE gamma-ray sources above 10 TeV (left panel) and comparison to the HGPS catalogue (right panel) [5]. Continuation of Figure 6.16.

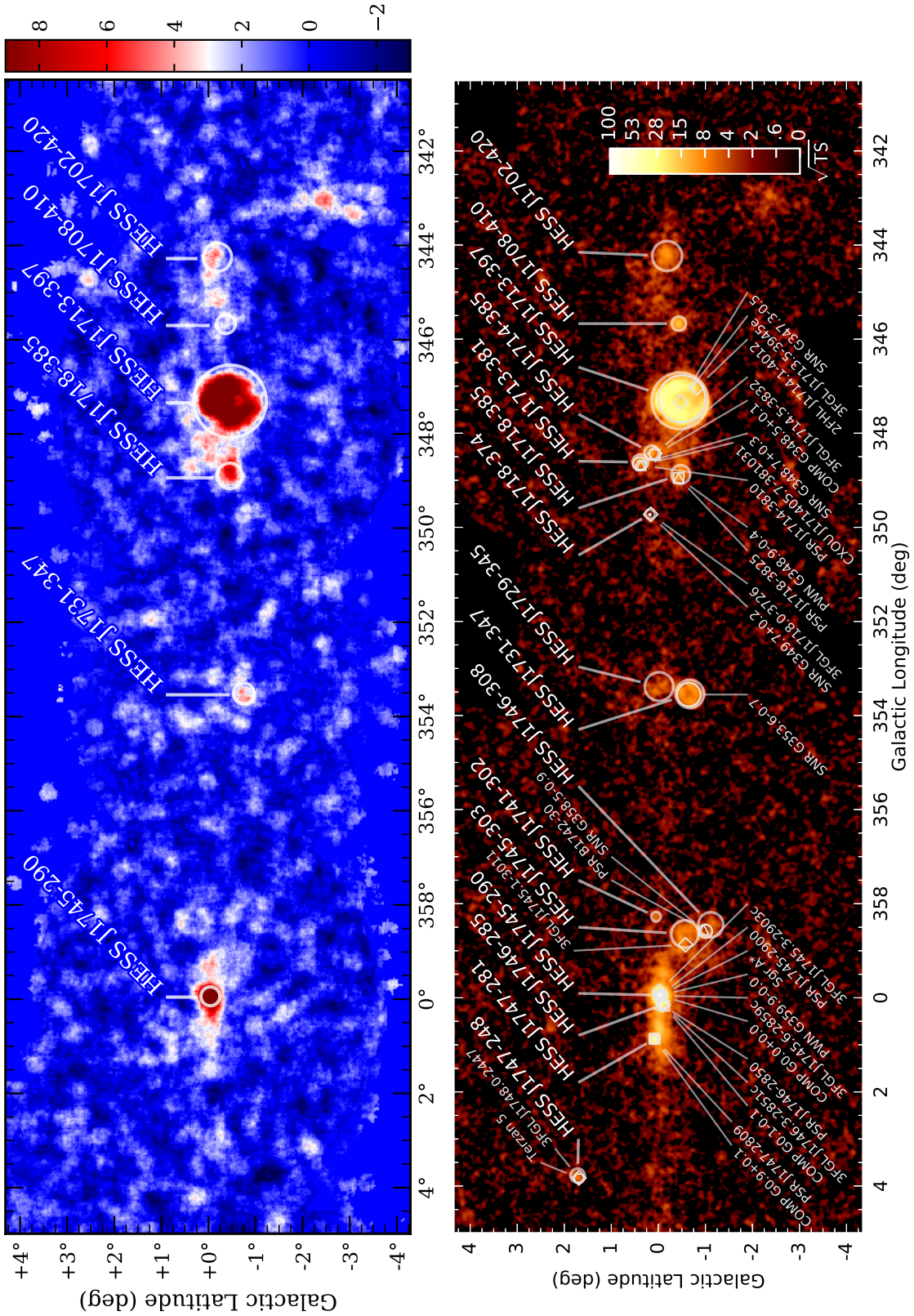

Figure 6.20: The VHE gamma-ray sources above 10 TeV (left panel) and comparison to the HGPS catalogue (right panel) [5]. Continuation of Figure 6.16.

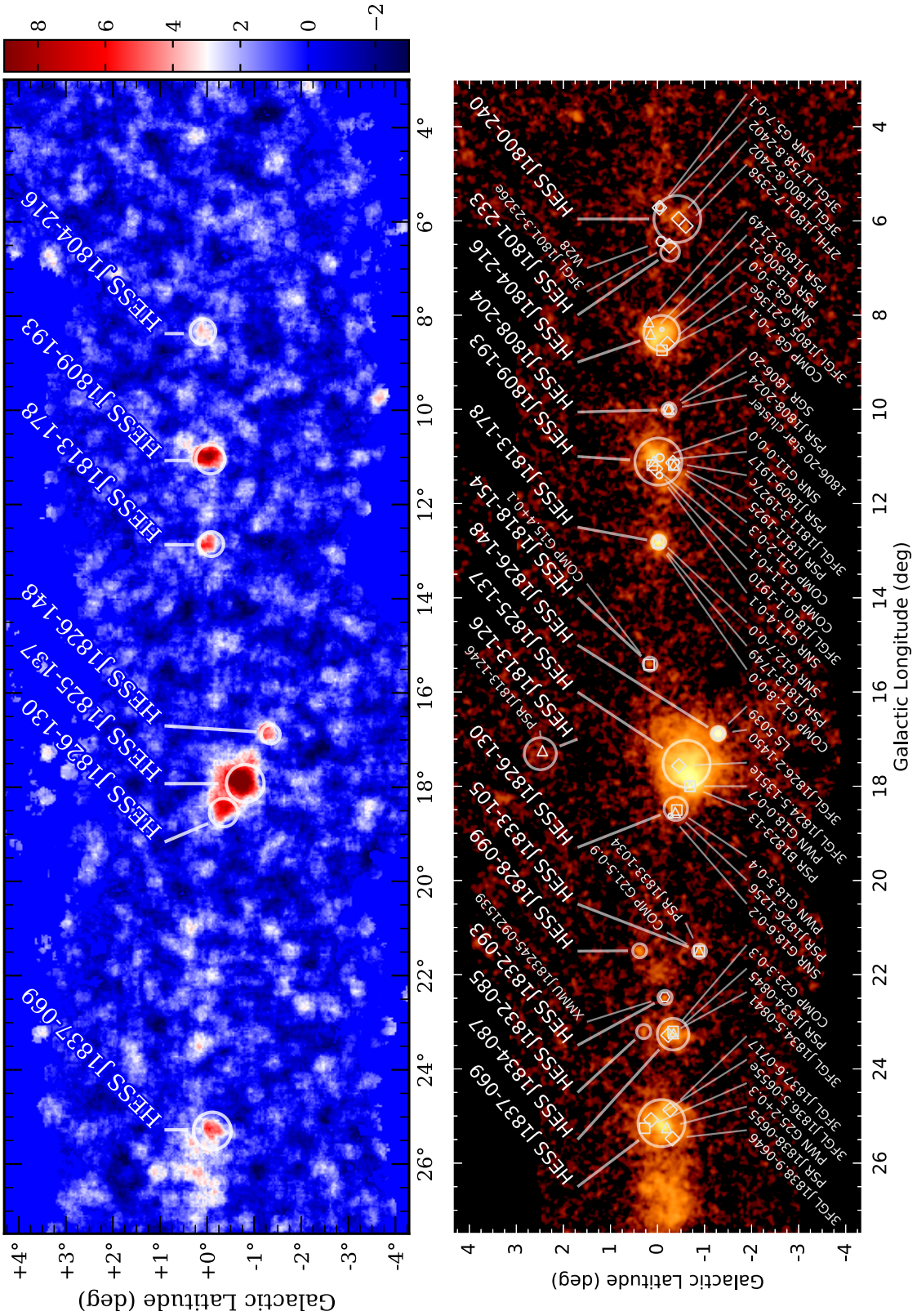

Figure 6.21: The VHE gamma-ray sources above 10 TeV (left panel) and comparison to the HGPS catalogue (right panel) [5]. Continuation of Figure 6.16.

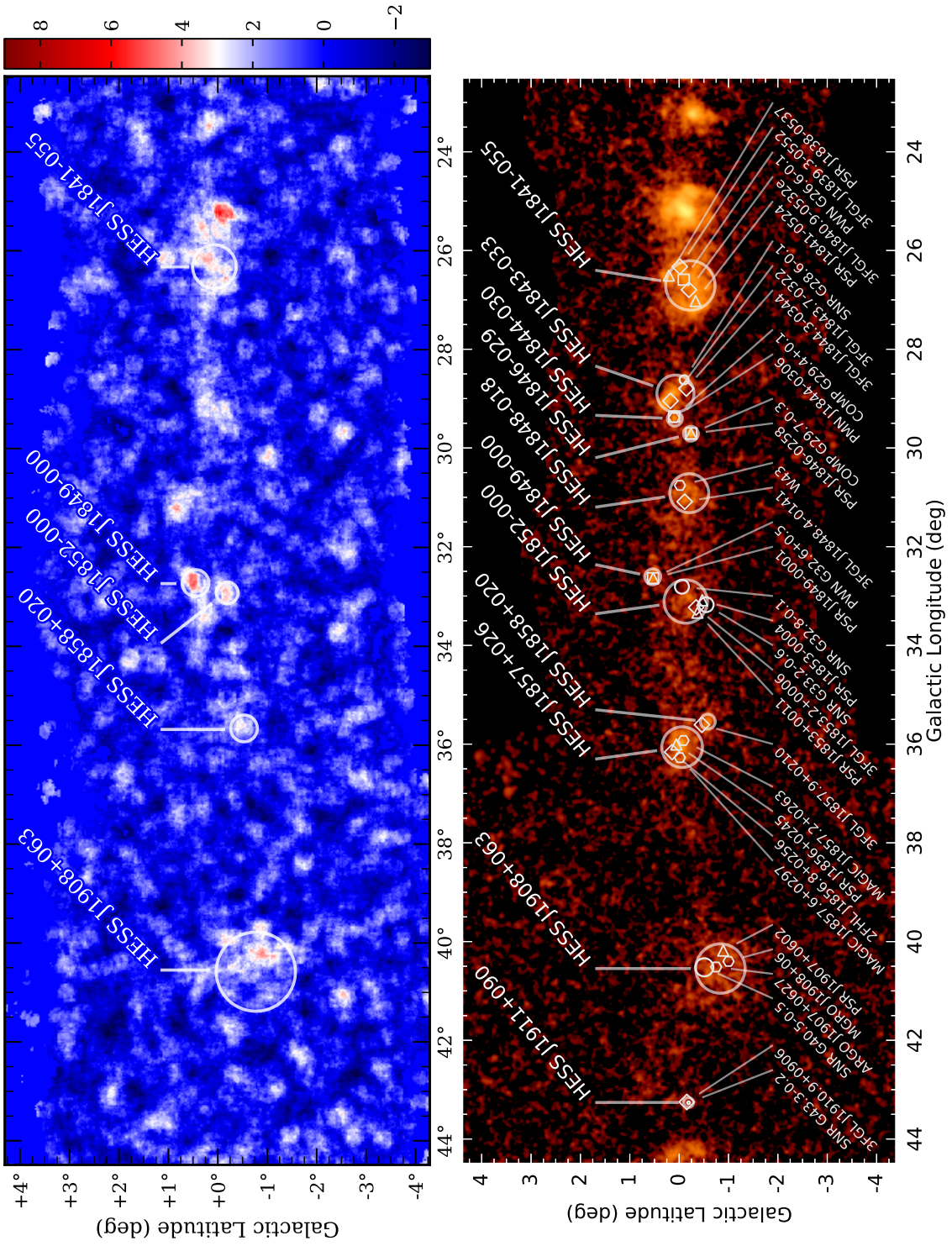

Figure 6.22: The VHE gamma-ray sources above 10 TeV (left panel) and comparison to the HGPS catalogue (right panel) [5]. Continuation of Figure 6.16.

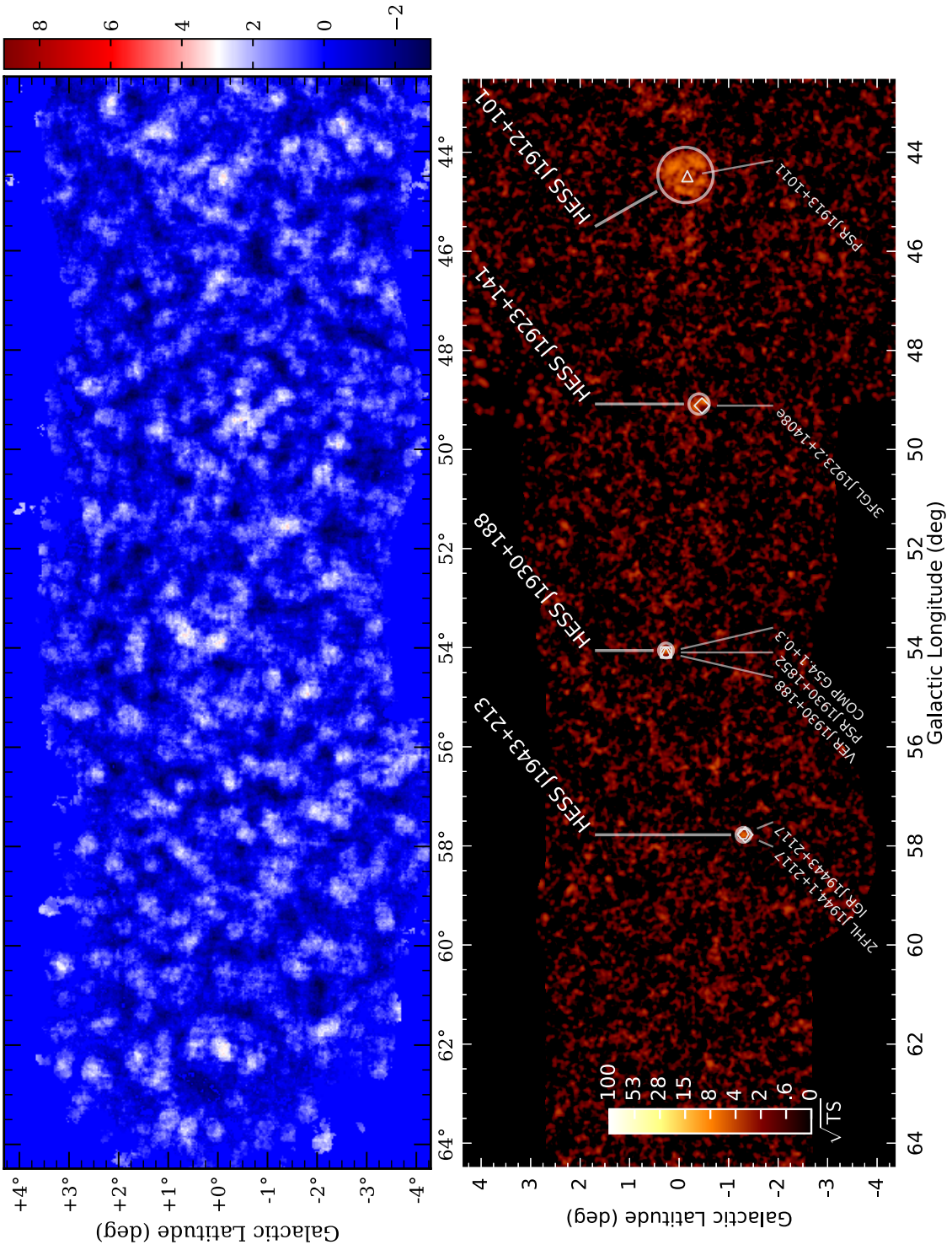

Figure 6.23: The VHE gamma-ray sources above 10 TeV (left panel) and comparison to the HGPS catalogue (right panel) [5]. Continuation of Figure 6.16.

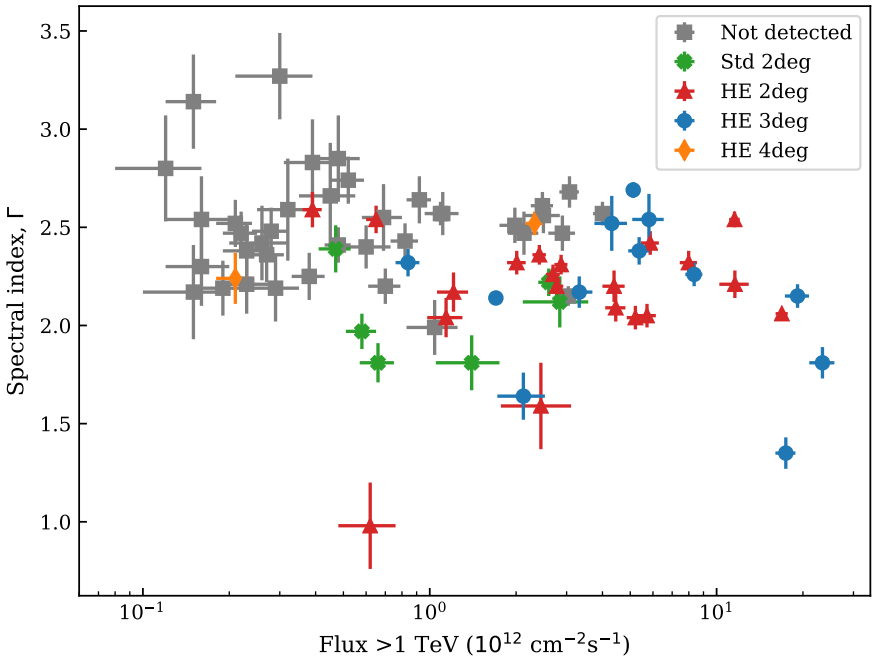

Figure 6.24: The source spectral characteristics and their detectability above 10 TeV. The sources that are not detected above 10 TeV in this study are shown with grey markers. Markers of other colours indicate the detected sources and the analysis configuration that resulted in the highest significance for each particular source. The spectral index Γ and flux above 1 TeV are taken from the HGPS catalogue [5].

6.3 Source classes identified above 10 TeV

There are different classes of astronomical objects in the Galaxy that can accelerate cosmic rays and, subsequently, emit high-energy gamma rays. The examples of such sources are supernova remnants (SNRs) [127], pulsar wind nebulae (PWNe) [108, 90] and pulsars themselves [56, 3] as well as different kinds of binary systems [98]. Currently, only 31 sources out of the 78 detected ones in the HGPS catalogue are firmly identified. They form four different source classes: binaries, SNRs, PWNe and composite objects, which exhibit both the shell-like structure of the SNR and the interior PWN, with the exact source of gamma-ray emission not yet resolved. The distribution of the HGPS sources into these four classes is displayed in the right panel of Figure 6.25. The left panel of this figure shows a similar distribution for the sources that are detected at energies above 10 TeV in this work[6]. As seen from the presented pie charts, the class distribution of the sources above 10 TeV is consistent with the one reported in the HGPS catalogue and there is no single source class dominance revealed in the more than 10 TeV domain. All firmly identified sources considered in this work and corresponding astronomical objects are also listed in Table B.11 in Appendix B.4.

[6]In this study, the procedure of the source association and identification is not performed, but is adapted from the HGPS catalogue [5].

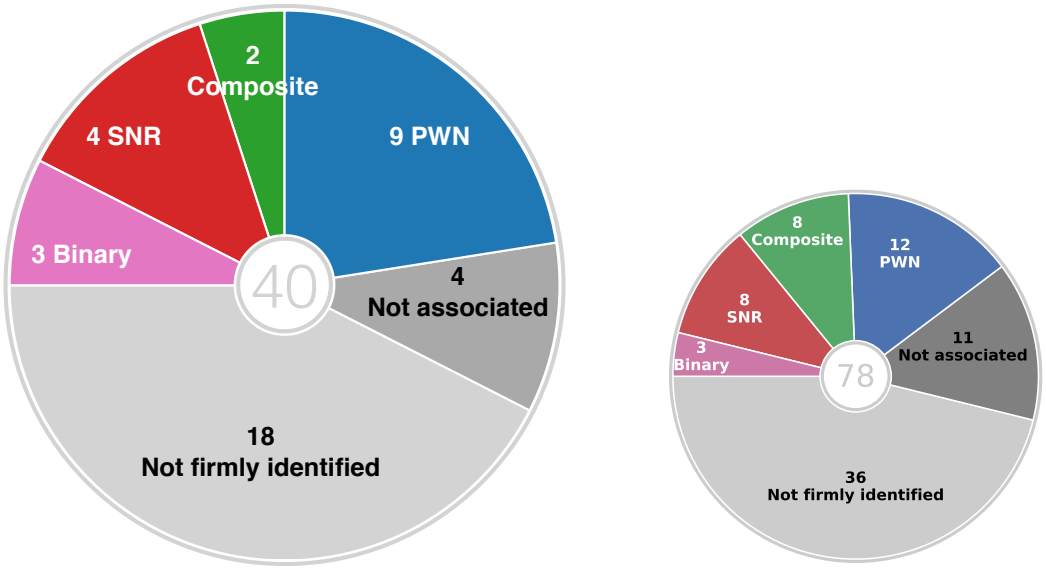

Figure 6.25: The distribution of the source classes above 10 TeV on the left and the comparison to the distribution of the HGPS sources [5] on the right.

6.3.1 Gamma-ray binaries

The HGPS catalogue contains three gamma-ray binary systems, namely HESS J1018−589 A [23], HESS J1302−638 [9] and HESS J1826−148 [42]. A gamma-ray binary comprises a compact object, a stellar-mass black hole or neutron star, orbiting a companion represented by a young massive star of O or B class [82]. The firm identification of the gamma-ray binary is possible if the signal variability due to orbital motion is measured. Unlike most of the Galactic accelerators, gamma-ray binaries are seen as point-like sources by Cherenkov telescopes. It is assumed that gamma-ray emission is produced as a result of the interaction of the relativistic outflow from the compact object with the wind or radiation field of the companion star [82]. However, in most cases, the nature of the compact object is unknown. Among the three binary systems discussed here, only for HESS J1302−638 is the compact object identified. The compact object in this system is the pulsar PSR B1259−63, which orbits the Oe class companion star LS 2883 with a period of 3.4 years [9]. For HESS J1018−589 A and HESS J1826−148, the orbital periods of both systems have timescales of several days; the companion stars have the spectral classes of O6V(f) and O6.5V(f), respectively, while the compact objects are not known, although the neutron star scenario is favoured in both cases [97, 176]. Nevertheless, all three binary systems that are present in the HGPS catalogue are also detected above 10 TeV in this study. These results additionally demonstrate that binary systems are not only very efficient particle accelerators, but are also able to accelerate particles to energies of tens of TeV.

6.3.2 SNRs, PWNe and composite objects

In the VHE regime, SNRs and PWNe are the most common Galactic particle accelerators. As seen from Figure 6.25, SNRs, PWNe and composite objects constitute the majority of

all firmly identified sources in the HGPS catalogue as well as in this work. In contrast to the binary systems discussed above, SNRs and PWNe are typically spatially extended and do not exhibit periodic flux variability. The identification of these sources is therefore more complicated and can be based on the source shape, position with regard to the associated astrophysical object, energy-dependent morphology and morphology correlations with other wavelengths.

According to the SNRcat catalogue [101], there are more than 200 SNRs detected in other wavelengths that are located in the region of the Galactic plane covered by the HGPS. Due to such a high density, the requirement on spatial coincidence is usually insufficient to claim a connection between gamma-ray emission and SNR seen at lower energies. Therefore, a clear shell-like structure observed in gamma rays, which also matches the one measured at lower energies, is typically a more convincing argument in favour of the SNR identification [4]. The HGPS catalogue was found to contain 8 firmly identified SNRs, half of which are also detected above 10 TeV in this work: Vela Junior (HESS J0852−463) [39], HESS J1442−624 [26], HESS J1713−397 [38] and HESS J1731−347 [15]. All four SNRs have a shell-like morphology at GeV - TeV energies. Above 10 TeV, the shell-like shape can be recognised only for HESS J1713−397. For the other three remnants, the emission above 10 TeV is better described by a spot within the shell that is observable in GeV - TeV energy range. HESS J1442−624 has a spectral cutoff at an energy of about 3.5 TeV [26], which might be the reason for the low significance of this source above 10 TeV despite a relatively high exposure (see Figure B.3 in Appendix B.2). Similarly, Vela Junior has a cutoff at 6.7 TeV [2]. HESS J1731−347 does not have a measured cutoff and is discussed in more detail later in this section.

The energetic pulsar that is left behind after the core-collapse supernova explosion may generate a highly relativistic wind of electrons and positrons, i.e. a PWN, inside the expanding SNR [108]. The system of PWN - SNR is very dynamic and its evolution can be divided into three stages: the free expansion of the PWN ($<$ 2 - 6 kyr), interaction of the PWN with the SNR reverse shock (up to some tens of kyr), and the relic stage, when the pulsar leaves the old nebula [6]. The PWN appearance is greatly influenced by its collision with the reverse shock, which in turn depends on the density of the surrounding medium and asymmetry of the supernova explosion. As a result, PWNe are rather diverse objects. This also makes their firm identification more complicated. The typical strategy to identify a PWN is to try to localise a young energetic pulsar in the vicinity of the putative PWN candidate and to observe a synchrotron nebula at lower energies, i.e. in the X-ray and radio domains. However, in the case of an evolved PWN, the best identification method is the energy-dependent morphology of the source. Since the energetic electrons and positrons, which are transported to the outskirts of the nebula, are cooling down [90], the source extent at energies of several hundred GeV is larger than in the TeV range. As discussed in the HGPS publication [5], currently, an energy-dependent morphology in the H.E.S.S. energy range is observed only for two sources, namely HESS J1303−631 and HESS J1825−137, which are also detected above 10 TeV in this work.

PWNe appear to be the most abundant source class in the HGPS catalogue and are very effective particle accelerators, resulting in 9 sources detected above 10 TeV out of the 12 sources presented in the HGPS [5]. They are: Vela X (HESS J0835−455) [45], HESS J1303−631 [20], HESS J1356−645 [17], HESS J1418−609 [43], HESS J1420−607 [43], HESS J1514−591 [40], HESS J1825−137 [44], HESS J1837−069 [157] and HESS J1849−000

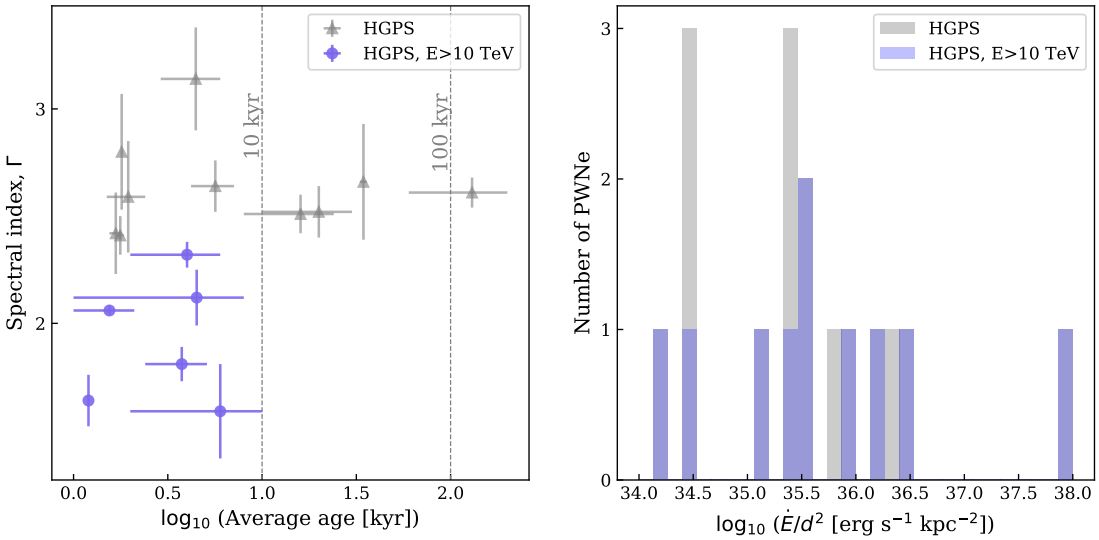

Figure 6.26: The SNR and PWN pulsar characteristics of the sources detected at more than 10 TeV energies and HGPS-detected sources of respective classes [5]. The left plot compares the age and gamma-ray spectral index of the SNRs and composite objects. The age error bars embrace minimum and maximum age estimates stated in the SNRcat [101] and other publications [88]. The spectral characteristics of the presented sources are taken from the HGPS catalogue [5]. The right plot shows the comparison of the spin-down energy flux of the pulsars that are associated with PWNe and composite sources. The corresponding values are taken from the ATNF catalogue [156].

[178]. Almost all of them are extremely strong sources, except for HESS J1849−000, which has a very hard spectrum which likely aided in its detection above 10 TeV. The three remaining PWNe in the HGPS list are fairly weak sources and it is not a surprise that they are not detected here at more than 10 TeV energies.

In addition, as mentioned above, there are sources considered as composite. Observations at lower energies show both a PWN and an SNR shell, whose angular size does not exceed the size of the VHE emission. In this case, it is difficult to clarify the exact origin, the SNR shell or PWN, of VHE emission. In the HGPS catalogue [5], there are 8 such sources. Only two of them are detected above 10 TeV in this work; specifically HESS J1640−465 [22] and HESS J1813−178 [105, 114]. All other composite sources within the HGPS catalogue are rather faint, except for HESS J1834−087 [24], whose spectral index of 2.47 [5], is perhaps too steep, and for which the exposure of the source region with H.E.S.S. is too low for the source to be detected above 10 TeV. In turn, HESS J1640−465 and HESS J1813−178 have steeper spectra as well as cutoffs at about 4 and 7 TeV, respectively [5].

Figure 6.26 compares some characteristics of SNRs and PWNe detected above 10 TeV and those detected in the HGPS [5]. The left side of the figure shows the relation between the estimated age of the SNRs [101, 88] and their spectral indices [5]. For composite objects, it is not known for certain where the emission is coming from, and hence they are included in this distribution. Twelve of the 16 SNRs/composite objects in the HGPS catalogue are younger than 10 kyr. Above 10 TeV energies, all SNRs/composite sources are younger than 10 kyr. This shows that relatively young and middle-aged SNRs (or PWNe that develop

after the explosion in composite objects), i.e. younger than 10 kyr, are able to accelerate cosmic rays and cosmic electrons to energies of more than several tens of TeV. However, it should be noted that the ages of SNRs as well as their spectral indices are rather uncertain in most of the cases.

The right side of Figure 6.26 compares the spin-down energy flux $\dot{E}/d^2$ of the pulsars that are associated with the identified PWNe. Similarly to the case discussed above, the composite objects are also included in this distribution because the TeV emission might be produced by the particles accelerated in the corresponding PWN. The $\dot{E}/d^2$ values for each pulsar considered in the distribution are taken from the ATNF catalogue [156]. However, there are a few sources for which the pulsed emission of the pulsar responsible for the PWN is not detected. This resulted in 16 sources being presented in the distribution, although there are 20 PWNe and composite objects together identified in the HGPS catalogue [5]. As seen from the plot, overall, the distribution of $\dot{E}/d^2$ parameter is consistent for the pulsars associated with the PWNe from the HGPS catalogue and the ones detected above 10 TeV. At larger $\dot{E}/d^2$ parameter values, the fraction of sources detected above 10 TeV is a bit bigger, which is expected since it is an indication of a more energetic pulsar. However, the statistics are too low to make further conclusions.

HESS J1731−347

HESS J1731−347 is one of the SNRs with a confirmed shell-like morphology in VHE gamma rays. It is associated with SNR G353.6−0.7 and is also seen in radio [180] and X rays [181]. HESS J1731−347 is the remnant of a core-collapse supernova explosion approximately 2 - 6 kyr ago [88]. The progenitor was a more than 20 solar mass ($M_\odot$) star [88]. Currently, two possible scenarios are discussed; namely, a 20 $M_\odot$ type IIL/b and 25 $M_\odot$ type Ib/c supernova explosion (the former better fits the TeV part of the HESS J1731−347 spectrum [87]). The observations in X rays have revealed a compact object XMMU J173203.3−344518 in the centre of the remnant [120, 143]. It lacks an optical or IR counterpart and is thought to be a neutron star. However, no pulsations have been observed at any wavelength so far.

Just outside of the shell there is another VHE gamma-ray source, HESS J1729−345 [15], which is not detected in this work above 10 TeV. The left panel of Figure 6.27 shows the more than 10 TeV significance map of HESS J1731−347 and, in addition, indicates the position of HESS J1729−345. In the HGPS catalogue, HESS J1729−345 is listed as one of the 11 sources without associations in other wavelengths [5]. However, HESS J1729−345 is spatially coincident with a molecular cloud [77, 159] and its gamma-ray emission can be interpreted as cosmic rays with energies of several tens of TeV that escaped the SNR HESS J1731−347 and interact with the molecular cloud [88]. In this case, it is surprising that HESS J1729−345 is not detected in this work above 10 TeV, although the non detection can be also a result of the low source flux and steep spectral index [5].

The western part of the SNR HESS J1731−347 is coincident with a very dense molecular cloud (MC) core region [159]. Both HESS J1731−347 and the MC-core region are detected by *Fermi*-LAT in GeV gamma rays [83]. Interestingly, the spectral analysis of the *Fermi*-LAT data shows that these two regions have very different spectral indices. Emission detected from the remnant is much harder than the emission from the MC-core region [87]. The authors of the corresponding study [87] suggest that the remnant collided with

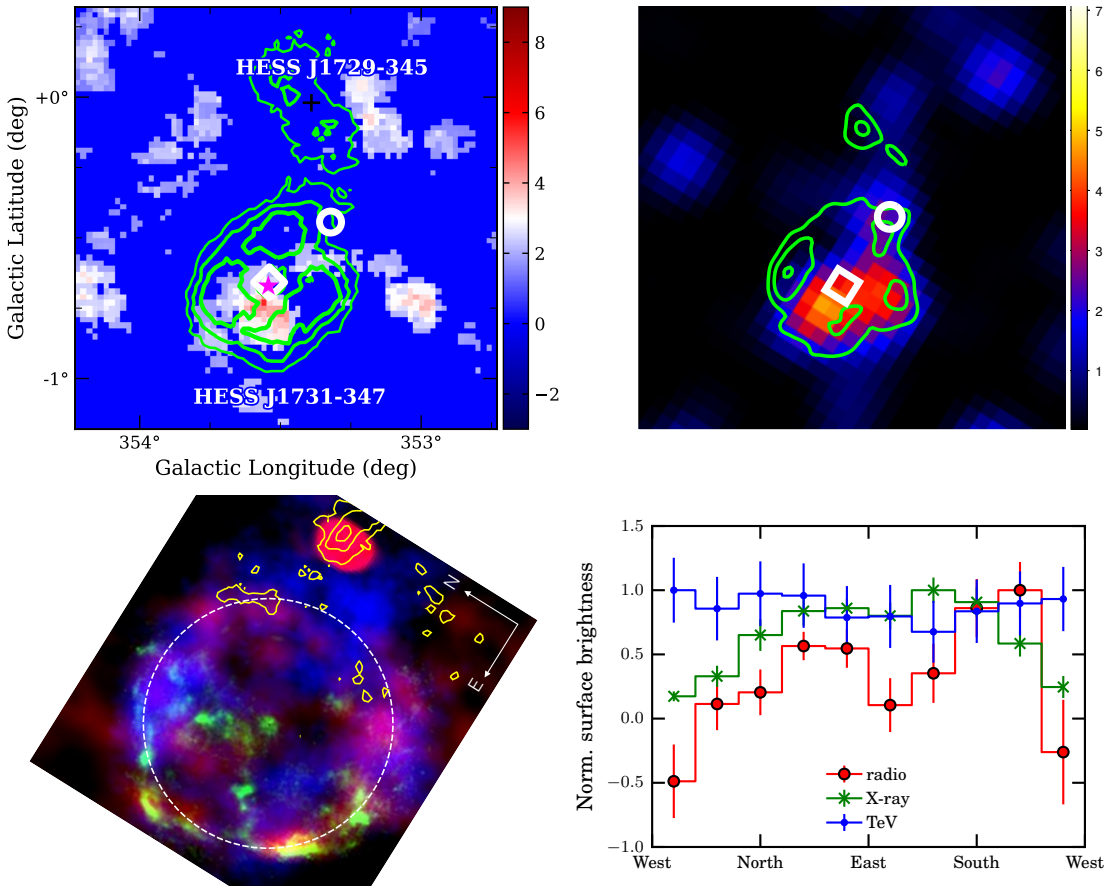

Figure 6.27: HESS J1731−347 in VHE gamma rays and multi-wavelength picture. The upper left panel shows the significance map of the HESS J1731−347 region obtained above 10 TeV in this work using the high-energy analysis with 3° maximum event offset (0.1° correlation radius). The black cross indicates the best fit position of HESS J1729−345 [5]. The magenta star marks the position of the compact object XMMU J173203.3−344518 in the centre of the remnant. The upper right panel shows the more than 10 GeV *Fermi*-LAT TS map [87]. Contours in both plots illustrate 4, 6 and 8 σ significance levels measured in the full energy range of the H.E.S.S. instrument [129, 15]. The square and circle markers indicate the best fit position of HESS J1731−347 in *Fermi*-LAT data and the molecular cloud core, respectively. The bottom left panel shows the source morphology in radio at 325 MHz from *GMRT* (red), X-ray 0.4 - 10 keV from *XMM-Newton* (green) and GeV - TeV range from H.E.S.S. (blue) [96]. The yellow contours denote emission in the sub-mm range that traces cold dense regions. The dashed circle illustrates an approximate extension of the SNR shell [96]. The bottom right panel displays the azimuthal surface brightness profile of the shell in different wavelengths. The shell is assumed to have radius from 0.18° to 0.24°.

the dense MC-core, and conclude that the gamma-ray emission from HESS J1731−347 consists of two components: one of them is hadronic from the collision region and another one is leptonic from the rest of the SNR. Thus, during the collision, the SNR shock wave

is rapidly stalled and cannot accelerate electrons up to several tens of TeV. In addition, GeV cosmic rays are released into the MC-core, which can explain the more than 1 GeV emission detected by *Fermi*-LAT around the MC-core position.

The left panel of Figure 6.27 displays the HESS J1731−347 significance map above 10 TeV obtained in this work. The right panel shows the test statistics (TS) map of the same region observed by *Fermi*-LAT at energies above 10 GeV [87]. As seen from the large number of empty bins in the significance map, the statistics above 10 TeV are very low. Nevertheless, it is possible to notice that the part of the remnant that has relatively high significance in this map above 10 TeV is roughly coincident with the bright region in the *Fermi*-LAT TS map above 10 GeV, which would be consistent with a leptonic scenario, assuming that the emission has the same origin.

This hypothesis is also supported by X-ray data. The bottom panel of Figure 6.27 compares the morphology of HESS J1731−347 in X-ray, radio and TeV[7] energy ranges [96]. It shows that the X-ray emission is suppressed towards the western part of the remnant, where the interaction region with MC-core is located. Somewhat similar picture can be also observed in radio range. The simplest explanation is that due to interactions with MC-core, the velocity of the cloud significantly decreased and therefore the synchrotron emission is no longer produced in the X-ray band [96]. The TeV profile is consistent with being flat, which might suggest that part of this TeV emission has a hadronic origin.

Analysis at more than 10 TeV energies nicely contributes to the energy-dependent picture of HESS J1731−347 and its surroundings and would be helpful for the source modelling. However, in order to be able to draw more firm conclusions regarding the gamma-ray emission localisation and origin, a dedicated analysis of the HESS J1731−347 region and extraction of the source spectrum is required, which is beyond the scope of this work.

Vela Junior and the PWN around PSR J0855−4644

HESS J0852−463 is a shell type SNR commonly referred to as Vela Junior, G266.2−1.2 [115] and RX J0852.0−4622 [60]. It is one of only a few remnants for which the shell structure is resolved in VHE gamma rays. Vela Junior belongs to the class of young SNRs, with an estimated age between 1.7 kyr and 4.3 kyr [141]. This remnant is plausibly the result of a core collapse supernova explosion [175], although the central compact object is not yet firmly identified [173].

The southeast rim of the shell spatially coincides with the Vela-like[8] radio pulsar PSR J0855−4644 [146]. Both the pulsar and Vela Junior are located at distances of less than 900 pc [29]. However, an association between them is very unlikely, since the estimated age of the SNR is below 4.3 kyr [141], while the pulsar is much older and has a characteristic age of 140 kyr [146]. *XMM-Newton* observations revealed a diffuse extended X-ray emission around PSR J0855−4644, interpreted as a PWN [29]. In addition, Chandra detected a much more compact nebula around the pulsar [154], similar to the inner PWN of the Vela pulsar (PSR B0833−45) [170]. It has an elongated morphology and consists of two

[7]Here, GeV - TeV energy range is assumed.

[8]There is a group of energetic pulsars with spin-down luminosities $\dot{E} \geq 10^{36}\,\mathrm{erg\,s^{-1}}$ and characteristic ages roughly within the range $10 \leq \tau_c \leq 100\,\mathrm{kyr}$, which share many properties with Vela pulsar (PSR B0833−45); e.g. X-ray or gamma-ray emission, presence of a PWN around the pulsar [146].

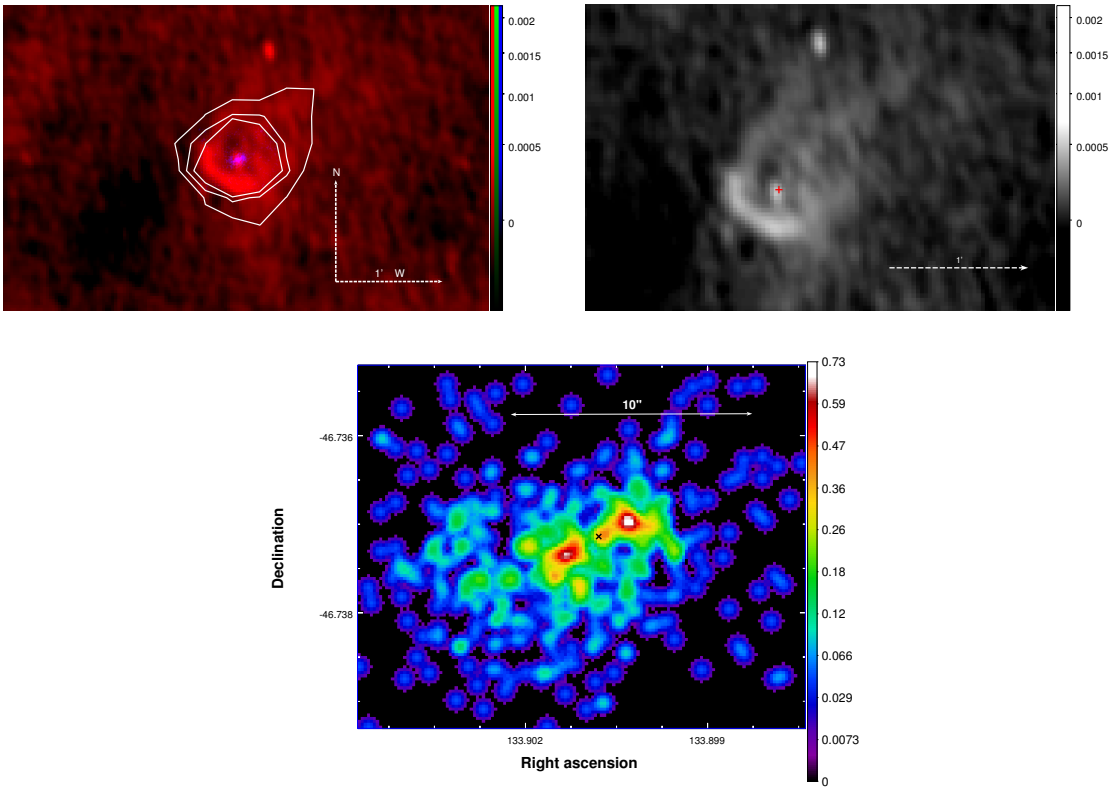

Figure 6.28: Multi-wavelength view of PSR J0855−4644 and its PWN. The top row shows the radio nebula around PSR J0855−4644 [155]. The left plot displays the 1.35 GHz radio image from *uGMRT* in red colour and 0.5 - 8 keV compact X-ray structure observed by *Chandra* in blue. White contours denote 3, 4 and 5 σ significance of the larger diffuse PWN seen by *XMM-Newton* at 1.2 - 6 keV energies [29]. In the right plot, the same radio image is slightly zoomed in and a red cross marks the pulsar PSR J0855−4644 position. The bottom row presents the compact nebula detected by *Chandra* (2 - 8 keV) [154], i.e. zoomed in view of the structure showed in blue colour in the upper left panel. The black x-marker indicates the pulsar position here.

lobes that lie on the symmetry axis, which is roughly oriented in the southeast-northwest direction as can be seen in the bottom panel of Figure 6.28. These two lobes can be explained as a double-torus and/or jet structure. The PWN around PSR J0855−4644 was recently also detected at radio wavelengths by *uGMRT* [155]. The radio image of the PWN is shown in the top panel of Figure 6.28, where it is also compared to the observations in the X-ray range. The radio nebula has a compatible size with the emission seen by *XMM-Newton*. Its morphology consists of a partial ring-like structure in the southeast and faint tail-like emission towards the northwest that resembles a bow shock nebula formed due to supersonic motion of the pulsar. However, the proper motion of PSR J0855−4644 has not been measured yet.

The spin-down energy flux of PSR J0855−4644 is rather large, $\dot{E}/d^2 \geq 10^{36}\,\mathrm{erg\,s^{-1}\,kpc^{-2}}$ [29], which suggests that the PWN powered by this pulsar should also be observable in VHE gamma rays. As can be seen in Figure 6.26, PWNe detected by H.E.S.S. in TeV

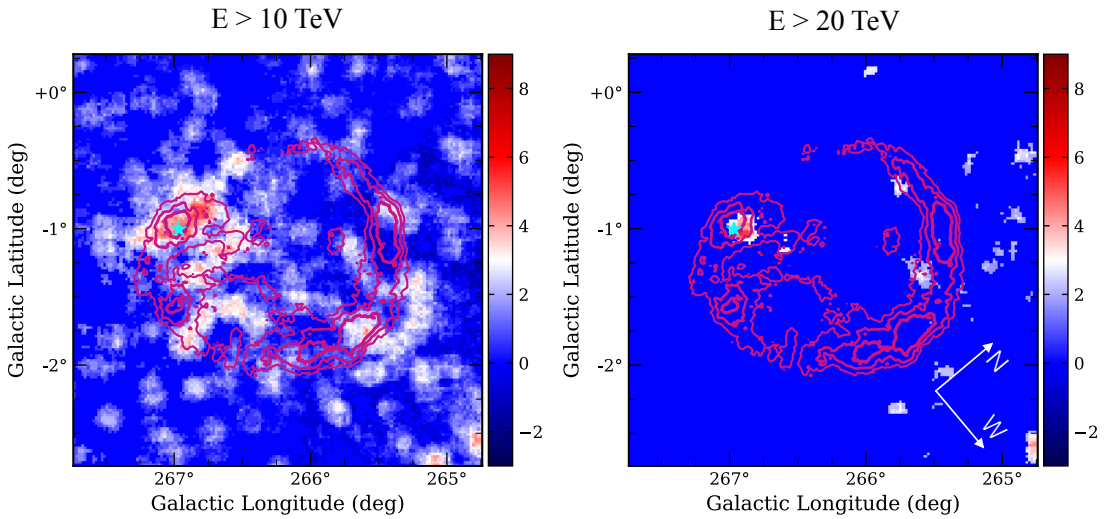

Figure 6.29: Significance map of Vela Junior region above 10 TeV and 20 TeV obtained in this work using the high-energy analysis with 3° maximum event offset (0.1° correlation radius). Contours illustrate 6, 8 and 10 σ significance levels measured in the full energy range of the H.E.S.S. instrument (taken from [129]). The cyan star marks the position of the pulsar PSR J0855−4644.

gamma rays as well as above 10 TeV have similar pulsar characteristics. However, the putative TeV PWN around PSR J0855−4644 overlaps with Vela Junior, which complicates its detection. A recent H.E.S.S. study of the Vela Junior region in the energy range between 0.3 TeV and 30 TeV showed a deviation of spectral parameters derived from the area, which might contain the putative PWN around PSR J0855−4644, from the spectral parameters of the whole Vela Junior SNR [2]. The investigation found a hint of a higher value of the spectral cutoff energy for the PWN region in comparison to the entire SNR. However, the significance of this measurement was not high enough to claim an association, and the contribution of this plausible PWN to the overall flux measured from Vela Junior is estimated to be less than 8%.

Figure 6.29 shows the significance map of the Vela Junior region at energies above 10 TeV and 20 TeV. As can be seen from the contours in the figure, the northwest rim is a very bright feature of the Vela Junior shell at lower energies [2]. However, almost all of the significant emission above 10 TeV is concentrated in the south and southeast part of the remnant. Furthermore, above 20 TeV, the only significant spot in the map coincides with the position of the pulsar PSR J0855−4644, which is strong evidence of the TeV PWN presence around this pulsar. The significance of the region within 0.2° of the pulsar position is 4.2 σ above 20 TeV when analysed with the high-energy analysis with 3° maximum event offset. Other analysis configurations yielded less than 3σ significance in the same region. The analyses with 2° maximum event offset result in a very low level of both excess and background counts. The analysis with 4° maximum event offset gains almost the same number of excess events as the analysis with 3° maximum event offset, but it also accumulates nearly three times more background events, resulting in a lower significance of the hotspot.

The results obtained in this work are in good agreement with the findings of the spatially

resolved spectroscopy analysis performed at lower energies [2], which is discussed above. Thus, with an energy cutoff at 6.7 TeV, gamma-ray emission from Vela Junior disappears from the map at energies above 20 TeV, while the PWN powered by PSR J0855−4644 has a higher spectral cutoff and can still be identified.

6.3.3 Sources without confirmed counterpart

A firm source identification requires solid evidence, and often it is hard to prove the connection between the VHE gamma-ray emission and the astronomical object, especially when the VHE source is rather extended and spatially coincident with several different sources at other wavelengths. Because of this, in the original HGPS catalogue [5], only 31 sources out of 78 detected ones are firmly identified. Another 36 sources have counterparts in other wavelengths, but their nature cannot be interpreted with certainty. There are also 11 sources that do not have associations with other astrophysical objects at all. At energies above 10 TeV, the situation is similar and among the 40 sources considered as detected in this work, 18 fall into the identified category. Another 18 sources are not firmly identified but have associations at lower energies. Finally, 4 sources detected above 10 TeV are lacking any counterpart. The sources considered as detected in this work that are not firmly identified – i.e. the ones which have only associations with other astronomical objects or not associated at all – are listed in Table B.12 in Appendix B.4.

6.4 HGPS above 10 TeV and counterpart candidates

The Galactic latitude and longitude distribution of the more than 10 TeV HGPS sources are shown in Figure 6.30 in the top and bottom panel, respectively, and compared to the distribution of all VHE sources presented in the HGPS catalogue [5]. On average, the distribution in the Galactic plane of the considered sources above 10 TeV is similar to the distribution of all HGPS sources. In particular, the Galactic latitude distribution of sources above 10 TeV has a comparable skewed shape as the distribution of all sources, with more sources located at negative Galactic latitudes. In addition, some degree of skewness can also be observed in the latitude distribution of the sources from the 3FHL catalogue [53] that are located within the ranges of the HGPS catalogue. The 3FHL catalogue contains the sources detected by *Fermi*-LAT in the energy range from 10 GeV to 2 TeV. The Galactic longitude distribution of the sources observed above 10 TeV is also fairly consistent with the distribution of the 3FHL sources. The exception is the Galactic Centre region, i.e. between $\pm 5^\circ$ in Galactic longitude. In this region, the 3FHL source distribution, as well as the HGPS source distribution, has a distinctive peak, while above 10 TeV there are a very few sources. According to the spectral characteristics of the sources presented in the HGPS catalogue [5], the sources in the vicinity of the Galactic Centre are typically weak with a rather steep spectral index, which could explain their non-detection above 10 TeV in this study.

Besides the 3FHL source catalogue, the latitude VHE source distributions are also compared to the distribution of SNRs and PWNe from the corresponding part of the Galactic plane, since these are so far the main classes of counterparts for the VHE gamma-ray sources. The distribution of SNRs and PWNe is taken from the high-energy catalogue of

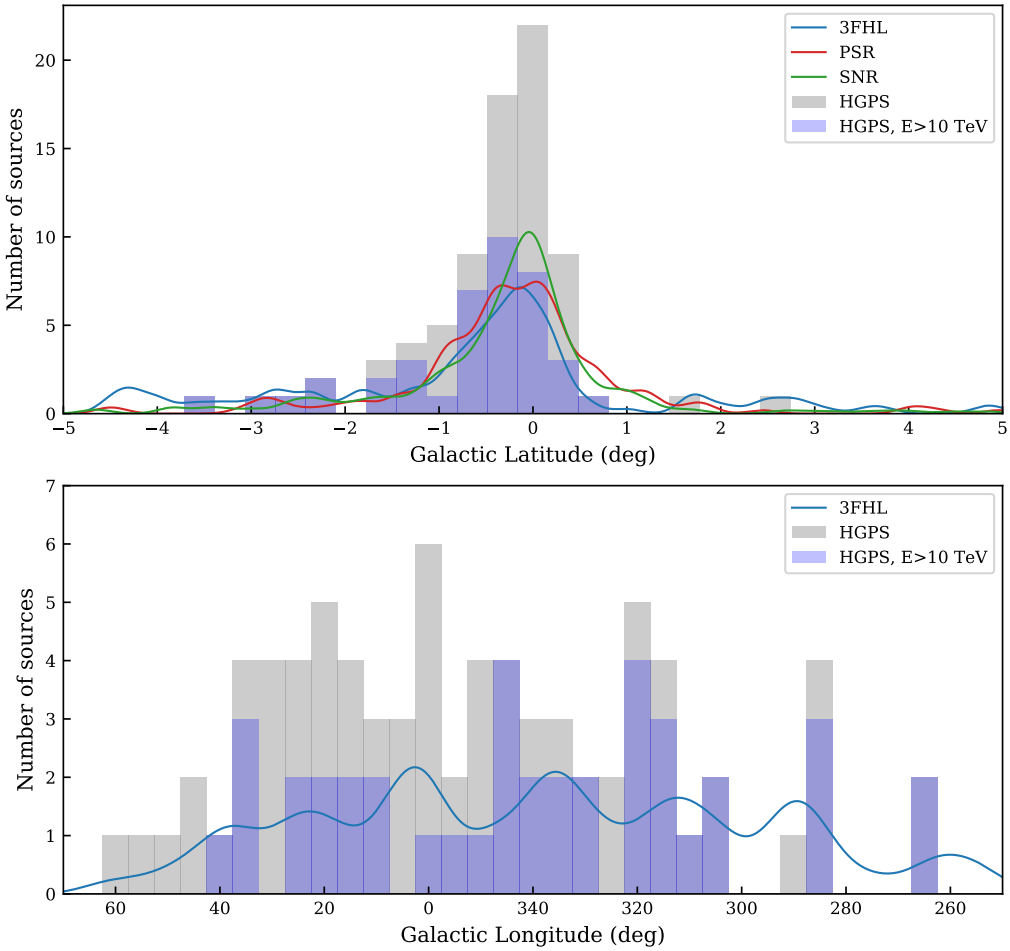

Figure 6.30: The Galactic latitude and longitude source distribution. The plots compare the distribution for the sources detected above 10 TeV (blue colour) and the distribution of the sources from the entire HGPS catalogue [5] (grey colour). In addition, distributions of the 3FHL catalogue sources [53], SNRs and PWNe from the SNRcat [101] and energetic pulsars from the ATNF catalogue [156] are shown. These curves are smoothed with Gaussians of width 0.15° and normalised to the total count of sources seen above 10 TeV in this work.

supernova remnants (SNRcat) [101], which in turn is based on the radio catalogue of supernova remnants by D. Green [115], but also includes other SNRs as well as PWNe without a detected shell. In addition, the latitude distribution of energetic pulsars is added for comparison, since they can power PWNe. The pulsar distribution is built using the ATNF catalogue of radio pulsars [156]. In order to select energetic pulsars that are powerful enough to sustain a nebula, millisecond pulsars as well as pulsars with spin-down energy flux $\dot{E}/d^2 < 10^{33}\,\mathrm{erg\,s^{-1}\,kpc^{-2}}$ and spin-down luminosity $\dot{E} < 10^{34}\,\mathrm{erg\,s^{-1}}$ are excluded from the consideration. As seen from the top panel of Figure 6.30, the latitude distribution of the sources detected above 10 TeV in this work is generally consistent with the distribution of these potential counterparts. In the bottom panel, the longitude distributions of SNRs and energetic pulsars are not included due to non-uniform Galactic plane coverage by the corresponding catalogues.

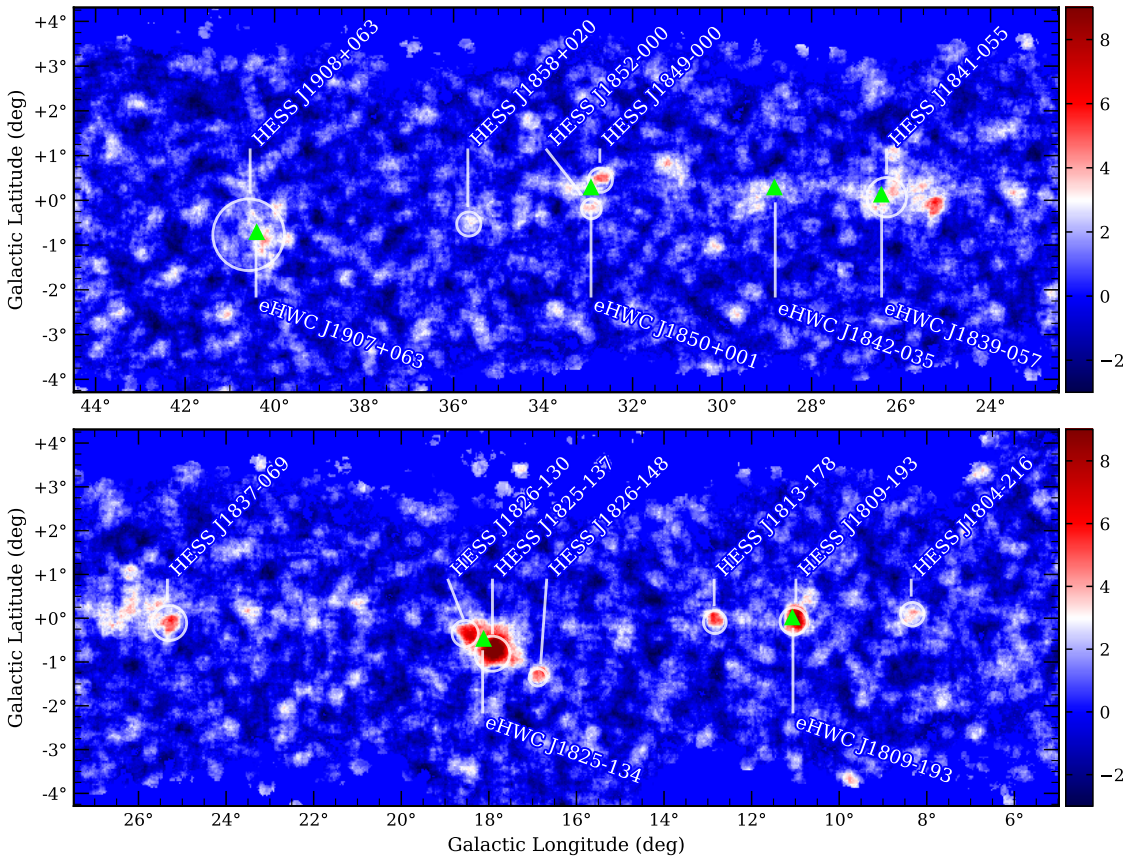

Figure 6.31: The comparison of the HGPS sources detected above 10 TeV and the sources seen by HAWC above 56 TeV. White circles show the position and extension of the sources above 10 TeV that are considered in this work. Green triangles indicate the location of the HAWC sources measured above 56 TeV [13]. The background image shows the significance map for energies above 10 TeV produced with the high-energy analysis with 3° maximum event offset. The correlation radius is 0.2°.

The part of the HGPS between approximately 5° and 60° in Galactic longitude is also accessible to the HAWC observatory [10], which is located in the Northern Hemisphere and operates at energies from few to hundreds TeV. Recently, HAWC has published a list of sources detected above 56 TeV [13]. Among the 9 reported sources, 6 are located in the region covered by the HGPS. Figure 6.31 shows the significance map above 10 TeV with overlaid positions of the HAWC sources above 56 TeV. As seen from the displayed map, 5 HAWC sources are located in close vicinity of the sources detected above 10 TeV in this work. Only eHWC J1842−035 does not have a counterpart among the sources detected in this work. However, it spatially coincides with two sources in the HGPS catalogue, HESS J1843−033 and HESS J1844−030 [5].

The HAWC source eHWC J1809−193 is very likely associated with HESS J1809−193 [48], one of the H.E.S.S. unidentified sources. This source is rather interesting since according to spectral studies in GeV - TeV domain, it might be a hadronic accelerator [58]. Currently, it is considered as one of the PeVatron candidates and is very important for a better under-

standing of particle acceleration processes in the Galaxy. The position of eHWC J1839−057 is located close to HESS J1841−055, an unidentified H.E.S.S. source with many plausible associations [49]. Although at lower energies in the HAWC energy range, this region of the sky accommodates the large elongated HAWC source 2HWC J1837−065 [11], which encloses HESS J1841−055 and HESS J1837−069 [157] (firmly identified as a PWN) and has the maximum of emission located towards the latter coincident source. Both HESS J1837−069 and HESS J1841−055 are detected above 10 TeV in this work. Another HAWC source above 56 TeV, eHWC J1850+001, might be associated with the PWN HESS J1849−000 [178]. In addition, there is one more H.E.S.S. unidentified TeV source in the vicinity, HESS J1852−000 [145], which, along with HESS J1849−000, is detected above 10 TeV in this work.

Furthermore, eHWC J1825−134 and eHWC J1907+063 are among the four sources[9] detected by HAWC above 100 TeV [13]. eHWC J1825−134 is located between two H.E.S.S. sources: HESS J1825−137 and HESS J1826−130. Both of these sources are detected in this work above 10 TeV. The first of them is a PWN, while the second source is currently unidentified and is famous for having one of the hardest energy spectra among known VHE sources [1]. However, it is not clear so far how much these two H.E.S.S. sources contribute to eHWC J1825−134. The second source observed above 100 TeV, eHWC J1907+063, is associated with the unidentified HESS J1908+063 [51], which is also detected above 10 TeV in this work. HESS J1908+063 is very extended and has several plausible counterparts including the SNR G40.5−0.5 and two energetic pulsars capable of powering a PWN [99].

The emission mechanism of the HAWC sources, which are discussed above, is yet to be identified. In addition, the angular resolution of the HAWC instrument [123] is slightly worse than the typical resolution of Cherenkov telescopes, resulting in difficulties with accurate emission localisation and potential source confusion. The H.E.S.S. instrument has a better angular resolution, especially at small event offsets. In addition, despite having a somewhat worse sensitivity than HAWC approximately above 5 TeV (see Figure 3.10 [86]), H.E.S.S. has a lot of archival data and their analysis at the highest energies can help to identify the nature of the most extreme accelerators in our Galaxy. Such a study requires a detailed investigation of each individual source, for which the method presented in this work can be the basis.

[9] Besides eHWC J1825−134 and eHWC J1907+063, there are two more sources detected by HAWC at energies beyond 100 TeV, specifically eHWC J2019+368 [13] and the Crab Nebula [12].

Chapter 7

Summary and outlook

The H.E.S.S. experiment is built to work in a wide energy range from approximately 100 GeV to several tens of TeV. H.E.S.S. analyses are typically optimised to have the best sensitivity at energies around 1 TeV or less. However, there are many topics in gamma-ray astronomy that would benefit from a better sensitivity at higher energies, where it is limited by small gamma-ray statistics due to typically steeply falling gamma-ray source spectra. This work focuses on the optimisation of the H.E.S.S. analysis at high energies and increasing of the gamma-ray statistics above 10 TeV. The analysis approach developed is applied to the analysis of the Galactic plane survey data above 10 TeV.

Studies of the H.E.S.S. gamma-ray acceptance curves shows that a substantial part of all detected events at high energies originate from large offset angles. However, due to the degradation of reconstruction accuracy as the event offset increases, a maximum event offset cut of approximately 2.5° is typically applied in the H.E.S.S. analysis and results in a rejection of large-offset events. This work investigates the possibility of increasing the maximum event offset from around 2.5° to approximately 4° as a promising way to improve the gamma-ray statistics at high energies. The main idea of this approach is that observations taken with an offset of up to 4° (instead of the standard 2.5°) to the source of interest can be considered for the analysis of this source. It increases the effective source exposure and potentially the high-energy event statistics. Good targets for the application of such a concept can be sources in the Galactic plane, since this is a densely populated region of the sky and the VHE sources are located relatively close to each other.

The major challenges of this approach are a degradation of the reconstruction accuracy and an increase of the background rate as the offset angle of events increases. In order to manage the issues encountered, the DISP direction reconstruction method [164] is implemented within the HAP analysis framework, and improvements to the standard BDT-based gamma-hadron separation method [167] are developed. In addition, improvements of the direction reconstruction and background rejection improve the sensitivity of the H.E.S.S. analysis for events at low offset angles, i.e. below 2.5°. More accurate direction reconstruction results in an improved angular resolution of the analysis and, therefore, a smaller size of the test region for point-like sources, which accumulates less background. Better gamma-hadron separation leads to a decrease of the background rate and, at the same time, an increased effective area for gamma-ray detection. Overall, a lower level of accumulated background and larger effective area are the key to a better instrument sensitivity.

Originally the DISP method was used for single Cherenkov telescope systems such as Whipple and MAGIC I. Nowadays, it is also widely used for stereoscopic systems like MAGIC II and VERITAS. In this work, the DISP method, originally developed for the CT 5 mono analysis [164], is extended for the stereoscopic reconstruction of events observed with CT 1 - 4 telescopes. At the preselection level, application of the DISP method yields 5 - 10% of an angular resolution improvement compared to the standard method of image major axes intersection. At 2° offset angle, the improvement is up to 20 - 30%, depending on the zenith angle, and increases with the event offset.

The improvement of the standard background rejection method [167] is accomplished by training the BDTs in different offset angle bands, increasing the number of energy bands for training between 5 TeV and 100 TeV and introducing additional training variable that improves the gamma-hadron separation. These modifications allow for a reduction of the background rate at large offset angles nearly to a level typically obtained at 0.5° event offset. The quality factor of the background rejection cut showed 20 - 50% improvement over the standard method at energies above 10 TeV for zenith angle of 20°, and 40 - 80% at 45 - 50° zenith angles. All together, the implementation of the DISP method and modifications to the background rejection results in a 10 - 20% improvement of sensitivity at offset angles below 2.5° and allowed for the usage of events at large offset angles up to approximately 4°, which was not possible before.

Although the analysis of the Galactic plane data demonstrates that promising results are already achieved with the analysis presented in this work, the proposed analysis approach would benefit from additional improvements in future. For instance, using a larger pool of gamma-ray simulations, the DISP method could be extended to cover different azimuth angles and energy bands. The latter could be useful for improving the angular resolution of the analysis as well as possibly reducing the energy bias. The modified background rejection method could also be further improved by finding additional training variables with gamma-hadron separation power.

In this study, the DISP method and improved background rejection are referred to as the high-energy analysis and used as a stand-alone analysis method. However, they can also be used in combination with the ImPACT technique [169]. The ImPACT technique uses a pixel-wise likelihood method for the reconstruction of the shower parameters and is employed to obtain a superior angular resolution. It is usually applied after the standard gamma-hadron separation step, which can be replaced by the improved version proposed in this work. The ImPACT method also uses the event direction reconstructed with the standard geometry method for the seeding of parameters. The DISP method is based on shower image parameters and has a better reconstruction accuracy than the geometry approach and can be used instead of it for the seed parameter evaluation, which would result in a better performance of the ImPACT method. Moreover, despite the fact that the DISP method was implemented into the HAP framework as a part of the high-energy analysis optimisation, it performs better than the standard geometry reconstruction at low energies as well. Therefore, the DISP method can be used for the event direction reconstruction in the full energy range accessible to the H.E.S.S. CT 1 - 4 telescopes.

The high-energy analysis proposed in this work is applied to the Galactic plane data above 10 TeV, which is discussed in the last chapter of this thesis. The data are analysed with three configurations of the high-energy analysis with maximum event offsets of 2°, 3° and 4°. The original Galactic plane survey resulted in 78 sources detected in a full energy

range [5]. In this work, 40 out of these 78 Galactic sources are detected above 10 TeV, i.e. they fulfil the detection criteria of reaching $3\,\sigma$ significance in at least two analysis configurations. Members of all source classes presented in the HGPS catalogue are also present among the sources detected above 10 TeV. They comprise: all three binary systems, 4 out of 8 SNRs, 9 out of 12 PWNe and 2 out of 8 composite sources. There are also 18 not firmly identified sources out of the 36 listed in the HGPS catalogue, as well as 4 out of the 11 sources that do not have associations in other wavelengths.

As expected, in general, the sources that have a high gamma-ray flux and hard gamma-ray spectra are typically detected above 10 TeV, while weak sources with steep spectral indices are not. Overall, the highest source significance in most cases is reached when they are analysed with the high-energy analysis with 2° and 3° maximum event offset. The high-energy analysis with 4° maximum event offset usually accumulates too many background events, which prevents it from attaining high significance values. On the other hand, the large-offset analyses most often gain the largest number of excess counts. In the case of strong sources, a large number of excess events can be more important than high significance, since it is an essential component for morphological or spectral studies.

In this thesis, two selected sources are also reviewed in greater detail. The first is HESS J1731−347 [38] – a 2 - 6 kyr old, middle-aged SNR. It is one of the few SNRs with its shell morphology seen in VHE gamma rays. The western part of the remnant is coincident with a dense molecular cloud core [159]. Based on the multi-wavelength data, there is a hypothesis that the remnant has collided with the MC-core and, as a result, the HE and VHE gamma-ray emission from the collision region has a hadronic origin, while the emission from the rest of the remnant is leptonic [87]. In this work, the more than 10 TeV emission is revealed only in the eastern part of the source, i.e. on the opposite side of the remnant from the MC-core. The location of this region is coincident with the emission detected by *Fermi*-LAT above 10 GeV [87]. Assuming the same origin of emission in both energy domains, the result obtained above 10 TeV in this study is consistent with the leptonic scenario and could support the overall hypothesis.

Another interesting region discussed here is the putative TeV PWN around the energetic pulsar PSR J0855−4644, which is spatially coincident (but not associated) with the south-eastern rim of the shell SNR Vela Junior (HESS J0852−463) [2]. The PWN is detected at X-ray and radio wavelengths [29, 154, 155]. Interestingly, the morphology at radio wavelengths resembles one that features a bow shock: a partial ring-like structure in the southeast and faint tails of emission in the northwest [155]. With a rather large spin-down energy flux $\dot{E}/d^2 \geq 10^{36}\,\mathrm{erg\,s^{-1}\,kpc^{-2}}$ [29], PSR J0855−4644 is assumed to power a TeV PWN. However, its detection in the H.E.S.S. energy range is complicated due to its overlap with the very bright Vela Junior SNR. A previous study revealed a cutoff at an energy of 6.7 TeV in the Vela Junior spectrum and an indication of the cutoff increase in the part of Vela Junior, which could be potentially contaminated by the PWN around PSR J0855−4644 [2]. However, the significance of these findings appeared to be too low to draw firm conclusions about the PWN. At more than 10 TeV energies, Vela Junior is rather faint due to the spectral cutoff. At these energies, the southeast part of the remnant, which is coincident with the pulsar position, is brighter than the northwestern part, while at lower energies the situation is opposite. However, above 20 TeV, there is only one significant region within the Vela Junior boundaries and it is positionally coincident with the pulsar. Moreover, the emission above 20 TeV is located mainly towards the northwest

from the pulsar position, i.e. roughly the same direction as the faint tail-like structures observed in the radio domain. Thus, the obtained results are in agreement with the multi-wavelength observations and are a strong indication of the existence of the TeV PWN around PSR J0855−4644. Keeping in mind that PSR J0855−4644 shows similarities with Vela pulsar (PSR B0833−45) [146], it is plausible that its TeV PWN is similar to Vela X (HESS J0835−455) [7] and might also have an IC peak in the spectrum around 10 TeV.

Additionally, during the background systematics study in this work, a hotspot in the vicinity of PSR J1413−6205 [156] is found. PSR J1413−6205 is a middle-aged pulsar energetic enough to sustain a TeV PWN. Recently, this region was also re-analysed above 1 TeV and 5 TeV, where more extended emission was detected, which shrinks toward the pulsar position as energy increases [109]. The findings above 10 TeV in this work are well in agreement with the results obtained at lower energies and strongly support the PWN scenario.

The dataset analysed in this work covers only the H.E.S.S. observation period between 2004 and 2013. In recent years, the amount of the H.E.S.S. archival data has significantly increased and should be included in future high-energy studies. The inclusion of this data can substantially increase the exposure in the Galactic plane and allow for more accurate morphological and spectral analysis of the sources. Results achieved analysing the H.E.S.S. data at high energies could serve as a guidance for future VHE gamma-ray experiments with outstanding sensitivity at high energies such as CTA [30], LHAASO [63] and SWGO [27]. In addition, studies of large-offset event analysis can be relevant for the middle and small-size telescopes in CTA, which will have a FoV larger than in the H.E.S.S. telescopes.

Overall, the analysis of sources at energies above 10 TeV can considerably contribute to the energy-dependent picture of VHE gamma-ray sources. Increased statistics at high energies can help to measure more precisely the cutoff region of the source spectra and potentially distinguish between leptonic and hadronic mechanisms of gamma-ray production in VHE sources. This is important for studies related to the origin of cosmic rays in general and, in particular, to the search for the PeVatrons in the Galaxy, which are responsible for the cosmic-ray acceleration up to energies of about 10^{15} eV. Also, precise spectral measurements of Extragalactic VHE gamma-ray sources at high energies can contribute to the EBL studies, and hence, to the understanding of formation and evolution of galaxies in the Universe.

Appendix

Appendix A

High-energy analysis (supplementary material)

This appendix consists of supplementary material mainly for Chapter 4, which discusses the usage of large-offset events (up to around 4°) in the analysis as a promising way to increase the gamma-ray statistics at high energies. Sections A.1 and A.3 show the distributions of the image parameters involved in the MLP training for the DISP method, which is implemented within the HAP framework in this work in order to overcome the problem of deteriorated angular resolution at large event offsets. In addition, the results of two different MLP training approaches are compared in Section A.2. Finally, Sections A.4 and A.5 presents the distributions of the input parameters for the BDT training as well as its performance for the gamma-hadron separation modified in this study to obtain a better background rejection and decrease the background rate at large offset angles.

A.1 Input parameters for the ANN training

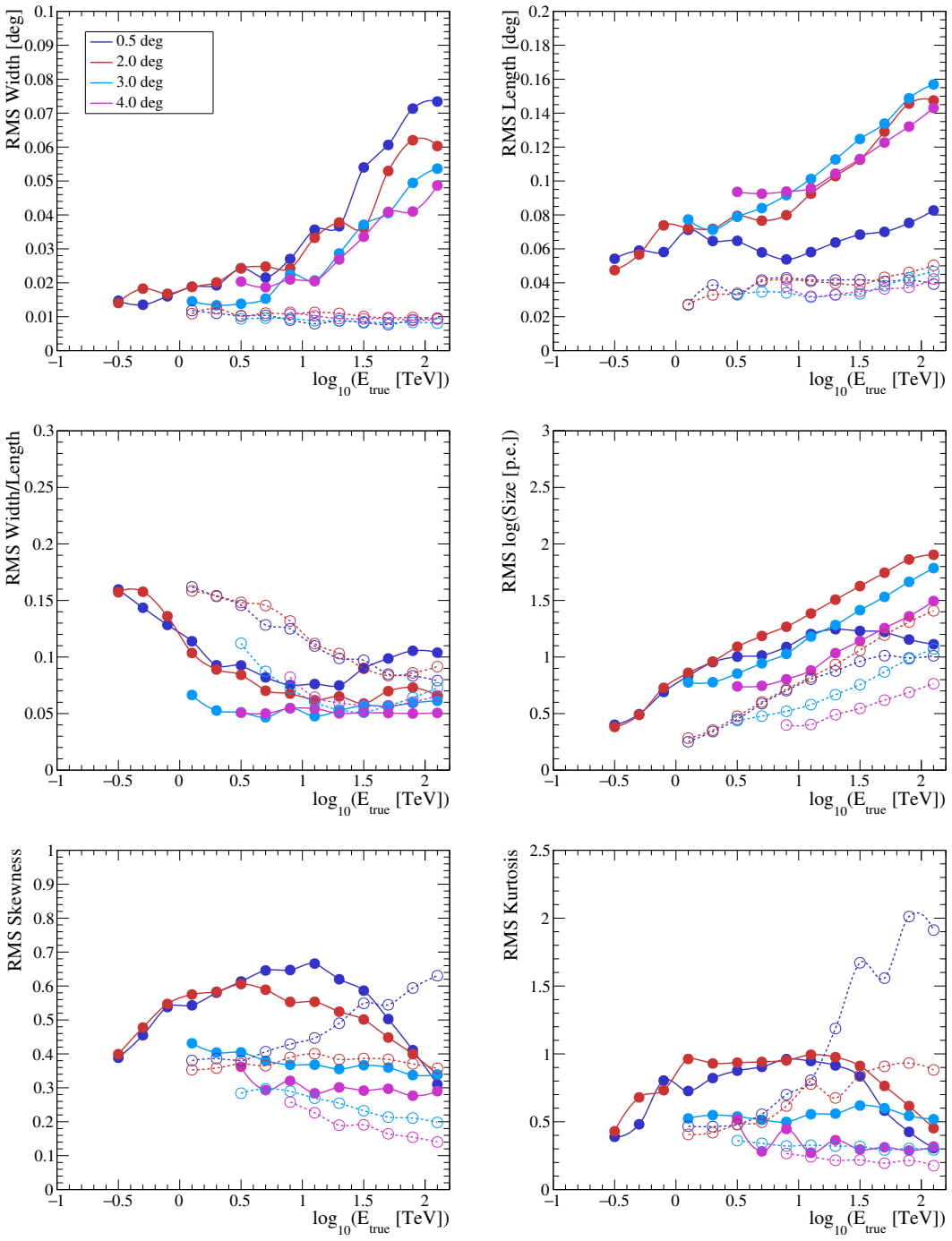

Figure A.1: RMS values of the input variable distributions for the MLP training in the DISP method. The six plots here represent the input variables, which are based on the image shape. Line colour shows different event offset bands. Solid and dashed lines show diffuse gamma rays simulated with zenith angles of around 20° and 60°, respectively.

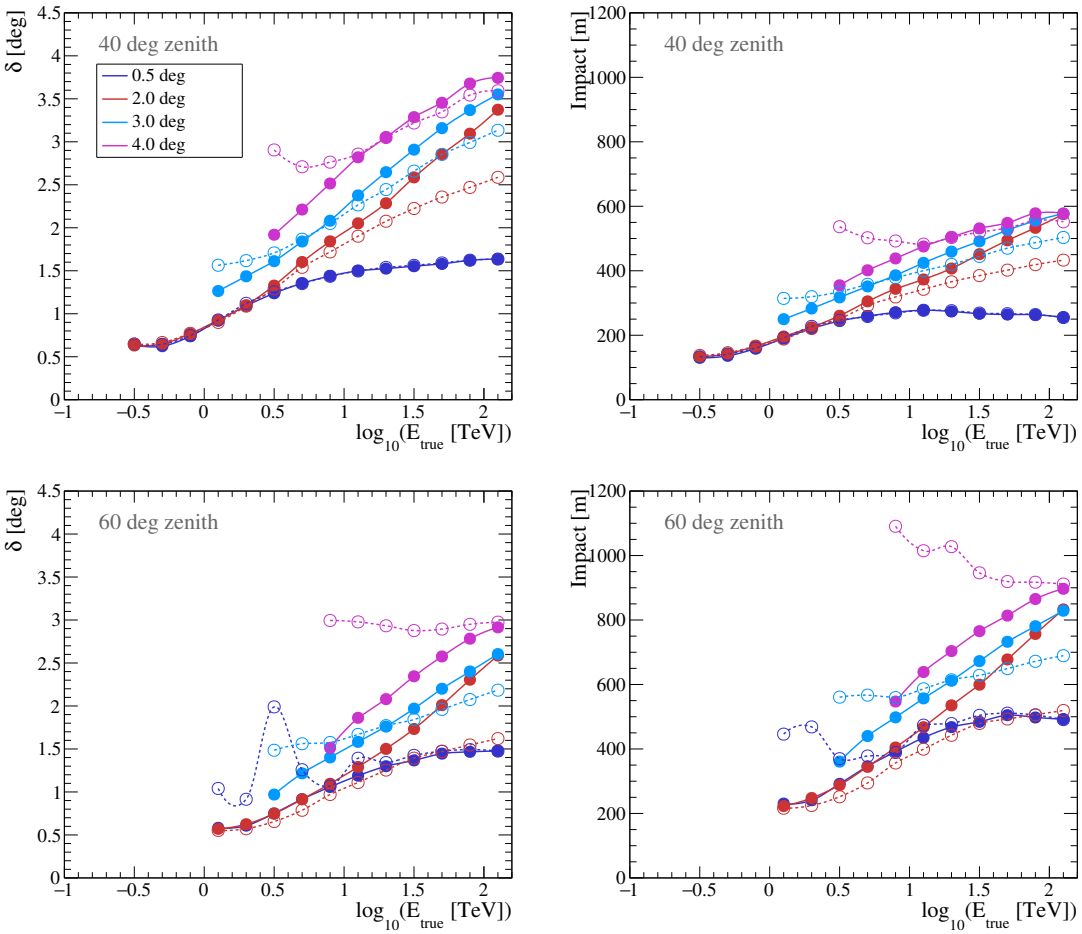

Figure A.2: Mean values of the seed and target variable distributions for the MLP training. Left column shows a comparison of δ_{true} (target, solid lines) and δ_{reco} (seeding parameter, dashed lines) for the network training used for the shower direction reconstruction. Right column shows a comparison of $Impact_{\text{true}}$ (target, solid lines) and $Impact_{\text{reco}}$ (seeding parameter, dashed lines) for the network training used for the shower core position reconstruction. Colour of lines indicates different offset angle bands. All plots are produced using diffuse gamma-ray simulations.

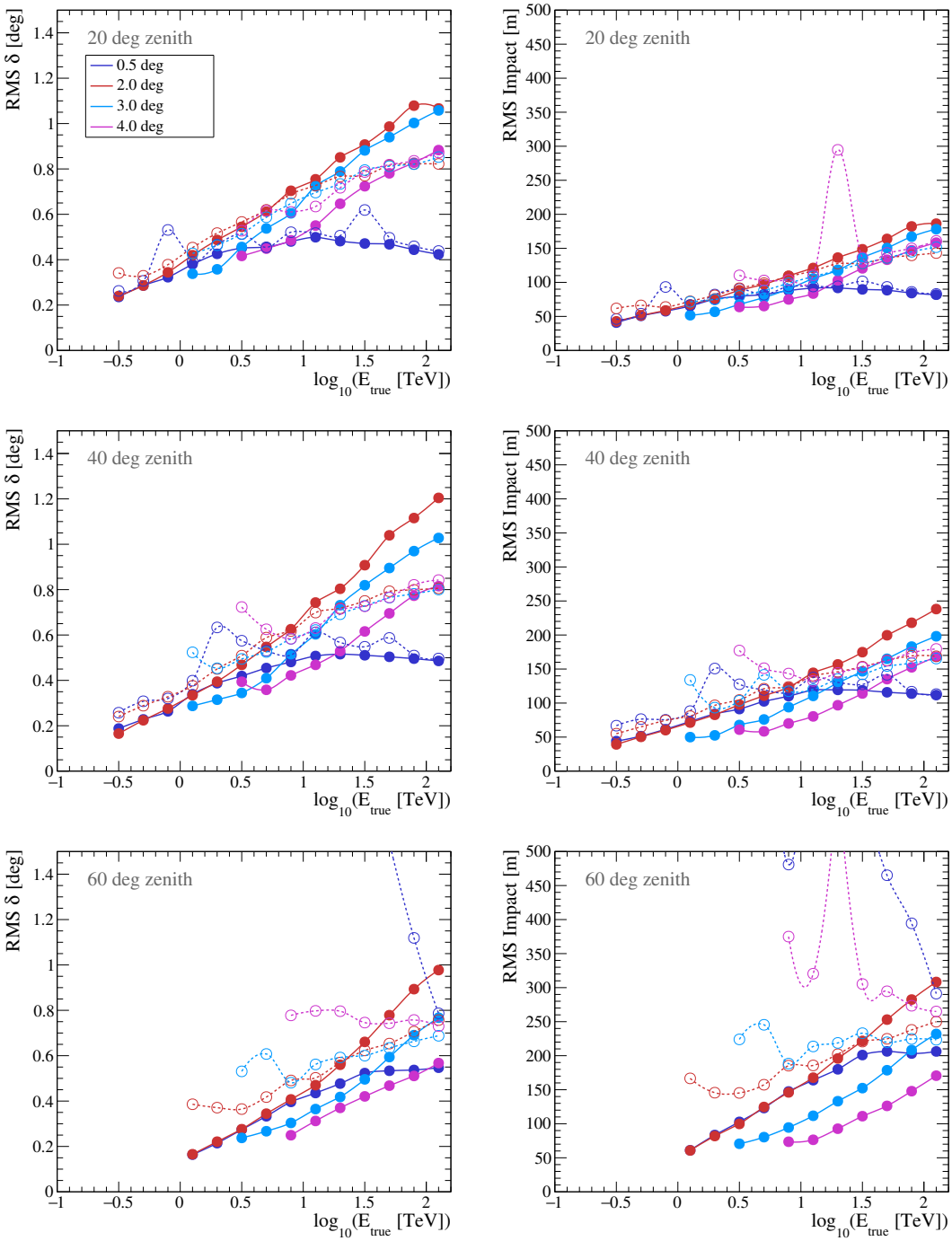

Figure A.3: RMS values of the seed and target variable distributions for the MLP training. Left column shows a comparison of δ_{true} (target, solid lines) and δ_{reco} (seeding parameter, dashed lines) for the network training used for the shower direction reconstruction. Right column shows a comparison of $Impact_{\text{true}}$ (target, solid lines) and $Impact_{\text{reco}}$ (seeding parameter, dashed lines) for the network training used for the shower core position reconstruction. Colour of lines indicates different offset angle bands. All plots are produced using diffuse gamma-ray simulations.

A.2 Comparison of two different ANN training approaches

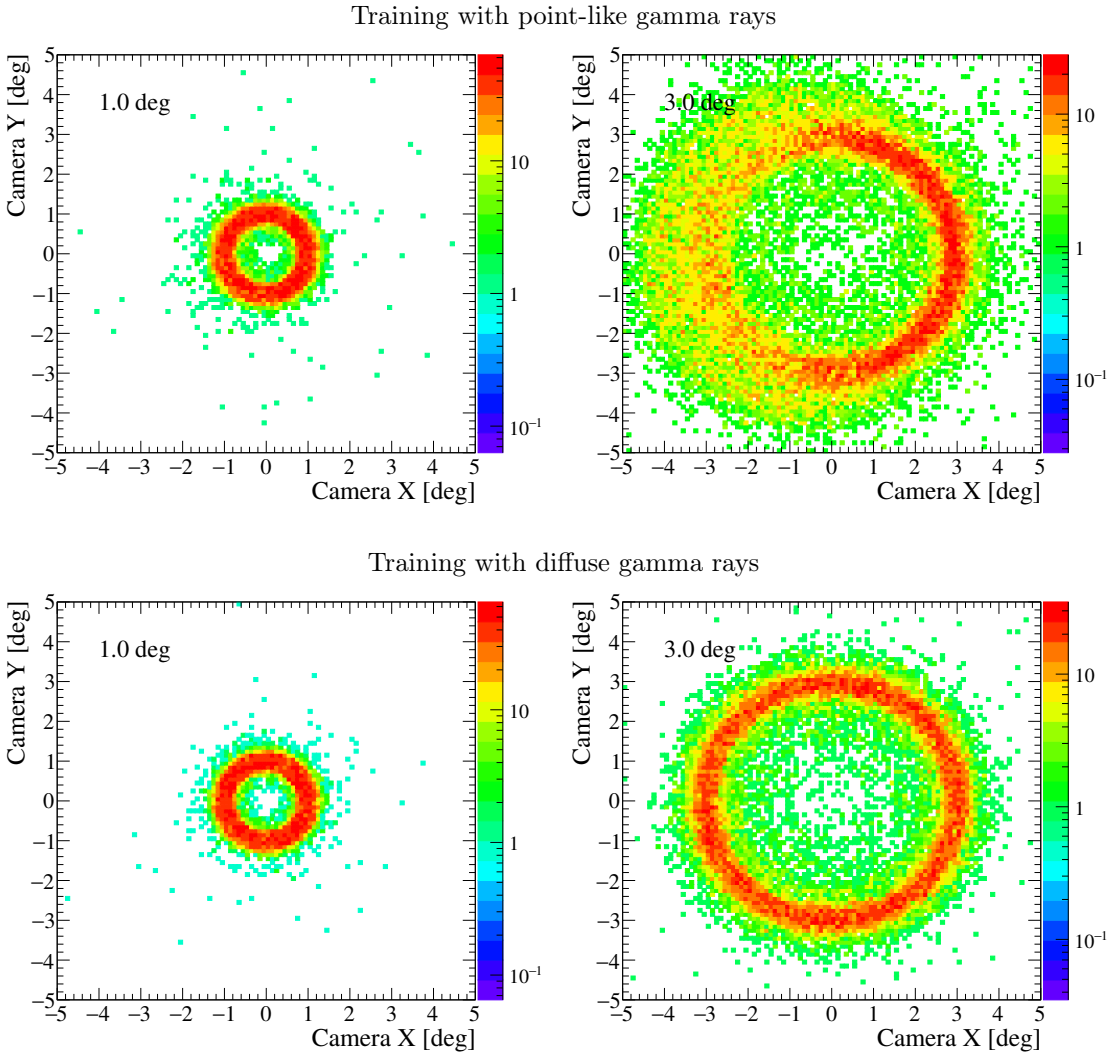

Figure A.4: The distribution of the reconstructed event directions in the camera plane in the case of the MLPs training produces with point-like (top row) and diffuse gamma ray simulation (bottom row). The examples show the direction distributions for the diffuse gamma rays simulated at around 1° and 3° offset angle. The width of the simulated ring is 0.5°.

A.3 Influence of optical efficiency on image parameters

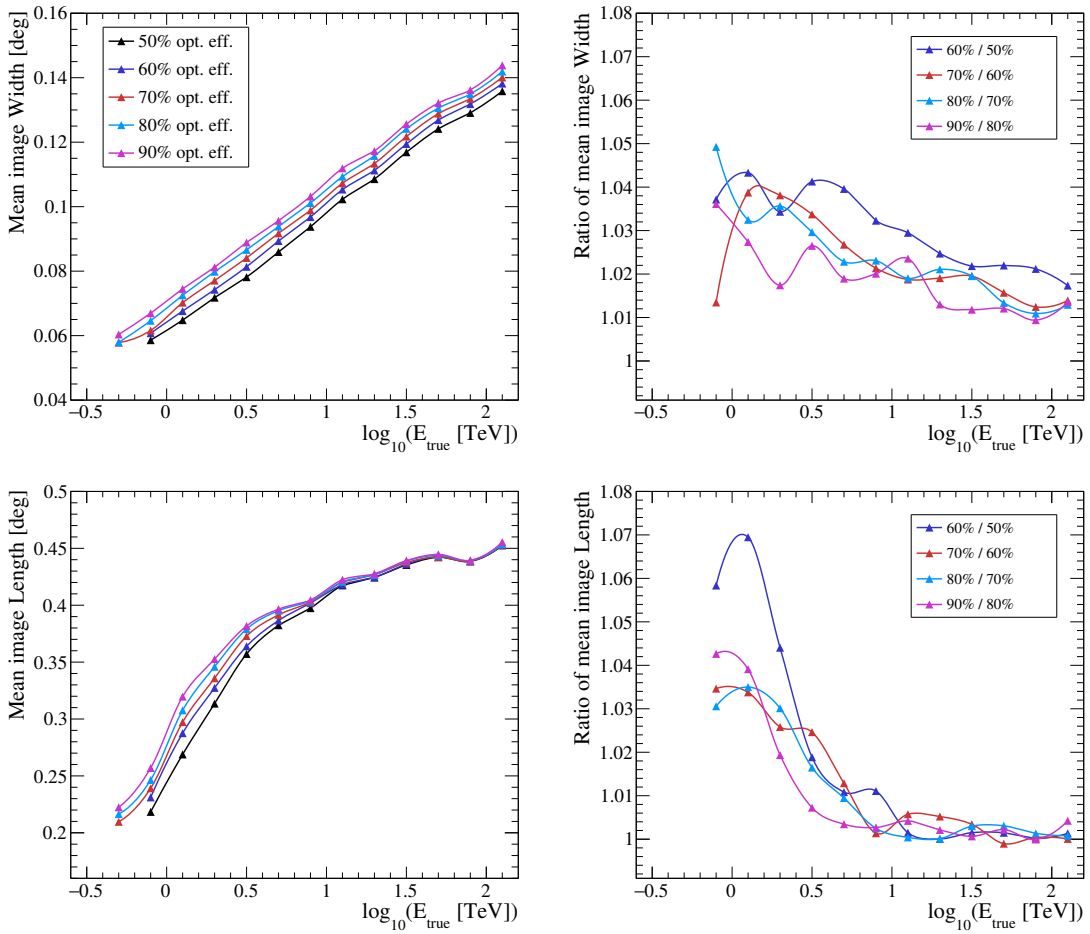

Figure A.5: Mean width and length of the shower images as a function of the primary energy depending on the telescope optical efficiency are presented in the top and bottom row, respectively. The left column shows the actual mean length and width values for different optical efficiencies, while the right column displays the ratio of these values. All plots are produced using gamma rays simulated at 20° zenith angle with 0.5° event offset.

A.4 Input parameters for the BDT training

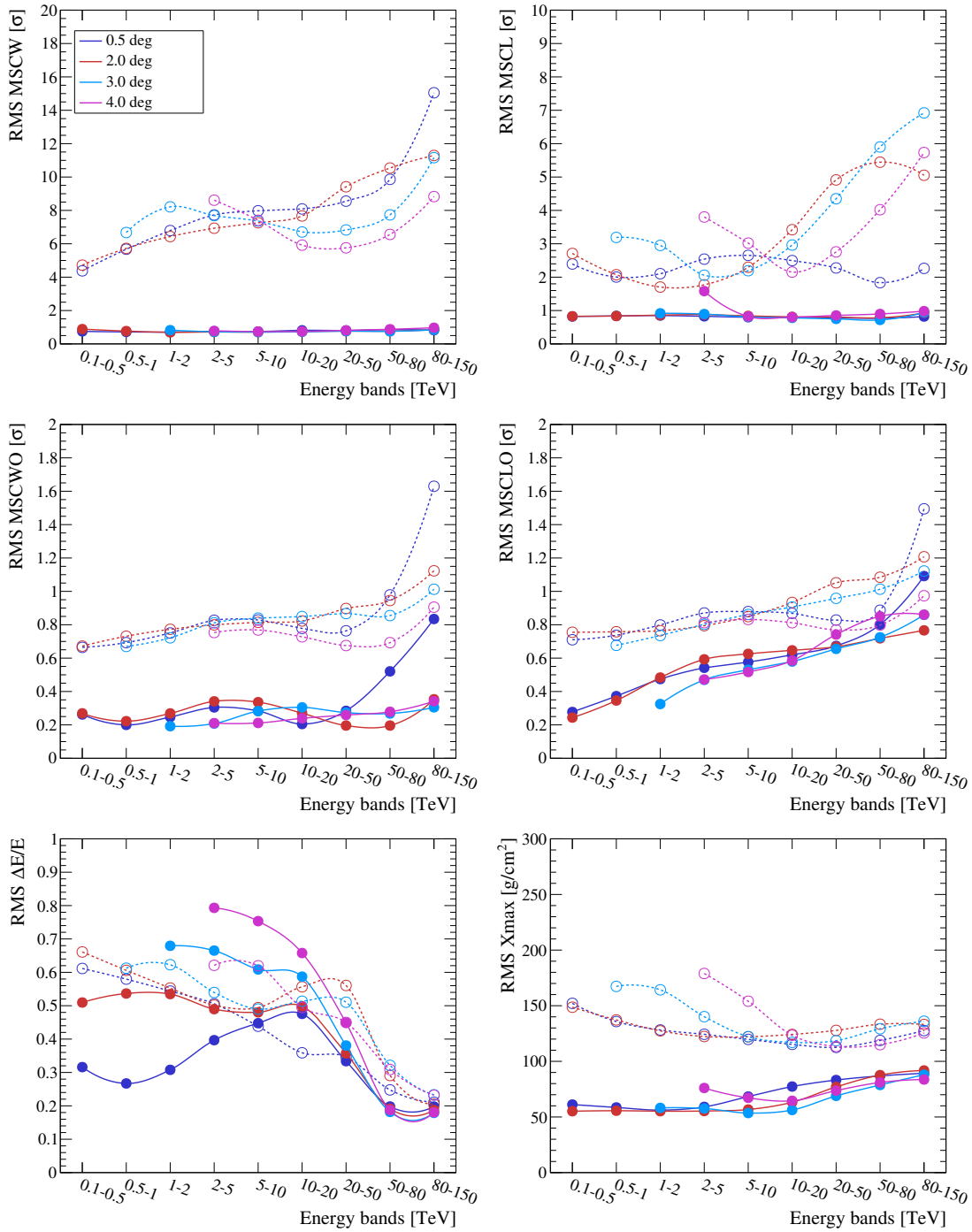

Figure A.6: RMS values of the input variable distributions for the BDT training. Line colours denote different event offset bands. Solid lines show point-like gamma rays simulated at 20° zenith, while dashed lines indicate real observations of empty fields, i.e. cosmic rays, in the zenith angle range between 15° and 25°.

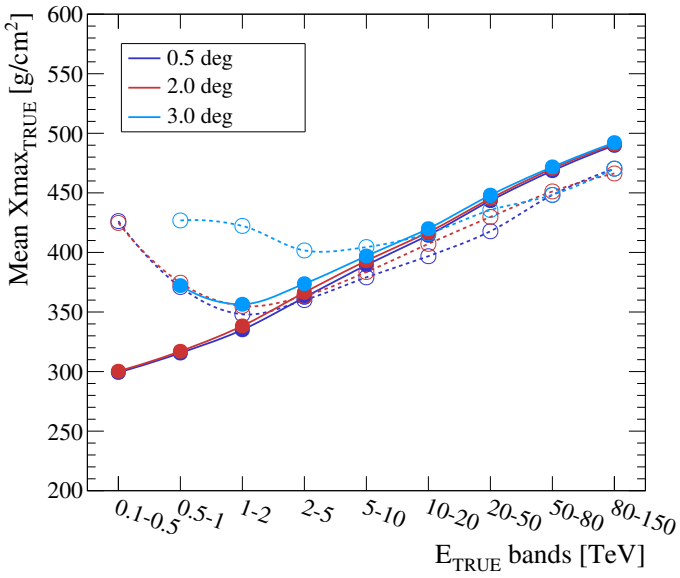

Figure A.7: Mean values of the true $X_{\max}$ distribution as a function of the true primary energy. Colour of the lines shows different offset angle band. Solid lines represent simulated point-like gamma rays, while dashed lines display simulated diffuse protons. The zenith angle for both simulation sets is 20°. A view-cone of the proton simulation is 3°, which is why the figure does not show a 4° offset curve. Curves that correspond to the proton and large-offset gamma-ray sample experience an upturn towards low energies. Most likely it is an effect of energy threshold. The energy threshold curves for gamma rays as a function of the offset angle are displayed in Figure 5.4. Hadronic showers for the same primary energy produce nearly three times less Cherenkov light than electromagnetic showers. Therefore, the energy threshold for protons would occur at higher energies than for gamma rays.

A.5 Performance of the modified gamma-hadron separation

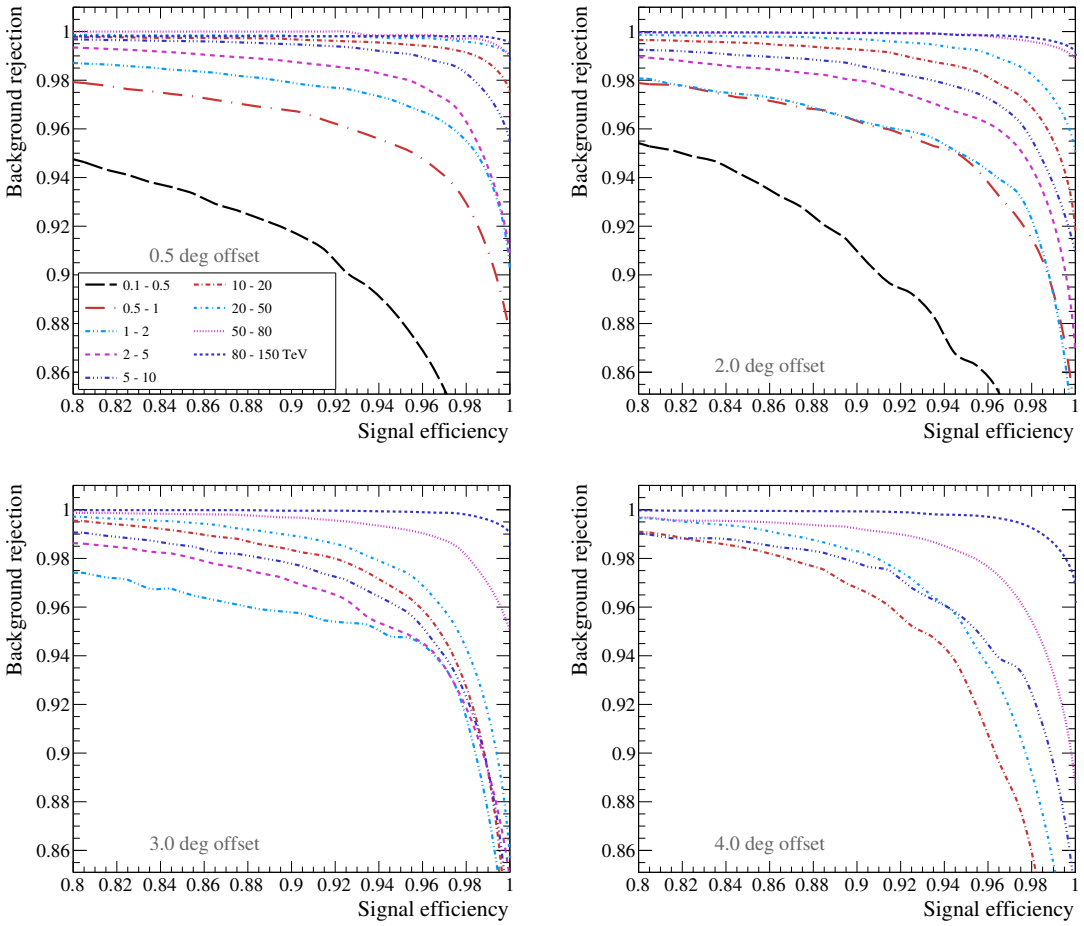

Figure A.8: The performance of the BDT training at different offset angles for the modified gamma-hadron separation. The number of trained energy bands decreases with offset angle increase since the energy threshold increases. All presented curves are taken from the training performed at 20° zenith angle.

Appendix B

The HGPS above 10 TeV (supplementary material)

The following sections contain an additional material for Chapter 6, which discusses the analysis of the Galactic plane survey at energies above 10 TeV using the high-energy analysis with 2°, 3° and 4° maximum event offset as well as the standard analysis with 2° maximum event offset for the comparison. Section B.1 of this appendix is part of the background systematics check and shows the 1D distribution of significance outside the excluded regions calculated for 0.1° correlation radius. Section B.2 presents the exposure of the Galactic plane within the HGPS region. Section B.3 contains several tables that list HGPS sources considered above 10 TeV, properties of their test regions constructed in this work and analysis characteristics obtained for these regions. Section B.4 presents the identifications of the more than 10 TeV sources detected in this work.

B.1 Excluded significance distributions for different analysis setups

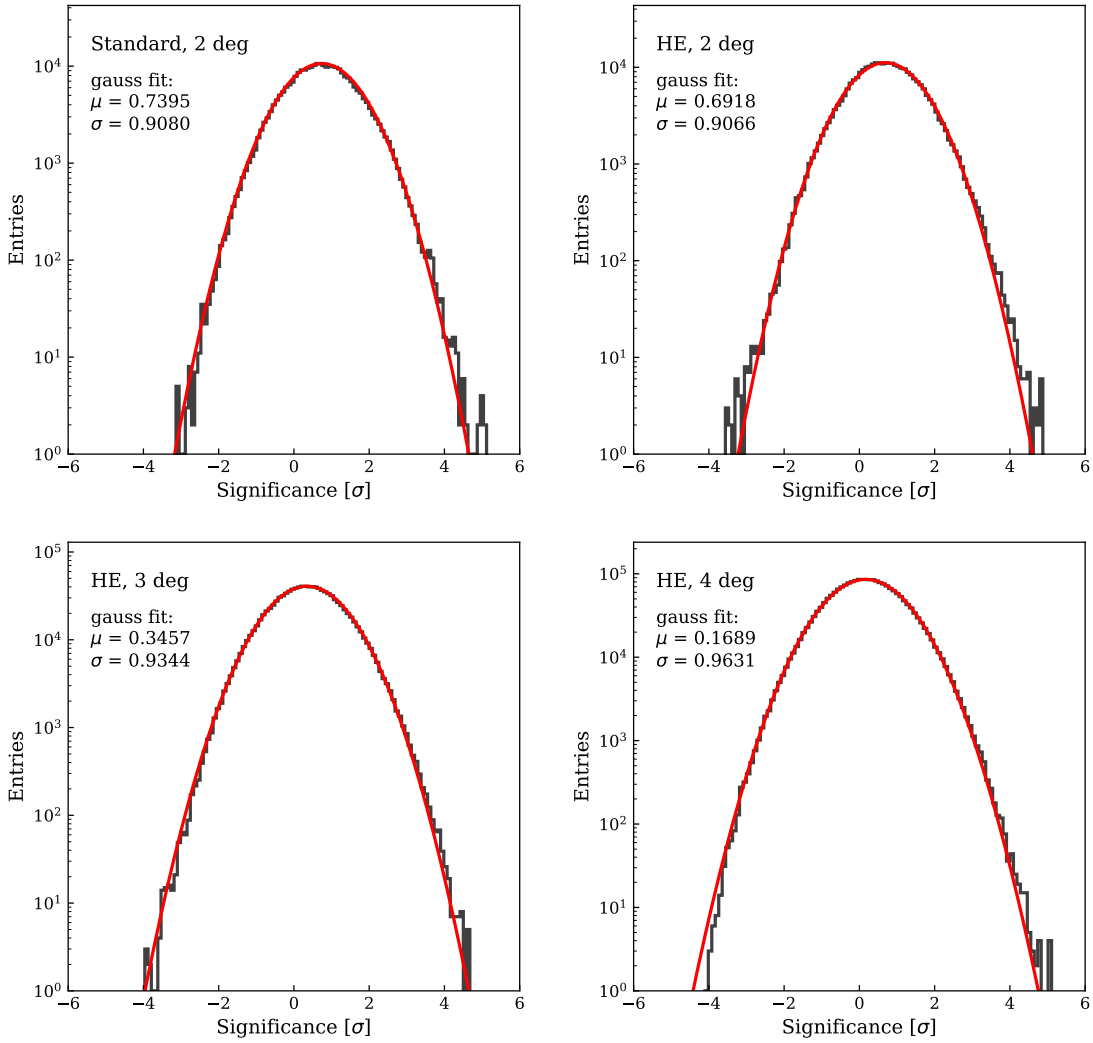

Figure B.1: The comparison of the 1D distributions of the excluded significance for the high energy analysis with 2°, 3° and 4° maximum event offset and the standard analysis with 2° maximum event offset at energies above 10 TeV. The black histogram shows the events outside the exclusion regions that are observed analysing the HGPS dataset, while the red line indicates the Gaussian fit. The correlation radius of the excluded significance map is 0.1°.

B.2 Exposure of the Galactic plane in the HGPS region

The sky exposure is presented here in the form of an *expected gamma-ray map*. It is one of the maps created automatically by the Galactic survey analysis pipeline. The expected gamma-ray map is produced on a run-by-run basis by multiplying the effective area (that corresponds to the observation conditions), observation time and assumed source spectrum, and integrating the result over the energy range of interest. The assumed energy spectrum is a power law with the index of $\Gamma = 2.3$ and flux normalisation at 1 TeV of $1\,\mathrm{TeV}^{-1}\,\mathrm{m}^{-2}\,\mathrm{s}^{-1}$. In this study, the Galactic plane analysis is performed from 10 to 300 TeV.

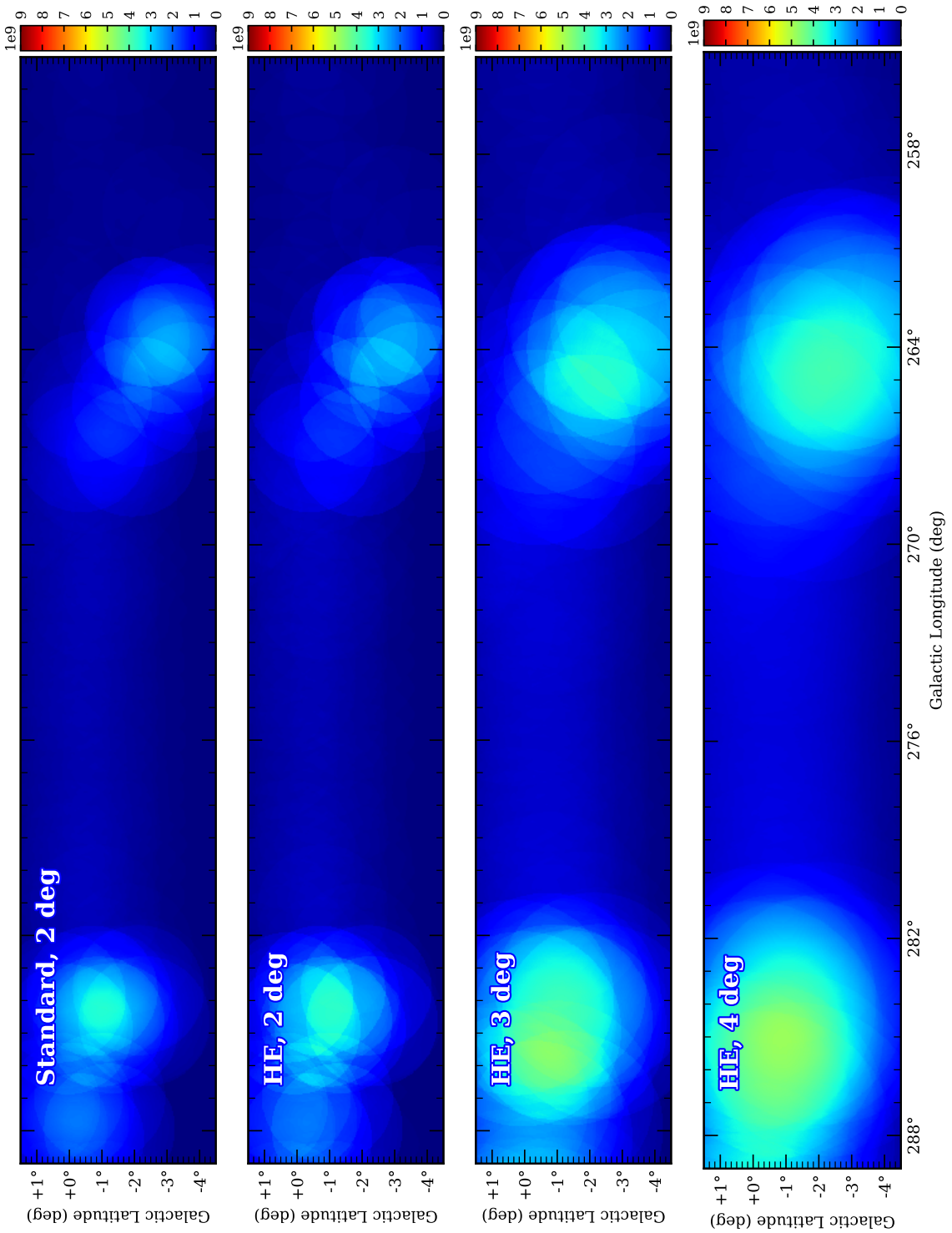

Figure B.2: The comparison of the expected gamma-ray maps at energies above 10 TeV for the high-energy analysis with 2°, 3° and 4° maximum event offset and the standard analysis with 2° maximum event offset. Regarding the details on the expected gamma-ray map production, see the beginning of this section.

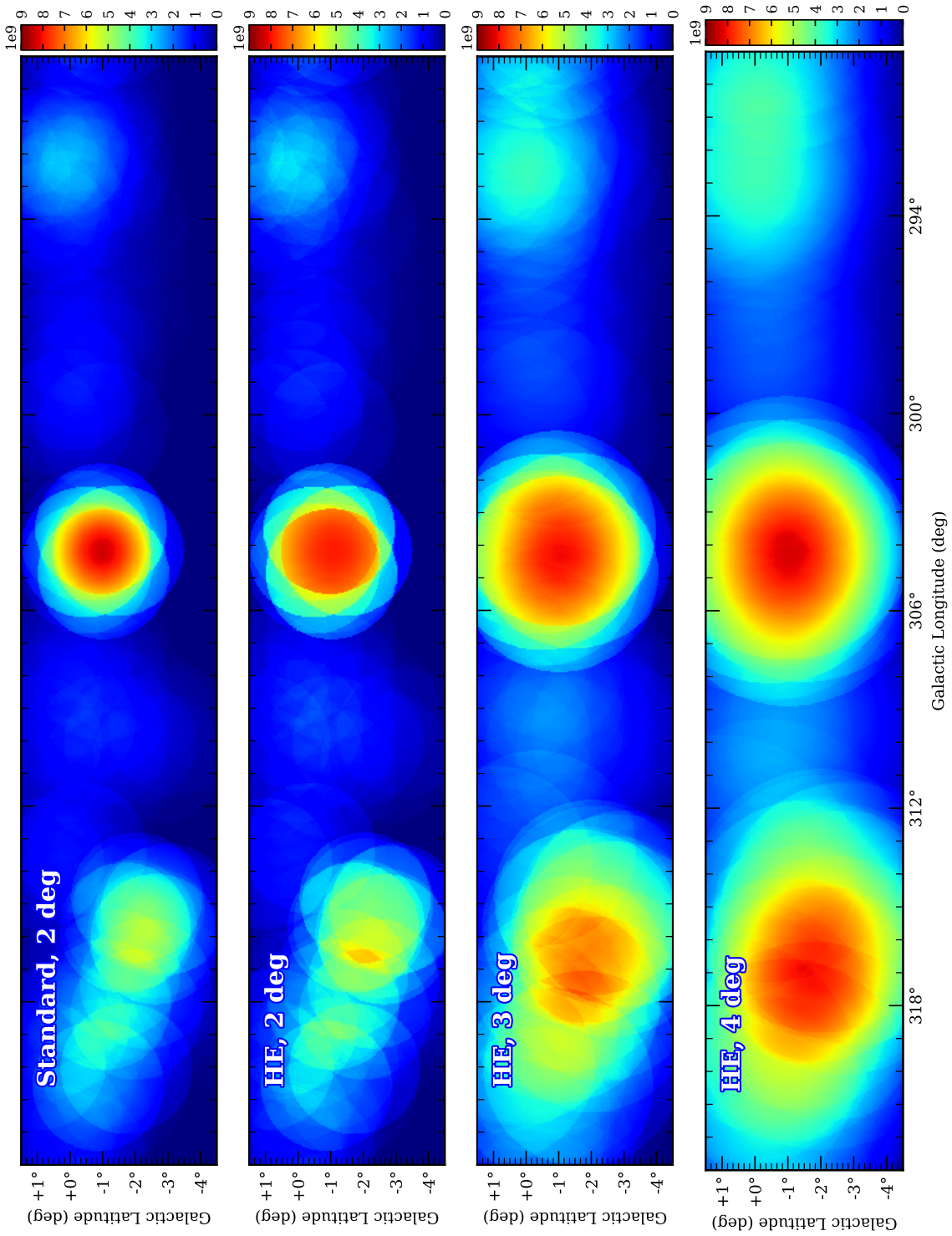

Figure B.3: The comparison of the expected gamma-ray maps at energies above 10 TeV. Continuation of Figure B.2. Regarding the details on the expected gamma-ray map production, see the beginning of this section.

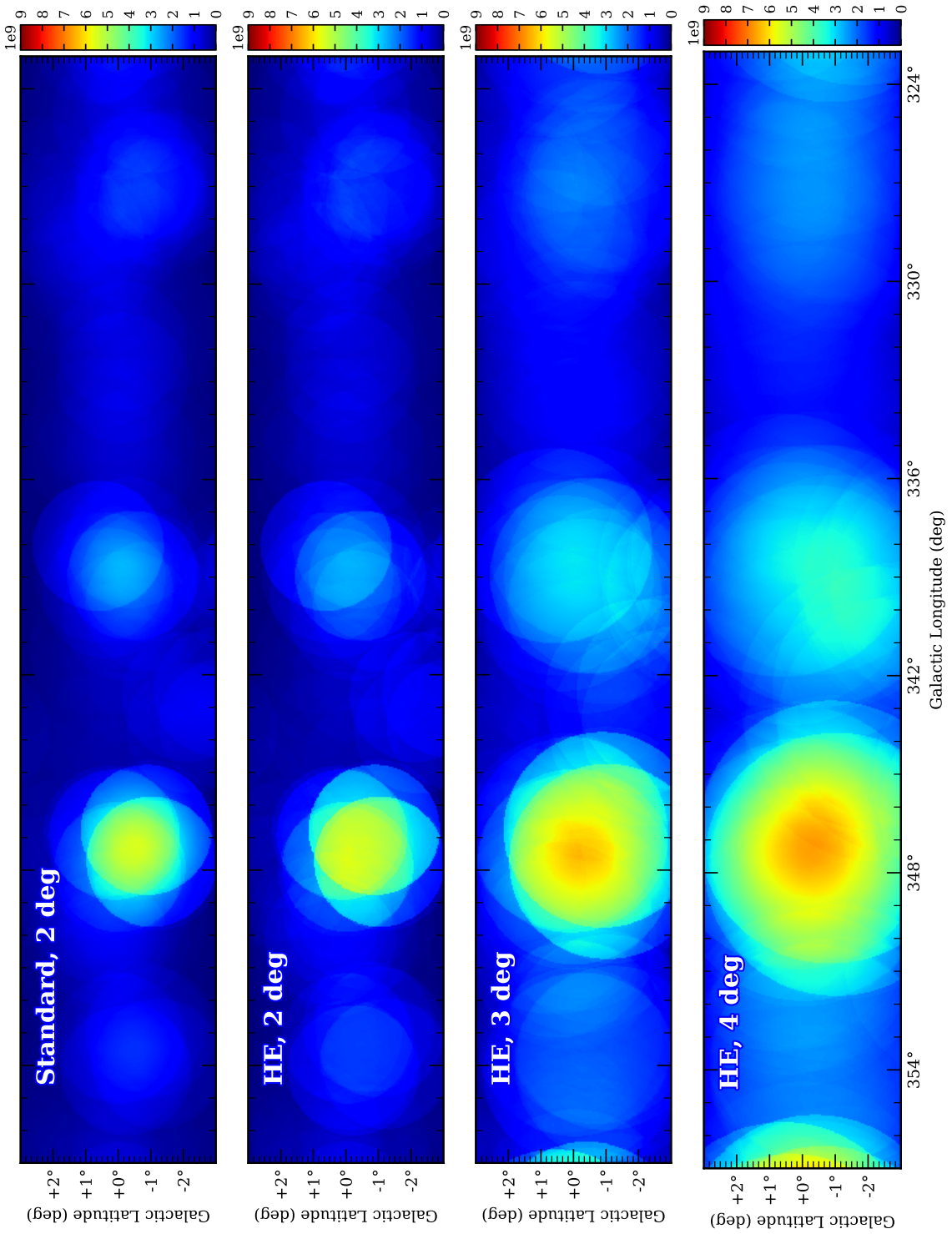

Figure B.4: The comparison of the expected gamma-ray maps at energies above 10 TeV. Continuation of Figure B.2. Regarding the details on the expected gamma-ray map production, see the beginning of this section.

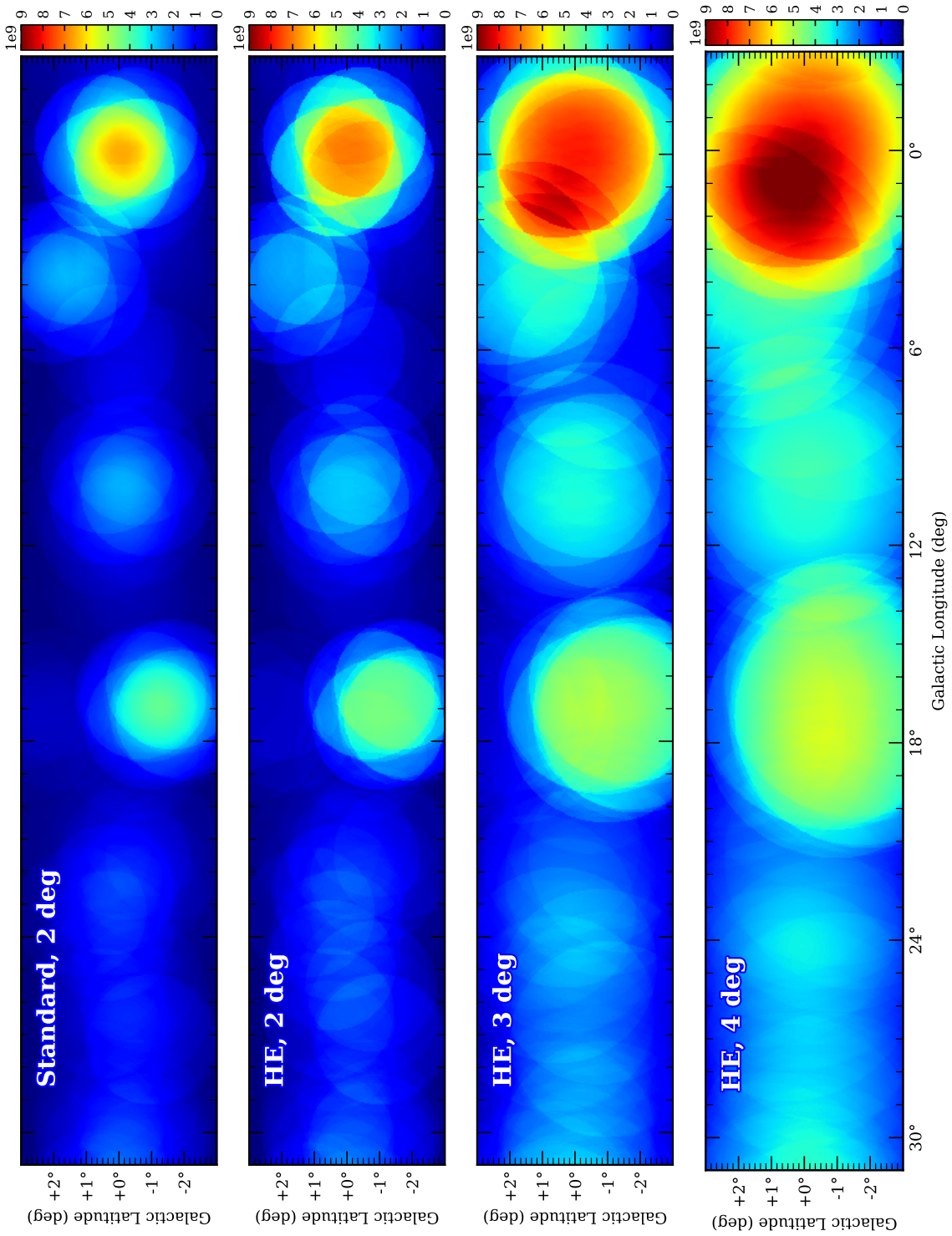

Figure B.5: The comparison of the expected gamma-ray maps at energies above 10 TeV. Continuation of Figure B.2. Regarding the details on the expected gamma-ray map production, see the beginning of this section.

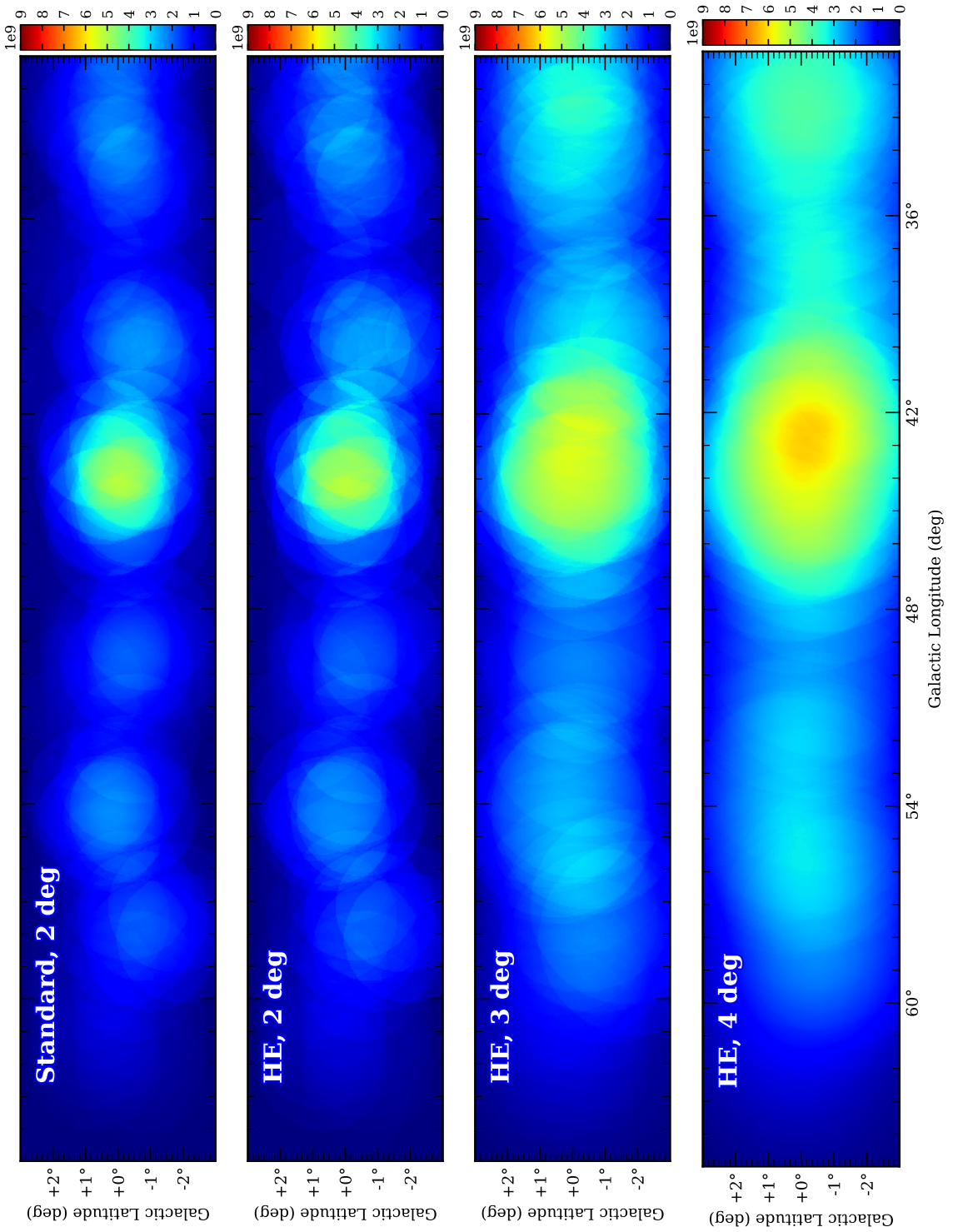

Figure B.6: The comparison of the expected gamma-ray maps at energies above 10 TeV. Continuation of Figure B.2. Regarding the details on the expected gamma-ray map production, see the beginning of this section.

B.3 Properties of the source test regions

The tables presented in this section comprise properties of the test regions defined for 42 preselected HGPS sources as well as analysis characteristics calculated for these test regions. Thus, Tables B.1 - B.2 list the test-region positions determined for four analysis setups used in this study for the HGPS data analysis above 10 TeV. Tables B.3 - B.10 contain the sizes of these test regions as well as analysis quantities such as the number of On and Off events, α parameter, number of excess and background counts, significance and signal-to-background ratio.

In the following tables, the sources marked with † are located to close to each other, and therefore, the positions of their test regions are taken from the HGPS catalogue [5] and the extensions are set to the values smaller than the defined minimum, i.e. smaller than 0.2°. The Galactic Centre source (indicated with ‡) is located in the complicated region with a lot of diffuse emission, thus, the standard value is taken as a position of its test region and extension is set to the minimum value typically used in this work, i.e. 0.2°. The test-region positions for the sources indicated with * are also taken from the HGPS catalogue or dedicated studies [19, 51] due to their complex morphology. The extension of these sources is found employing the θ^2 distribution as for all other sources in Tables B.1 - B.10.

Source name	Size [deg][5]	Position [5]		Position, HE 4 deg		Position, HE 3 deg		Position, HE 2 deg		Position, Standard 2 deg	
		l [deg]	b [deg]	l [deg]	b [deg]	l [deg]	b [deg]	l [deg]	b [deg]	l [deg]	b [deg]
HESS J0835−455*	0.58	263.96	−3.05	263.96	−3.05	263.96	−3.05	263.96	−3.05	263.96	−3.05
HESS J0852−463*	1.00	266.29	−1.24	266.29	−1.24	266.29	−1.24	266.29	−1.24	266.29	−1.24
HESS J1018−589 A	0.00	284.35	−1.67	284.44	−1.75	284.40	−1.73	284.38	−1.73	284.38	−1.65
HESS J1023−575	0.17	284.19	−0.40	284.18	−0.45	284.12	−0.47	284.24	−0.51	284.30	−0.53
HESS J1026−582	0.13	284.85	−0.52	284.90	−0.57	284.92	−0.57	284.94	−0.53	284.96	−0.57
HESS J1302−638	0.01	304.18	−1.00	304.20	−1.03	304.18	−1.03	304.18	−1.03	304.22	−1.01
HESS J1303−631	0.18	304.24	−0.35	304.18	−0.29	304.20	−0.33	304.20	−0.31	304.16	−0.33
HESS J1356−645	0.23	309.79	−2.50	309.70	−2.71	309.72	−2.59	309.76	−2.67	309.74	−2.57
HESS J1418−609†	0.11	313.24	0.14	313.24	0.14	313.24	0.14	313.24	0.14	313.24	0.14
HESS J1420−607†	0.08	313.58	0.27	313.58	0.27	313.58	0.27	313.58	0.27	313.58	0.27
HESS J1442−624	0.30	315.43	−2.29	315.41	−2.53	315.43	−2.53	315.29	−2.35	315.31	−2.17
HESS J1457−593	0.33	318.35	−0.42	318.41	−0.51	318.51	−0.67	318.45	−0.55	318.37	−0.51
HESS J1458−608	0.37	317.95	−1.70	317.81	−1.61	317.89	−1.69	317.91	−1.67	318.05	−1.85
HESS J1507−622	0.18	317.97	−3.48	318.15	−3.55	318.13	−3.55	318.21	−3.39	317.99	−3.75
HESS J1514−591	0.14	320.32	−1.19	320.37	−1.23	320.33	−1.19	320.35	−1.23	320.33	−1.23
HESS J1614−518	0.42	331.47	−0.60	331.35	−0.67	331.29	−0.67	331.29	−0.77	331.31	−0.73
HESS J1616−508	0.23	332.48	−0.17	332.41	0.09	332.39	0.07	332.31	0.05	332.49	0.01
HESS J1632−478	0.18	336.39	0.26	336.45	0.33	336.45	0.33	336.45	0.33	336.47	0.35
HESS J1634−472	0.17	337.12	0.26	337.09	0.41	337.07	0.47	337.05	0.37	337.21	0.31

Table B.1: The positions of the test regions defined for the sources of interest. The second and third column shows the size and source position presented in the HGPS catalogue [5]. The remained columns list the region positions derived in this work for four used analysis configurations, i.e. the high-energy analysis with 2° , 3° and 4° maximum event offset and the standard analysis with 2° maximum event offset. For the explanation of † ‡ and * markings see the beginning of this section.

Source name	Size [deg][5]	Position [5]		Position, HE 4 deg		Position, HE 3 deg		Position, HE 2 deg		Position, Standard 2 deg	
		l [deg]	b [deg]	l [deg]	b [deg]	l [deg]	b [deg]	l [deg]	b [deg]	l [deg]	b [deg]
HESS J1640−465†	0.11	338.28	−0.04	338.28	−0.04	338.28	−0.04	338.28	−0.04	338.28	−0.04
HESS J1641−463†	0.04	338.52	0.08	338.52	0.08	338.52	0.08	338.52	0.08	338.52	0.08
HESS J1646−458*	0.50	339.33	−0.78	339.55	−0.49	339.55	−0.49	339.55	−0.49	339.55	−0.49
HESS J1702−420	0.20	344.23	−0.19	344.29	−0.05	344.25	−0.19	344.33	−0.11	344.37	−0.13
HESS J1708−410	0.06	345.67	−0.44	345.71	−0.33	345.67	−0.37	345.65	−0.45	345.79	−0.57
HESS J1708−443	0.28	343.07	−2.32	343.07	−2.31	343.13	−2.53	343.07	−2.47	343.03	−2.41
HESS J1713−397*	0.50	347.31	−0.46	347.31	−0.46	347.31	−0.46	347.31	−0.46	347.31	−0.46
HESS J1718−385	0.12	348.88	−0.48	348.89	−0.47	348.89	−0.45	348.89	−0.45	348.91	−0.49
HESS J1731−347	0.27	353.54	−0.67	353.55	−0.79	353.51	−0.75	353.51	−0.75	353.71	−0.85
HESS J1745−290‡	–	359.94	−0.04	359.94	−0.04	359.94	−0.04	359.94	−0.04	359.94	−0.04
HESS J1747−281	–	0.87	0.08	0.91	−0.03	0.91	−0.01	0.91	−0.01	0.89	−0.03
HESS J1804−216	0.24	8.38	−0.09	8.39	0.09	8.33	0.09	8.39	−0.07	8.27	0.01
HESS J1809−193	0.40	11.11	−0.02	11.04	−0.07	11.04	−0.07	11.04	−0.09	11.02	−0.03
HESS J1813−178	0.05	12.82	−0.03	12.82	−0.07	12.84	−0.09	12.84	−0.09	12.82	−0.07
HESS J1825−137	0.46	17.53	−0.62	17.92	−0.75	17.92	−0.81	17.90	−0.73	17.90	−0.75
HESS J1826−130	0.15	18.48	−0.39	18.54	−0.35	18.54	−0.35	18.54	−0.35	18.42	−0.37
HESS J1826−148	0.01	16.88	−1.29	16.86	−1.35	16.88	−1.35	16.88	−1.35	16.84	−1.35
HESS J1837−069	0.36	25.15	−0.09	25.28	−0.09	25.30	−0.11	25.30	−0.07	25.26	−0.11
HESS J1841−055	0.41	26.71	−0.23	26.22	0.01	26.32	0.07	26.22	0.19	26.26	−0.03
HESS J1849−000	0.09	32.61	0.53	32.72	0.45	32.72	0.45	32.76	0.41	32.74	0.45
HESS J1852−000	0.28	33.11	−0.13	32.90	−0.13	32.92	−0.19	32.98	−0.21	33.02	−0.19
HESS J1858+020	0.08	35.54	−0.58	35.68	−0.45	35.66	−0.53	35.58	−0.41	35.54	−0.51
HESS J1908+063*	0.49	40.55	−0.84	40.58	−0.77	40.58	−0.77	40.58	−0.77	40.58	−0.77

Table B.2: The positions of the test regions defined for the sources of interest. Continuation of Table B.1. For the explanation of † ‡ and * markings see the beginning of this section.

Source name	Size [deg]	Non	Noff	Alpha $\times 10^{-3}$	Background	Excess	Significance [σ]	S/N
HESS J0835−455*	1.10	1905	2197199	0.375	828.32	1076.68	32.14	1.31
HESS J0852−463*	1.22	1733	2915475	0.456	1325.52	407.48	10.58	0.30
HESS J1018−589 A	0.20	59	173118	0.208	36.17	22.83	3.49	0.63
HESS J1023−575	0.35	205	618589	0.229	141.73	63.27	4.96	0.44
HESS J1026−582	0.27	167	451679	0.211	95.24	71.76	6.64	0.75
HESS J1302−638	0.20	124	194827	0.240	46.94	77.06	9.35	1.65
HESS J1303−631	0.46	662	1016275	0.396	398.84	263.16	11.84	0.65
HESS J1356−645	0.40	147	392645	0.215	84.16	62.84	6.16	0.74
HESS J1418−609†	0.18	92	226280	0.271	61.22	30.78	3.66	0.50
HESS J1420−607†	0.18	100	221285	0.278	61.52	38.48	4.50	0.63
HESS J1442−624	0.22	90	318910	0.187	59.48	30.52	3.66	0.51
HESS J1457−593	0.44	676	1135917	0.456	515.38	160.62	6.64	0.31
HESS J1458−608	0.31	281	960663	0.232	224.02	56.98	3.73	0.26
HESS J1507−622	0.20	109	380732	0.204	77.62	31.38	3.34	0.40
HESS J1514−591	0.35	402	613616	0.290	179.27	222.73	14.39	1.26
HESS J1614−518	0.26	47	91723	0.297	27.29	19.71	3.42	0.72
HESS J1616−508	0.31	56	75675	0.415	31.87	24.13	3.94	0.78
HESS J1632−478	0.28	74	82890	0.465	38.70	35.30	5.05	0.92
HESS J1634−472	0.36	130	130904	0.422	55.82	74.18	8.55	1.36

Table B.3: The characteristics obtained for the high-energy analysis with 4° maximum event offset. For the explanation of † ‡ and * markings see the beginning of this section.

Source name	Size [deg]	Non	Noff	Alpha $\times 10^{-3}$	Background	Excess	Significance [σ]	S/N
HESS J1640−465†	0.15	32	29822	0.367	10.94	21.06	5.15	1.92
HESS J1641−463†	0.14	12	25506	0.357	9.11	2.89	0.91	0.32
HESS J1646−458*	1.00	796	1591665	0.405	649.09	146.91	5.74	0.23
HESS J1702−420	0.30	171	325634	0.337	109.73	61.27	5.39	0.56
HESS J1708−410	0.22	75	145268	0.351	51.02	23.98	3.13	0.47
HESS J1708−443	0.21	44	104773	0.260	27.00	17.00	2.95	0.62
HESS J1713−397*	0.86	1615	1729175	0.419	723.68	891.32	28.41	1.23
HESS J1718−385	0.27	178	326547	0.281	91.64	86.36	7.96	0.94
HESS J1731−347	0.20	27	50428	0.307	15.51	11.49	2.64	0.74
HESS J1745−290‡	0.20	189	91544	0.552	50.54	138.46	14.88	2.74
HESS J1747−281	0.20	86	143840	0.465	67.06	18.94	2.23	0.29
HESS J1804−216	0.31	96	164665	0.351	57.99	38.01	4.57	0.66
HESS J1809−193	0.31	124	91752	0.488	44.88	79.12	9.69	1.77
HESS J1813−178	0.20	70	137576	0.344	47.28	22.72	3.08	0.48
HESS J1825−137	0.40	337	282412	0.514	145.13	191.87	13.55	1.32
HESS J1826−130	0.30	162	349992	0.262	91.96	70.04	6.61	0.77
HESS J1826−148	0.20	49	49297	0.529	26.09	22.91	3.99	0.88
HESS J1837−069	0.31	121	134372	0.540	72.63	48.37	5.18	0.67
HESS J1841−055	0.44	224	258983	0.570	147.91	76.09	5.83	0.52
HESS J1849−000	0.27	93	183080	0.302	55.30	37.70	4.61	0.68
HESS J1852−000	0.31	127	284161	0.305	86.80	40.20	4.04	0.46
HESS J1858+020	0.31	119	239923	0.359	85.84	33.16	3.35	0.38
HESS J1908+063*	0.80	1519	3976864	0.331	1319.83	199.17	5.43	0.15

Table B.4: The characteristics obtained for the high-energy analysis with 4° maximum event offset. Continuation of Table B.3. For the explanation of † ‡ and * markings see the beginning of this section.

Source name	Size [deg]	Non	Noff	Alpha $\times 10^{-3}$	Background	Excess	Significance [σ]	S/N
HESS J0835−455*	1.10	1664	1715731	0.354	613.21	1050.79	35.18	1.74
HESS J0852−463*	1.22	1100	1643702	0.453	737.04	362.96	12.16	0.48
HESS J1018−589 A	0.20	36	122387	0.174	21.29	14.71	2.91	0.69
HESS J1023−575	0.41	206	558468	0.204	113.86	92.14	7.73	0.81
HESS J1026−582	0.38	239	653444	0.223	145.56	93.44	7.08	0.64
HESS J1302−638	0.20	111	176449	0.205	36.36	74.64	9.95	2.07
HESS J1303−631	0.44	577	761746	0.391	295.17	281.83	14.33	0.94
HESS J1356−645	0.48	157	337005	0.214	72.07	84.93	8.62	1.17
HESS J1418−609†	0.18	54	74560	0.288	21.47	32.53	5.88	1.52
HESS J1420−607†	0.18	60	75231	0.331	24.91	35.09	5.94	1.41
HESS J1442−624	0.22	62	222594	0.186	41.34	20.66	2.98	0.50
HESS J1457−593	0.44	455	566358	0.528	297.75	157.25	8.35	0.52
HESS J1458−608	0.27	178	506229	0.286	144.94	33.06	2.66	0.23
HESS J1507−622	0.26	100	293124	0.257	75.48	24.52	2.69	0.32
HESS J1514−591	0.27	271	241636	0.350	85.04	185.96	16.05	2.20
HESS J1614−518	0.31	40	55146	0.279	15.36	24.64	5.22	1.60
HESS J1616−508	0.26	33	29598	0.444	13.29	19.71	4.59	1.51
HESS J1632−478	0.28	59	55112	0.523	28.99	30.01	4.92	1.05
HESS J1634−472	0.36	107	96539	0.454	44.32	62.68	8.04	1.44

Table B.5: The characteristics obtained for the high-energy analysis with 3° maximum event offset. For the explanation of † ‡ and * markings see the beginning of this section.

Source name	Size [deg]	Non	Noff	Alpha $\times 10^{-3}$	Background	Excess	Significance [σ]	S/N
HESS J1640−465†	0.15	25	22746	0.333	7.57	17.43	4.98	2.30
HESS J1641−463†	0.14	10	19620	0.320	6.29	3.71	1.36	0.59
HESS J1646−458*	1.00	542	1017598	0.395	407.46	134.54	6.63	0.35
HESS J1702−420	0.30	101	123962	0.515	63.92	37.08	4.28	0.58
HESS J1708−410	0.20	48	99857	0.351	35.04	12.96	2.07	0.37
HESS J1708−443	0.25	35	57467	0.194	11.18	23.82	5.68	2.13
HESS J1713−397*	0.77	1300	1124255	0.431	484.39	815.61	30.56	1.68
HESS J1718−385	0.27	167	253279	0.336	85.04	81.96	7.83	0.96
HESS J1731−347	0.22	23	29671	0.229	6.82	16.18	4.86	2.38
HESS J1745−290‡	0.20	162	61651	0.516	31.82	130.18	16.33	4.09
HESS J1747−281	0.20	66	102707	0.430	44.31	21.69	3.06	0.49
HESS J1804−216	0.27	61	69861	0.435	30.36	30.64	4.88	1.01
HESS J1809−193	0.31	121	80139	0.492	39.41	81.59	10.41	2.07
HESS J1813−178	0.26	57	70287	0.343	24.08	32.92	5.69	1.37
HESS J1825−137	0.40	276	185528	0.485	90.12	185.88	15.69	2.06
HESS J1826−130	0.30	129	203852	0.319	65.08	63.92	6.97	0.98
HESS J1826−148	0.20	45	37547	0.497	18.68	26.32	5.15	1.41
HESS J1837−069	0.40	154	154764	0.555	85.92	68.08	6.60	0.79
HESS J1841−055	0.44	132	142119	0.537	76.59	55.41	5.77	0.73
HESS J1849−000	0.27	79	116071	0.355	41.14	37.86	5.22	0.92
HESS J1852−000	0.22	59	98077	0.319	31.28	27.72	4.41	0.89
HESS J1858+020	0.27	65	113689	0.365	41.49	23.51	3.36	0.56
HESS J1908+063*	0.80	945	2172207	0.340	741.05	203.95	7.26	0.28

Table B.6: The characteristics obtained for the high-energy analysis with 3° maximum event offset. Continuation of Table B.5. For the explanation of † ‡ and * markings see the beginning of this section.

Source name	Size [deg]	Non	Noff	Alpha $\times 10^{-3}$	Background	Excess	Significance [σ]	S/N
HESS J0835−455*	1.10	1409	1195960	0.428	516.95	892.05	32.53	1.75
HESS J0852−463*	1.28	620	699348	0.559	389.34	230.66	10.67	0.59
HESS J1018−589 A	0.20	32	85588	0.203	17.38	14.62	3.14	0.85
HESS J1023−575	0.35	131	277982	0.220	60.86	70.14	7.75	1.15
HESS J1026−582	0.27	94	171132	0.241	41.20	52.80	7.02	1.28
HESS J1302−638	0.20	108	173386	0.195	33.96	74.04	10.12	2.19
HESS J1303−631	0.41	522	543946	0.449	244.07	277.93	15.40	1.14
HESS J1356−645	0.36	73	83304	0.207	17.21	55.79	9.96	3.24
HESS J1418−609†	0.18	35	31463	0.202	6.36	28.64	7.88	4.50
HESS J1420−607†	0.18	32	29358	0.200	5.88	26.12	7.50	4.45
HESS J1442−624	0.27	59	246460	0.136	33.66	25.34	3.95	0.75
HESS J1457−593	0.54	348	383744	0.565	213.45	134.55	8.18	0.61
HESS J1458−608	0.22	46	96690	0.242	23.58	22.42	4.11	0.96
HESS J1507−622	0.26	31	64543	0.211	13.66	17.34	4.02	1.27
HESS J1514−591	0.27	163	97566	0.313	30.76	132.24	16.75	4.33
HESS J1614−518	0.31	26	20845	0.330	6.90	19.10	5.56	2.78
HESS J1616−508	0.36	36	23456	0.401	9.60	26.40	6.59	2.83
HESS J1632−478	0.28	32	19440	0.607	11.82	20.18	4.84	1.71
HESS J1634−472	0.36	70	36701	0.552	20.42	49.58	8.61	2.46

Table B.7: The characteristics obtained for the high-energy analysis with 2° maximum event offset. For the explanation of † ‡ and * markings see the beginning of this section.

Source name	Size [deg]	Non	Noff	Alpha $\times 10^{-3}$	Background	Excess	Significance [σ]	S/N
HESS J1640−465†	0.15	20	18246	0.345	6.29	13.71	4.34	2.18
HESS J1641−463†	0.14	9	14772	0.344	5.07	3.93	1.57	0.77
HESS J1646−458*	1.00	381	557722	0.484	271.30	109.70	6.36	0.41
HESS J1702−420	0.30	24	13162	0.280	3.66	20.34	7.02	5.51
HESS J1708−410	0.20	35	43725	0.404	17.63	17.37	3.64	0.98
HESS J1708−443	0.25	24	44829	0.158	7.09	16.91	4.97	2.38
HESS J1713−397*	0.68	1081	672752	0.499	334.96	746.04	32.19	2.22
HESS J1718−385	0.27	109	86961	0.484	41.97	67.03	8.58	1.59
HESS J1731−347	0.22	21	23266	0.224	5.23	15.77	5.19	3.03
HESS J1745−290‡	0.20	147	55961	0.525	29.37	117.63	15.42	4.00
HESS J1747−281	0.20	48	69686	0.477	33.26	14.74	2.40	0.44
HESS J1804−216	0.27	27	20607	0.526	10.86	16.14	4.12	1.49
HESS J1809−193	0.31	101	58107	0.520	30.15	70.85	10.11	2.34
HESS J1813−178	0.22	27	19850	0.415	8.22	18.78	5.15	2.28
HESS J1825−137	0.40	241	119550	0.693	82.50	158.50	14.07	1.91
HESS J1826−130	0.30	82	38491	0.666	25.85	56.15	8.82	2.20
HESS J1826−148	0.20	38	34461	0.515	17.76	20.24	4.17	1.14
HESS J1837−069	0.51	154	138612	0.612	84.99	69.01	6.73	0.82
HESS J1841−055	0.40	94	61987	0.679	41.75	52.25	6.87	1.23
HESS J1849−000	0.27	48	54777	0.383	20.96	27.04	5.04	1.29
HESS J1852−000	0.27	49	61418	0.347	21.31	27.69	5.12	1.30
HESS J1858+020	0.27	34	48256	0.418	20.09	13.91	2.80	0.69
HESS J1908+063*	0.80	454	905118	0.375	340.76	113.24	5.91	0.34

Table B.8: The characteristics obtained for the high-energy analysis with 2° maximum event offset. Continuation of Table B.7. For the explanation of † ‡ and * markings see the beginning of this section.

Source name	Size [deg]	Non	Noff	Alpha $\times 10^{-3}$	Background	Excess	Significance [σ]	S/N
HESS J0835−455*	0.87	1087	727392	0.524	382.13	704.87	29.40	1.85
HESS J0852−463*	1.22	609	722426	0.572	414.03	194.97	8.99	0.47
HESS J1018−589 A	0.20	38	102367	0.256	26.18	11.82	2.17	0.45
HESS J1023−575	0.35	141	312347	0.267	83.24	57.76	5.75	0.69
HESS J1026−582	0.27	117	186096	0.278	51.53	65.47	7.78	1.26
HESS J1302−638	0.20	107	174275	0.362	63.10	43.90	5.03	0.70
HESS J1303−631	0.38	495	499858	0.545	272.66	222.34	12.08	0.82
HESS J1356−645	0.40	95	141810	0.230	32.72	62.28	8.85	1.91
HESS J1418−609†	0.18	31	33515	0.241	8.06	22.94	6.13	2.84
HESS J1420−607†	0.18	34	33760	0.241	8.14	25.86	6.75	3.18
HESS J1442−624	0.31	108	359078	0.219	78.82	29.18	3.14	0.37
HESS J1457−593	0.54	329	367424	0.544	199.90	129.10	8.34	0.65
HESS J1458−608	0.22	56	100060	0.271	27.18	28.82	4.84	1.06
HESS J1507−622	0.26	42	55465	0.264	14.47	27.53	5.81	1.87
HESS J1514−591	0.22	121	63702	0.384	24.59	96.41	13.92	3.95
HESS J1614−518	0.26	17	15001	0.386	5.78	11.22	3.77	1.94
HESS J1616−508	0.31	30	20330	0.512	10.38	19.62	4.93	1.88
HESS J1632−478	0.28	38	32902	0.591	19.44	18.56	3.71	0.95
HESS J1634−472	0.36	97	67949	0.553	37.52	59.48	8.07	1.58

Table B.9: The characteristics obtained for the standard analysis with 2° maximum event offset. For the explanation of † ‡ and * markings see the beginning of this section.

Source name	Size [deg]	Non	Noff	Alpha $\times 10^{-3}$	Background	Excess	Significance [σ]	S/N
HESS J1640−465†	0.15	32	22405	0.416	9.33	22.67	5.79	2.43
HESS J1641−463†	0.14	19	19066	0.423	8.06	10.94	3.27	1.36
HESS J1646−458*	1.00	500	678967	0.547	372.42	127.58	6.33	0.35
HESS J1702−420	0.30	15	8866	0.345	3.06	11.94	4.88	3.91
HESS J1708−410	0.22	46	67290	0.475	32.02	13.98	2.33	0.44
HESS J1708−443	0.21	23	38361	0.207	7.96	15.04	4.33	1.89
HESS J1713−397*	0.63	1079	869938	0.574	499.05	579.95	22.43	1.16
HESS J1718−385	0.27	111	95427	0.528	50.44	60.56	7.35	1.20
HESS J1731−347	0.22	20	27210	0.316	8.62	11.38	3.31	1.33
HESS J1745−290‡	0.20	129	78858	0.570	44.96	84.04	10.18	1.87
HESS J1747−281	0.20	49	69373	0.576	39.96	9.04	1.38	0.23
HESS J1804−216	0.27	25	17073	0.518	8.86	16.14	4.43	1.83
HESS J1809−193	0.36	118	80443	0.557	44.72	73.28	9.06	1.64
HESS J1813−178	0.26	29	20377	0.423	8.60	20.40	5.44	2.37
HESS J1825−137	0.40	213	117217	0.695	81.28	131.72	12.09	1.62
HESS J1826−130	0.30	78	40331	0.709	28.71	49.29	7.59	1.73
HESS J1826−148	0.20	44	40259	0.611	24.61	19.39	3.52	0.79
HESS J1837−069	0.40	73	75755	0.597	45.27	27.73	3.79	0.61
HESS J1841−055	0.44	86	82868	0.602	49.84	36.16	4.63	0.72
HESS J1849−000	0.31	61	68055	0.417	28.32	32.68	5.30	1.15
HESS J1852−000	0.22	42	47347	0.367	17.38	24.62	4.99	1.42
HESS J1858+020	0.22	29	32379	0.417	13.52	15.48	3.65	1.15
HESS J1908+063*	0.80	449	907900	0.396	361.51	87.49	4.56	0.25

Table B.10: The characteristics obtained for the standard analysis with 2° maximum event offset. Continuation of Table B.9. For the explanation of † ‡ and * markings see the beginning of this section.

B.4 Identifications of sources above 10 TeV

Source name	Source class	Identified object	Reference
HESS J1018−589 A	Binary	1FGL J1018.6−5856	[23]
HESS J1302−638	Binary	PSR B1259−63	[9]
HESS J1826−148	Binary	LS 5039	[42]
HESS J0852−463	SNR	Vela Junior	[39]
HESS J1442−624	SNR	RCW 86	[26]
HESS J1713−397	SNR	RX J1713.7−3946	[38]
HESS J1731−347	SNR	G353.6−0.7	[15]
HESS J0835−455	PWN	Vela X	[45]
HESS J1303−631	PWN	G304.10−0.24	[20]
HESS J1356−645	PWN	G309.92−2.51	[17]
HESS J1418−609	PWN	G313.32+0.13	[43]
HESS J1420−607	PWN	G313.54+0.23	[43]
HESS J1514−591	PWN	MSH 15−52	[40]
HESS J1825−137	PWN	G18.00−0.69	[44]
HESS J1837−069	PWN	G25.24−0.19	[157]
HESS J1849−000	PWN	G32.64+0.53	[178]
HESS J1640−465	Composite	G338.3−0.0	[22]
HESS J1813−178	Composite	G12.8−0.0	[105, 114]

Table B.11: A list of the firmly identified HGPS sources above 10 TeV [5].

Source name	Source class	Reference
HESS J1023−575	Not firmly identified	[14]
HESS J1026−582	Not firmly identified	[14]
HESS J1458−608	Not firmly identified	[91]
HESS J1507−622	Not firmly identified	[28]
HESS J1614−518	Not firmly identified	[47]
HESS J1616−508	Not firmly identified	[47]
HESS J1632−478	Not firmly identified	[47]
HESS J1634−472	Not firmly identified	[47]
HESS J1646−458	Not firmly identified	[19]
HESS J1708−443	Not firmly identified	[16]
HESS J1718−385	Not firmly identified	[48]
HESS J1745−290	Not firmly identified	[25]
HESS J1804−216	Not firmly identified	[47]
HESS J1809−193	Not firmly identified	[48]
HESS J1826−130	Not firmly identified	[1]
HESS J1841−055	Not firmly identified	[49]
HESS J1852−000	Not firmly identified	[145]
HESS J1908+063	Not firmly identified	[51]
HESS J1457−593	Not associated	[137]
HESS J1702−420	Not associated	[47]
HESS J1708−410	Not associated	[47]
HESS J1858+020	Not associated	[49]

Table B.12: A list of the HGPS sources above 10 TeV without firm identification or association [5].

Bibliography

[1] H. Abdalla et al. An extreme particle accelerator in the Galactic plane: HESS J1826−130. Forthcoming.

[2] H. Abdalla et al. Deeper H.E.S.S. observations of Vela Junior (RX J0852.0−4622): Morphology studies and resolved spectroscopy. *A&A*, 612:A7, 2018.

[3] H. Abdalla et al. First ground-based measurement of sub-20 GeV to 100 GeV γ-rays from the Vela pulsar with H.E.S.S. II. *A&A*, 620:A66, 2018.

[4] H. Abdalla et al. Population study of Galactic supernova remnants at very high energies with H.E.S.S. *A&A*, 612:A3, 2018.

[5] H. Abdalla et al. The H.E.S.S. Galactic plane survey. *A&A*, 612:A1, 2018.

[6] H. Abdalla et al. The population of TeV pulsar wind nebulae in the H.E.S.S. Galactic Plane Survey. *A&A*, 612:A2, 2018.

[7] H. Abdalla et al. H.E.S.S. and *Suzaku* observations of the Vela X pulsar wind nebula. *A&A*, 627:A100, 2019.

[8] H. Abdalla et al. Resolving the Crab pulsar wind nebula at teraelectronvolt energies. *Nature Astronomy*, 4(2):167–173, 2019.

[9] H. Abdalla et al. H.E.S.S. and *Fermi*-LAT observations of PSR B1259−63/LS 2883 during its 2014 and 2017 periastron passages. *A&A*, 633:A102, 2020.

[10] A. U. Abeysekara et al. Observation of the Crab Nebula with the HAWC Gamma-Ray Observatory. *The Astrophysical Journal*, 843(1):39, 2017.

[11] A. U. Abeysekara et al. The 2HWC HAWC Observatory Gamma-Ray Catalog. *The Astrophysical Journal*, 843(1):40, 2017.

[12] A. U. Abeysekara et al. Measurement of the Crab Nebula Spectrum Past 100 TeV with HAWC. *The Astrophysical Journal*, 881(2):134, 2019.

[13] A. U. Abeysekara et al. Multiple Galactic Sources with Emission Above 56 TeV Detected by HAWC. *Physical Review Letters*, 124(2), 2020.

[14] A. Abramowski et al. Revisiting the Westerlund 2 field with the H.E.S.S. telescope array. *A&A*, 525:A46, 2010.

[15] A. Abramowski et al. A new SNR with TeV shell-type morphology: HESS J1731−347. *A&A*, 531:A81, 2011.

[16] A. Abramowski et al. Detection of very-high-energy emission from the vicinity of PSR B1706−44 and G343.1−2.3 with H.E.S.S. *A&A*, 528:A143, 2011.

[17] A. Abramowski et al. Discovery of the source HESS J1356−645 associated with the young and energetic PSR J1357−6429. *A&A*, 533:A103, 2011.

[18] A. Abramowski et al. H.E.S.S. observations of the globular clusters NGC 6388 and M 15 and search for a Dark Matter signal. *The Astrophysical Journal*, 735(1):12, 2011.

[19] A. Abramowski et al. Discovery of extended VHE emission from the vicinity of the young massive stellar cluster Westerlund 1. *A&A*, 537:A114, 2012.

[20] A. Abramowski et al. Identification of HESS J1303−631 as a pulsar wind nebula through gamma-ray, X-ray, and radio observations. *A&A*, 548:A46, 2012.

[21] A. Abramowski et al. Discovery of the hard spectrum VHE γ-ray source HESS J1641−463. *The Astrophysical Journal*, 794(1):L1, 2014.

[22] A. Abramowski et al. HESS J1640−465 – an exceptionally luminous TeV gamma-ray supernova remnant. *Monthly Notices of the Royal Astronomical Society*, 439(3):2828–2836, 2014.

[23] A. Abramowski et al. Discovery of variable VHE γ-ray emission from the binary system 1FGL J1018.6−5856. *A&A*, 577:A131, 2015.

[24] A. Abramowski et al. Probing the gamma-ray emission from HESS J1834−087 using H.E.S.S. and *Fermi*-LAT observations. *A&A*, 574:A27, 2015.

[25] A. Abramowski et al. Acceleration of petaelectronvolt protons in the Galactic Centre. *Nature*, 531(7595):476–479, 2016.

[26] A. Abramowski et al. Detailed spectral and morphological analysis of the shell type supernova remnant RCW 86. *A&A*, 612:A4, 2018.

[27] P. Abreu et al. The Southern Wide-Field Gamma-Ray Observatory (SWGO): A Next-Generation Ground-Based Survey Instrument for VHE Gamma-Ray Astronomy. 2019.

[28] F. Acero et al. Discovery and follow-up studies of the extended, off-plane, VHE gamma-ray source HESS J1507−622. *A&A*, 525:A45, 2011.

[29] F. Acero et al. A new nearby pulsar wind nebula overlapping the RX J0852.0−4622 supernova remnant. *A&A*, 551:A7, 2013.

[30] B. S. Acharya et al. *Science with the Cherenkov Telescope Array*. World Scientific, 2019.

[31] M. Ackermann et al. The First *Fermi*-LAT Catalog of Sources Above 10 GeV. *The Astrophysical Journal Supplement Series*, 209(2):34, 2013.

[32] M. Ackermann et al. 2FHL: The Second Catalog of Hard *Fermi*-LAT Sources. *The Astrophysical Journal Supplement Series*, 222(1):5, 2016.

[33] R. Adam et al. Planck 2015 results – X. Diffuse component separation: Foreground maps. *A&A*, 594:A10, 2016.

[34] C. C. Aggarwal. *Neural Networks and Deep Learning*. Springer, Cham, 2018.

[35] F. A. Aharonian et al. Evidence for TeV gamma ray emission from Cassiopeia A. *A&A*, 370(1):112–120, 2001.

[36] F. A. Aharonian et al. A search for TeV gamma-ray emission from SNRs, pulsars and unidentified GeV sources in the Galactic plane in the longitude range between -2° and 85° . *A&A*, 395(3):803–811, 2002.

[37] F. A. Aharonian et al. Calibration of cameras of the H.E.S.S. detector. *Astroparticle Physics*, 22:109–125, 2004.

[38] F. A. Aharonian et al. High-energy particle acceleration in the shell of a supernova remnant. *Nature*, 432(7013):75–77, 2004.

[39] F. A. Aharonian et al. Detection of TeV gamma-ray emission from the shell-type supernova remnant RX J0852.0-4622 with H.E.S.S. *A&A*, 437(1):L7–L10, 2005.

[40] F. A. Aharonian et al. Discovery of extended VHE gamma-ray emission from the asymmetric pulsar wind nebula in MSH 15−52 with H.E.S.S. *A&A*, 435(1):L17–L20, 2005.

[41] F. A. Aharonian et al. H.E.S.S. observations of PKS 2155−304. *A&A*, 430(3):865–875, 2005.

[42] F. A. Aharonian et al. 3.9 day orbital modulation in the TeV γ-ray flux and spectrum from the X-ray binary LS 5039. *A&A*, 460(3):743–749, 2006.

[43] F. A. Aharonian et al. Discovery of the two 'wings' of the Kookaburra complex in VHEs with H.E.S.S. *A&A*, 456(1):245–251, 2006.

[44] F. A. Aharonian et al. Energy dependent morphology in the pulsar wind nebula HESS J1825−137. *A&A*, 460(2):365–374, 2006.

[45] F. A. Aharonian et al. First detection of a VHE gamma-ray spectral maximum from a cosmic source: H.E.S.S. discovery of the Vela X nebula. *A&A*, 448(2):L43–L47, 2006.

[46] F. A. Aharonian et al. Observations of the Crab nebula with H.E.S.S. *A&A*, 457:899–915, 2006.

[47] F. A. Aharonian et al. The H.E.S.S. Survey of the Inner Galaxy in Very High Energy Gamma Rays. *The Astrophysical Journal*, 636(2):777–797, 2006.

[48] F. A. Aharonian et al. Discovery of two candidate pulsar wind nebulae in very-high-energy gamma rays. *A&A*, 472(2):489–495, 2007.

[49] F. A. Aharonian et al. H.E.S.S. very-high-energy gamma-ray sources without identified counterparts. *A&A*, 477(1):353–363, 2008.

[50] F. A. Aharonian et al. Observations of the Sagittarius dwarf galaxy by the H.E.S.S. experiment and search for a dark matter signal. *Astroparticle Physics*, 29(1):55 – 62, 2008.

[51] F. A. Aharonian et al. Detection of very high energy radiation from HESS J1908+063 confirms the Milagro unidentified source MGRO J1908+06. *A&A*, 499(3):723–728, 2009.

[52] M. L. Ahnen et al. Performance of the MAGIC telescopes under moonlight. *Astroparticle Physics*, 94:29 – 41, 2017.

[53] M. Ajello et al. 3FHL: The Third Catalog of Hard *Fermi*-LAT Sources. *The Astrophysical Journal Supplement Series*, 232(2):18, 2017.

[54] J. Aleksić et al. Search for an extended VHE gamma-ray emission from Mrk 421 and Mrk 501 with the MAGIC Telescope. *A&A*, 524:A77, 2010.

[55] J. Aleksić et al. Performance of the MAGIC stereo system obtained with Crab Nebula data. *Astroparticle Physics*, 35(7):435–448, 2012.

[56] E. Aliu et al. Observation of Pulsed Gamma-Rays Above 25 GeV from the Crab Pulsar with MAGIC. *Science*, 322(5905):1221–1224, 2008.

[57] R. Aloisio, V. Berezinsky, and A. Gazizov. Transition from galactic to extragalactic cosmic rays. *Astroparticle Physics*, 39-40:129–143, 2012.

[58] M. Araya. GeV Emission in the Region of HESS J1809−193 and HESS J1813−178: Is H.E.S.S. J1809−193 a Proton PeVatron? *The Astrophysical Journal*, 859(1):69, 2018.

[59] S. Archambault et al. Gamma-ray observations under bright moonlight with VERITAS. *Astroparticle Physics*, 91:34 – 43, 2017.

[60] B. Aschenbach. Discovery of a young nearby supernova remnant. *Nature*, 396(1):141–142, 1998.

[61] T. Ashton et al. A NECTAr-based upgrade for the cherenkov cameras of the H.E.S.S. 12-meter telescopes. *Astroparticle Physics*, 118:102425, 2020.

[62] W. B. Atwood et al. The Large Area Telescope on the Fermi Gamma-ray Space Telescope Mission. *The Astrophysical Journal*, 697(2):1071–1102, 2009.

[63] X. Bai et al. The Large High Altitude Air Shower Observatory (LHAASO) Science White Paper. *arXiv e-prints*, page arXiv:1905.02773, 2019.

[64] A. Barrau et al. The CAT imaging telescope for very-high-energy gamma-ray astronomy. *Nuclear Instruments and Methods in Physics Research A*, 416:278–292, 1998.

[65] A. R. Bell. Turbulent amplification of magnetic field and diffusive shock acceleration of cosmic rays. *Monthly Notices of the Royal Astronomical Society*, 353(2):550–558, 2004.

[66] D. Berge. *A detailed study of the gamma-ray supernova remnant RX J1713.7−3946 with H.E.S.S.* PhD thesis, Ruperto-Carola University of Heidelberg, 2006.

[67] D. Berge, S. Funk, and J. Hinton. Background modelling in very-high-energy γ-ray astronomy. *A&A*, 466(3):1219–1229, 2007.

[68] K. Bernlöhr. Home page. `https://www.mpi-hd.mpg.de/hfm/~bernlohr/index.html.en`.

[69] K. Bernlöhr. `sim_telarray`: Home page. `https://www.mpi-hd.mpg.de/hfm/~bernlohr/sim_telarray/`.

[70] K. Bernlöhr. Impact of atmospheric parameters on the atmospheric Cherenkov technique. *Astroparticle Physics*, 12(4):255–268, 2000.

[71] K. Bernlöhr. Geomagnetic effects on showers relevant for the H.E.S.S. experiment. *H.E.S.S. internal note*, 2005.

[72] K. Bernlöhr. Simulation of imaging atmospheric Cherenkov telescopes with CORSIKA and `sim_telarray`. *Astroparticle Physics*, 30(3):149–158, 2008.

[73] K. Bernlöhr. *CORSIKA and `sim_telarray` – Simulation of the imaging atmospheric Cherenkov technique*, Last revised: 2019.

[74] K. Bernlöhr et al. The optical system of the H.E.S.S. imaging atmospheric Cherenkov telescopes, Part 1: Layout and components of the system. *Astroparticle Physics*, 20:111–128, 2003.

[75] J. Bolmont et al. The camera of the fifth H.E.S.S. telescope. Part I: System description. *Nuclear Instruments and Methods in Physics Research Section A*, 761:46–57, 2014.

[76] R. Brun and F. Rademakers. ROOT – An object oriented data analysis framework. *Nuclear Instruments and Methods in Physics Research Section A*, 389(1):81–86, 1997. `http://root.cern.ch/`.

[77] M. Capasso et al. The TeV supernova remnant shell HESS J1731−347 and its surroundings. *AIP Conference Proceedings*, 1792(1):040026, 2017.

[78] S. Carrigan, C. Deil, and H. Gast. New methods implemented in `hap` for the Galactic Plane Survey: Adaptive ring background method, Automatically generated exclusion maps, Flux maps. *H.E.S.S. internal note*, 2012.

[79] J.-M. Casandjian and I. A. Grenier. A revised catalogue of EGRET γ-ray sources. *A&A*, 489(2):849–883, 2008.

[80] P. M. Chadwick et al. Geomagnetic effects on atmospheric Cherenkov images. *Journal of Physics G: Nuclear and Particle Physics*, 25(6):1223–1233, 1999.

[81] R. Chalme-Calvet, M. de Naurois, and J.-P. Tavernet. Muon efficiency of the H.E.S.S. telescope, 2014.

[82] M. Chernyakova and D. Malyshev. Gamma-ray binaries, 2020.

[83] B. Condon et al. Detection of Two TeV Shell-type Remnants at GeV Energies with *Fermi*-LAT: HESS J1731−347 and SN 1006. *The Astrophysical Journal*, 851(2):100, 2017.

[84] R. Cornils et al. The optical system of the H.E.S.S. imaging atmospheric Cherenkov telescopes, Part 2: Mirror alignment and point spread function. *Astroparticle Physics*, 20:129–143, 2003.

[85] CORSIKA. COsmic Ray SImulations for KAscade: Home page. `https://www.ikp.kit.edu/corsika/index.php`.

[86] CTA Collaboration. Cherenkov Telescope Array: Home page. `https://www.cta-observatory.org/`.

[87] Y. Cui et al. Is the SNR HESS J1731−347 Colliding with Molecular Clouds? *The Astrophysical Journal*, 887(1):47, 2019.

[88] Y. Cui, G. Pühlhofer, and A. Santangelo. A young supernova remnant illuminating nearby molecular clouds with cosmic rays. *A&A*, 591:A68, 2016.

[89] A. Daum. First results on the performance of the HEGRA IACT array. 1997.

[90] O. C. de Jager and A. Djannati-Ataï. *Implications of H.E.S.S. Observations of Pulsar Wind Nebulae*, volume 357 of *Astrophysics and Space Science Library*, page 451. 2009.

[91] R. de los Reyes, A. Zajczyk, and R. C. G. Chaves. A newly discovered VHE gamma-ray PWN candidate around PSR J1459−60. *Proceedings of the 32nd International Cosmic Ray Conference*, 7, 2012.

[92] M. de Naurois and L. Rolland. A high performance likelihood reconstruction of γ-rays for imaging atmospheric Cherenkov telescopes. *Astroparticle Physics*, 32(5):231–252, 2009.

[93] J. P. Denance et al. Proposal for the H.E.S.S. experiment electronics (LPNHE-PARIS). *H.E.S.S. internal note*, 1999.

[94] P. Doll et al. The Karlsruhe cosmic ray project KASCADE. Report KfK 4686, Kernforschungszentrum Karlsruhe, 1990.

[95] E. Domingo-Santamaria et al. The DISP analysis method for point-like or extended gamma source searches/studies with the MAGIC Telescope. *Proceedings of the 29th International Cosmic Ray Conference*, 5:363–366, 2005.

[96] V. Doroshenko et al. *XMM-Newton* observations of the non-thermal supernova remnant HESS J1731−347 (G353.6−0.7). *A&A*, 608:A23, 2017.

[97] G. Dubus. Gamma-ray binaries and related systems. *The Astronomy and Astrophysics Review*, 21(1), 2013.

[98] G. Dubus. Gamma-ray emission from binaries in context. *Comptes Rendus Physique*, 16(6):661–673, 2015.

[99] L. Duvidovich, A. Petriella, and E. Giacani. Radio study of the extended TeV source VER J1907+062. *Monthly Notices of the Royal Astronomical Society*, 491(4):5732–5739, 2019.

[100] T. Edwards. *Separation of γ-Ray, Electron and Proton induced Air Showers applied to Diffuse Emission Studies with H.E.S.S.* PhD thesis, Ruperto-Carola University of Heidelberg, 2017.

[101] G. Ferrand and S. Safi-Harb. A census of high-energy observations of Galactic supernova remnants. *Advances in Space Research*, 49(9):1313–1319, 2012. `http://snrcat.physics.umanitoba.ca/`.

[102] V. P. Fomin et al. New methods of atmospheric Cherenkov imaging for gamma-ray astronomy. I. The false source method. *Astroparticle Physics*, 2(2):137–150, 1994.

[103] Y. Freund and R. E. Schapire. A Decision-Theoretic Generalization of On-Line Learning and an Application to Boosting. *Journal of Computer and System Sciences*, 55(1):119–139, 1997.

[104] S. Funk et al. The Trigger system of the H.E.S.S. Telescope array. *Astroparticle Physics*, 22:285–296, 2004.

[105] S. Funk et al. *XMM-Newton* observations of HESS J1813−178 reveal a composite Supernova remnant. *A&A*, 470(1):249–257, 2007.

[106] S. Funk, J. A. Hinton, and CTA Consortium. Comparison of Fermi-LAT and CTA in the region between 10 - 100 GeV. *Astroparticle Physics*, 43:348–355, 2013.

[107] S. Gabici and F. A. Aharonian. Searching for Galactic Cosmic-Ray PeVatrons with Multi-TeV Gamma Rays and Neutrinos. *The Astrophysical Journal*, 665(2):L131–L134, 2007.

[108] B. M. Gaensler and P. O. Slane. The evolution and structure of pulsar wind nebulae. *Annual Review of Astronomy and Astrophysics*, 44(1):17–47, 2006.

[109] Y. Gallant et al., 2020. Observation proposal.

[110] H. Gast. A new lookup scheme for `hap`. *H.E.S.S. internal note*, 2012.

[111] G. Giavitto, 2016. Private communication.

[112] S. Gillessen. *Sub-Bogenminuten-genaue Positionen von TeV-Quellen mit H.E.S.S.* PhD thesis, Ruperto-Carola University of Heidelberg, 2004.

[113] N. Globus, D. Allard, and E. Parizot. A complete model of the cosmic ray spectrum and composition across the galactic to extragalactic transition. *Physical Review D*, 92(2), 2015.

[114] E. V. Gotthelf and J. P. Halpern. Discovery of a Highly Energetic X-ray Pulsar Powering HESS J1813−178 in the Young Supernova Remnant G12.82−0.02. *The Astrophysical Journal*, 700(2):L158–L161, 2009.

[115] D. A. Green. A revised catalogue of 294 Galactic supernova remnants. *Journal of Astrophysics and Astronomy*, 40(4):36, 2019. `http://www.mrao.cam.ac.uk/surveys/snrs/`.

[116] P. K. F. Grieder. *Extensive Air Showers: Volume 1.* Springer-Verlag Berlin Heidelberg, 2010.

[117] P. K. F. Grieder. *Extensive Air Showers: Volume 2*. Springer-Verlag Berlin Heidelberg, 2010.

[118] E. Gross and O. Vitells. Trial factors for the look elsewhere effect in high energy physics. *The European Physical Journal C*, 70(1-2):525–530, 2010.

[119] J. Hahn et al. Heidelberg Data Quality Selection. *H.E.S.S. internal note*, 2013.

[120] J. P. Halpern and E. V. Gotthelf. Two Magnetar Candidates In H.E.S.S. Supernova Remnants. *The Astrophysical Journal*, 710(2):941–947, 2010.

[121] Hamamatsu Photonics K. K. *Photomultiplier Tubes*. Hamamatsu Photonics K. K. Electron Tube Division, 3a edition, 2007.

[122] T. Hassan et al. Monte Carlo performance studies for the site selection of the Cherenkov Telescope Array. *Astroparticle Physics*, 93:76–85, 2017.

[123] HAWC Collaboration. High-Altitude Water Cherenkov Gamma-Ray Observatory: Home page. `https://www.hawc-observatory.org/`.

[124] D. Heck et al. CORSIKA: a Monte Carlo code to simulate extensive air showers. Report FZKA 6019, Forschungszentrum Karlsruhe, 1998.

[125] D. Heck and T. Pierog. *Extensive Air Shower Simulation with CORSIKA: A User´s Guide*, Last revised: 2019.

[126] W. Heitler. *Quantum theory of radiation*. Dover Publications; Third edition (October 18, 2010), 3rd edition, 2010.

[127] E. A. Helder et al. Observational Signatures of Particle Acceleration in Supernova Remnants. *Space Science Reviews*, 173(1-4):369–431, 2012.

[128] V. Hess. On the Observations of the Penetrating Radiation during Seven Balloon Flights. arXiv:1808.02927. English translation.

[129] H.E.S.S. Collaboration. H.E.S.S. Galactic Plane Survey webpage. `https://www.mpi-hd.mpg.de/hfm/HESS/hgps/`.

[130] H.E.S.S. Collaboration. High Energy Stereoscopic System: Home page. `https://www.mpi-hd.mpg.de/hfm/HESS/`.

[131] A. M. Hillas. Cerenkov light images of EAS produced by primary gamma. *International Cosmic Ray Conference*, 3, 1985.

[132] A. M. Hillas. Evolution of ground-based gamma-ray astronomy from the early days to the Cherenkov Telescope Arrays. *Astroparticle Physics*, 43:19–43, 2013.

[133] A. M. Hillas and J. R. Patterson. Characteristics and brightness of Cerenkov shower images for gamma-ray astronomy near 1 TeV. *Journal of Physics G: Nuclear and Particle Physics*, 16(8):1271–1281, 1990.

[134] A. Hillert, F. Brun, and R. D. Parsons. Improving H.E.S.S. cosmic-ray background rejection by means of a new Gamma-Ray Air Shower Parametrisation (GRASP). *PoS*, ICRC2015:775, 2016.

[135] A. Hoecker et al. TMVA: Toolkit for Multivariate Data Analysis. *PoS*, ACAT:040, 2007.

[136] W. Hofmann et al. Comparison of techniques to reconstruct VHE gamma-ray showers from multiple stereoscopic Cherenkov images. *Astroparticle Physics*, 12:135–143, 1999.

[137] P. Hofverberg et al. Discovery of VHE gamma-rays from the vicinity of the shell-type SNR G318.2+0.1 with H.E.S.S. 2011.

[138] M. Holler. *Photon Reconstruction for the H.E.S.S. 28 m Telescope and Analysis of Crab Nebula and Galactic Centre Observations*. PhD thesis, University of Potsdam, 2014.

[139] M. Holler et al. Observations of the Crab Nebula with H.E.S.S. Phase II. *PoS*, ICRC2015:847, 2016.

[140] V. Joshi, 2019. Private communication.

[141] S. Katsuda, H. Tsunemi, and K. Mori. The Slow X-Ray Expansion of the Northwestern Rim of the Supernova Remnant RX J0852.0−4622. *The Astrophysical Journal*, 678(1):L35–L38, 2008.

[142] N. Kelley-Hoskins. *A Search for Extended Gamma-Ray Emission from the Galactic Center with VERITAS*. PhD thesis, Humboldt University of Berlin, 2019.

[143] D. Klochkov et al. A non-pulsating neutron star in the supernova remnant HESS J1731−347/G353.6−0.7 with a carbon atmosphere. *A&A*, 556:A41, 2013.

[144] A. Kohnle et al. Stereoscopic imaging of air showers with the first two HEGRA Cherenkov telescopes. *Astroparticle Physics*, 5(2):119–131, 1996.

[145] K. Kosack, R. C. G. Chaves, and F. Acero. HESS J1852−000: A Very High Energy Gamma-ray source near Supernova Remnant Kes 78. In *International Cosmic Ray Conference*, volume 7 of *International Cosmic Ray Conference*, pages 76–78, 2011.

[146] M. Kramer et al. The Parkes Multibeam Pulsar Survey – III. Young pulsars and the discovery and timing of 200 pulsars. *Monthly Notices of the Royal Astronomical Society*, 342(4):1299–1324, 2003.

[147] D. P. Kroese et al. Why the Monte Carlo method is so important today. *WIREs Computational Statistics*, 6(6):386–392, 2014.

[148] S. Le Bohec et al. A new analysis method for very high definition imaging atmospheric Cherenkov telescopes as applied to the CAT telescope. *Nuclear Instruments and Methods in Physics Research A*, 416:425–437, 1998.

[149] R. Lessard et al. A new analysis method for reconstructing the arrival direction of TeV gamma rays using a single imaging atmospheric Cherenkov telescope. *Astroparticle Physics*, 15(1):1–18, 2001.

[150] T.-P. Li and Y.-Q. Ma. Analysis methods for results in gamma-ray astronomy. *The Astrophysical Journal*, 272:317–324, 1983.

[151] M. S. Longair. *High Energy Astrophysics: Volume 1, Particles, Photons and their Detection*. Cambridge University Press, 2nd edition, 2004.

[152] C.-C. Lu. *An advanced direction reconstruction technique and application to the observation with H.E.S.S.* PhD thesis, Ruperto-Carola University of Heidelberg, 2013.

[153] G. Maier. The origin of cosmic rays and TeV gamma-ray astronomy. *EPJ Web Conf.*, 52:10001, 2013.

[154] C. Maitra, F. Acero, and C. Venter. Constraining the geometry of PSR J0855−4644: A nearby pulsar wind nebula with double torus/jet morphology. *A&A*, 597:A75, 2017.

[155] C. Maitra et al. Discovery of a radio nebula around PSR J0855−4644. *Monthly Notices of the Royal Astronomical Society*, 477(1):L66–L69, 2018.

[156] R. N. Manchester et al. The Australia Telescope National Facility Pulsar Catalogue. *The Astronomical Journal*, 129(4):1993–2006, 2005. `https://www.atnf.csiro.au/research/pulsar/psrcat/`.

[157] V. Marandon et al. A closer look at HESS J1837−069 following the pulsar discovery. *AIP Conference Proceedings*, 1085(1):320–323, 2008.

[158] J. Matthews. A Heitler model of extensive air showers. *Astroparticle Physics*, 22:387–397, 2005.

[159] N. Maxted et al. Probing the local environment of the supernova remnant HESS J1731−347 with CO and CS observations. *Monthly Notices of the Royal Astronomical Society*, 474(1):662–676, 2017.

[160] N. Metropolis. The beginning of the Monte Carlo method. *Los Alamos Science*, (15):125–130, 1987.

[161] A. Mitchell. *Optical Efficiency Calibration for Inhomogeneous IACT Arrays and a Detailed Study of the Highly Extended Pulsar Wind Nebula HESS J1825−137*. PhD thesis, Ruperto-Carola University of Heidelberg, 2016.

[162] L. Mohrmann et al. Validation of open-source science tools and background model construction in γ-ray astronomy. *A&A*, 632:A72, 2019.

[163] T. Murach. *Monoscopic Analysis of H.E.S.S. Phase II Data on PSR B1259−63/LS 2883*. PhD thesis, Humboldt University of Berlin, 2017.

[164] T. Murach, M. Gajdus, and R. D. Parsons. A Neural Network-Based Monoscopic Reconstruction Algorithm for H.E.S.S. II, 2015.

[165] C. L. Naumann et al. New electronics for the cherenkov telescope array (NECTAr). *Nuclear Instruments and Methods in Physics Research Section A*, 695:44–51, 2012.

[166] S. Ohm. *Advanced gamma/hadron separation technique and application to particular gamma-ray sources with H.E.S.S.* PhD thesis, Ruperto-Carola University of Heidelberg, 2010.

[167] S. Ohm, C. van Eldik, and K. Egberts. γ/hadron separation in very-high-energy γ-ray astronomy using a multivariate analysis method. *Astroparticle Physics*, 31:383–391, 2009.

[168] R. D. Parsons, 2020. Private communication.

[169] R. D. Parsons and J. A. Hinton. A Monte Carlo template based analysis for air-Cherenkov arrays. *Astroparticle Physics*, 56:26–34, 2014.

[170] G. G. Pavlov et al. Variability of the Vela Pulsar Wind Nebula Observed with Chandra. *The Astrophysical Journal*, 554(2):L189–L192, 2001.

[171] C. Pittori et al. First AGILE catalog of high-confidence gamma-ray sources. *A&A*, 506(3):1563–1574, 2009.

[172] J. R. Quinlan. Simplifying decision trees. *International Journal of Man-Machine Studies*, 27(3):221–234, 1987.

[173] E. M. Reynoso et al. The interior of the SNR RX J0852.0−4622 (Vela Jr) at radio wavelengths. *A&A*, 449(1):243–250, 2006.

[174] P. M. Saz Parkinson et al. Eight γ-ray pulsars discovered in blind frequency searches of *Fermi*-LAT data. *The Astrophysical Journal*, 725(1):571–584, 2010.

[175] P. Slane and othes. RX J0852.0−4622: Another Nonthermal Shell-Type Supernova Remnant (G266.2−1.2). *The Astrophysical Journal*, 548(2):814–819, 2001.

[176] J. Strader et al. Optical Spectroscopy of the High-mass Gamma-Ray Binary 1FGL J1018.6−5856: A Probable Neutron Star Primary. *The Astrophysical Journal Letters*, 813(2):L26, 2015.

[177] M. Tanabashi et al. Review of Particle Physics. *Phys. Rev.*, D 98:030001, 2018.

[178] R. Terrier et al. Discovery of a pulsar wind nebula associated with IGR J18490−0000. *AIP Conference Proceedings*, 1085:312–315, 2008.

[179] TeVCat online source catalog. Home page. `http://tevcat.uchicago.edu`.

[180] W. W. Tian et al. Discovery of the Radio and X-Ray Counterpart of TeV γ-Ray Source HESS J1731-347. *The Astrophysical Journal*, 679(2):L85–L88, 2008.

[181] W. W. Tian et al. X-Ray Emission from HESS J1731−347/SNR G353.6−0.7 and Central Compact Source XMMS J173203−344518. *The Astrophysical Journal*, 712(2):790–796, 2010.

[182] L. Tomankova, 2020. Private communication.

[183] H. J. Völk and K. Bernlöhr. Imaging very high energy gamma-ray telescopes. *Experimental Astronomy*, 25(1-3):173–191, 2009.

[184] T. C. Weekes. The Atmospheric Cherenkov Imaging Technique for Very High Energy Gamma-ray Astronomy, 2005.

[185] T. C. Weekes et al. Observation of TeV Gamma Rays from the Crab Nebula Using the Atmospheric Cerenkov Imaging Technique. *The Astrophysical Journal*, 342:379, 1989.

[186] T. C. Weekes et al. VERITAS: the Very Energetic Radiation Imaging Telescope Array System. *Astroparticle Physics*, 17(2):221–243, 2002.

[187] A. Weinstein. The VERITAS Survey of the Cygnus Region of the Galactic Plane. *PoS(INTEGRAL 2010)*, 2011.

[188] J. Zorn and H.E.S.S. Collaboration. Sensitivity Improvements of Very-High-Energy Gamma-Ray Detection with the Upgraded H.E.S.S. I Cameras using Full Waveform Processing, 2019.

List of Figures

List of Tables

Acknowledgments

The last several years, I have spent working at DESY, a wonderful place full of great, motivated, open-minded people. I want to thank Prof. Christian Stegmann for giving me an opportunity to do my PhD work at DESY, which is summarised in this thesis. I am also grateful to Prof. Jamie Holder and Prof. Lutz Wisotzki for agreeing to review this thesis as well as to all members of my defence committee.

I want to say a very big thanks to my supervisor Stefan Ohm for the support through all these years. The door of his office was always open when I had questions or needed some advice. He could always find time for his student even if the daily schedule is full. Also, many-many thanks to my first PhD supervisor Stefan Klepser, who helped me to do the first steps in my research, introduced me to the H.E.S.S. experiment and collaboration. Thank you for involving me in the H.E.S.S. camera upgrade. I have learnt a lot and enjoyed the work with the upgrade team in Namibia very much, and would like to thank all of them as well as the local crew for a great time. I also want to thank David Berge for the support and help when I needed it.

I want to thank Sylvia and Heike for reading this thesis and giving me very useful comments. Also, I am very thankful to every member of the H.E.S.S. group at DESY and Uni Potsdam for the interesting and inspiring discussions during coffee and after-lunch breaks at the lakeside. I was happy to work alongside all of you. I am also grateful to members of other DESY groups for the friendly, warm and creative atmosphere.

Big thanks to Alina and Igor for their friendship, board-game weekends and our great hiking holidays. Also, I want to give thanks to Maxim for being my friend and advisor through all these years. Our conversations over a beer and sometimes disputes were very helpful and supportive for me.

I am very grateful to my family for the understanding and endless belief in me. In the end, I want to thank my husband, Andrii, who also read this thesis and gave valuable comments and suggestions. Without you, I would not achieve all that I have now. Thank you for your love and patience, for sharing all my ups and downs, pushing me forward and always supporting and encouraging me in my research.

Selbstständigkeitserklärung

Ich versichere, dass ich die vorliegende Arbeit selbständig und nur mit den angegeben Quellen und Hilfsmitteln angefertigt habe. Alle Stellen der Arbeit, die ich aus diesen Quellen und Hilfsmitteln dem Wortlaut oder dem Sinne nach entnommen habe, sind kentlich gemacht und im Literaturverzeichnis aufgeführt. Weiterhin versichere ich, dass ich die vorliegende Arbeit, weder in der vorliegenden, noch in einer mehr oder weniger abgewandelten Form, als Dissertation an einer anderen Hochschule eingereicht habe.

Potsdam Iryna Lypova